technische universität
dortmund

Dissertation
zur Erlangung des Grades
Dr. rer. nat.
im Fach Physik

Flavorful BSM from Asymptotic Safety

Tim Fabian Höhne
geboren in Mülheim a. d. Ruhr

Dortmund, März 2024

Lehrstuhl für theoretische Physik IV
Fakultät Physik
Technische Universität Dortmund

Gutachter der Dissertation:
Prof. Dr. Gudrun Hiller
Prof. Dr. Emmanuel Stamou
Prof. Dr. Michael Spannowsky

Datum der Abgabe:
08.03.2024

Vorsitzender des Promotionsausschusses:
Prof. Dr. Markus Betz

Datum der mündlichen Prüfung:
07.05.2024

Kurzfassung

Diese Dissertation beinhaltet aktuelle Anwendungen des auf der Renormierungsgruppe (RG) basierenden Konzepts der Planckskalensicherheit (PS) in der Modellbildung jenseits des Standardmodells der Teilchenphysik (SM, BSM). PS bezeichnet dabei ein RG-Laufen aller Kopplungen bis zum Quantengravitationsregime an der Planckskala ohne Vakuuminstabilitäten und Landau-Pole. Dazu muss die Metastabilität des SM Higgspotentials behoben werden. Wir gehen diese Aufgabe in minimalen SM-Erweiterungen mit vektorartigen Fermionen, Singulett-Skalaren oder beiden, mit oder ohne *flavor* an. Dazu untersuchen wir die RG-Flüsse dieser Modelle in höheren Schleifenordnungen sowie die gesamten durch BSM-Massen, -Multiplizitäten, -Ladungen und -Kopplungen aufgespannten verfügbaren Parameterräume. Dabei enthüllen und charakterisieren wir mehrere fundamentale RG-Mechanismen für PS, sowie deren Zusammenspiel. Die Forderung nach PS impliziert dann Bedingungen an die BSM-Parameter. Wir studieren auch die Beschleunigerphänomenologie unsere Modelle, insbesondere im Hinblick auf die Komplementarität zwischen phänomenologischen und PS-Bedingungen an Parameter. Danach widmen wir uns einer komplexeren Klasse von BSM Modellen, nämlich anomaliefreien, *flavor*-vollen Z'-Modellen. Das Z'-Boson kann *flavor*-verändernde neutrale Ströme auf Baumgraphenniveau induzieren, die im SM Schleifen- und Cabibbo-Kobayashi-Maskawa-unterdrückt sind. Daher sind Z'-Modelle natürliche Kandidaten um experimentell gemessene Abweichungen einiger *flavor*-Observablen von ihrer SM-Vorhersage zu erklären. Insbesondere fokussieren wir uns dabei auf die anhaltenden Anomalien im Zusammenhang mit $b \to s\mu^+\mu^-$ Übergängen sowie die unerwartet große CP- und U-Spin-Verletzung in $D^0 \to K^+K^-$, $\pi^+\pi^-$ Zerfällen. Allerdings treten in Z'-Modellen typischerweise niederenergetische Landau-Pole auf, durch die die Theorien ihre Vorhersagekraft verlieren. Wir zeigen, wie in Z'-Modellen die Anomalien im *beauty*- und *charm*-Sektor jeweils aufgelöst und gleichzeitig Landau-Pole hinter die Planckskala geschoben werden können. Dadurch ergeben sich präzise Vorhersagen für charakteristische, phänomenologische Signaturen, die an Beschleunigern gesucht werden können.

Abstract

This thesis comprises recent applications of the renormalization group (RG) based concept of Planck safety (PS) in beyond the Standard Model of particle physics (SM, BSM) model building. PS refers to a RG flow of all couplings up to the quantum gravity regime at the Planck scale without any vacuum instabilities or Landau poles. This requires to cure the metastability of the SM Higgs potential. We tackle this task in several minimal SM extensions featuring vector-like fermions, singlet scalars or both, with or without flavor. We investigate the higher loop-order RG flows of these models, scrutinizing their complete available parameter spaces spanned by BSM masses, multiplicities, charges and couplings. Thereby, we unveil and characterize several fundamental mechanisms for PS as well as their interplay. Requiring PS then results in constraints on BSM parameters. We also study the collider phenomenology of our models, focusing in particular on the complementarity between phenomenological and PS constraints. We then turn to a class of more complex BSM models, namely flavorful, anomaly-free Z' models. The Z' boson can induce flavor-changing neutral current transitions at tree-level, which in the SM are loop- and Cabibbo-Kobayashi-Maskawa-suppressed. Therefore, Z' models are natural candidates to address several experimentally measured deviations from the SM in flavor observables. In particular, we focus on the persistent anomalies in $b \to s\mu^+\mu^-$ transitions as well as the large CP and U-spin breaking in $D^0 \to K^+K^-$, $\pi^+\pi^-$ decays. On the other hand, Z' models are generically plagued by low-energy Landau poles spoiling the predictivity of the theory. We show how the flavor anomalies in the beauty and charm sector can respectively be resolved in Z' models while the notorious Landau pole is simultaneously pushed beyond the Planck scale. This results in distinct predictions of characteristic phenomenological signatures that can be searched for at colliders.

Acknowledgments

The past few years have been an amazing and fascinating time for me and I want to thank everyone who accompanied and supported me on this journey.

I am very thankful to the *Studienstiftung des Deutschen Volkes* for laying the financial foundations for this thesis by supporting me with a generous scholarship and in addition financially facilitating my participation in several international conferences. I am also very grateful for the opportunity to participate in a variety of stimulating interdisciplinary events with amazing people that broadened my perspective and were always a lot of fun.

I would like to thank my supervisor Gudrun Hiller for the possibility to work in the fascinating field of theoretical particle physics and the whole experience that came along with it. For all the ideas, research projects and the continuous support. For enabling me to go on a variety of international conferences, workshops, schools and trips which allowed me to learn a lot about physics and meet many amazing people in the scientific community from all over the world.

Thanks also to Emmanuel Stamou for accepting to be the second referee for this thesis.

A big thank you goes to my office mate Tom. Thanks for all the joint projects and discussions! Thank you also in particular for sharing all your computational codes and always helping me out when I was struggling with my laptop in order to properly use them[1].

Moreover, I would like to thank my further collaborators Daniel, Hector, Rigo and Kai. It was always a pleasure to work with you!

Thanks also to the (former) T3/T4 members Dominik H., Kai, Daniel, Sara, Lara, Mustafa, Dominik S., Max, Patrick, Jordi, Tim, Miriam, Marcel, Stefan, Nico, Dominik D., Peter, Maggi, Mathias, Dimitrios, Dennis, Kevin and Clara who made my time at the department as pleasant as it was. Thanks for all the coffee breaks, pool nights, dinners, Christmas parties and everything else!

A special thank you goes to to all the people that proofread parts of this thesis.

Finally, I want to thank all my friends and family. Thank you all for always believing in me and for your continuous support. Thanks also for all the joint free-time activities that always helped me to ease my mind and recharge my inner battery.

---

[1] Sorry, I will still stay with Windows.

Publications

This thesis is based on the following publications by the author, Refs. [1–4]:

- Rigo Bause, Gudrun Hiller, Tim Höhne, Daniel F. Litim, Tom Steudtner
  "B-anomalies from flavorful $U(1)'$ extensions, safely",
  In: *Eur. Phys. J. C* ***82*** *(2022) no.1, 42*,
  DOI: 10.1140/epjc/s10052-021-09957-1,
  e-Print: 2109.06201 [hep-ph]

- Gudrun Hiller, Tim Höhne, Daniel F. Litim, Tom Steudtner
  "Portals into Higgs vacuum stability",
  In: *Phys. Rev. D 106 (2022) 11, 115004*,
  DOI: 10.1103/PhysRevD.106.115004,
  e-Print: 2207.07737 [hep-ph]

- Rigo Bause, Hector Gisbert, Gudrun Hiller, Tim Höhne, Daniel F. Litim, Tom Steudtner
  "U-spin-CP anomaly in charm",
  In: *Phys. Rev. D 108 (2023) 3, 035005*,
  DOI: 10.1103/PhysRevD.108.035005
  e-Print: 2210.16330 [hep-ph]

- Gudrun Hiller, Tim Höhne, Daniel F. Litim, Tom Steudtner
  "Vacuum Stability in the Standard Model and Beyond",
  In: *submitted for publication* ,
  e-Print: 2401.08811 [hep-ph]

and the conference proceedings, Refs. [5, 6]:

- Gudrun Hiller, Tim Höhne, Daniel F. Litim, Tom Steudtner,
  "Vacuum Stability as a Guide for Model Building",
  Contribution to: 57th Rencontres de Moriond on Electroweak Interactions and Unified Theories (Moriond EW 2023),
  e-Print: 2305.18520 [hep-ph],
  Speaker: Daniel F. Litim

- Rigo Bause, Hector, Gisbert, Gudrun Hiller, Tim Höhne, Daniel F. Litim, Tom Steudtner,
  "Old and new Anomalies in Charm",
  Contribution to: 21st International Conference on B-Physics at Frontier Machines (Beauty2023),
  e-Print: 2309.04513 [hep-ph],
  Speaker: Tim Höhne

and the following work in preparation, Ref. [7]

- Gudrun Hiller, Tim Höhne, Daniel F. Litim, Tom Steudtner,
  "Planck Safety from Vector-like Quarks and Flavorful Scalars",

Contents

1 Introduction

Revealing the elementary building blocks of nature as well as their fundamental interactions is one of the major challenges in modern natural science and is studied in the field of elementary particle physics. An enormous joint effort from mathematics, theory and experiment in the middle of the past century resulted in the formulation of the Standard Model of particle physics (SM), unifying the strong, weak and electromagnetic forces in a quantum field theory (QFT) framework obeying the bizarre principles of quantum mechanics and special relativity. Ever since, it has been validated with great precision in a vast number of measurements by several different experiments promoting it to the most successful theory at the quantum level these days. It was completed in 2012 by the discovery of the Higgs boson [8, 9] at the Large Hadron Collider (LHC) unveiling the last postulated particle of the SM [10–13].

Despite its tremendous success, the SM cannot be the fundamental description of nature as it suffers from several shortcomings and unexplained observations. First of all, it does not incorporate a quantum theory of gravity, the force dominating the dynamics of the universe at large scales. It also lacks an explanation for dark matter and dark energy which according to cosmological observations account for 95% of the total energy of the universe [14]. Finally the amount of CP violation in the SM is orders of magnitude too low to explain the observed baryon asymmetry of the universe (BAU), i.e. the dominance of matter over antimatter [15]. Eventually, the discovery of neutrino oscillations [16, 17] evidenced tiny but non-zero neutrino masses which is incompatible with the strictly vanishing neutrino masses in the SM. The above shortcomings altogether imply the existence of physics beyond the Standard Model (BSM), whose imprints are hunted for in close interplay between theory and experiment.

Additional theoretical shortcomings of the SM are related to its renormalization group (RG) evolution. The postulation of the RG [18–23] encoding the scale dependence of couplings was a major breakthrough in formal QFT and famously allowed to simultaneously explain the phenomena of confinement and asymptotic freedom (AF) in quantum chromodynamics (QCD) [24, 25]. The running of couplings is thereby encoded in their renormalization group equations (RGEs), which can be computed in the perturbative loop expansion with systematically increasing precision. While there is a whole industry pushing this frontier by deriving general RGEs in template QFTs, e.g. [26–31], the results are encoded in software packages such as [32–35] which allow to compute the RGEs of a specific model in an automated way.

Solving the RGEs of the SM, one finds that its RG flow exhibits two unpleasant features. Firstly, in the deep ultraviolet (UV) at $\mu \simeq 10^{41}$ GeV the hypercharge coupling runs into a Landau pole, where perturbation theory breaks down and the SM looses its predictivity. Secondly, precision computations revealed that the effective Higgs potential becomes metastable around $\mu \simeq 10^{11}$ GeV [36–38]. One ansatz to avoid these shortcomings is the notion of asymptotic safety (AS) [39], demanding that couplings run into a UV fixed point. Hence, the corresponding theory is valid up to arbitrarily high energy scales. The discovery of AS in gauge-Yukawa (GY) theories [40] a decade ago then opened the door for asymptotically safe BSM model building [41–46]. Within this thesis we deploy the deduced concept of Planck safety (PS) where the requirement of a UV fixed point is relaxed to demanding a well-behaved RG flow of couplings without any Landau poles or vacuum instabilities until the the Planck scale $M_{\text{Pl}} \simeq 10^{19}$ GeV where quantum gravity effects are expected to set in. Demanding PS in a BSM model then results in constraints on model parameters which are complementary to phenomenological ones promoting PS to a promising guideline for BSM model building. The main part of this thesis is therefore devoted to analyzing the possibility of achieving PS in BSM models. In particular, we work out the basic RG mechanisms giving rise to PS in minimal models based on vector-like fermions (VLFs) and scalars. Moreover, we also investigate more sophisticated models with characteristic phenomenology which simultaneously resolve other issues of the SM.

From the phenomenological side, there are three main frontiers in the quest for new physics (NP). At the *energy frontier* mostly hadron machines such as the LHC explore energies at the TeV scale in search for the direct production of heavy BSM particles which are predicted in several BSM models. At lower energies, at the *precision frontier* experiments such as Large Hadron Collider beauty (LHCb) or BELLE-II search for small deviations of precision observables from their SM prediction. Such deviations can be caused by quantum effects of virtual NP particles and allow to also indirectly probe higher energy scales than direct searches. The correct framework for these model-independent, indirect searches are effective field theories (EFTs), in particular Weak Effective Theory (WET) and Standard Model Effective Field Theory (SMEFT), which allow to link BSM models in the UV with low-energy observables. As they can be used both in top-down and bottom-up direction they provide an ideal interface between theory and experiment. The set of frontiers is completed by the *cosmological frontier*.

While direct evidence for BSM particles is still absent, some hints are emerging at the precision frontier. Several of them are related to the field of flavor physics. In particular flavor observables related to rare flavor changing neutral current (FCNC) processes provide an excellent testing ground for BSM physics, as they are severely Cabibbo-Kobayashi-Maskawa (CKM)-, loop- and partially Glashow-Iliopolus-Maiani (GIM)-suppressed in the SM. Scrutinizing these processes in experiments revealed some systematic deviations from SM predictions in rare $b \to s\mu^+\mu^-$ transitions, which are jointly referred to as the B anomalies. In particular, several related lepton flavor universality (LFU) ratios [47–50], branching ratios [51–53], and angular observables [54, 55] were found to individually deviate from the SM at the 1-3σ level. Another puzzle recently emerged in the charm sector, where the direct CP asymmetries in hadronic $D^0 \to \pi^+\pi^-, K^+K^-$ decays [56, 57] hint at a simultaneous, severe breaking of the approximate SM CP and U-spin symmetries.

We address these anomalies in the framework of flavorful Z' models, e.g. [58–61]. They are based on extending the SM by an additional $U(1)'$ gauge symmetry mediated by a massive Z' boson. While being subject to several, severe theoretical and experimental constraints, in particular from anomaly cancellation, electroweak precision observables, meson mixing and notorious low energy Landau poles, the Z' induces tree-level FCNC couplings which are potentially able to explain the observed deviations in rare FCNC decays. Within this thesis, we therefore explore if and how the anomalies can be resolved in flavorful Z' models and whether simultaneously PS can be realized.

This thesis is based on [1–7] by the author and structured as follows: In Chap. 2 we briefly review the SM, its shortcomings as well as SM-based EFTs. Afterwards, we discuss RGEs in general gauge-Yukawa theories with special focus on the SM and introduce the concept of PS as well as our analysis workflow in Chap. 3. We then analyze whether and how PS can be realized in minimal BSM models featuring VLFs, singlet scalars or both. In Chap. 4, we focus on VLF models and identify the gauge- and Yukawa portal mechanism for PS. The subsequent Chap. 5 deals with scalar singlet extensions, that allow to achieve PS via the direct and indirect Higgs portal mechanism and have implications for Higgs phenomenology. We combine both sectors in Chap. 6, which gives rise to a novel PS mechanism based on a pure BSM Yukawa interaction. We also work out collider signatures. Chap. 7 is then devoted to an introduction to Z' models as well as a discussion of the central theoretical and phenomenological constraints. We apply these findings in context of the B anomalies in Chap. 8, where we construct Planck-safe Z' models resolving the anomalies. Afterwards, in Chap. 9 we build different Z' models, designed to resolve the U-spin-CP anomaly in hadronic charm decays. We conclude in Chap. 10. Several supplementary technical details are relegated to the appendix.

The presented research works were performed using the software packages [32, 33, 62, 63].

2 The Standard Model of Particle Physics and Beyond

Following the literature [64–66], in this chapter we briefly review the SM. We introduce the fields and interactions in Sec. 2.1, before recapitulating the mechanism of electroweak symmetry breaking (EWSB) in Sec. 2.2 and the SM flavor structure in Sec. 2.3. Afterwards, we summarize motivations for BSM physics in Sec. 2.4 and introduce the framework of EFTs in Sec. 2.5.

2.1 Fields and Interactions

The SM is a four-dimensional, renormalizable gauge QFT with local gauge group

$$\mathcal{G}_{\text{SM}} = U(1)_Y \times SU(2)_L \times SU(3)_C \,, \tag{2.1}$$

which describes all known elementary particles and their interactions except gravity at the most fundamental level. Here $SU(3)_C$ represents the strong interaction coined QCD [24, 25, 67–69] whereas $SU(2)_L \times U(1)_Y$ describes the electroweak interaction [70–72] which is spontaneously broken to the $U(1)_{\text{em}}$ of quantum electrodynamics (QED). The charges of fields under the $SU(3)_C$, $SU(2)_L$ and $U(1)_Y$ gauge interactions are referred to as color, weak isospin and hypercharge, respectively. The electric charge Q_e of a field is related to its weak isospin component T^3 and its hypercharge Y via the Gell-Mann-Nishijima relation

$$Q_e = T^3 + Y \,. \tag{2.2}$$

The field content of the SM is split into fermions of spin $\frac{1}{2}$ and bosons of spin 0 or 1. The SM fermion fields are classified according to their charges under $\mathcal{G}_{\text{SM}}$ and summarized in Tab. 2.1. They are divided into color-charged quarks and colorless leptons. According to their representation under $SU(2)_L$ it is further distinguished between left-handed (LH) quark doublets Q and right-handed (RH) singlets U, D as well as LH lepton doublets L and RH singlets E. Thus, LH and RH fermions carry different charges under $\mathcal{G}_{\text{SM}}$ rendering the SM a chiral theory, see App. A.1 for the definitions of chiral field components. The upper and lower $SU(2)_L$ components of Q and L correspond to LH up- u and down-type d quarks as well as LH neutrinos ν and charged leptons ℓ, respectively. Note that neutrinos in the SM do not have a RH counterpart. Interestingly, all SM fermion representations Q, U, D, L, E come in three different copies called *generations*, *families* or *flavors* that share the same quantum numbers and only differ in their masses.

The $U(1)_Y$, $SU(2)_L$ and $SU(3)_C$ gauge interactions between fields are mediated by spin-1 gauge bosons. These are the electroweak bosons B_μ, W^a_μ and the gluons G^b_μ, respectively, where $a = 1, 2, 3$ and $b = 1, ..., 8$ corresponding to the $N^2 - 1$ generators of the respective $SU(N)$. The SM particle content is completed by the Higgs boson H which is a complex scalar $SU(2)_L$ doublet uncharged under $SU(3)_C$.

The SM Lagrangian density can be compactly written as[1]

$$\mathcal{L}_{\text{SM}} = \mathcal{L}_{\text{G}} + \mathcal{L}_{\text{F}} + \mathcal{L}_{\text{Y}} + \mathcal{L}_{\text{H}} \,, \tag{2.3}$$

$$\mathcal{L}_{\text{G}} = -\frac{1}{4}\left(B_{\mu\nu}B^{\mu\nu} + W^a_{\mu\nu}W_a^{\mu\nu} + G^b_{\mu\nu}G_b^{\mu\nu}\right) \,, \tag{2.4}$$

$$\mathcal{L}_{\text{F}} = +\,\mathrm{i}\overline{Q}_i \not{D} Q_i + \mathrm{i}\overline{U}_i \not{D} U_i + \mathrm{i}\overline{D}_i \not{D} D_i + \mathrm{i}\overline{L}_i \not{D} L_i + \mathrm{i}\overline{E}_i \not{D} E_i \,, \tag{2.5}$$

$$\mathcal{L}_{\text{Y}} = -\,\overline{Q}_i H Y_d^{ij} D_j - \overline{Q}_i H^c Y_u^{ij} U_j - \overline{L}_i H Y_\ell^{ij} E_j + \text{h.c.} \,, \tag{2.6}$$

$$\mathcal{L}_{\text{H}} = +\,(D_\mu H)^\dagger (D^\mu H) - V_H \,, \tag{2.7}$$

---

[1] Here we omit the phenomenologically irrelevant gauge-fixing and ghost terms. Moreover, we neglect the CP violating QCD Θ-term $\Theta_{\text{QCD}} \frac{g_3^2}{32\pi^2} \epsilon^{\mu\nu\rho\sigma} G^a_{\mu\nu} G^a_{\rho\sigma}$ as it is extremely constrained by measurements of the neutron electric dipole moment [73] to $\overline{\Theta}_{\text{QCD}} \lesssim 10^{-13}$ [74].

Field	Flavors	$U(1)_Y \times SU(2)_L \times SU(3)_C$	T^3	Q_e
Q_i	$\begin{pmatrix}u\\d\end{pmatrix}_L$, $\begin{pmatrix}c\\s\end{pmatrix}_L$, $\begin{pmatrix}t\\b\end{pmatrix}_L$	$(+\frac{1}{6}, \mathbf{2}, \mathbf{3})$	$\frac{1}{2}$ $-\frac{1}{2}$	$\frac{2}{3}$ $-\frac{1}{3}$
U_i	u_R, c_R, t_R	$(+\frac{2}{3}, \mathbf{1}, \mathbf{3})$	0	$\frac{2}{3}$
D_i	d_R, s_R, b_R	$(-\frac{1}{3}, \mathbf{1}, \mathbf{3})$	0	$-\frac{1}{3}$
L_i	$\begin{pmatrix}\nu_e\\e\end{pmatrix}_L$, $\begin{pmatrix}\nu_\mu\\\mu\end{pmatrix}_L$, $\begin{pmatrix}\nu_\tau\\\tau\end{pmatrix}_L$	$(-\frac{1}{2}, \mathbf{2}, \mathbf{1})$	$\frac{1}{2}$ $-\frac{1}{2}$	0 -1
E_i	e_R, μ_R, τ_R	$(-1, \mathbf{1}, \mathbf{1})$	0	-1
H	$\begin{pmatrix}\phi^+\\\phi^0\end{pmatrix}$	$(\frac{1}{2}, \mathbf{2}, \mathbf{1})$	$\frac{1}{2}$ $-\frac{1}{2}$	1 0

Table 2.1: SM field content including the representation under the SM gauge group (2.1). Different fermion flavors ($i = 1, 2, 3$) as well as the Higgs H are indicated in terms of their $SU(2)_L$ components that differ by the associated weak isospin T^3 and electric charge Q_e. Fermion subscripts L, R refer to LH and RH chirality, respectively.

where we implicitly summed over all gauge a, b as well as flavor i, j indices and employed Feynman slash notation $\not{D} = D_\mu \gamma^\mu$ with the Dirac matrices γ^μ. $\mathcal{L}_\mathrm{G}$ (2.4) contains the kinetic terms of the gauge fields $F^l_{k,\mu} = B_\mu$, W^a_μ, G^b_μ for $k = 1$, 2, 3 with their field strength tensors

$$F^l_{k,\mu\nu} = \partial_\mu F^l_{k,\nu} - \partial_\nu F^l_{k,\mu} + \mathrm{i} g_k \, f^{lmn}_k F^m_{k,\mu} F^n_{k,\nu} \, , \tag{2.8}$$

where g_k and f^{lmn}_k correspond to the gauge couplings and structure constants of $U(1)_Y$, $SU(2)_L$ and $SU(3)_C$, respectively. Thus, for non-Abelian gauge groups with non-vanishing structure constants $\mathcal{L}_\mathrm{G}$ gives rise to gauge boson self interactions. $\mathcal{L}_\mathrm{F}$ (2.5) contains the kinetic terms and gauge interactions of fermions encoded in the covariant derivative

$$D_\mu = \partial_\mu + \mathrm{i} g_1 Y B_\mu + \mathrm{i} g_2 W^a_\mu T^a + \mathrm{i} g_3 G^b_\mu t^b \, , \tag{2.9}$$

where T^a $(a = 1, 2, 3)$ and t^b $(b = 1, ..., 8)$ correspond to the canonically normalized $SU(2)_L$ and $SU(3)_C$ generators of the field representation they are acting on, respectively. $\mathcal{L}_\mathrm{Y}$ (2.6) contains the Yukawa matrices Y^{ij}_u, Y^{ij}_d, Y^{ij}_ℓ which encode the couplings of up-type quarks, down-type quarks and charged leptons to the Higgs boson, respectively. Here $H^c = \mathrm{i}\sigma_2 H^*$ denotes the charge conjugated Higgs with the second Pauli matrix σ_2. $\mathcal{L}_H$ (2.7) finally encodes the kinetic term, gauge interactions and (tree-level) potential V_H of the Higgs. Note that any explicit fermion and gauge boson mass terms are forbidden by gauge invariance. They are generated by the Higgs mechanism [10–13] during EWSB. This is discussed in the next section.

2.2 Electroweak Symmetry Breaking

The SM Higgs potential at tree-level is given as

$$V_H = -\mu^2 H^\dagger H + \lambda (H^\dagger H)^2 \, . \tag{2.10}$$

For positive parameters $\mu^2, \lambda > 0$ the potential has its global minimum[2] at

$$(H^\dagger H) = \frac{\mu^2}{2\lambda} = \frac{v_h^2}{2}\,, \tag{2.11}$$

where H acquired a vacuum expectation value (VEV) $v_h \simeq 246\,\mathrm{GeV}$. Choosing the specific ground state $\langle H \rangle = \frac{1}{\sqrt{2}}(0,\, v_h)^T$ out of the infinitely many degenerate minima in (2.11) spontaneously breaks the SM gauge symmetry as

$$SU(3)_C \times SU(2)_L \times U(1)_Y \quad \xrightarrow{\langle H \rangle} \quad SU(3)_C \times U(1)_{\mathrm{em}}. \tag{2.12}$$

After EWSB the Higgs field in unitary gauge is given as

$$H = \frac{1}{\sqrt{2}} \begin{pmatrix} 0 \\ v_h + h \end{pmatrix}\,, \tag{2.13}$$

where the electrically neutral real scalar field h denotes the physical Higgs boson with mass $M_h \simeq 125\,\mathrm{GeV}$ [8, 9]. The broken Higgs potential

$$V_h = \frac{\lambda}{4} h^4 + \lambda v_h h^3 + \lambda v_h^2 h^2 - \frac{\lambda v_h^4}{4} \equiv \kappa_4 h^4 + \kappa_3 h^3 + \frac{1}{2} M_h^2 h^2 - V_0 \tag{2.14}$$

then features a quartic κ_4 as well as trilinear κ_3 Higgs self-coupling and the mass term M_h^2. Note that the independent determination of M_h and v_h fixes the quartic as $\lambda = \frac{M_h^2}{2v_h^2}$ in the SM. After spontaneous symmetry breaking (SSB), of a priori four degrees of freedom (d.o.f.) in H there is only a single physical d.o.f. h left. Each of the other three d.o.f. corresponds to a broken generator of $SU(2)_L \times U(1)_Y$ which according to Goldstone's theorem [75] each yield a massless scalar Goldstone boson. However, when inserting (2.13) into $\mathcal{L}_H$ the Higgs VEV generates mass terms for B_μ and W_μ^a, that are diagonalized via

$$W_\mu^\pm = \frac{1}{\sqrt{2}} \left(W_\mu^1 \mp \mathrm{i}\, W_\mu^2 \right)\,, \qquad \begin{pmatrix} Z_\mu \\ A_\mu \end{pmatrix} = \begin{pmatrix} \cos\theta_W & -\sin\theta_W \\ \sin\theta_W & \cos\theta_W \end{pmatrix} \begin{pmatrix} W_\mu^3 \\ B_\mu \end{pmatrix}\,, \tag{2.15}$$

where the weak mixing angle θ_W is defined as

$$\sin\theta_W = \frac{g_1}{\sqrt{g_1^2 + g_2^2}}\,. \tag{2.16}$$

This yields the massive electroweak gauge bosons $W_\mu^\pm$ and Z_μ as well as the massless photon $\gamma\,(A_\mu)$ as physical d.o.f., where the Goldstone modes have been absorbed in the additional longitudinal polarizations of the massive $W_\mu^\pm$ and Z_μ. The W- and Z-boson masses are given as

$$m_W = \tfrac{1}{2} g_2 v_h \qquad m_Z = \frac{m_W}{\cos\theta_W}\,. \tag{2.17}$$

We can now rewrite the electroweak part of the covariant derivative (2.9) as

$$D_\mu = \partial_\mu - \mathrm{i}\frac{g_2}{\sqrt{2}}(W_\mu^+ T^+ + W_\mu^- T^-) - \mathrm{i}\frac{g_2}{\cos\theta_W} Z_\mu (T^3 - \sin^2\theta_W Y) - \mathrm{i}e A_\mu Q_e\,, \tag{2.18}$$

---

[2] The full effective Higgs potential additionally contains higher-order corrections which may modify its shape and alter the extrema structure, e.g. [36–38], see also Subsec. 3.2.3.

with $T^{\pm} = T^1 \pm iT^2$ for the $SU(2)_L$ generators and the electromagnetic coupling

$$e = g_1 \cos\theta_W = g_2 \sin\theta_W \,. \tag{2.19}$$

2.3 Flavor

The fermion kinetic Lagrangian $\mathcal{L}_F$ (2.5) is diagonal in flavor space and features a global flavor symmetry

$$U(3)^5 = U(3)_q^3 \times U(3)_\ell^2 = [U(3)_Q \times U(3)_U \times U(3)_D] \times [U(3)_L \times U(3)_E] \tag{2.20}$$

under unitary transformations on the chiral fermion fields Q_i, U_i, D_i, L_i, E_i. This flavor symmetry is explicitly broken by the Yukawa sector (2.6) to

$$U(3)^5 \xrightarrow{Y_{u,d,e}} U(1)_B \times U(1)_e \times U(1)_\mu \times U(1)_\tau \,, \tag{2.21}$$

corresponding to baryon number (B) and lepton family numbers (e, μ, τ), which are exact global symmetries of the full SM Lagrangian (2.3).

After EWSB the Higgs VEV in $\mathcal{L}_Y$ generates mass terms $M_f^{ij} = \frac{v_h}{\sqrt{2}} Y_f^{ij}$ for $f = u$, d, ℓ. To obtain the physical fermion fields we have to go to the fermion mass basis. Thus, we have to diagonalize the Yukawa matrices which are a priori unconstrained, complex matrices by a bi-unitary transformation

$$y_f = V_L^f Y_f V_R^{f\dagger} \,. \tag{2.22}$$

This corresponds to applying unitary transformations on the chiral fermion fields

$$f'_{L,R} = V_{L,R}^f f_{L,R} \,, \tag{2.23}$$

where primed (unprimed) fields denotes the mass (gauge) basis. We then obtain the fermion mass terms

$$-\mathcal{L}_{\text{mass}} = m_u^i \bar{u}_L^i u_R^i + m_d^i \bar{d}_L^i d_R^i + m_\ell^i \bar{\ell}_L^i \ell_R^i \,, \tag{2.24}$$

with the masses $m_f = \frac{v_h}{\sqrt{2}} y_f$ where we dropped the primes for notational convenience. The numerical values of quark and lepton masses are collected in App. A.2. They exhibit a strong hierarchy that remains unexplained within the SM and is part of the *SM flavor puzzle* [76]. Neutrinos on the other hand are strictly massless in the SM.

Most of the fermion field transformations (2.23) are unphysical and do not have any observable effect. The reason is that most terms in $\mathcal{L}_F$ are $\propto \bar{f}_{L,R}\gamma^\mu f_{L,R}$, so that the fermion field transformations immediately drop out due to unitarity. The only exception are charged current interactions of quarks with the $W^\pm$-bosons via

$$\mathcal{L}_{cc} = \frac{g_2}{\sqrt{2}} \left(\bar{u}_L^i V_{ij} \gamma^\mu d_R^j + \bar{\nu}_L^i \gamma^\mu \ell_L^i \right) W_\mu^+ \; + \; \text{h.c.} \,, \tag{2.25}$$

which couple LH up- and down-type quarks. The CKM matrix [77, 78]

$$V = V_{\text{CKM}} = V_L^{u\dagger} V_L^d = \begin{pmatrix} V_{ud} & V_{us} & V_{ub} \\ V_{cd} & V_{cs} & V_{cb} \\ V_{td} & V_{ts} & V_{tb} \end{pmatrix} \tag{2.26}$$

is the only combination of fermion transformations $V_{L,R}^f$ that becomes physical and gives rise to flavor changing charged currents. In contrast, there are no tree-level FCNCs in the SM. Note that in the lepton sector due to the absence of RH neutrinos in the SM we can apply the unitary transformation V_L^ℓ also to ν_L, such that the leptonic charged current interactions remain flavor diagonal.

In the SM, the CKM matrix is strictly unitary and contains four free parameters, namely three mixing angles and a CP-violating phase. It exhibits a very peculiar hierarchy, i.e. it is numerically close to the unit matrix. This can be conveniently seen in the Wolfenstein parametrization [79]

$$V_{\text{CKM}} = \begin{pmatrix} 1-\frac{\lambda^2}{2} & \lambda & A\lambda^3\left(\rho-\mathrm{i}\eta\right) \\ -\lambda & 1-\frac{\lambda^2}{2} & A\lambda^2 \\ A\lambda^3\left(1-\rho-\mathrm{i}\eta\right) & -A\lambda^2 & 1 \end{pmatrix} + \mathcal{O}(\lambda^4)\,, \tag{2.27}$$

where we expanded in the small Wolfensteinparameter $\lambda \simeq 0.2$. Note that up to $\mathcal{O}(\lambda^3)$ CP violation just occurs in the CKM elements V_{td} and V_{ub} while it is absent elsewhere.

We can now examine the number of independent free parameters in the SM. These are the three gauge couplings g_i, the parameters of the Higgs potential μ^2 and λ, nine fermion masses and four CKM parameters summing up to 18 parameters[3], of which 13 are related to flavor. At first glimpse, this number seems large. However, these 18 parameters allow to simultaneously explain several hundreds of measurements which impressively demonstrates the predictive power of the SM.

2.4 Motivation and Directions for BSM

Despite its tremendous success the SM is not the most fundamental theory of nature. The reason are several observed phenomena that remain unexplained within the SM and prove the existence of NP.

A prominent example is the discovery of neutrino oscillations [16, 17] which provides evidence for non-vanishing mixing of the three SM neutrino flavors. It is encoded in the Pontecorvo-Maki-Nakagawa-Sakata (PMNS) matrix which is the leptonic counterpart of the CKM matrix and implies the existence of lepton flavor violation (LFV). Moreover, neutrino oscillations demonstrated that at least two neutrinos have non-zero masses which however have to be several order of magnitude smaller than the other SM fermion masses [14].

Several shortcomings of the SM are related to cosmological observations. First of all, it does not incorporate a quantum theory of gravity which is the fundamental force dominating our universe on large scales. Furthermore, SM matter just accounts for roughly 5% of the energy budget of the universe [14]. The majority of the universes energy is stored in dark matter and dark energy which are not part of the SM. Finally, the SM does not offer an explanation for the observed BAU which quantifies the dominance of matter over antimatter in the universe. The BAU can only have been generated in processes fulfilling the three Sakharov conditions [80]. Besides out of equilibrium dynamics, these also require the violation of baryon number B and CP. In the SM B violation is completely absent and the magnitude of CP violation is significantly too small to explain the measured value of the baryon-to-photon-ratio in the observable universe [15]. Thus, additional BSM sources of B and CP violation have to exist.

Moreover, precision computations [4, 36–38] have evidenced the metastability of the SM Higgs potential. This metastability can potentially be cured by NP. Although the lifetime of the false vacuum is larger than the age of the universe and thus metastability is not in conflict with observations the stabilization of the SM vacuum has become an active new direction in BSM model building. We discuss this in more detail in Subsec. 3.2.3.

Another open question is the origin of the SM flavor structure that constitutes the *SM flavor puzzle* [76]. In the flavor sector both the fermion mass spectrum and the CKM matrix exhibit large hierarchies. This is

---

[3] In this counting we omitted again the QCD Θ-term.

in principle allowed as fermion masses and quark mixing angles are free parameters of the SM. However, the peculiar patterns of these parameters are often interpreted as hints for some more fundamental underlying dynamics.

In addition, several anomalies related to flavor observables have emerged in experiments during the last years. In particular, a set of systematic deviations from the SM coined the B anomalies has been experimentally observed in the past decade in several observables related to rare $b \to s\mu^+\mu^-$ FCNC transitions. This is discussed in detail in Subsec. 8.1.1. Interestingly, also hints for an excess in the branching ratio of the related $B^+ \to K^+\nu\bar{\nu}$ decay have been reported by the Belle II experiment [81, 82]. In the charm sector, hints for BSM sources of CP and U-spin violation have been recently gathered by LHCb, cf. Sec. 9.1. In this thesis we aim at explaining these flavor anomalies in anomaly-free, flavorful $U(1)'$ extensions of the SM in Chap. 8 and Chap. 9, respectively. A key tool for this purpose are EFTs, which constitute an interface between experimental low-energy data and BSM models in the UV.

2.5 Effective Field Theories

Despite the clear evidence for BSM physics discussed in Sec. 2.4 up to now no new particles have been directly discovered. Therefore, indirect and model-independent NP searches have become increasingly important. The crucial theoretical framework for this task are EFTs, see e.g. [83–88] for more comprehensive and detailed reviews.

The basic idea of an EFT is to describe physical processes in a certain energy range just in terms of the relevant, dynamical d.o.f.. Sufficiently heavier d.o.f. are systematically decoupled from the the low energy description of the process [89]. Thereby, EFTs allow to disentangle low energy (long distance) and high energy (short distance) physics contributions in a given process. The low-energy physics is encoded in higher-dimensional operators $O_i^{(d)}$ with mass dimension $d > 4$ constructed of the dynamical fields. At each mass dimension all possible operators obtained from field combinations respecting gauge invariance and possible additional symmetries of the system have to be taken into account. Short-distance contributions on the other hand are captured in dimensionful effective couplings of these operators. This separative approach is formally referred to as operator product expansion (OPE) [90]. The effective couplings can further be expressed as ratios $C_i^{(d)}/\Lambda^{d-4}$ with dimensionless Wilson coefficients (WCs) $C_i^{(d)}$ suppressed by d-4 powers of a high scale Λ.

An EFT can be used in two different ways. In a *top-down* approach one starts from a renormalizable model in the UV and obtains the WCs in a low energy EFT by integrating out the heavy fields. In a model-independent *bottom-up* approach in contrast the WCs are treated as free parameters. Observables are computed in the EFT as functions of the WCs and their allowed values are determined by fits to experimental data. This allows to extract widely model independent constraints on heavy NP contributions to the WCs providing directions for model building.

A prominent historical example of an EFT is Fermi's theory [91] which constitutes an effective description of the charged current weak interactions (2.25) in the SM. The full effective Lagrangian of Fermi's theory is given as

$$\mathcal{L}_{\text{Fermi}} = -\frac{4G_F}{\sqrt{2}} J^{-\mu} J^+_\mu + \mathcal{O}\left(\frac{q^2}{m_W^2}\right) , \tag{2.28}$$

with the charged current

$$J^+_\mu = V_{ij}\bar{u}_{L,i}\gamma_\mu d_{L,j} + \bar{\nu}_{L,i}\gamma_\mu e_{L,i}, \quad J^-_\mu = (J^+_\mu)^\dagger , \tag{2.29}$$

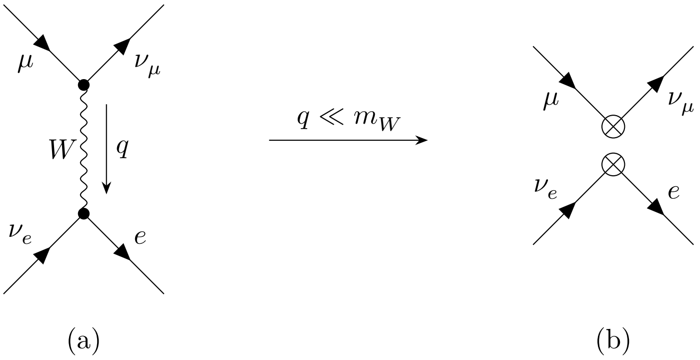

Figure 2.1: Leading order (LO) Feynman diagrams for muon decay in the SM (left) and Fermi's theory (right). The crosses indicate a local four-fermion operator in the EFT. The WC of the operators for $q \ll m_W$ is obtained by integrating out the W-boson.

where the summation over flavor indices i, j is understood and we introduced the Fermi constant

$$G_F = \frac{\sqrt{2} g_2^2}{8 m_W^2} = \frac{1}{\sqrt{2} v_h^2} \tag{2.30}$$

as effective coupling of the theory.

We illustrate the derivation of the EFT description from the full theory in a top-down study of muon decay. The corresponding LO Feynman diagrams in the SM as well as Fermi's theory are depicted in Fig. 2.1. The energy scale of the decay is set by the momentum transfer $q^2 \sim m_\mu^2 \ll m_W^2$. Thus, we can treat the W-boson as approximately static, i.e. collapse the propagator $\frac{1}{q^2 - m_W^2} \to -\frac{1}{m_W^2} + \mathcal{O}(\frac{q^2}{m_W^2})$. This gives rise to an effective four fermion operator $(\bar{e}_L \gamma^\mu \nu_{eL})(\bar{\nu}_{\mu L} \gamma_\mu \mu_L) \supset J^{-\mu} J_\mu^+$ with the effective coupling $G_F \propto \frac{1}{m_W^2}$ containing the high energy information about the W-boson. Hence, the precise value of $G_F \equiv \frac{C}{\Lambda^2}$ in (2.30) is fixed by matching the amplitude in the full theory to the EFT. Historically, G_F was extracted from data in a bottom-up approach, demonstrating the power of EFTs to perform low-energy computations completely agnostic of the high-energy dynamics.

The precision of the EFT computation can be systematically improved by considering corrections of higher orders in the small expansion parameter $\frac{q^2}{m_W^2}$. This gives rise to higher-dimensional operators with corresponding WCs suppressed by higher powers of $\frac{1}{m_W^2}$. Thus, the increasing precision comes at the price of an increasing number of operators and WCs that have to be considered. When expanding to all orders in $\frac{q^2}{m_W^2}$ the EFT is formally equivalent to the full theory. However, as the expansion parameter is typically tiny for practical purposes it is often sufficient to consider LO contributions.

To compare low energy data to high-energy predictions from UV models we have to relate the values of WCs at different energy scales μ. Demanding the effective Lagrangian

$$\mathcal{L}_{\text{eff}} = -\frac{1}{\Lambda^2} \sum_i C_i(\mu) O_i(\mu) \tag{2.31}$$

to be independent of the scale μ implies a running and mixing of WCs C_i obeying

$$\frac{\mathrm{d}C_i}{\mathrm{d}\ln\mu} = \gamma_{ij}^T C_j \,. \tag{2.32}$$

It is governed by the so-called anomalous dimension matrix (ADM) γ_{ij} defined through the renormalization of operators due to QCD corrections reading $\frac{\mathrm{d}O_i}{\mathrm{d}\ln\mu} \equiv -\gamma_{ij} O_j$. It can be systematically computed order by order in perturbation theory. Crucially, solving (2.32) for γ_{ij} at k-loop order also resums potentially large logarithmic terms $\propto \alpha_s^{k-1}(\alpha_s \ln \frac{\Lambda}{\mu})^n \ \forall n \in \mathbb{N}$. We now introduce two SM-based EFTs that are relevant for this work in more detail.

2.5.1 Standard Model Effective Field Theory

The SMEFT is extensively applied in model-independent searches for heavy NP, see e.g. [92]. It is a generalization of the SM, i.e. operators are constructed of all SM fields and respect the full SM gauge symmetry $\mathcal{G}_{SM}$ (2.1). SMEFT just makes use of two central assumptions: Firstly, all possible BSM particles have masses well above the electroweak scale and secondly EWSB is linearly realized by a $SU(2)_L$ doublet Higgs[4]. Apart from that, the SMEFT approach is completely model independent. The SMEFT Lagrangian is given as

$$\mathcal{L}_{\text{SMEFT}} = \mathcal{L}_{\text{SM}} + \sum_{d=5}^{\infty} \mathcal{L}^{(d)} \quad \text{with} \quad \mathcal{L}^{(d)} = \sum_i \frac{1}{\Lambda^{d-4}} C_i^{(d)} Q_i^{(d)} \,, \tag{2.33}$$

where $C_i^{(d)}$ and $Q_i^{(d)}$ denote the WCs and operators at mass dimension d, respectively. As $\mathcal{L}_{\text{SMEFT}}$ contains the full $\mathcal{L}_{\text{SM}}$ all WCs strictly vanish within the SM. SMEFT operator bases are explicitly known up to $d = 8$ [94–97] as well as an algorithm to construct operator bases at arbitrary dimension [97, 98]. The leading $\mathcal{L}^{(5)}$ contains only the lepton number violating Weinberg operator [94] which can give rise to Majorana mass terms for neutrinos. In fact, all operators of odd mass dimension necessarily violate either baryon or lepton number [99] and are therefore not relevant for this work. Thus, the leading NP contributions to observables in SMEFT typically arise from $\mathcal{L}^{(6)}$. The first complete generating set of operators for $\mathcal{L}^{(6)}$ was derived in [100]. Later on, redundant operators were successfully removed in [95] by applying equations of motion and integration by parts relations yielding the so-called *Warsaw basis* for $\mathcal{L}^{(6)}$. Assuming baryon and lepton number conservation, $\mathcal{L}^{(6)}$ contains 59 linearly independent operators and 2499 real parameters [101]. The large number of parameters is mainly related to the fermion fields and corresponding WCs carrying flavor indices and can be drastically reduced by assuming flavor symmetries. For maximal $U(3)^5$ flavor symmetry there remain 76 real parameters[5] [101], which as of now are still too many to perform a full fit. Thus, in bottom-up fits typically just a subset of operators is considered and certain flavor symmetries are imposed on the WCs. In contrast, for the top-down approach a completely general tree-level dictionary is available to match any renormalizable UV model to SMEFT [102]. In both cases the running of WCs between the NP scale and the typical scales of observables has to be taken into account. The corresponding SMEFT ADM is known completely at 1-loop [101, 103, 104] and partially at 2-loop [105].

2.5.2 Weak Effective Theory

At energies below the electroweak scale SMEFT is not the appropriate framework, as the heavy SM fields t, H, Z, W decouple and the electroweak symmetry is broken down to QED. Accordingly, operators should

---

[4] There is also a more general EFT called Higgs Effective Field Theory (HEFT) where this assumption is dropped, see [93] for a review.

[5] Some of the 59 WCs are complex-valued yielding two real parameters.

not contain fermion doublets but their weak isospin components separately. The EFT realizing these features is called WET[6]. To relate observables above and below the electroweak scale it is crucial to match WCs in SMEFT onto those in WET which is typically done at $\mu = m_W$. The matching conditions at tree-level as well as one-loop are completely known [106]. Note that in contrast to SMEFT in WET several WCs are already induced in the SM by integrating out the heavy t, H, Z, W fields.

A central application of WET are B decays, see e.g. [107]. In particular, we are interested in rare semileptonic $b \to s\ell^+\ell^-$ FCNC transitions, which are the subject of Chap. 8. The part of the WET Lagrangian that gives rise to such transitions at tree-level reads

$$\mathcal{L}_{\text{WET}}^{bs\ell\ell} = \frac{4G_F}{\sqrt{2}}\frac{\alpha_e}{4\pi}V_{tb}V_{ts}^* \left[c_7 O_7 + c_7' O_7' + \sum_{\ell=e,\mu,\tau}\sum_{i=9,10,S,P}(c_i^\ell O_i^\ell + c_i'^\ell O_i'^\ell) + \sum_{i=T,T5} c_i^\ell O_i^\ell\right] , \tag{2.34}$$

with the fine structure constant $\alpha_e = \frac{e^2}{4\pi}$ and the semileptonic dimension-six operators

$$\begin{aligned} O_9^\ell &= (\bar{s}_L\gamma_\mu b_L)(\bar{\ell}\gamma^\mu\ell), & O_{10}^\ell &= (\bar{s}_L\gamma_\mu b_L)(\bar{\ell}\gamma^\mu\gamma^5\ell), \\ O_S^\ell &= m_b(\bar{s}_L b_R)(\bar{\ell}\ell), & O_P^\ell &= m_b(\bar{s}_L b_R)(\bar{\ell}\gamma^5\ell), \\ O_T^\ell &= \frac{1}{2}(\bar{s}\sigma_{\mu\nu}b)(\bar{\ell}\sigma^{\mu\nu}\ell), & O_{T5}^\ell &= \frac{1}{2}(\bar{s}\sigma_{\mu\nu}b)(\bar{\ell}\sigma^{\mu\nu}\gamma_5\ell), \end{aligned} \tag{2.35}$$

where $\sigma_{\mu\nu} = \frac{i}{2}[\gamma_\mu, \gamma_\nu]$. The electromagnetic dipole operator

$$O_7 = \frac{m_b}{e}(\bar{s}_L\sigma_{\mu\nu}b_R)F^{\mu\nu} \tag{2.36}$$

can also contribute indirectly to $b \to s\ell^+\ell^-$ transitions via electromagnetic penguins. Primed operators $O_i^{\ell\prime}$ for $i = 7, 9, 10, S, P$ are obtained by interchanging the quark chiralities $L \leftrightarrow R$. Note that we do not consider possible lepton flavor violating (LFV) operators $O^{\ell\ell'}$ with $\ell \neq \ell'$. The WCs

$$c_i^{(\prime)\ell} = C_i^{(\prime)\text{SM}} + C_i^{(\prime)\ell,\text{NP}} \tag{2.37}$$

contain a LFU SM contribution $C_i^{(\prime)\text{SM}}$ and a potential, flavor specific NP contribution $C_i^{(\prime)\ell,\text{NP}}$. In the SM the (pseudo-)scalar, tensor and primed WCs are negligibly small at $\mu_b \sim m_b$ whereas $C_{7,9,10}^{\text{SM}}(\mu_b)$ read $C_7^{\text{SM}}(\mu_b) \simeq -0.29$, $C_9^{\text{SM}}(\mu_b) = -4.31$ and $C_{10}^{\text{SM}}(\mu_b) = 4.07$ at NNLO [108].

At 1-loop, $b \to s\ell^+\ell^-$ transitions additionally receive LFU contributions from the charged-current four-quark operators

$$O_1^q = (\bar{s}_L^\alpha\gamma_\mu q_L^\alpha)(\bar{q}_L^\beta\gamma^\mu b_L^\beta), \qquad O_2^q = (\bar{s}_L^\alpha\gamma_\mu q_L^\beta)(\bar{q}_L^\beta\gamma^\mu b_L^\alpha), \tag{2.38}$$

with $q = u$, c and color indices α, β. The corresponding WCs C_1^q as well as through RG-mixing also C_2^q are induced at tree level in the SM and constitute a central source of theoretical uncertainties in predictions for $b \to s\ell^+\ell^-$ observables, e.g. [109].

---

[6] In the literature there is a subtle ambiguity in the use of the term WET. Processes at scales $m_b \lesssim \mu \lesssim m_W$ should be described by the 'traditional' WET also called WET-5 referring to the five active quark flavors u, d, s, c, b. Unless stated otherwise, within this thesis when speaking of WET we always refer to WET-5, which is the correct tool for B physics. However, at lower scales $m_c \lesssim \mu \lesssim m_b$ the bottom quark has to be integrated out yielding a different EFT called WET-4 which is the right framework for charm physics.

3 Renormalization Group Running as Tool for Model Building

A crucial feature of QFTs is the dependence of coupling constants on the energy scale μ due to quantum fluctuations. In perturbation theory this phenomenon manifests itself in the frequent appearance of unphysical UV divergences in the evaluation of corresponding higher-order loop diagrams. These have to be cancelled in the computation of physical observables, which is achieved in the processes of *regularization* and *renormalization*, see e.g. [64, 65] for a detailed pedagogical introduction of the concepts. The divergences are first analytically parametrized by employing a certain regularization method and then absorbed into the bare parameters of the theory by choosing a proper renormalization scheme. Common choices are dimensional regularization [110] and the modified minimal subtraction scheme ($\overline{\text{MS}}$-scheme) [111] which are also employed within this thesis. However, physical observables are scheme-independent, i.e. all explicit dependencies on the regularization and renormalization method have to cancel in their computation. This condition is encoded in the Callan-Symanzik equation [18–23] which implies RGEs for the renormalized parameters in the theory. For coupling constants α_g the RGEs read

$$\frac{\mathrm{d}\alpha_g}{\mathrm{d}\,\ln\mu} = \beta_g\,, \tag{3.1}$$

where μ is the renormalization scale and β_g denotes the β-function of the coupling α_g. It can be systematically computed in the perturbative loop expansion, i.e.

$$\beta_g = \sum_{n=1}^{\infty} \beta_g^{(n)}\,, \tag{3.2}$$

where $\beta_g^{(n)}$ denotes the n-loop contribution to β_g. The $\beta_g^{(n)}$ depend on the couplings and field content of the theory with each successive loop order being proportional to higher powers of coupling constants. Once the β-functions are known the RGEs can be solved for some starting values $\alpha_g(\mu_0)$ at a reference scale μ_0. The dependence of the coupling constants $\alpha_g(\mu)$ on the renormalization scale implied by the RGEs is referred to as RG *evolution, flow* or *running*. Crucially, the precision in the determination of the running can be systematically improved by including higher loop orders in the β-functions.

In this chapter we first investigate the RGEs in GY theories in general and the SM in particular in Sec. 3.1 before introducing the concepts of asymptotic safety and Planck safety as guidelines for BSM model building in Sec. 3.2.

3.1 Gauge-Yukawa Running

The SM is a GY theory, promoting them to objects of crucial interest in particle physics. Thus, large efforts have been made to investigate the RGEs in GY systems [26–31, 112–117]. For this purpose, it is convenient to introduce redefined coupling constants

$$\alpha_X = \frac{X^2}{16\pi^2}, \qquad \alpha_Y = \frac{Y^2}{16\pi^2}, \qquad \alpha_Z = \frac{Z}{16\pi^2}\,, \tag{3.3}$$

where X, Y and Z refer to gauge, Yukawa and scalar quartic couplings, respectively. In this specific convention, all loop factors $1/(4\pi)^2$ are incorporated in $\alpha_{X,Y,Z}$ and hence removed from the β-functions. Moreover, the powers of fundamental coupling constants for the different interactions in (3.3) are chosen such that all n-loop diagrams contributing to a β-function are of $\mathcal{O}(\alpha^n)$. Accordingly, all $\beta^{(n)}$ are of $\mathcal{O}(\alpha^{n+1})$ yielding a simple method to identify the loop order of a given term in a β-function. To shorten the notation, we define the `lmn` approximation (also `lmn` loop order) as taking into account `l`-, `m`- and `n`-loop order in the gauge, Yukawa and scalar quartic sector, respectively.

The complete set of 2-loop template β-functions in a fully general GY theory has been first worked out in [112–114] and corrected in [115, 116]. As of now, template RGEs are available up to `432` loop order [26–28]. General 3-loop scalar quartic β-functions are subject of active research and only partially known [29–31] as computations in theories featuring chiral fermions and charged scalars are significantly complicated by the correct treatment of γ_5 in dimensional regularization, see [118] and references therein for details. For some special cases results at higher loop orders are also available[1]. However, obtaining multi-loop RGEs in a specific model from the GY template β-functions remains quite an involved task. While a first attempt to simplify the process was put forward in [126] it is nowadays performed with the help of computer codes. Prominent examples are `PYR@TE 3` [34], `RGBeta` [35], `ARGES` [32] and `FoRGEr` [33]. In this work we made use of the latter two as the application of symbolic rather than numeric computation methods allows us also to leave some parameters such as field multiplicities and representations unspecified. We now examine the general anatomy of β-functions in the different sectors.

3.1.1 Gauge Couplings

The 1-loop β-function $\beta_g^{(1)}$ of a gauge coupling α_g is given as

$$\beta_g^{(1)} = -B\,\alpha_g^2\,, \tag{3.4}$$

where we introduced the 1-loop coefficient B which depends on the gauge group and particle content of the theory. We see that $\beta_g^{(1)} \propto \alpha_g^2$. In fact, all terms in β_g up to arbitrary loop order are $\propto \alpha_g^k$ with $k \geq 2$ [2] [28]. Thus, gauge couplings α_g cannot be RG induced if they vanish at some scale μ_0. This feature is referred to as *technical naturalness* and always protected by a symmetry. We also see that $\beta_g^{(1)}$ is independent of all other gauge, Yukawa or quartic couplings that might be present in the theory. Solving the 1-loop RGEs analytically yields

$$\alpha_g(\mu) = \frac{\alpha_g(\mu_0)}{1 + \alpha_g(\mu_0)\,B\,\ln\frac{\mu}{\mu_0}}\,. \tag{3.5}$$

Assuming that the inclusion of higher loop orders does not change the running significantly, we can deduce the RG behavior of α_g depending on the sign of B. For $B > 0$ the coupling constant $\alpha_g(\mu)$ decreases towards higher energies and asymptotically approaches zero in the UV. This behavior is referred to as *asymptotic freedom* and was first observed in QCD [24, 25]. For $B < 0$ on the other hand α_g grows with increasing energy and finally diverges. This phenomenon is referred to as a *Landau pole* and occurs at the scale

$$\mu_{\mathrm{LP}} = \mu_0 \exp\left(\frac{1}{B\alpha_g(\mu_0)}\right). \tag{3.6}$$

When approaching this scale in the UV, perturbation theory breaks down and our capability to make predictions is compromised.

In a $SU(N)$ gauge theory with N_F Weyl fermions in the representation R_F under the gauge group and

---

[1] In the SM, the full 3-loop β-function of the Higgs quartic coupling α_λ was derived in [119, 120]. In pure QCD and QED the full 5-loop gauge β-functions are known [121–124]. In pure scalar theories 6-loop β-functions were pioneered in [125].

[2] The sole exception to this rule arises from kinetic mixing of two abelian gauge fields (see Sec. 7.2 for details) with gauge couplings α_i with $i = 1, 2$ in a semi-simple gauge group [28]. In this case, the kinetic mixing parameter η induces terms in β_i that are of lower power in α_i but contain powers of α_j instead. The terms of lowest power in α_i are $\beta_i^{(1)} \supset \eta^2\alpha_i\alpha_j$ for $i \neq j$ [28, 127]. These terms are however still $\propto \alpha_i$, quadratic in gauge couplings and vanish for $\eta = 0$.

N_S scalars with representation R_S the 1-loop coefficient reads [112]

$$B = \frac{22}{3}N - \frac{4}{3}N_F S_2(R_F) - \frac{2}{3}N_S S_2(R_S)\,. \tag{3.7}$$

The Dynkin index $S_2(R)$ is defined as $S_2(R)\delta^{AB} = \mathrm{Tr}\left[t^A(R)t^B(R)\right]$ with $t^A(R)$ denoting the generators of the representation R and takes the values $S_2(F) = \frac{1}{2}$, $S_2(\overline{S}) = \frac{1}{2}(N-2)$, $S_2(S) = \frac{1}{2}(N+2)$ and $S_2(A) = N$ for the fundamental F, anti-symmetric $\overline{S}$, symmetric S and adjoint representation A of $SU(N)$. The first term in (3.7) arises from gauge boson self-interactions. Thus, (3.7) also applies for a $U(1)$ gauge theory when setting $N = 0$. Interestingly, there is a competition between gauge bosons on the one hand as well as charged fermions and scalars on the other hand. While the first contribute positively to B pushing the theory towards asymptotic freedom, the latter contribute negatively promoting the occurrence of a Landau pole. Thus, in $SU(N)$ theories the UV fate is determined by the specific gauge group and field content of the theory. For $U(1)$ gauge theories in contrast we invariably encounter a Landau pole in the UV unless all fields are uncharged (quantum triviality).

In the SM and denoting with B_i the 1-loop coefficient for α_i with $i = 1, 2, 3$ we find

$$B_1^{\mathrm{SM}} = -\frac{41}{3}, \qquad B_2^{\mathrm{SM}} = \frac{19}{3}, \qquad B_3^{\mathrm{SM}} = 14\,, \tag{3.8}$$

implying asymptotic freedom for $\alpha_{2,3}$ whereas the hypercharge coupling α_1 runs into a Landau pole at roughly 10^{41} GeV. This can also be seen in Fig. 3.1, where the full 3-loop SM RG flow from the TeV scale up to transplanckian energies is shown. The strong coupling α_3 in contrast diverges in the infrared (IR) around $\Lambda_{\mathrm{QCD}} \simeq \mathcal{O}(0.1\ \mathrm{GeV})$ causing confinement.

Starting from 2-loop, β_i also receives contributions from the other gauge and Yukawa couplings in the theory. Assuming for now a simple gauge group with gauge coupling α_g and a single Yukawa coupling α_y the gauge coupling β-function reads

$$\beta_g^{(2)} = \alpha_g^2(-B + C\alpha_g - D\alpha_y)\,, \tag{3.9}$$

where we applied the notation from [40, 128] and C, D depend on field content of the theory. The coefficient C can have either sign but $B \leq 0$ always implies $C > 0$ [128]. Thus, for $B \leq 0$ the 2-loop gauge contribution is not able to prevent the occurrence of a Landau pole. For the Yukawa contribution in contrast it holds $D \geq 0$ offering a mechanism to slow down the growth of gauge couplings [128]. For semi-simple gauge groups and several Yukawa couplings the constants B, C are generalized to matrices in coupling space, respectively, without changing the qualitative findings derived above [128]. Going to higher orders β_g eventually also receives contributions of quartic couplings of (un-)charged scalars starting from 3-loop (4-loop) [129].

3.1.2 Yukawa Couplings

The 1-loop β-function of a Yukawa coupling α_y in a theory featuring a simple gauge group and a single Yukawa coupling reads

$$\beta_y^{(1)} = \alpha_y(E\alpha_y - F\alpha_g)\,, \tag{3.10}$$

where the coefficients E, F depend on the field content. We see that also α_y, like all Yukawa couplings occurring in this thesis, is technically natural due to underlying protective symmetries. Moreover, β_y already contains a term involving α_g at leading order. In particular, as E, F are always positive [128], the Yukawa contribution itself induces a growth of α_y whereas the gauge coupling contribution brakes it.

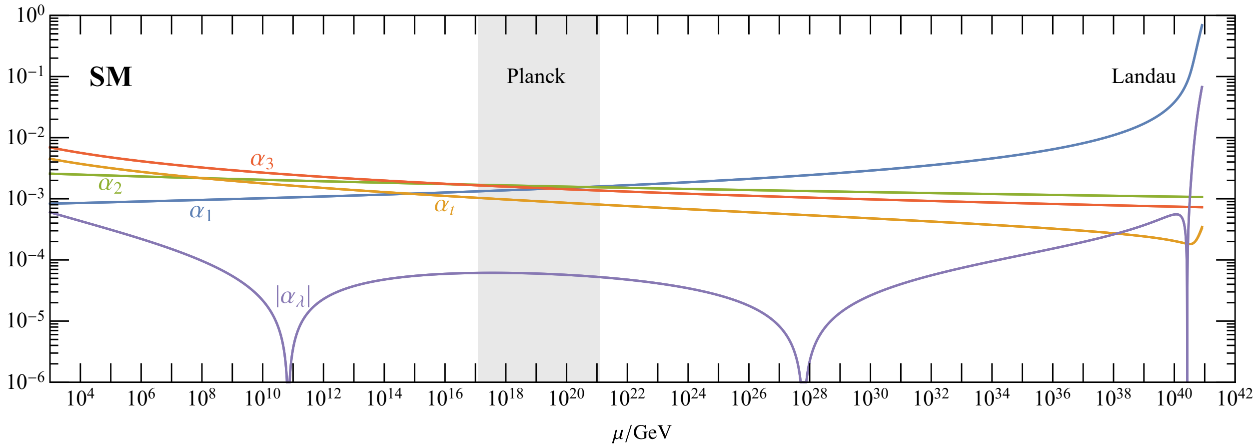

Figure 3.1: SM 3-loop running of the Higgs quartic [119, 120], top Yukawa [130, 131], and gauge couplings [117, 132, 133] between the TeV and the Planck scale (gray band), and further up to the Landau pole of the hypercharge coupling. The Higgs quartic becomes negative around $\mu \approx 10^{11}$ GeV and remains so up to the Planck scale. Plot adapted from [2].

Consequently, whether α_y grows or decreases towards the UV depends on the field content and the initial values of $\alpha_{g,y}$. In case of several gauge and Yukawa couplings E, F are promoted to matrices sharing the discussed features [128].

In the SM the leading order β-functions of the top- and bottom Yukawa couplings read

$$\begin{aligned}\beta^{(1)}_{t,\mathrm{SM}} =&\alpha_t \left(9\alpha_t + 3\alpha_b - \frac{17}{6}\alpha_1 - \frac{9}{2}\alpha_2 - 16\alpha_3\right),\\ \beta^{(1)}_{b,\mathrm{SM}} =&\alpha_b \left(9\alpha_b + 3\alpha_t - \frac{5}{6}\alpha_1 - \frac{9}{2}\alpha_2 - 16\alpha_3\right),\end{aligned} \tag{3.11}$$

where we neglected contributions from the Yukawas of all lighter fermions. The dominant contribution stems from the strong gauge coupling α_3 yielding $\beta_{t,b} < 0$ throughout the running which induces a decrease of $\alpha_{t,b}$ towards high energies as observed in Fig. 3.1.

Starting from 2-loop also scalar quartic couplings contribute to β_y, yielding a full connection of the Yukawa RG evolution to all other sectors.

3.1.3 Scalar Quartic Couplings

In the scalar sector, already at leading order β-functions can receive contributions from all other sectors. In a theory with a single gauge α_g, Yukawa α_y and quartic coupling α_q, respectively, the 1-loop quartic β-function has the structure [114]

$$\beta^{(1)}_q = H\alpha_q^2 - I_g\alpha_g\alpha_q + I_y\alpha_y\alpha_q + J_g\alpha_g^2 - J_y\alpha_y^2\,, \tag{3.12}$$

where the constants H, $I_{g,y}$, $J_{g,y}$ depend on the details of the theory and are typically positive [134]. If more couplings of a kind are present, the constants H, $I_{g,y}$, $J_{g,y}$ are promoted to three index objects in coupling space. Crucially, there can be contributions which do not contain the scalar quartic coupling itself at all, i.e. in contrast to gauge and protected Yukawa couplings quartics are in general not technically natural. Hence, even if a quartic is set to zero at some scale it can be switched on radiatively if not protected by a symmetry. Moreover, the quartic can become negative within its RG evolution.

In the SM the 1-loop Higgs quartic β-function reads[3]

$$\beta^{(1)}_{\lambda,\mathrm{SM}} = -6\alpha_t^2 + \frac{3}{8}(\alpha_1^2 + 2\alpha_1\alpha_2 + 3\alpha_2^2) + (12\alpha_t - 3\alpha_1 - 9\alpha_2)\,\alpha_\lambda + 24\alpha_\lambda^2\,, \tag{3.13}$$

where we neglected all Yukawas except from the top. As the Higgs is a color singlet there is no contribution from α_3 at leading order. The numerically dominant contribution is negative and stems from the top Yukawa. It induces a decrease of α_λ towards higher energies which can be seen in Fig. 3.1. Notably, α_λ turns negative around $\mu^{\mathrm{SM}}_{\mathrm{inst.}} \simeq 10^{11}$ GeV indicating the loss of absolute stability of the SM Higgs potential, see Subsec. 3.2.3 for details. After taking a minimal value of $\alpha_\lambda \simeq -10^{-4}$ closely prior to M_{Pl} around 10^{17} GeV it becomes positive again in the transplanckian regime around 10^{28} GeV. This second sign change is fueled by the steady growth of the hypercharge coupling. Eventually, in the very deep UV there is a third sign change immediately below the hypercharge Landau pole where α_λ becomes negative again and diverges towards large negative values at the pole.

3.2 Concepts from SM to BSM

Having reviewed the anatomy of GY RGEs we now investigate how RG running can provide directions for BSM model building. The SM RG flow Fig. 3.1 exhibits two unpleasant features. Firstly, in incorporates a Landau pole of the hypercharge coupling in the deep UV around $\mu \simeq 10^{41}$ GeV. While not being unphysical, the occurrence of such poles impedes our comprehension of physics beyond certain scales. Hence, it is worth to explore the opportunity to avoid Landau poles due to the presence of BSM physics in more detail. Secondly, we encountered a negative value of α_λ in the vast range $10^{11}\,\mathrm{GeV} \lesssim \mu \lesssim 10^{28}\,\mathrm{GeV}$ hinting metastability of the SM Higgs potential, see Subsec. 3.2.3 for details. Despite vacuum metastability with sufficiently long lifetime not being in conflict with observations, a theory of nature with an absolutely stable ground state is desirable and seems most intuitive. Driven by this thought, restoring absolute Higgs stability due to a modified RG evolution has become a common objective in BSM model building, see [2] for a thorough overview of approaches and existing works. More importantly, BSM running can also worsen the stability w.r.t. the SM. This can result in a metastability with lifetime smaller than the age of the universe or even an unstable BSM potential. Both cases are in conflict with observations and hence excluded. Thus, checking for vacuum stability is a crucial task and should actually be performed in any BSM model. A promising approach to tackle both problems at the same time are the concepts of AS and PS where AS constitutes a *top-down* approach and PS is its *bottom-up* counterpart.

3.2.1 Asymptotic Safety

In the previous section we have learned that some coupling constants asymptotically approach zero in the deep UV, a phenomenon coined AF. AS generalizes this scenario by observing that couplings in the UV may also run into an interacting fixed point (FP) rather than a free one. On a technical level, AS is related to the zeros of the β-functions β_i of all couplings α_i in a theory that define a FP α_i^* via

$$\beta_i|_* \equiv \left.\frac{\partial \alpha_i}{\partial \ln \mu}\right|_{\alpha_i = \alpha_i^*} = 0. \tag{3.14}$$

---

[3] Note that there are different conventions for the normalization of λ yielding different but equivalent β-functions. We apply the normalization of (2.10) with quartic term $\lambda(H^\dagger H)^2$ but also the normalization $\frac{\lambda}{2}(H^\dagger H)^2$ is common.

The RG flow can have several different FPs. For a FP to be physical and perturbative it has to hold $0 \leq \alpha_i^* \lesssim 1$[4]. In general, FPs can be *Gaussian* (free), partially interacting or fully interacting as well as UV or IR attractive. The set of coupling configurations that give rise to RG trajectories running into a FP in the deep UV is referred to as *UV critical surface*. They correspond to QFTs that remain controlled and predictive up to arbitrarily high energies. Crucially, the UV critical surface typically has lower dimensionality than the full coupling space. In this case, demanding AS reduces the number of independent coupling constants which strongly increase the predictive power of the theory.

Initially put forward as a scenario for quantum gravity [39], AS within the last decade also gained increasing attention in the context of GY theories. An important proof of existence was provided in [40] demonstrating that exact AS with a stable ground state can arise in GY theories featuring a $SU(N)$ gauge group under strict perturbative control in the Veneziano limit[5]. Up to now all known examples for AS in four-dimensional, non-supersymmetric, renormalizable, weakly coupled GY theories uniquely trace back to this model in the large N limit [134]. The phenomenon was then studied in more detail in several subsequent works [41–46, 128, 136–151]. Highlights investigating AS in template GY theories include extensions beyond the Veneziano limit [138, 139, 141], to semi-simple gauge groups [144] and supersymmetric theories [139, 140]. Furthermore, several necessary conditions as well as strict no-go theorems for AS to arise in weakly coupled GY without gravity were derived in [128, 136]. In particular, it was proven that Yukawa interactions together with elementary scalar fields offer a unique key towards AS [128]. In addition, the presence of weakly coupled UV FPs strictly requires non-Abelian gauge interactions [136].

The FP structure of a GY RGE system depends on the loop order taken into account in the different sectors. Thus, a detailed study at different loop orders is crucial to check the perturbative stability of FPs. The complexity of the RGEs then increases as the various couplings successively start to mix in the different β-functions. In the `210` approximation, which is the leading order for AS to appear, the GY system is decoupled and the running of scalar couplings is not taken into account at all. However, the scalar sector is crucial for two reasons. Firstly, in SM extensions the running of scalar couplings can induce instabilities in the potential. Secondly, an enlarged scalar potential can give rise to a nontrivial vacuum structure with important phenomenological consequences. Thus, it is necessary to include also the RGEs of scalar quartics in the analysis.

Due to the fast progress in template GY theories also realistic BSM model building guided by AS has become a very active business [41–46, 145–149]. Directions include SM extensions with VLFs and matrix singlet scalars [41–46] inspired by [40], grand unified theories (GUTs) [147], supersymmetry [149] and two Higgs doublet models [145, 146]. Applying AS as top-down guideline for BSM model building has two main advantages. Firstly, it yields QFTs that remain controlled and predictive up to arbitrarily high energies. Secondly, it allows to significantly constrain the viable parameter space of a given model due to the typically reduced dimensionality of the UV critical surface. Demanding also the existence of UV-IR connecting trajectories narrows the available parameter space further down. Finally, the derived constraints are widely independent of and often complementary to those from phenomenology. Hence, combining both increases the predictivity of the theory.

3.2.2 Planck Safety

In spite of the success of AS in BSM model building it has a shortcoming. Quantum gravity effects are expected to modify the RG flow starting from the Planck scale $M_{\text{Pl}} = \sqrt{\hbar c / G_N} \simeq 10^{19}$ GeV where G_N denotes Newton's constant. Thus, discussing the RG evolution of a BSM model without gravity up to

---

[4] There exist exceptions to the positivity criterium for some scalar quartic couplings that might also become moderately negative without spoiling vacuum stability.

[5] In the Veneziano limit the number of fermion flavors N_F and the rank of the gauge group N_C are sent to infinity while their ratio is fixed and kept as continuous parameter [135].

arbitrarily high energies is rather academic. Therefore, in the deduced concept of PS requiring a physical and perturbative UV FP is alleviated to demanding a RG flow without vacuum instabilities or Landau poles up to M_{Pl}, while the RG evolution in the transplanckian regime is not taken into account. This concept was first pioneered in [45, 46] and further explored in [1, 2, 4, 5, 7].

Despite sharing a similar ansatz, there are some differences between PS and AS. While AS constitutes a top-down approach, PS works bottom-up. Moreover and in contrast to AS, demanding PS does typically not fix a parameter (combination) to an exact value but rather constrains it to an allowed range. We refer to the subset of parameter values that make it safely up to the Planck scale as *BSM critical surface*. Normally, it still has the same dimensionality as the full parameter space but with reduced volume. Thus, also PS yields enhanced predictive power yet not as much as AS. In a similar manner, demanding the existence of a physical and perturbative UV FPs severely narrows down the shape of viable models [128, 136] posing a challenge to realistic BSM model building. In particular, requiring AS leads to a prima facie exclusion of potentially viable models featuring a physical and perturbative RG evolution up to the Planck scale that only exhibit shortcomings in the transplanckian regime.

An important example are models in which the RG flow features a *walking regime*. There, the running of a subset of couplings is significantly slowed down such that they stay locked at almost constant values for several orders of magnitude. On a technical level, this phenomenon is related to approximate zeros of the the β-functions, which arise in the vicinity of pseudo FPs. These can be FPs in the RGEs of a subset of couplings or FPs featuring unphysical, e.g. complex, coupling values. Walking regimes have first been observed in the gauge sector of technicolor and composite Higgs models, see e.g. [152, 153]. More recently, they have also been noticed in the scalar and Yukawa sector [1, 2, 4, 5, 7, 45, 46]. If walking regimes now capture gauge or quartic couplings they can enforce PS by preventing the occurrence of subplanckian Landau poles and vacuum instabilities, respectively. This effect is of high relevance for this thesis.

Another advantage of PS is the possible connection of effects in the UV to low energy physics. The loss of absolute SM vacuum stability is a high energy effect far out of reach of present and future colliders. However, the scale of the metastability does not point to a mass scale of NP to cure it. Its remedy may arise from new phenomena at much lower scales, possibly as low as a TeV. Thus, PS opens a door to indirectly test stability at existing and future colliders. Note that in our methodology the absence of a cutoff scale below M_{Pl} thereby constitutes an important conceptual difference w.r.t. the EFT approach.

PS also constitutes a new ansatz for model building on its own right. Up to now, particle physics experiments have mostly confirmed the predictions of the SM with tremendous accuracy in a plethora of measurements at various experiments. This is contrasted by just a few anomalies and the absence of clear NP signatures at colliders or elsewhere, calling for novel theory ideas. PS provides such a new direction in a well-motivated manner. Hence, a central goal of this thesis is to establish and improve PS as powerful tool for BSM model building by exploring the underlying RG mechanisms as well as the interplay of PS with phenomenology.

3.2.3 Vacuum Stability

A crucial feature of Planck-safe models is the stability of the scalar potential which has to be explicitly assured throughout the RG flow. The existence of a stable vacuum requires the scalar potential to be bounded from below. In case of the SM Higgs potential (2.10) the simple condition

$$\lambda > 0 \tag{3.15}$$

assures tree-level vacuum stability but is broken in the SM for $10^{11}\,\mathrm{GeV} \lesssim \mu \lesssim 10^{28}\,\mathrm{GeV}$. In order to rigorously investigate the stability of a scalar potential, additional corrections from loops and higher-order operators have to be taken into account. To do so, one has to compute the full Coleman-Weinberg effective

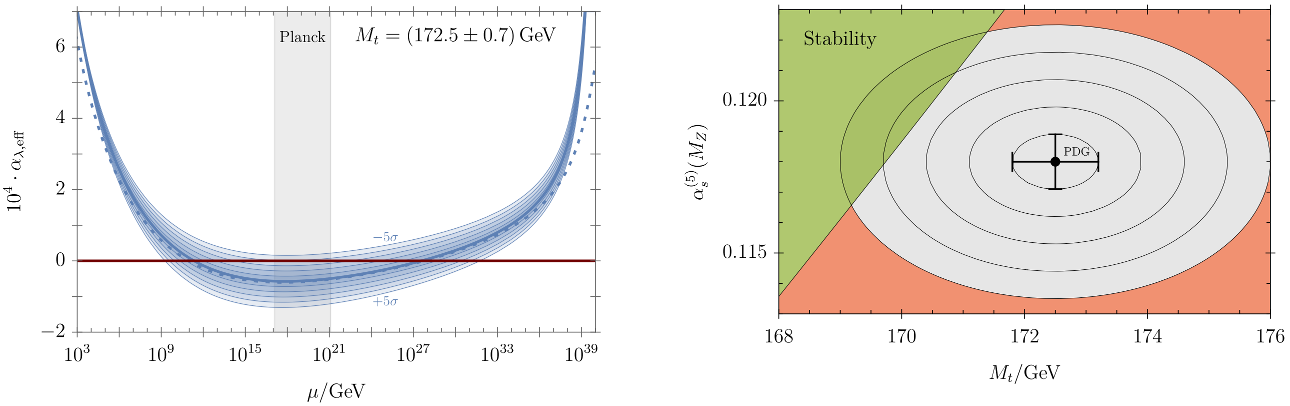

(a) Running of the effective Higgs quartic coupling $\alpha_{\lambda,\mathrm{eff}}(\mu)$ using the PDG central value of the top mass M_t from cross section-measurements [155] (thick line) and five standard deviations in either direction (thin lines), while the gray band indicates the Planck scale. Also shown is the running of the tree-level quartic coupling $\alpha_\lambda(\mu)$ for comparison (thick dashed line). The full effective potential is absolutely stable if $\alpha_{\lambda,\mathrm{eff}}(\mu)$ stays manifestly positive during the whole RG evolution.

(b) (In-)stability regions of the full effective SM Higgs potential up to M_{Pl} as a function of the top mass M_t from cross section-measurements and the strong coupling constant $\alpha_s^{(5)}(M_Z)$. Color-coding indicates absolute stability $\alpha_{\lambda,\mathrm{eff}}(\mu) \geq 0$ for all $\mu_0 \leq \mu \leq M_{\mathrm{Pl}}$ (green) or its loss $\min \alpha_{\lambda,\mathrm{eff}}(\mu) < 0$ (red/gray). Central values (crosshairs) and uncertainties taken from PDG [155]. We also show the first five 1σ uncertainty rings (thin lines) with deviations added in quadrature.

Figure 3.2: Stability of the SM effective potential at state-of-the-art accuracy. Plots taken from [4].

potential [154] and to subsequently perform a detailed analysis of its extrema structure. If the potential features local minima, the lifetime of each false vacuum has to be inferred by computing the tunneling probability to the true vacuum. Only if the lifetime of the false vacuum is sufficiently larger then the age of the universe it constitutes a viable ground state of the theory.

In the SM, corresponding computations [36–38] evidenced the metastability of the full effective Higgs potential V_{eff} with a sufficiently large lifetime. The loss of absolute stability of V_{eff} is indicated by a sign change of the effective Higgs quartic coupling

$$\alpha_{\lambda,\mathrm{eff}} = \alpha_\lambda + \mathcal{O}(\alpha^2)\,, \tag{3.16}$$

which explicitly contains the mentioned higher-order effects, see App. A in [4] and references therein for a pedagogical derivation and precise definition. We reanalyzed the stability of the SM Higgs vacuum in [4], exceeding the precision of previous computations by applying the highest available loop orders for the effective potential, β-functions and matching, respectively, as well as the most precise available determination of input parameters. Here, we only briefly review the central results referring to [4] for details. Overall, the evidence for the loss of vacuum stability in the SM is sharpened. This can be seen in Fig. 3.2a, which displays the running of $\alpha_{\lambda,\mathrm{eff}}$. At the reference scale $\mu_{\mathrm{ref}} = 200$ GeV, $\alpha_{\lambda,\mathrm{eff}}(\mu_{\mathrm{ref}})$ is 17% larger than its tree-level pendant $\alpha_\lambda(\mu_{\mathrm{ref}})$. However, it still turns negative around $\mu \simeq 2 \cdot 10^{11}$ GeV close to the scale of sign change of the tree-level quartic and stays slightly negative $\alpha_{\lambda,\mathrm{eff}} \gtrsim -10^{-4}$ until beyond the Planck scale. This reflects our previous finding from Subsec. 3.1.3 that the Higgs quartic is subdominant to its own RG evolution. We conclude that the loss of SM vacuum stability is mainly RG induced while the impact of finite order corrections to the effective potential on stability is rather small.

Rigorously inferring the loss of Higgs stability at the 5σ level is however still prevented by experimental uncertainties of input parameters, in particular the top mass and the strong coupling constant[6]. This is illustrated in Fig. 3.2b. Absolute vacuum stability is restored if the PDG average for the top quark mass from direct cross-section measurements $M_t = 172.5 \pm 0.7$ GeV[7] or the 5-flavor strong coupling constant at the Z mass $\alpha_s^{(5)}(M_Z) = 0.1180 \pm 0.0009$ deviate by -3.9σ (cf. Fig. 3.2a) and $+8.0\sigma$ from their central values, respectively. Neglecting possibly relevant correlations [157] and adding uncertainties in quadrature, already a 3.5σ shift would suffice to achieve stability. Notably, all other input parameters for the stability analysis are either numerically too small (e.g. masses of fermions except for the top) or determined with a too small uncertainty (e.g. $\alpha_{1,2}$, M_Z, M_h) for their uncertainties to matter at the level of M_t and $\alpha_s^{(5)}(M_Z)$ for the stability of the effective potential.

Unfortunately, repeating the full effective potential analysis in BSM models is quite intricate and computationally expensive. Moreover, our model building goal is rather to identify Planck-safe parameter space regions and to qualitatively understand the underlying RG mechanisms than to perform high precision stability analyses. Therefore, in this work we apply a more efficient approach by just checking for tree-level stability. This naturally limits the precision of our computation but in exchange facilitates a comparatively fast and automated stability analysis. We also recall that finite-order corrections to the SM effective potential are only of minor impact for stability, which is rather dominated by RG effects, cf. Fig. 3.2a. Thus, the tree-level analysis constitutes a good and well-justified approximation for checking vacuum stability.

Nevertheless, we also try to estimate the reach of higher-order contributions to stabilize the effective potential. A mild violation of tree-level stability might in fact be compensated by such higher-order corrections yielding a metastable potential as in the SM [4, 37, 38]. Strong violations of tree-level stability on the other hand are expected to correspond to instabilities of the effective potential. In case of the Higgs potential we therefore distinguish between metastabilities $-10^{-4} < \alpha_\lambda < 0$ and instabilities $\alpha_\lambda < -10^{-4}$ roughly estimating the critical value from [37, 38]. On a technical level, this also implies the discrimination between RG flows exhibiting *strict* and *soft* PS, which we define as:

- **strict Planck safety**: No Landau poles below M_{Pl},
  absolute tree-level vacuum stability $\forall \mu \in [\mu_0, M_{\text{Pl}}]$

- **soft Planck safety**: As strict PS,
  but allowing for an *intermediate, moderately negative* Higgs quartic[8]
  $-10^{-4} \lesssim \alpha_\lambda(\mu) \lesssim 0$ for $\mu \in [\mu_0, M_{\text{Pl}})$ but $\alpha_\lambda(M_{\text{Pl}}) > 0$.

Here μ_0 denotes a low scale, typically the scale of NP. This distinction is exemplarily illustrated in Fig. 3.3. In both cases, the RG flow has to be free of subplanckian Landau poles but the vacuum stability requirements differ in rigor. The notion of strict PS demands absolute tree-level vacuum stability during the complete RG flow all the way up to M_{Pl}. Thus, strict PS provides a conservative criterium for stability. Note that strict PS always requires the NP scale μ_0 to be lower than the scale of the sign change of α_λ in the SM of $\sim 10^{11}$ GeV. Soft PS on the other hand also allows for intermediate, SM-like metastabilities of the Higgs potential. However, instabilities are forbidden and the potential has to be fully stable at M_{Pl}. Interestingly, the last condition is also beneficial for asymptotically safe models of quantum gravity, as matching them to the SM typically disfavors SM-like $\alpha_\lambda(M_{\text{Pl}}) < 0$, e.g. [158, 159]. Hence, soft PS

---

[6] Note that although contributing only starting from 2-loop to both β_λ and the effective potential, the strong coupling and its uncertainty still have a crucial impact on stability due to the numerically sizeable value of α_3 (and α_t).

[7] We stress that the methodology for an accurate extraction of the top quark mass from data is quite intricate and subject of an ongoing debate [4, 156].

[8] If a BSM stability condition in a model with extended scalar sector is not well-defined for $\alpha_\lambda < 0$, we conservatively deploy this condition in the limit $\alpha_\lambda \to 0$.

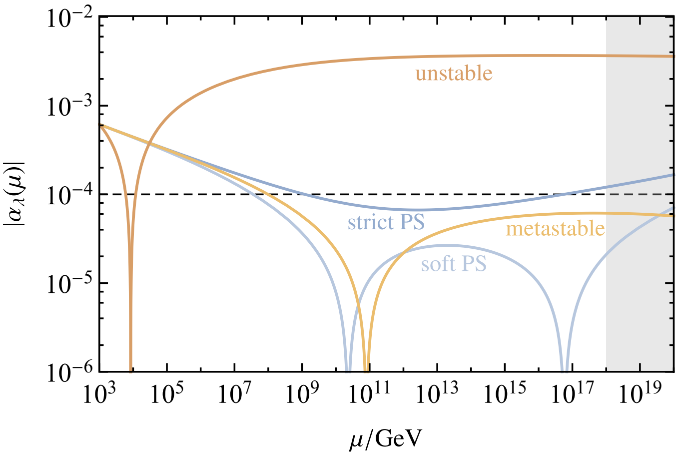

Figure 3.3: The different possible RG fates of the Higgs quartic α_λ. Trajectories with $\min\alpha_\lambda(\mu) < -10^{-4}$ correspond to an unstable potential (brown). For $-10^{-4} \leq \min\alpha_\lambda(\mu) \leq 0$ the trajectory features metastabilities. In this case we label the trajectory as metastable (yellow) if $\alpha_\lambda(M_{\mathrm{Pl}}) \leq 0$ or softly Planck-safe (light blue) if $\alpha_\lambda(M_{\mathrm{Pl}}) > 0$ corresponding to Planck scale stability. If finally $\min\alpha_\lambda(\mu) > 0$ the RG evolution is strictly Planck-safe and features absolute stability all the way up to M_{Pl}.

still constitutes an improvement w.r.t. the SM, exploring the maximum reach for Planck scale stability by imposing stabilization due to neglected higher-order corrections at intermediate scales. Thus, soft PS provides a more optimistic estimate for vacuum stability.

Note that BSM models featuring new scalars, imply additional vacuum stability conditions complementing (3.15). Tree-level vacuum stability conditions for arbitrary potentials can be derived following the methods of [137, 160, 161] using copositivity criteria and typically imply a set of inequality conditions for scalar quartic couplings[9]. Quantifying the effect of violating these tree-level BSM stability conditions on vacuum stability would require a rigorous analysis of the full BSM effective potential from which we refrain. Consequently, we do not allow for any violation of BSM stability conditions but demand all of them to be fulfilled at all scales up to M_{Pl} for both strict and soft PS.

3.2.4 Strategy and Workflow

The starting point our PS analysis in BSM models are the values of SM couplings at a scale $\mu_{\mathrm{ref}} = 200\,\mathrm{GeV}$, which have been determined at high precision in [162] from experimental data. The precise values are given in App. A.2. The couplings are evolved towards the UV using the SM β-functions at full 3-loop order in the gauge [117, 132, 133], Yukawa [130, 131] and scalar [119, 120] sector. This is done by numerically solving the RGEs using `Mathematica` [63]. In order to reduce the complexity and computing time we thereby neglect all Yukawa couplings other than the top and bottom one. This approximation is well justified, as the neglected Yukawas are significantly smaller than all other SM couplings.

The next task is to match the SM RG flow to the BSM one at the NP scale μ_{NP} which is set by the mass scale of BSM particles M_{BSM}. We restrict ourselves to scenarios where the NP scale is well above the electroweak scale, i.e. $\mu_{\mathrm{EW}} < \mu_{\mathrm{NP}} \simeq M_{\mathrm{BSM}}$. Typically we assume NP around the TeV scale which allows

---

[9] The asymptotic shape of the potential for very large field values is dictated by the scalar quartic couplings. Thus, the conditions for boundedness from below, i.e. the existence of a stable vacuum, only depend on the quartics and are independent of all other parameters in the scalar sector.

for collider signatures at the LHC. Moreover, we assume that the BSM particles exhibit no large mass hierarchies, so that from the RG point of view our model is characterized by just a single scale[10]. If not stated otherwise, SM couplings are matched to their BSM counterparts at tree level via

$$\alpha^{\text{BSM}}_{1,2,3,t,b,\lambda}(\mu_{\text{NP}}) = \alpha^{\text{SM}}_{1,2,3,t,b,\lambda}(\mu_{\text{NP}}). \tag{3.17}$$

The values of BSM couplings are treated as free model parameters above μ_{NP} and set to zero below.

We then employ the tools `ARGES` [32] and `FoRGEr` [33] to infer the β-functions of all couplings in the BSM model at full 2-loop order. As couplings in all sectors can be of similar size we refrain from including available higher loop orders in the gauge- and Yukawa β-functions for the sake of consistency of the perturbative expansion[11]. β-functions of SM couplings in the full model above μ_{NP} are composed of the SM contribution and a BSM one

$$\beta_{1,2,3,t,b,\lambda} = \beta^{\text{SM}}_{1,2,3,t,b,\lambda} + \beta^{\text{BSM}}_{1,2,3,t,b,\lambda}, \tag{3.18}$$

whereas β-functions of BSM couplings are purely BSM and just switched on above μ_{NP}. Note that in our matching procedure the BSM fields have been implicitly approximated as infinitely heavy below μ_{NP} and as massless above. However, at loop level threshold corrections to this approximation induced by finite BSM particle masses arise which replace the dependence on the unphysical matching scale μ_{NP} by the physical mass M_{BSM}, see e.g. [163] for a pedagogical introduction. Pleasantly, when matching at $\mu_{\text{NP}} = M_{\text{BSM}}$ all threshold corrections $\propto \ln \frac{\mu_{\text{NP}}}{M_{\text{BSM}}}$ induced by the heavy BSM fields vanish. Thus, in our procedure threshold corrections are minimized which justifies our approximation.

Having the complete set of β-functions as well as SM coupling values at the matching scale at hand, we also fix the values of BSM parameters in order to solve the full RGEs up to M_{Pl} and analyze the obtained RG flow to determine its RG fate. This task is automated in a `Mathematica` [63] routine. It numerically integrates the RGEs and subsequently evaluates the numerical solution which is a function of $\log \mu$ at several hundred intermediate energies $\mu_0 \le \mu_i \le M_{\text{Pl}}$[12]. If a numerical RG trajectory features a very large coupling $\alpha(\mu_i) > 10$ or derivative $\frac{\mathrm{d}\,\alpha}{\mathrm{d}\,\log \mu}(\mu_i) > 500$ for any μ_i[13], we categorize it as featuring a *pole*. For a pole-free RG flow, we next determine $\min_i \alpha_\lambda(\mu_i)$. If $\min_i \alpha_\lambda(\mu_i) \le -10^{-4}$ we label the trajectory as *Higgs unstable*. For RG flows without a Higgs instability we also evaluate (potential) BSM stability conditions $\forall \mu_i$, deploying them in the limit $\lambda \to 0$ at μ_i iff $\lambda(\mu_i) < 0$ and they would be ill-defined otherwise. If there is a violation of BSM stability at any μ_i, we categorize the trajectory as *vacuum unstable*. If not, we compute $\alpha_\lambda(M_{\text{Pl}})$ and label the flow as *Higgs metastable* if $\alpha_\lambda(M_{\text{Pl}}) < 0$, *softly Planck-safe* if $\alpha_\lambda(M_{\text{Pl}}) > 0$, $-10^{-4} < \min_i \alpha_\lambda(\mu_i) < 0$ and eventually *strictly Planck-safe* if $\min_i \alpha_\lambda(\mu_i) > 0$. We stress that the order of the steps is crucial to determine the labeling of trajectories exhibiting several unpleasant features, i.e. a pole *and* a Higgs instability[14].

This procedure can straightforwardly be repeated for other values of BSM parameters in a systematic scan over the available parameter space in order to determine the BSM critical surface of a model.

---

[10] Obviously the situation is different from the view point of phenomenology where the exact particle masses are crucial to e.g. determine kinematically allowed decay channels of BSM particles.

[11] The absence of 3-loop quartic template β-functions prevents us from employing `333` loop order also in the full theory.

[12] We thereby use the same grid points that Mathematica dynamically determined as anchors for the numerical integration, with the step-width depending on the slope of the flow.

[13] The numbers have been carefully adjusted such that it is very improbable to mislabel a trajectory as pole. The derivative criterium filters out rare, unphysical trajectories featuring evident numerical instabilities close to an apparent pole that can arise for large numbers of couplings.

[14] We thereby intentionally chose to first check for the occurrence of poles, as affected trajectories quite often entail a loss of vacuum stability closely below the pole. Our convention aims at only correspondingly labeling trajectories with vacuum stability problems in the well perturbative regime while not including those with pole-induced instabilities.

4 Stabilizing the Higgs with Vector-like Fermions

In this chapter we systematically explore the possibility to render the SM Planck-safe by extending it with VLFs, closely following [2, 5]. The presented BSM models offer a promising, minimally invasive approach towards Higgs stability as they comprise just a single BSM field and are hence controlled by just a few free parameters. However, this ansatz towards Higgs stability based solely on VLFs has so far received surprisingly little attention. The few existing works [164–169] mostly restrict themselves to models with additional, weakly coupled BSM Yukawa interactions. In particular, stabilization in the absence of BSM Yukawas was only fragmentarily studied for certain colorful VLFs in [169]. Also the regime of tiny or strongly coupled Yukawas up to now has hardly been explored at all. We close this gap by performing an in-depth analysis of minimal VLF models in order to identify the different vacuum stabilization mechanisms arising in the RG flow, quantify their effect on the Higgs potential and examine their phenomenological implications.

We start with presenting our setup and notation. In our models, the SM is extended by N_F generations of VLFs ψ of mass M_F in the representation (Y_F, d_2, d_3) under the SM gauge group $U(1)_Y \times SU(2)_L \times SU(3)_C$, that may or may not allow for a Yukawa portal coupling κ to SM fields. Here, vector-like refers to the equal representation of the LH ψ_L and RH ψ_R components of ψ under the SM gauge group which constitutes an important qualitative difference to chiral SM fermions. The implementation of the VLFs in a BSM model is by design quite straightforward for two reasons. Firstly, our models are free of gauge anomalies which would spoil the consistency of the theory but can only be caused by chiral fermions, see [170] for a detailed review. Secondly, the vector-like representation allows for explicit Dirac mass terms of the VLFs which for chiral fermions are forbidden by gauge invariance. Hence, the VLFs acquire a mass even without the Higgs mechanism. In this work, we generically assume the VLF mass to be $M_F \gtrsim 1\,\text{TeV}$.

We now first explore the possibility to stabilize the Higgs via a modified running of gauge couplings in Sec. 4.1 before turning to models with an extended Yukawa sector in Sec. 4.2. We also briefly comment on phenomenological implications of our findings.

4.1 Gauge Portals

The core of the gauge portal mechanism for Higgs vacuum stability is the addition of charged BSM matter to the SM. More precisely, we add N_F VLFs charged under the SM as $(Y_F,\, d_2,\, d_3)$, without introducing any new interactions. Therefore, for now we focus on VLF representations that do not allow for a Yukawa coupling to SM fields or assume possible Yukawa couplings to be negligibly small, a property that is conserved in the RG flow due to their technical naturalness. The addition of charged matter manifests itself in a modified running of the respective gauge couplings. The Higgs β-function in contrast remains unchanged. Hence, a stabilization of the Higgs can only arise indirectly and is channeled through the modified running of gauge couplings and the top Yukawa.

In order to understand the RG dynamics of the gauge portal mechanism we make use of the general properties of β-functions in GY theories, which have been discussed in detail in Sec. 3.1. In particular, we work out the leading order deviations of the RG flow in our VLF models from the SM one. Integrating the 1-loop gauge coupling RGEs (3.4)

$$\beta_i = -B_i \alpha_i^2 \tag{4.1}$$

we obtain their well-known RG evolution (3.5)

$$\alpha_i(\mu) = \frac{\alpha_i(\mu_0)}{1 + \alpha_i(\mu_0)\, B_i\, \ln \frac{\mu}{\mu_0}}. \tag{4.2}$$

from the matching scale μ_0 to some high scale μ. The relevant 1-loop coefficients

$$B_1 = -\frac{41}{3} - \delta B_1, \qquad B_2 = \frac{19}{3} - \delta B_2, \qquad B_3 = 14 - \delta B_3 \tag{4.3}$$

consist of the SM contributions as well as a BSM ones

$$\delta B_1 = \tfrac{8}{3} N_F \, d_2 \, d_3 \, Y_F^2, \qquad \delta B_{2,3} = \tfrac{8}{3} N_F \, d_{3,2} \, S_2(d_{2,3}) \,, \tag{4.4}$$

where $S_2(d_{2,3})$ denote the respective Dynkin indices of the $SU(2)_L$ and $SU(3)_C$ representations. The magnitude of the δB_i is controlled by the multiplicity N_F and representation (Y_F, d_2, d_3) of the VLFs. Crucially, the BSM contribution is always positive, i.e. $\delta B_i \geq 0$. Thus, the gauge couplings above the NP scale generically take larger values than in the SM. Quantitatively, from (4.2) we find

$$\frac{1}{\alpha_i(\mu)} - \frac{1}{\alpha_i^{\text{SM}}(\mu)} = -\delta B_i \ln\left(\frac{\mu}{\mu_0}\right) < 0 \tag{4.5}$$

for the enhancement w.r.t. the SM. Consequently, all models still feature the hypercharge Landau pole at an equal or lower scale than in the SM $\mu_{\text{LP}} \leq \mu_{\text{LP}}^{\text{SM}} \simeq 10^{41}$ GeV which can be subplanckian. More so, if $\delta B_{2,3}$ are too large, also AF of $SU(2)_L$ and $SU(3)_C$ is lost and $\alpha_{2,3}$ run into a Landau pole, too. Hence, the δB_i should not be too large in order to avoid any Landau poles below M_{Pl}.

The modified running of gauge couplings imprints itself also on the running of the top Yukawa, which due to its size has a crucial impact on the running of the Higgs quartic coupling. In contrast to the gauge sector, the 1-loop top β-function does not receive any direct BSM contributions from the charged new fields. It remains the same as in the SM (3.11)

$$\beta_t \simeq \alpha_t \left(9\alpha_t - \tfrac{17}{6}\alpha_1 - \tfrac{9}{2}\alpha_2 - 16\alpha_3\right) \,, \tag{4.6}$$

where we neglected the bottom Yukawa due to its smallness. Nevertheless, also the top running is modified due to the gauge contributions to β_t. Crucially, β_t receives negative contributions from all gauge couplings α_i, so that the increase in the RG evolution of gauge couplings (4.5) results in a accelerated decrease of α_t in comparison to the SM. Analytically integrating the RG flow to leading order in couplings and δB_i as well as to leading logarithmic accuracy, we find

$$\alpha_t(\mu) - \alpha_t^{\text{SM}}(\mu) \approx -\alpha_t(\mu_0) \left(\tfrac{17}{12}\delta B_1 \, \alpha_1^2 + \tfrac{9}{4}\delta B_2 \, \alpha_2^2 + 8 \, \delta B_3 \, \alpha_3^2\right) \ln^2\left(\frac{\mu}{\mu_0}\right) < 0 \tag{4.7}$$

as approximate result for the decrease of α_t w.r.t. the SM. As (4.1) and (4.6) are both 1-loop the deviation from SM running is a resummation effect which is signaled by the squared logarithmic term in (4.7). Thus, the leading deviation of $\alpha_t(\mu)$ manifests itself at 2-loop due to the modified 1-loop running of gauge couplings contained within (4.6). Note that there is also a competing effect at the same order in couplings from the direct modification of the top β-function at 2-loop due to additional VLF gauge contribution. However, this contribution is only linear in the large logarithm $\ln\frac{\mu}{\mu_0}$ and therefore a subleading effect w.r.t. the resummed deviation (4.7).

Turning to the running of the Higgs quartic, we note that at 1-loop β_λ does not receive any direct BSM contributions and is thus given by its SM pendant (3.13). Nevertheless, analogously to the top Yukawa also the running of the Higgs quartic is indirectly modified due to the altered RG evolution of the gauge and Yukawa sector. Direct BSM contributions to the Higgs β-function at higher loop orders in contrast are of subleading logarithmic accuracy and therefore neglected. Given that α_λ around the electroweak scale is much smaller than the top Yukawa and gauge couplings, cf. (A.6), β_λ is numerically dominated by the inhomogeneous 1-loop terms and can be approximated as

$$\beta_\lambda \simeq \frac{3}{8}(\alpha_1^2 + 2\alpha_1\alpha_2 + 3\alpha_2^2) - 6\alpha_t^2. \tag{4.8}$$

Crucially, the gauge contributions are positive while the top one is negative. Thus, both the increase of gauge couplings (4.5) and the decrease of the top-Yukawa (4.7) relatively to the SM result in an increase of β_λ. To quantify the effect on the Higgs quartic, we integrate the RG flow of α_λ in (4.8) deploying (4.5) and (4.7). To leading order in δB_i and couplings as well as leading logarithmic accuracy we finally obtain

$$\begin{aligned} \alpha_\lambda(\mu) - \alpha_\lambda^{\mathrm{SM}}(\mu) \approx &+ \tfrac{3}{8}\alpha_1^2(\mu_0)\,[\alpha_1(\mu_0) + \alpha_2(\mu_0)]\,\delta B_1\,\ln^2\left(\frac{\mu}{\mu_0}\right) \\ &+ \tfrac{3}{8}\alpha_2^2(\mu_0)\,[\alpha_1(\mu_0) + 3\alpha_2(\mu_0)]\,\delta B_2\,\ln^2\left(\frac{\mu}{\mu_0}\right) \\ &+ 32\,\alpha_t^2(\mu_0)\,\alpha_3^2(\mu_0)\,\delta B_3\,\ln^3\left(\frac{\mu}{\mu_0}\right)\,, \end{aligned} \tag{4.9}$$

which constitutes the central result of our semi-analytical analysis.

We learn that an uplift of the electroweak gauge couplings $\alpha_{1,2}$ directly results in an uplift $\propto \delta B_{1,2}$ in α_λ at 2-loop order. In case of the strong coupling there is no such effect as the Higgs is uncharged under QCD. This is reflected in the absence of an α_3 contribution to β_λ at 1-loop (4.8). Hence, the leading effect of δB_3 on the running of α_λ arises at 3-loop and is channeled through the altered top running. Despite being of higher loop order, this effect turns out to be numerically comparable to electroweak contributions due to larger values of both the numerical coefficient in (4.9) and $\alpha_{3,t}(\mu_0)$. Analogous 3-loop enhancements of α_λ due to modified top running arise $\propto \delta B_{1,2}$ from the electroweak gauge couplings. They are however not included in (4.9) as they are subleading with respect to the explicitly given direct electroweak effects. The strong gauge portal mechanism via the top Yukawa has already been noticed in [169]. A systematic derivation of the RG dynamics as presented here as well as a rigorous analysis of the available parameter space are however missing. Beyond that, the direct electroweak portal mechanisms so far to our knowledge have not been considered at all in the literature and constitute a main novelty of this work.

Notably, all δB_i contribute positively to (4.9). Hence, the effects of all three gauge portals constructively add up jointly pushing the Higgs towards stability. We infer that the presence of BSM matter charged arbitrarily under at least one SM gauge interaction invariably results in an uplift of the Higgs quartic

$$\alpha_\lambda(\mu) - \alpha_\lambda^{\mathrm{SM}}(\mu) > 0 \tag{4.10}$$

and potentially vacuum stability. This establishes the viability of the gauge portal mechanism. In particular, we aim at finding Planck safety windows in the model parameter space, where the δB_i are sufficiently sizeable to enable vacuum stability but still below the threshold to cause subplanckian Landau poles. Note that the magnitude of the different contributions in (4.9) is not only set by the size of the δB_i but also increases with the RG time $\ln\frac{\mu}{\mu_0}$ that has passed since the matching at $\mu_0 \simeq M_F$. This is not surprising, as the resummed effect of the modified BSM accumulates when contributing increasingly long to the RG evolution.

Given that the leading order scalar and Yukawa β-functions are the same as in the SM, the overall shape of the RG trajectory $\alpha_\lambda(\mu)$ also approximately resembles the SM case Fig. 3.1. In particular, the extrema structure of the trajectory is preserved. However, an important difference arises when the enhanced running of gauge couplings (4.5) generates a Landau pole below the SM hypercharge one $\mu_{\mathrm{LP}} < \mu_{\mathrm{LP}}^{\mathrm{SM}} \simeq 10^{41}$ GeV.

In this case, the accelerated running of gauge couplings also results in an accelerated running of $\alpha_\lambda(\mu)$ between the matching scale and the Landau pole but still approximately along its SM trajectory. More precisely, it holds $\alpha_\lambda(\mu) \approx \alpha_\lambda^{\text{SM}}(\mu^{\text{SM}}(\mu))$ with $\mu_{\text{SM}}(\mu) \geq \mu$ bijectively mapping $[\mu_0, \mu_{\text{LP}}] \to [\mu_0, \mu_{\text{LP}}^{\text{SM}}]$. This squeezing can exemplarily be seen for the hypercharge portal in Fig. 4.4 and is discussed in more detail in Subsec. 4.1.3. Hence, there are two net effects of the gauge portal mechanism on the running of α_λ w.r.t the SM: A compression of the RG trajectory and a moderate uplift (4.9). The relative size of this effects depends on the choices of parameters and varies for the three different gauge portals.

Crucially, these two modifications of the trajectory imply that $\alpha_\lambda(\mu)$ is bounded from below by its minimal value in the SM. Discarding the tiny region in μ close to the hypercharge Landau pole after the third sign change of α_λ, this yields $\alpha_\lambda(\mu) \gtrsim \alpha_\lambda^{\text{min,SM}} \simeq -10^{-4}$. Moreover, due to the squeezing and the increase of the uplift with $\ln \frac{\mu}{\mu_0}$ the minimum of $\alpha_\lambda(\mu)$ always appears at lower or equal scales than in the SM, i.e. at $\mu_{\text{min}} \leq \mu_{\text{min}}^{\text{SM}} \simeq 10^{17}\,\text{GeV}$. Recalling that the minimal SM value corresponds to metastability of the full effective potential with sufficiently large lifetime [37, 38], we conclude that also in any gauge portal extension the effective potential is at least metastable. In particular, any observationally forbidden instabilities are automatically excluded justifying the tree-level approach for stability.

4.1.1 Strong Portal

In order to analyze the strong gauge portal in more detail, we now study VLFs in the representation $(0, \mathbf{1}, d_3)$ that only interact via $SU(3)_C$. Hence, the running of the strong coupling is enhanced by $\delta B_3 > 0$ whereas the evolution of electroweak gauge couplings remains SM-like with $\delta B_{1,2} = 0$, see (4.4). The model is characterized by just three parameters: the multiplicity N_F, mass M_F and $SU(3)$ representation d_3 of the VLFs.

To begin, we focus on VLQs with $d_3 = \mathbf{3}$. We compute the full 2-loop RG evolution of couplings from the matching scale $\mu_0 \simeq M_F$ up to the Planck scale, scanning over the free parameters (M_F, N_F) as described in Subsec. 3.2.4. The result is depicted in Fig. 4.1a, where different colors indicate different RG fates. In regions of relatively low N_F or large M_F we end up with a metastable potential at the Planck scale (yellow), similar as in the SM. For large N_F and low M_F we encounter subplanckian Landau poles (red).However, there is also a wedge-shaped region in between where these problems are avoided and the vacuum is stable at the Planck scale (blue). It corresponds to a Planck-safe RG evolution and constitutes the BSM critical surface constrained by upper and lower bounds on N_F as well as an upper bound on M_F.

This division of the parameter space can be understood by recalling the results (4.9) of our semi-analytical analysis. The strong portal mechanism is controlled by δB_3 which is proportional to N_F (4.4). For low N_F, the uplift in the Higgs quartic (4.9) induced by the enhanced running of α_3 is not sizeable enough to render α_λ positive at the Planck scale. This implies a lower bound on N_F for PS. For sizeable N_F in contrast also δB_3 is sizeable and above $N_F \gtrsim 10$ AF of the strong coupling is lost, in excellent agreement with the 1-loop estimate $N_F \gtrsim \frac{21}{2}$ from (4.4). Hence, we encounter an α_3 Landau pole in the UV, which for large N_F and sufficiently low M_F occurs below the Planck scale. This gives rise to the (M_F-dependent) upper bound on N_F. The upper bound on M_F arises as the values of $\alpha_{3,t}(\mu_0)$ for large $\mu_0 \simeq M_F$ have already severely decreased due to their SM running. Hence, the uplift $\propto \alpha_3^2(\mu_0)\alpha_t^2(\mu_0)$ is not sizeable enough anymore and the strong portal mechanism becomes insufficient to ensure stability. Moreover, for larger M_F there is less RG time left between $\mu_0 \simeq M_F$ and $\mu = M_{\text{Pl}}$ for the uplift $\propto \ln^3 \frac{\mu}{\mu_0}$ in α_λ to sufficiently set in. This explains the wedged shape of the Planck-safe region in Fig. 4.1 which generically requires larger multiplicities N_F for increasing masses M_F.

The BSM critical surface is further subdivided into regions of soft (light blue) and strict (dark blue) PS, where the vacuum is stable at or even all the way up to M_{Pl}, respectively. These different stability regions arise due to different stabilization mechanisms. Strict PS is achieved by an uplift in α_λ from (4.9) that is

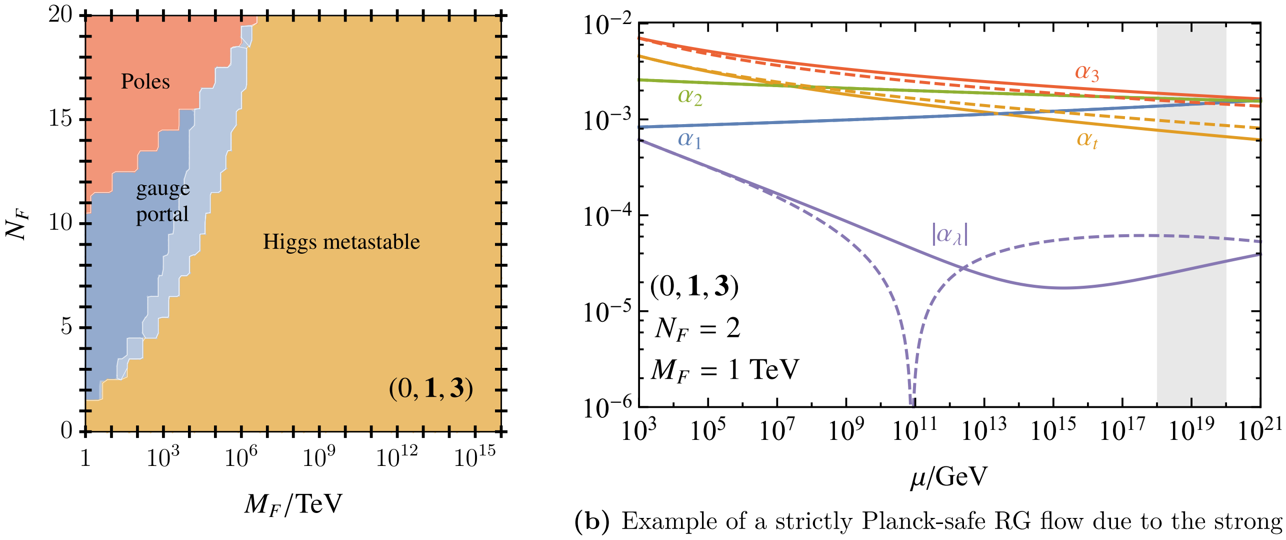

(a) BSM critical surface in the (N_F, M_F) plane. Different colors indicate strict (dark blue) as well as soft (light blue) PS, a metastable vacuum at the Planck scale (yellow) or a subplanckian Landau pole (red).

(b) Example of a strictly Planck-safe RG flow due to the strong portal mechanism. We show the RG evolution of couplings until the Planck scale (gray) at full 2-loop order in a model featuring $N_F = 2$ vector-like quarks (VLQs) (solid lines) with mass $M_F = 1\,\text{TeV}$ together with SM 3-loop running (dashed lines) for reference.

Figure 4.1: The strong gauge portal for a SM extensions with VLQs charged as $(0, \mathbf{1}, \mathbf{3})$ under the SM. Shown is the BSM critical surface in the (N_F, M_F) plane (a) as well as an exemplary strictly Planck-safe RG evolution (b). Figures adapted from [2].

sufficiently large to render its minimum value positive and prevent subplanckian metastability. An example for a strictly Planck-safe RG evolution due to the strong portal mechanism is depicted in Fig. 4.1b for the case of $N_F = 2$ VLQs of mass $M_F = 1\,\text{TeV}$. As expected from our semi-analytical estimate, in this scenario (solid lines) we observe a mild enhancement of α_3 along with a decrease in α_t w.r.t. the SM (dashed lines) that is sufficient to ensure vacuum stability all the way up to M_{Pl}.

In the regions of soft PS in contrast the uplift is not sizeable enough to render the minimum positive. Nevertheless, the uplift can be sufficient to shrink the metastability interval such that the second sign change already appears below M_{Pl}. This is mostly relevant for small N_F. In addition, there is a collaborating effect from the squeezing of the RG trajectory of $\alpha_\lambda(\mu)$. It starts being relevant as soon as AF in α_3 is lost and its Landau pole appears below the hypercharge one, i.e. $N_F \gtrsim 10 - 12$ with slight dependence on M_F. The squeezing then has the same effect, namely pulling the second sign change below M_{Pl} enabling soft PS. Putting it all together, we obtain from Fig. 4.1a the conditions

$$\begin{aligned} M_F &\lesssim 10^4\,\text{TeV}, \qquad 2 \le N_F \le 15, \\ (M_F &\lesssim 10^6\,\text{TeV}, \qquad 2 \le N_F \le 19) \end{aligned} \tag{4.11}$$

for strict (soft) PS, which demonstrates the predictive power of PS.

Of particular interest are the borders between the different regions in the parameter space. At the boundary between soft PS and metastability at M_{Pl} we find $\alpha_\lambda(M_{\text{Pl}}) \simeq 0$ whereas at the frontier between soft and strict PS the minimum value of the Higgs quartic is $\alpha_\lambda^{\text{min}}(\mu) \simeq 0$, indicating Higgs *criticality*.

We now turn to higher representations $d_3 > \mathbf{3}$ under $SU(3)_C$. The Dynkin-Index $S_2(d_3)$ increases for

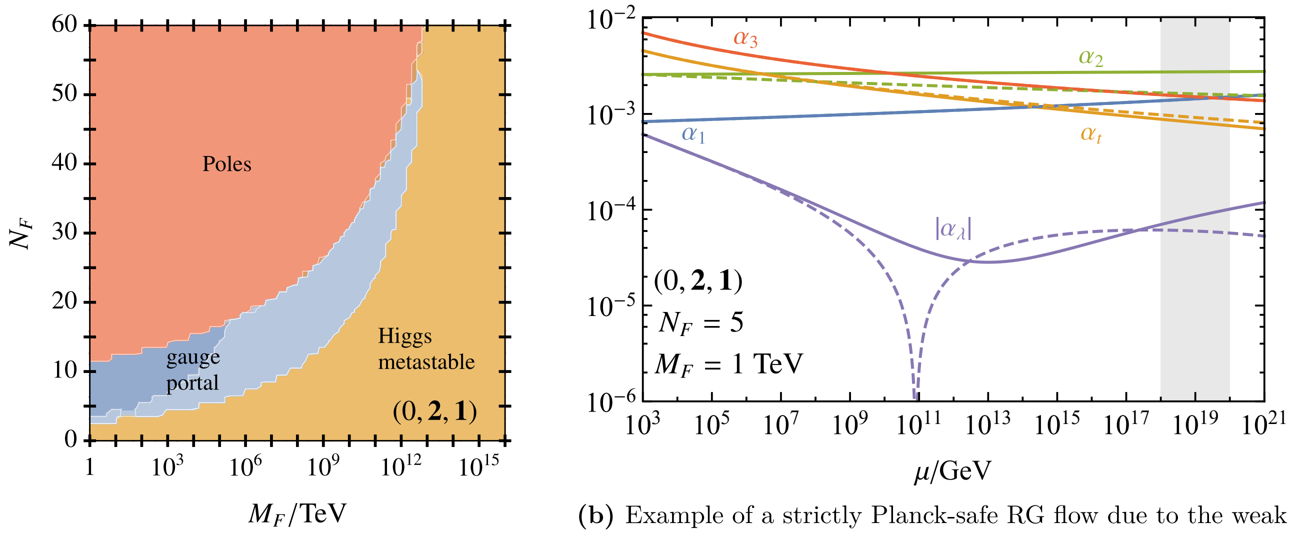

(a) BSM critical surface in the (N_F, M_F) plane. Same color coding as Fig. 4.1. The weak portal extents far into the region of large M_F and N_F.

(b) Example of a strictly Planck-safe RG flow due to the weak portal mechanism. Shown is the RG evolution of couplings at full 2-loop order in a model featuring $N_F = 5$ vector-like leptons (VLLs) (solid lines) with mass $M_F = 1\,\text{TeV}$ together with SM 3-loop running (dashed lines) for reference.

Figure 4.2: The weak gauge portal for a SM extensions with VLLs charged as $(0, \mathbf{2}, \mathbf{1})$ under the SM. Shown is the BSM critical surface in the (N_F, M_F) plane (a) as well as an exemplary strictly Planck-safe RG evolution (b). Figures adapted from [2].

larger d_3, cf. Subsec. 3.1.1, yielding larger contributions δB_3 for fixed N_F (4.4). Hence, the N_F window of the BSM critical surface is shifted towards lower values and shrinks, see also Fig. B.2 in App. B. For $d_3 = \mathbf{6}, \mathbf{8}$ PS can still be achieved implying qualitatively similar conditions as (4.11). For $d_3 = \mathbf{10}$ however, already adding $N_F = 1$ VLFs with a mass in the multi-TeV range generates a subplanckian Landau pole and the PS window ceases to occur. This excludes PS for all representations $d_3 \geq \mathbf{10}$.

We stress that the gauge portal mechanism operates at weak coupling in the safely perturbative regime. Thus, we expect our full 2-loop order results to be a good approximation such that the existence and shape of the gauge portal should not be relevantly altered at higher loop orders. We verified this for the highest available loop order 432 in the gauge, Yukawa and scalar sector, respectively, see Fig. B.1. There, we can see that increasing the loop order to 432 indeed has negligible impact on the BSM critical surface.

Color charged VLFs in the TeV range without (or with super feeble) Yukawas can be probed at colliders in R-hadron and dijet searches, see [42] for details. Moreover, it is possible to hunt for the direct impact on the running of $\alpha_3(\mu)$ which was measured up to $\mu \simeq 4\,\text{TeV}$ by the ATLAS collaboration [171]. For the masses $M_F \gtrsim 1\,\text{TeV}$ we are interested in, the respective bounds however do not constrain relevant fractions of the BSM critical surface.

4.1.2 Weak Portal

For the analysis of the weak gauge portal, we focus on SM extensions featuring N_F colorless VLFs of mass $M_F \gtrsim 1\,\text{TeV}$ in the representation $(0, d_2, \mathbf{1})$ which are charged solely under $SU(2)_L$. This implies an uplift $\delta B_2 \geq 0$ whereas $\delta B_{1,3} = 0$. An exemplary strictly Planck-safe RG evolution at 2-loop is shown for $d_2 = \mathbf{2}$,

$M_F = 1\,\text{TeV}$ and $N_F = 5$ in Fig. 4.2b.

We also provide the BSM critical surface in the $M_F - N_F$ plane for $d_2 = \mathbf{2}$ in Fig. 4.2. We again encounter a sizeable, wedged PS window situated right between the region of subplanckian α_2 Landau poles (low M_F and high N_F) and Higgs metastability at M_{Pl} (low N_F or very high M_F). The different regions arise in the same manner as in the strong portal case. Interestingly, AF in α_2 is lost already starting from $N_F \gtrsim 5$ in accord with the 1-loop estimate $N_F \geq \frac{19}{4}$ from (4.4). However, for TeV-ish VLLs the α_2 pole only occurs below the hypercharge one for $N_F \geq 8$ and below M_{Pl} for $N_F \geq 11$.Note that these N_F values increase with increasing $\mu_0 = M_F$ due to the decrease of α_2 in the SM. From Fig. 4.2a we obtain the conditions

$$\begin{aligned} M_F &\lesssim 10^5\,\text{TeV}, \qquad 4 \leq N_F \leq 16, \\ (M_F &\lesssim 10^{12}\,\text{TeV}, \qquad 3 \leq N_F \leq 53) \end{aligned} \tag{4.12}$$

for strict (soft) PS. Notably, for soft PS the upper bounds on M_F and N_F are quite large which is different to the strong portal. The reason is, that the SM decrease in α_2 for a wide range of M_F can still be compensated by a large N_F causing large δB_2 (4.4). The resulting direct uplift and squeezing of α_λ are sufficient to pull the second sign change below M_{Pl} and still enable soft PS. This explains the 'banana shape' of the soft PS window. Due to the reduced RG time until the Planck scale for large $\mu_0 = M_F$, the stabilizing effect is for a long time not spoiled by the appearance of subplanckian α_2 Landau poles.

For higher representations $d_2 \geq \mathbf{3}$ the allowed range in N_F shrinks and shifts towards lower values due to larger contributions δB_2 analogously as for the strong portal case, see also Fig. B.3 in App. B. For $d_2 \geq \mathbf{5}$ PS is excluded for VLFs in the TeV-range, as there is already a subplanckian α_2 pole for $N_F = 1$.

4.1.3 Hypercharge Portal

We now consider VLFs in the representation $(Y_F, \mathbf{1}, \mathbf{1})$ under the SM in order to investigate the hypercharge portal. We obtain an enhancement $\delta B_1 \geq 0$ whereas the running of the non-abelian gauge couplings remains SM-like with $\delta B_{2,3} = 0$. The model is characterized by multiplicity N_F, mass M_F and the hypercharge Y_F which in contrast to $d_{2,3}$ is a continuous parameter. At first glimpse, the existence of the hypercharge portal seems counterintuitive as the hypercharge Landau pole in comparison to the SM is shifted towards lower, eventually subplanckian energies when adding $U(1)_Y$ charged matter. However, we find that PS can also be realized via the hypercharge portal mechanism. We investigate this in more detail for $Y_F = \frac{1}{2}$, see Fig. 4.3. An exemplary, softly Planck-safe RG flow is depicted for $N_F = 20$ of these VLLs with a mass of $M_F = 1\,\text{TeV}$ in Fig. 4.3b. The running of α_1 is strongly enhanced w.r.t. the SM with the Landau pole looming close-by in the transplanckian regime around $\mu \simeq 10^{22}\,\text{GeV}$. The induced uplift of α_λ is still not sufficient to render the vacuum stable all the way up to M_{Pl} in contrast to the non-abelian gauge portals. However, the squeezing of the trajectory pulls down the second sign change below M_{Pl} yielding $\alpha_\lambda(M_{\text{Pl}}) > 0$ and hence soft PS.

This effect is further illustrated in Fig. 4.4 for fixed $N_F = 34$ and different values of M_F. The squeezing is most pronounced for the lowest masses M_F, as the enhanced growth of α_1 starts earlier. For large masses, we still encounter a metastable vacuum at M_{Pl} as the squeezing w.r.t. the SM is not sufficient. For lower masses, the squeezing is sufficient to pull-down the second sign change of α_λ to subplanckian energies, yielding a stable vacuum at M_{Pl}. However, when further decreasing M_F eventually also the third sign change triggered by $\alpha_1 \gtrsim \mathcal{O}(10^{-2}$ becomes subplanckian, destabilizing again the vacuum at M_{Pl}. For slightly lower masses finally the Landau pole itself becomes subplanckian.

The different RG fates are also reflected in the BSM critical surface Fig. 4.3a. While regions of strict PS are absent, there is a sizeable window for soft PS which extends deep into the high mass and multiplicity region. Interestingly, there is a narrow instability ridge (brown) located between the pole region and the BSM critical surface which precisely corresponds to the situation where the third sign change is subplanckian,

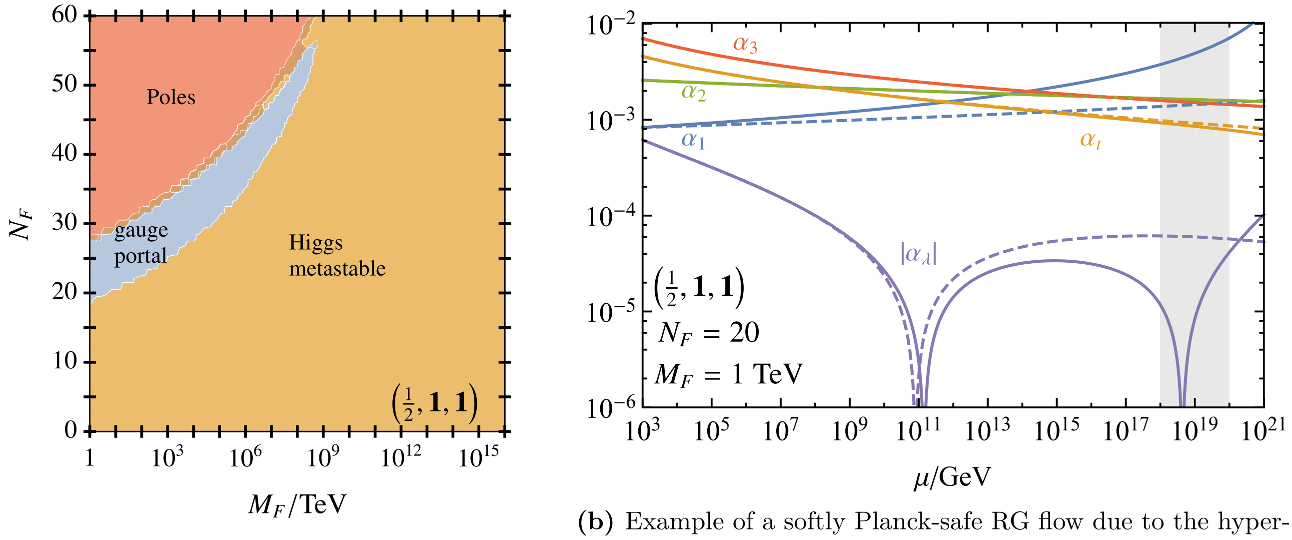

(a) BSM critical surface in the (N_F, M_F) plane. Same color coding as Fig. 4.1, also indicating instabilities of the Higgs potential $\alpha_\lambda < -10^{-4}$ (brown).

(b) Example of a softly Planck-safe RG flow due to the hypercharge portal mechanism. We show the RG evolution of couplings at full 2-loop order in a model featuring $N_F = 20$ VLLs (solid lines) with mass $M_F = 1\,\text{TeV}$ together with SM 3-loop running (dashed lines) for reference.

Figure 4.3: The hypercharge portal for a SM extensions with VLLs charged as $(\frac{1}{2}, \mathbf{1}, \mathbf{1})$ under the SM. Shown is the BSM critical surface in the (N_F, M_F) plane (a) as well as an exemplary softly Planck-safe RG evolution (b). Figures adapted from [2].

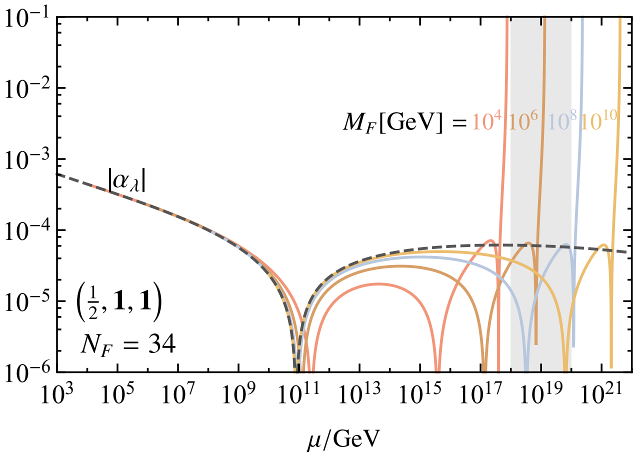

Figure 4.4: Illustration of the squeezing of the RG trajectory of the Higgs quartic. Shown is the 2-loop running of α_λ in a SM extension featuring $N_F = 34$ VLLs in the representation $(\frac{1}{2}, \mathbf{1}, \mathbf{1})$ for different masses M_F (solid lines) indicated by different colors compared to SM running (dashed line). While, the location of the first sign flip hardly changes, the second and third sign changes experience a significant pull down from the deep transplanckian regime (Fig. 3.1) to M_{Pl} and below. The pull-down is larger for lower M_F. Figure adapted from [2].

but the Landau pole is not. The PS window shares the well-known 'banana shape' of the weak portal caused by the requirement of larger δB_1 for higher masses M_F to achieve a stabilization within less RG time $\ln \frac{\mu}{\mu_0}$ between $\mu_0 \simeq M_F$ and $M_{\rm Pl}$. The window finally closes for very large masses and multiplicities, yielding the soft PS conditions

$$M_F \lesssim 10^9\,\text{TeV}, \qquad 19 \leq N_F \leq 55\,. \tag{4.13}$$

Turning to higher (lower) values of $|Y_F|$, the value of δB_1 increases (decreases), cf. (4.4). Thus, the PS window in N_F moves towards lower (higher) values and shrinks (widens), see also Fig. B.4. As $\delta B_1 \propto N_F Y_F^2$, there is to a good approximation an anti-proportionality between the allowed ranges in N_F and Y_F^2 which is just broken by the 2-loop term $8 N_F Y_F^4 \alpha_1^3 \subset \beta_1$. The maximum allowed value of Y_F is obtained for the lowest number of flavors, i.e. $N_F = 1$. For a TeV-ish VLL PS is achieved for $2.16 \leq Y_F \leq 2.53$. The allowed range gets more narrow and shifts towards higher values when increasing the mass, e.g. to $3.33 \leq Y_F \leq 3.45$ for $M_F = 10^{11}$ GeV, shortly before the stability window finally closes.

Theory constraints on VLL parameters from demanding PS can be confronted with experimental measurements of the electroweak precision parameters [172]

$$Y = \tfrac{3}{50}\alpha_1 \frac{m_W^2}{M_F^2}\delta B_1, \qquad W = \tfrac{1}{10}\alpha_2 \frac{m_W^2}{M_F^2}\delta B_2, \tag{4.14}$$

which directly depend on M_F [173] and N_F via $\delta B_{1,2}$ (4.4). However, for $M_F \gtrsim 1$ TeV the existing constraints are not restricting the weak or hypercharge stability windows. Moreover, for VLLs without Yukawa couplings LHC searches for long lived charged particles [174], as well as $\bar{\psi}\psi$ resonances decaying to diphotons apply. Corresponding limits are available for electric charge ≥ 1 and $N_F = 1$, and up to now do not exceed $M_F \gtrsim 1$ TeV.

4.2 Yukawa Portals

We now turn to VLFs representations allowing for a renormalizable Yukawa portal coupling κ to the Higgs and a SM fermion. In total, there are 13 of these VLF representations that are listed in Tab. 4.1. The presence of the BSM Yukawa coupling crucially influences the RG flow of the models as it contributes to the gauge, Yukawa and Higgs quartic β-functions (3.9) starting at 2-, 1- and 1-loop order, respectively, cf. (3.9), (3.10) and (3.12). In particular, the negative contribution to the gauge β-functions

$$\beta_i \subset -D_{i\kappa}\alpha_i^2\alpha_\kappa\,, \tag{4.15}$$

with $D_{i\kappa} \geq 0$ offers a unique mechanism to slow down the growth of gauge couplings [128] and hence to prevent subplanckian Landau poles. The most relevant contributions to the Higgs quartic β-function read

$$\beta_\lambda \subset +I_{\lambda\kappa}\alpha_\lambda\alpha_\kappa - J_{\kappa\kappa}\alpha_\kappa^2 + K_{\kappa\kappa\kappa}\alpha_\kappa^3\,, \tag{4.16}$$

with $I_{\lambda\kappa}$, $J_{\kappa\kappa}$, $K_{\kappa\kappa\kappa} \geq 0$ and can either stabilize or destabilize the Higgs vacuum depending on the values of α_κ and the relevant coefficients. Note that for charged VLFs also the gauge portal mechanism is active. In order to disentangle the different effects simultaneously influencing the RG evolution we first consider feeble Yukawas before allowing for sizeable Yukawa couplings to a single or all three generations of SM fermions.

Model	(Y_F, d_2, d_3)	$-\mathcal{L}^Y_{\text{portal}}$
A	$(-1, \mathbf{1}, \mathbf{1})$	$\kappa_{ij}\,\overline{L}_i H \psi_{Rj} + \text{h.c.}$
B	$(-1, \mathbf{3}, \mathbf{1})$	$\kappa_{ij}\,\overline{L}_i \psi_{Rj} H + \text{h.c.}$
C	$(-\frac{1}{2}, \mathbf{2}, \mathbf{1})$	$\kappa_{ij}\,\overline{\psi}_{Li} H E_j + \text{h.c.}$
D	$(-\frac{3}{2}, \mathbf{2}, \mathbf{1})$	$\kappa_{ij}\,\overline{\psi}_{Li} H^c E_j + \text{h.c.}$
E	$(\ 0,\ \mathbf{1}, \mathbf{1})$	$\kappa_{ij}\,\overline{L}_i H^c \psi_{Rj} + \text{h.c.}$
F	$(\ 0,\ \mathbf{3}, \mathbf{1})$	$\kappa_{ij}\,\overline{L}_i \psi_{Rj} H^c + \text{h.c.}$
G	$(-\frac{1}{3}, \mathbf{1}, \mathbf{3})$	$\kappa_{ij}\,\overline{Q}_i H \psi_{Rj} + \text{h.c.}$
H	$(+\frac{2}{3}, \mathbf{1}, \mathbf{3})$	$\kappa_{ij}\,\overline{Q}_i H^c \psi_{Rj} + \text{h.c.}$
I	$(-\frac{1}{3}, \mathbf{3}, \mathbf{3})$	$\kappa_{ij}\,\overline{Q}_i \psi_{Rj} H + \text{h.c.}$
J	$(+\frac{2}{3}, \mathbf{3}, \mathbf{3})$	$\kappa_{ij}\,\overline{Q}_i \psi_{Rj} H^c + \text{h.c.}$
K	$(+\frac{1}{6}, \mathbf{2}, \mathbf{3})$	$\kappa^u_{ij}\,\overline{\psi}_{Li} H^c U_j + \kappa^d_{ij}\,\overline{\psi}_{Li} H D_j + \text{h.c.}$
L	$(+\frac{7}{6}, \mathbf{2}, \mathbf{3})$	$\kappa_{ij}\,\overline{\psi}_{Li} H U_j + \text{h.c.}$
M	$(-\frac{5}{6}, \mathbf{2}, \mathbf{3})$	$\kappa_{ij}\,\overline{\psi}_{Li} H^c D_j + \text{h.c.}$

Table 4.1: List of all VLF extensions of the SM allowing for a renormalizable Yukawa portal coupling κ with a SM fermion and the Higgs (two portals $\kappa^{u,d}$ exist in Model K). Shown are the VLF representation (Y_F, d_2, d_3) under the SM and the explicit BSM Yukawa interaction $\mathcal{L}^Y_{\text{portal}}$. Table adapted from [2].

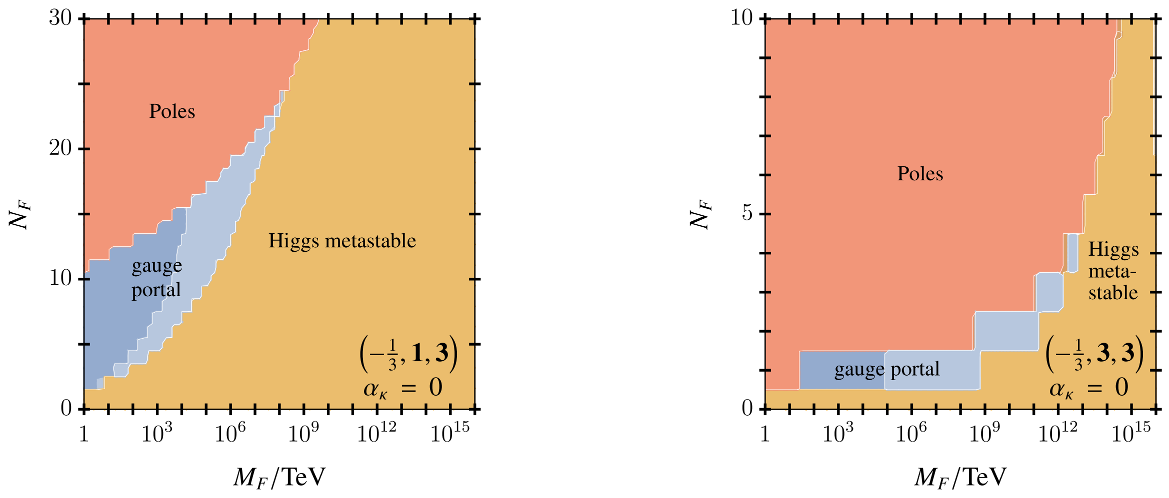

(a) Model G. The pole region corresponds to subplanckian α_3 Landau poles. The BSM critical surface is qualitative similar to the pure strong portal case Fig. 4.1a but extends further into the high M_F and N_F region due to the collaborating hypercharge portal. Figure adapted from [2].

(b) Model I. The pole region corresponds to subplanckian α_2 Landau poles. Stabilization arises from collaboration between all three gauge portals with the weak portal being dominant. PS can only be realized for relatively heavy VLFs with $M_F \gtrsim 30\,\text{TeV}$ and low multiplicities N_F.

Figure 4.5: Collaboration of gauge portals for vanishing Yukawa portal coupling $\alpha_\kappa = 0$. Shown is the BSM critical surface in the (N_F, M_F) plane for model G (a) and I (b). Same color coding as in Fig. 4.1.

Model		**Poles**		**Planck safety**	
	(Y_F, d_2, d_3)	N_F^{pole}	α^{pole}	soft	strict
A	$(-1, \mathbf{1}, \mathbf{1})$	7	α_1	$N_F = 6$	X
B	$(-1, \mathbf{3}, \mathbf{1})$	3	α_1	$1 \leq N_F \leq 2$	$1 \leq N_F \leq 2$
C	$(-\frac{1}{2}, \mathbf{2}, \mathbf{1})$	12	α_2	$3 \leq N_F \leq 11$	$5 \leq N_F \leq 11$
D	$(-\frac{3}{2}, \mathbf{2}, \mathbf{1})$	2	α_1	$N_F = 1$	X
E	$(\ 0\ , \mathbf{1}, \mathbf{1})$	∞		X	X
F	$(\ 0\ , \mathbf{3}, \mathbf{1})$	3	α_2	$1 \leq N_F \leq \frac{5}{2}$	$\frac{3}{2} \leq N_F \leq \frac{5}{2}$
G	$(-\frac{1}{3}, \mathbf{1}, \mathbf{3})$	11	α_3	$2 \leq N_F \leq 10$	$2 \leq N_F \leq 10$
H	$(+\frac{2}{3}, \mathbf{1}, \mathbf{3})$	6	α_1	$2 \leq N_F \leq 5$	$2 \leq N_F \leq 5$
I	$(-\frac{1}{3}, \mathbf{3}, \mathbf{3})$	1	α_2	X	X
J	$(+\frac{2}{3}, \mathbf{3}, \mathbf{3})$	1	α_2	X	X
K	$(+\frac{1}{6}, \mathbf{2}, \mathbf{3})$	4	α_2	$1 \leq N_F \leq 3$	$1 \leq N_F \leq 3$
L	$(+\frac{7}{6}, \mathbf{2}, \mathbf{3})$	1	α_1	X	X
M	$(-\frac{5}{6}, \mathbf{2}, \mathbf{3})$	2	α_1	$N_F = 1$	$N_F = 1$

Table 4.2: Planck fate of VLFs models A-M from Tab. 4.1 for different multiplicities N_F assuming $M_F = 1$ TeV and vanishing Yukawa portals $\alpha_\kappa|_{M_F} \simeq 0$. For $N_F \geq N_F^{\text{pole}}$, the gauge coupling α^{pole} runs into a subplanckian Landau pole. Allowed ranges of N_F for soft and strict PS are also indicated. Model E remains metastable as in the SM, whereas Models I, J, and L develop Landau poles below M_{Pl} already for $N_F = 1$. Note that since the BSM fermion representations are real in Models E and F, half-integer values for N_F (odd number of Weyl fermions) are compatible with the cancellation of gauge anomalies [170]. Table adapted from [2].

4.2.1 Feeble Yukawas

Yukawa portal couplings are technically natural. Hence, when chosen feebly small or vanishing at the matching scale this property is conserved during the RG evolution. In this case, the influence of α_κ on the RG flow is negligible. The gauge portal mechanism is however still active, and potentially capable of ensuring vacuum stability. For VLFs charged nontrivially under more than one SM gauge interaction the effects from the different gauge portals add up according to (4.9), see also Fig. 4.5. Adding too many charged VLFs for feeble $\alpha_\kappa \simeq 0$ gives rise to a subplanckian Landau pole of the gauge coupling corresponding to the dominant portal mechanism. Hence, we search for Planck safety windows where the enhanced running of gauge couplings is sufficient to stabilize the Higgs but does not yet cause Landau poles below M_{Pl}.

For $M_F = 1\,\text{TeV}$, the results of our analyses in model A-M are summarized in Tab. 4.2. Strict PS can be realized for some ranges of N_F in models B,C,F[1],G,H,K,M. Models A and D do not allow for strict but for soft PS. This is understandable as stabilization in model A (D) proceeds purely (mostly) via the hypercharge portal. PS cannot be achieved in models E,I,J,L. The VLFs in model E are SM singlets, thus the gauge portal is inactive and the Higgs remains metastable as in the SM independent of N_F. Models I,J,L on the other hand develop subplanckian Landau poles already for $N_F = 1$. The reason is the large color factor $d_3 = \mathbf{3}$ contributing to $\delta B_{1,2}$ (4.4) which in combination with sizeable $d_2 = \mathbf{3}$ $(Y_F = \frac{7}{6})$ gives

---

[1] Note that VLFs in models E and F come in real representations under the SM gauge group. Hence, an odd number of Weyl fermions corresponding to an half-integer number of Dirac fermions N_F is compatible with the cancellation of gauge anomalies [170].

	Model	**Interactions**	**Planck fate**	**Gauge Portal**		**Yukawa Portal**	
	(Y_F, d_2, d_3)	$-\mathcal{L}_Y^{\text{portal}}$	for $\alpha_\kappa = 0$	$\alpha_{\kappa,\mathbf{max}}^{\mathbf{strict}}\vert_{M_F}$	$\alpha_{\kappa,\mathbf{max}}^{\mathbf{soft}}\vert_{M_F}$	$\alpha_{\kappa,\mathbf{min}}^{\mathbf{soft}}\vert_{M_F}$	$\alpha_{\kappa,\mathbf{min}}^{\mathbf{strict}}\vert_{M_F}$
A	$(-1, \mathbf{1}, \mathbf{1})$	$\kappa\,\overline{L}_3 H \psi_R$	metastability	X	X	$6 \cdot 10^{-3}$	0.2
B	$(-1, \mathbf{3}, \mathbf{1})$	$\kappa\,\overline{L}_3 \psi_R H$	strict PS	$2 \cdot 10^{-4}$	$1.6 \cdot 10^{-3}$	$1.6 \cdot 10^{-2}$	0.4
C	$(-\frac{1}{2}, \mathbf{2}, \mathbf{1})$	$\kappa\,\overline{\psi}_L H E_3$	metastability	X	X	$6 \cdot 10^{-3}$	0.2
D	$(-\frac{3}{2}, \mathbf{2}, \mathbf{1})$	$\kappa\,\overline{\psi}_L H^c E_3$	soft PS	X	$3 \cdot 10^{-5}$	$8 \cdot 10^{-3}$	0.2
E	$(\ 0,\ \mathbf{1}, \mathbf{1})$	$\kappa\,\overline{L}_3 H^c \psi_R$	metastability	X	X	$5 \cdot 10^{-3}$	0.2
F	$(\ 0,\ \mathbf{3}, \mathbf{1})$	$\kappa\,\overline{L}_3 \psi_R H^c$	soft PS	X	$1 \cdot 10^{-3}$	$1.6 \cdot 10^{-2}$	0.4
G	$(-\frac{1}{3}, \mathbf{1}, \mathbf{3})$	$\kappa\,\overline{Q}_3 H \psi_R$	metastability	X	X	$1 \cdot 10^{-2}$	0.2
H	$(+\frac{2}{3}, \mathbf{1}, \mathbf{3})$	$\kappa\,\overline{Q}_3 H^c \psi_R$	metastability	X	X	$6 \cdot 10^{-3}$	0.2
I	$(-\frac{1}{3}, \mathbf{3}, \mathbf{3})$	$\kappa\,\overline{Q}_3 \psi_R H$	α_2-pole	X	X	0.3	0.6
J	$(+\frac{2}{3}, \mathbf{3}, \mathbf{3})$	$\kappa\,\overline{Q}_3 \psi_R H^c$	α_2-pole	X	X	0.3	0.6
K	$(+\frac{1}{6}, \mathbf{2}, \mathbf{3})$	$\kappa_t\,\overline{\psi}_L H^c U_3$	strict PS	$1 \cdot 10^{-5}$	$1 \cdot 10^{-4}$	0.13	0.25
		$+\kappa_b\,\overline{\psi}_L H D_3$		$1 \cdot 10^{-5}$	$1 \cdot 10^{-4}$	0.13	0.25
L	$(+\frac{7}{6}, \mathbf{2}, \mathbf{3})$	$\kappa\,\overline{\psi}_L H U_3$	α_1-pole	X	X	$1 \cdot 10^{-2}$	0.2
M	$(-\frac{5}{6}, \mathbf{2}, \mathbf{3})$	$\kappa\,\overline{\psi}_L H^c D_3$	strict PS	$8 \cdot 10^{-4}$	$1.4 \cdot 10^{-3}$	$8 \cdot 10^{-3}$	0.2

Table 4.3: Planck safety windows of SM extensions featuring a single VLF of mass $M_F = 1\,\text{TeV}$ with Yukawa coupling α_κ only to third generation SM fermions and the Higgs. The allowed soft and strict PS ranges in $\alpha_\kappa|_{M_F}$ for both the gauge and the Yukawa portal are indicated in each model, respectively. For model K, the indicated ranges correspond to the case of just one Yukawa coupling $\kappa_{t,b}$ being switched on at a time, respectively. Notably, for large $\alpha_\kappa|_{M_F}$ the Yukawa portal mechanism allows for strict PS in all models due to the occurrence of strongly coupled walking regimes. The gauge portal mechanism on the other hand can only render a few models Planck-safe. For vanishing Yukawas, the Planck fate of each model is indicated and the results of Tab. 4.2 are recovered. Table adapted from [2].

rise to an α_2 (α_1) pole below M_{Pl} in model I,J (L). The subplanckian poles can be avoided by choosing larger $\mu_0 \simeq M_F$. This is illustrated for model I in Fig. 4.5 where a PS window opens up for $M_F \gtrsim 30\,\text{TeV}$ implying a lower mass bound for PS. We also observe the characteristic wedge shape of the PS window which can exemplarily be seen in Fig. 4.5a for model G.

4.2.2 Third Generation Yukawa Portals

In full generality, the portal coupling κ_{ij} is a matrix in flavor space with $3\,N_F$ independent components. However, in the spirit of minimality for the remainder of this section we restrict ourselves to $N_F = 1$ generations of VLFs[2]. This reduces the number of free parameters and simplifies the analysis of the emerging RG dynamics. To start, we assume only a single non-negligible Yukawa coupling of the VLF to the third SM fermion generation to be switched on. This setup is popular also in experimental analyses, e.g. [175, 176], as models A-M are then fully characterized by the VLF mass M_F and the value of the portal coupling α_κ.

The results of our analysis are summarized in Tab. 4.3 assuming $M_F = 1\,\text{TeV}$. For vanishing Yukawas

---

[2] Two models with $N_F = 3$ and additional BSM scalar fields are studied in Chap. 6. In comparison to the minimal models they exhibit a rich phenomenology coming at the price of a large number of free BSM parameters.

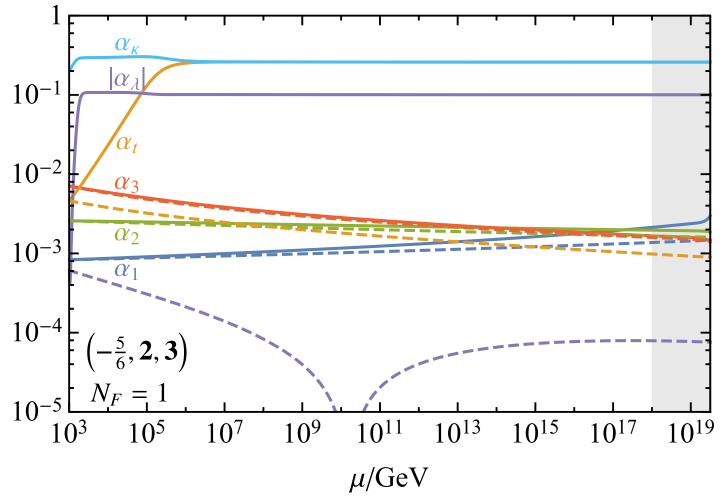

Figure 4.6: Illustration of the Yukawa portal mechanism. Exemplarily shown is the strictly Planck-safe RG flow in Model M of Tab. 4.3 for a single VLF with mass $M_F \simeq 1\,\text{TeV}$ and Yukawa coupling $\alpha_\kappa|_{M_F} = 0.2$ at full 2-loop order (solid). The large initial value of the Yukawa coupling induces a walking regime closely above the matching scale. The Yukawas $\alpha_{\kappa,t}$ as well as α_λ are kept at strongly coupled values all the way up to the Planck scale. The gauge couplings on the other hand do not participate in the walking but continue to run at weak coupling all the way up to the Planck scale, similar as in the SM (dashed). Figure adapted from [2].

$\alpha_\kappa|_{M_F} \simeq 0$, the models exhibit diverse phenomena such as strict (B,K,M) and soft (D,F) PS due to the gauge portal mechanism, Higgs metastability at M_{Pl} (A,C,E,G,H) or subplanckian Landau poles (I,J,L), in agreement with our findings from Subsec. 4.2.1. The gauge portal window in models B,D,F,K,M generically implies model-dependent upper limits on $\alpha_\kappa|_{M_F}$ for strict and soft PS in the ballpark of $10^{-5} - 10^{-3}$, see Tab. 4.3. This is not a surprise as increasing $\alpha_\kappa|_{M_F}$ destabilizes the Higgs due to the negative contribution $\beta_\lambda \supset -J_{\kappa\kappa}\alpha_\kappa^2$, cf. (4.16). This destabilizing effect was already observed in [164–169]. Hence, for intermediate, weakly coupled values $\alpha_\kappa|_{M_F}$ PS cannot be realized.

When further increasing the Yukawa coupling, the situation however changes. Sizeable values of $\alpha_\kappa|_{M_F}$ induce walking regimes, where some couplings almost stop running and nearly stay constant for several orders of magnitude. This behavior is related to approximate zeros of the β-functions of involved couplings, see Subsec. 3.2.2 for details. An example is illustrated in Fig. 4.6 for model M with $M_F = 1\,\text{TeV}$ and $\alpha_\kappa|_{M_F} = 0.2$. While the running of gauge couplings stays SM-like, the Yukawa and quartic couplings $\alpha_{t,\kappa,\lambda}$ enter the walking regime closely above the matching scale and are captured at sizeable, positive values all the way up to M_{Pl}[3]. In particular, the walking renders α_λ positive throughout until the Planckian regime, enforcing vacuum stability. Moreover, the sizeable values of the Yukawas $\alpha_{\kappa,t}$ decelerate the growth of gauge couplings and push Landau poles further towards the UV. Hence, the walking regime allows to stabilize the Higgs and to prevent subplanckian Landau poles and a new PS window opens up at large $\alpha_\kappa|_{M_F}$ which we refer to as Yukawa portal. Notably, we find that the emergence of such walking regimes is quite generic and PS can be achieved via the Yukawa portal mechanism in all models A-M for sufficiently large $\alpha_\kappa|_{M_F}$. In some models, soft PS can already arise for couplings as low as $\alpha_\kappa|_{M_F} \gtrsim$ few $\times\, 10^{-3}$. For strongly coupled $\alpha_\kappa|_{M_F} \gtrsim$ few $\times\, 10^{-1}$ we finally obtain strict PS in all models. This constitutes a central result of our analysis.

---

[3] Interestingly, $\alpha_{\kappa,t}$ asymptote to very similar values as up to subleading corrections from $\alpha_{1,b,\lambda}$ their β-functions are identical after exchanging $\alpha_\kappa \leftrightarrow \alpha_t$.

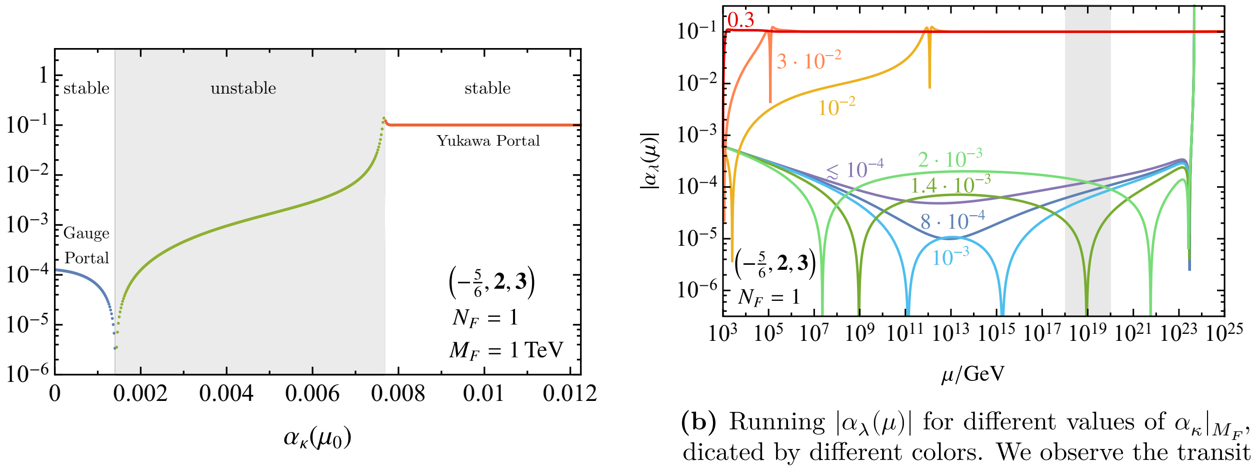

(a) Absolute value of the Higgs quartic coupling at the Planck scale $|\alpha_\lambda(M_{\text{Pl}})|$ as a function of the Yukawa portal coupling at the matching scale $\alpha_\kappa|_{M_F}$. Stability can be achieved via the gauge portal (blue) or the Yukawa portal (red) for feebly or strongly coupled $\alpha_\kappa|_{M_F}$, respectively. In between, weakly coupled $\alpha_\kappa|_{M_F}$ destabilize the Higgs potential and render $\alpha_\lambda(M_{\text{Pl}})$ negative (green).

(b) Running $|\alpha_\lambda(\mu)|$ for different values of $\alpha_\kappa|_{M_F}$, indicated by different colors. We observe the transition from the gauge to the Yukawa portal by varying $\alpha_\kappa|_{M_F}$. For feeble α_κ (violet, dark blue) strict PS is achieved via the gauge portal. Increasing $\alpha_\kappa|_{M_F}$ renders the minimum of α_λ negative, giving rise to a subplanckian metastability interval (light blue). When further increasing $\alpha_\kappa|_{M_F}$, the second sign change moves beyond M_{Pl} yielding Planck scale metastability (green). Eventually, for $\alpha_\kappa \gtrsim 10^{-2}$ (yellow, orange, red) soft and strict PS are restored due to a strongly coupled walking regime.

Figure 4.7: Gauge and Yukawa portal mechanism for different values of $\alpha_\kappa|_{M_F}$. Exemplarily shown are plots for model M with a single VLF of mass $M_F \simeq 1\,\text{TeV}$. For feeble values of $\alpha_\kappa|_{M_F}$, PS is achieved via the gauge portal mechanism. In the weakly coupled regime, the Yukawa destabilizes the Higgs vacuum. Finally, strongly coupled $\alpha_\kappa|_{M_F}$ allows for PS again. Figures taken from [2].

We stress that the Yukawa portal relies on a completely different mechanism than the gauge portal. In the gauge portal mechanism, the mild enhancement in the running of gauge couplings indirectly causes an higher-order uplift and squeezing of α_λ. This results in a mild deformation of the RG trajectories w.r.t. the SM. In the Yukawa portal mechanism in contrast, the shape of Yukawa and quartic RG trajectories is drastically changed due to large α_κ contributions to their β-functions already at leading order.

The dominant RG mechanisms that are operative for different magnitudes of the Yukawa coupling are further illustrated in comparison in Fig. 4.7. There, the impact of the value of $\alpha_\kappa|_{M_F}$ on vacuum stability is investigated exemplarily in model M for $M_F = 1\,\text{TeV}$. Fig. 4.7a shows $|\alpha_\lambda(M_{\text{Pl}})|$ as a function of $\alpha_\kappa|_{M_F}$ whereas Fig. 4.7b depicts the full RG trajectory $|\alpha_\lambda(\mu)|$ for selected values of $\alpha_\kappa|_{M_F}$. From Fig. 4.7b we see that for feeble and weak Yukawas $\alpha_\kappa|_{M_F} \lesssim 10^{-2}$ the hypercharge Landau pole occurs above M_{Pl} around $\mu \simeq 5 \cdot 10^{23}$ GeV. The minimum value $\alpha_\lambda^{\text{min}}$ is realized around $\mu_{\text{min}} \simeq 10^{13}$ GeV. For feeble Yukawa couplings (violet, dark blue) the Higgs quartic stays positive throughout the running and we obtain a strictly Planck-safe RG evolution due to the gauge portal mechanism. When increasing the Yukawa, $\alpha_\lambda^{\text{min}}$ decreases and eventually turns negative for $\alpha_\kappa|_{M_F} \gtrsim 8 \cdot 10^{-4}$. This give rise to a metastability interval of quickly increasing width. At first, the second sign change stays subplanckian (light blue) and we still encounter soft PS with $\alpha_\lambda(M_{\text{Pl}}) > 0$, see also Fig. 4.7a (blue). Above $\alpha_\kappa|_{M_F} \gtrsim 1.4 \cdot 10^{-3}$ in contrast the second change is pushed in the transplanckian regime and the gauge portal closes due to the loss of Planck

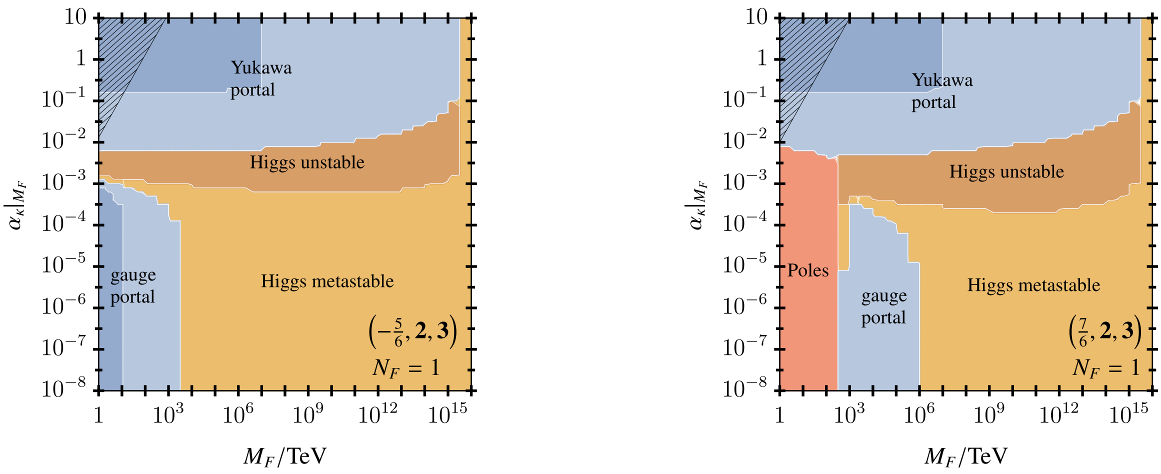

(a) Model M. **(b)** Model L.

Figure 4.8: BSM critical surfaces in the $M_F - \alpha_\kappa|_{M_F}$ plane for Model M (a) and L (b) from Tab. 4.1 for $N_F = 1$ and coupling to third generation SM fermions only. Same color coding as Fig. 4.1, also indicating unstable potentials $\alpha_\lambda < -10^{-4}$ (brown). 90% confidence level (c.l.) exclusion regions on α_κ / M_F^2 from SMEFT fits [177, 178] are indicated as black hatched regions. Figures taken from [2].

scale stability (green).

This changes again for $\alpha_\kappa|_{M_F} \gtrsim 8 \cdot 10^{-3}$, when the Yukawa portal opens up and α_λ is captured in a walking regime at sizeable, positive $\alpha_\lambda \simeq 10^{-1}$. The second sign change is thereby again enforced below M_{Pl}, rendering the trajectory softly Planck-safe (yellow, orange)[4]. The onset of walking occurs earlier for larger $\alpha_\kappa|_{M_F}$. Above $\alpha_\kappa|_{M_F} \gtrsim 0.2$ the walking starts immediately above the matching scale, even preventing the first sign flip and inducing strict PS again.

We are now in the position to study the impact of varying the matching scale $\mu_0 \simeq M_F$ on the RG flow. To this end, we perform systematic scans over the $M_F - \alpha_\kappa|_{M_F}$ parameter space in all models A-M. In Fig. 4.8 we exemplarily show the BSM critical surfaces for models M and L, of which the first exhibits a gauge portal for TeV-ish M_F while the latter does not.

More precisely, in model M we find that the strict (soft) PS via the gauge portal mechanism is achieved for small $\alpha_\kappa|_{M_F} \lesssim 10^{-3} - 10^{-4}$ and $M_F \lesssim 10\,\text{TeV}$ ($M_F \lesssim 3 \cdot 10^3$ TeV), in accord with our previous findings. For higher masses, the gauge portal closes as there is not enough RG time left to render $\alpha_\lambda(M_{\text{Pl}})$ positive and we encounter Planck scale metastability. For $10^{-3} \lesssim \alpha_\kappa|_{M_F} \lesssim 10^{-2}$ we observe the characteristic vacuum instability strip due to the destabilizing contribution $\supset -J_{\kappa\kappa}\alpha_\kappa^2 \subset \beta_\lambda$. Above, the Yukawa portal opens up at $\alpha_\kappa|_{M_F} \gtrsim 10^{-2}$ ($\alpha_\kappa|_{M_F} \gtrsim 10^{-1}$) for soft (strict) PS. In contrast to the gauge portal, the soft and strict Yukawa portal window stays open almost all the way up to their natural cut-off scales, i.e. M_{Pl} and $M_F \simeq 10^7$ TeV where α_λ becomes negative in the SM, respectively. The reason are the inhomogeneous α_κ contributions to β_λ which dominate for large $\alpha_\kappa|_{M_F}$ and can cause α_λ to enter a stabilizing walking regime almost immediately above the matching scale.

In model L in contrast there is no gauge portal for TeV-ish M_F, due to the hypercharge Landau pole being subplanckian around $\mu = 10^{14}$ TeV. When increasing the mass the Landau pole is however pushed into the transplanckian regime and for $3 \cdot 10^2\ \text{TeV} \lesssim M_F \lesssim 10^6$ TeV, a gauge portal into soft PS opens up.

---

[4] Interestingly, the walking regime also pushes the hypercharge Landau pole further towards the UV.

The rest of the parameter space looks qualitatively similar to model M. In fact, this is the case for all models. At large mass and low coupling we encounter metastability as in the SM. Intermediate values of $\alpha_\kappa|_{M_F}$ cause an instability band, above which the Yukawa portal for soft and finally strict PS opens up. Qualitative differences only arise in the low M_F and $\alpha_\kappa|_{M_F}$ region, which can exhibit a gauge portal window, metastability or subplanckian Landau poles.

We also studied the impact of coupling the VLF to first or second instead of third generation SM fermions. While the phenomenological implications differ (see Subsec. 4.2.4), the BSM critical surfaces are almost identical to the third generation case. The reason is that mixed terms containing both SM and BSM Yukawas in the β-functions are numerically small and hardly influence the RG flow.

The Yukawa portal mechanism is sourced by large values of the Yukawa coupling which induce walking regimes and often requires $\alpha_\kappa|_{M_F} \gtrsim 10^{-1}$. This is close to the perturbativity limit $\alpha_\kappa \simeq 1$ and hence raises the question whether the Yukawa portal and the associated walking regimes are perturbatively stable, i.e. whether they persist at higher loop orders. At the highest available loop order which is 432 in the gauge, Yukawa and scalar sector, respectively, the Yukawa portal disappears due to Landau poles in the Yukawa sector, see Fig. B.5. However, given that walking regimes typically also attract the Higgs quartic at similarly sizeable values $\alpha_\lambda \gtrsim 10^{-1}$ as the Yukawas, applying the 432 β-functions seems inconsistent. To clarify the situation an analysis at full 3-loop order is needed. Unluckily, up to now this is not possible due to the lack of a template formula for scalar quartic β-functions at 3-loop order.

4.2.3 Flavorful Yukawa Portals

So far, we considered Yukawa couplings of VLFs only to a single SM fermion at a time. However, it seems natural to allow for all renormalizable couplings compatible with symmetries to be present in the theory. Therefore, while still keeping precisely $N_F = 1$ BSM fermion we now generalize our analysis by taking into account three VLF Yukawa couplings κ_i to the three SM fermion generations, respectively. In the spirit of minimality, we make use of the approximate SM flavor symmetry

$$U(2)_Q \times U(2)_U \times U(2)_D \times U(3)_L \times U(3)_E \,, \tag{4.17}$$

cf. (2.20) which is only broken mildly by small SM Yukawas of leptons as well as first- and second-generation quarks. Accordingly, we use the ansatz

$$\kappa_i = \begin{cases} (\kappa,\, \kappa,\, \kappa) & \text{for VLLs} \\ (\kappa,\, \kappa,\, \tilde{\kappa}) & \text{for VLQs} \end{cases}, \tag{4.18}$$

which reduces the number of independent BSM Yukawa couplings to two (one) for VLQs (VLLs).

We find, that the BSM critical surfaces in all models are qualitatively very similar to their pendants in the Subsec. 4.2.2 with coupling to third generation SM fermions only. The only systematic deviation is a shift of the PS windows towards lower values of $\alpha_\kappa|_{M_F}$ compared to the single Yukawa case. In VLL models A-F this shift amounts roughly to a factor of $\lesssim 3$. The reason is that α_κ contributions to the β-functions stemming from fermion bubble diagrams pick up an additional factor three from all SM fermion generations running in the loop. This also reflects our finding from Subsec. 4.2.2 that the RG evolution is hardly influenced by the choice of the SM fermion generation a VLF couples to.

In the case of VLQs, the flavor symmetry (4.17) suggests two independent Yukawa couplings $\alpha_{\kappa,\tilde{\kappa}}$. For flavor-universal $\alpha_\kappa|_{M_F} = \alpha_{\tilde{\kappa}}|_{M_F}$ we again find the downwards shift in $\alpha_{\kappa=\tilde{\kappa}}|_{M_F}$ to amount to a factor $\lesssim 3$, cf. Fig. 4.9 exemplarily for model L and M, in complete analogy to the VLL case. Fig. 4.9 also shows the BSM critical surfaces of model L and M in the $\alpha_\kappa|_{M_F} - \alpha_{\tilde{\kappa}}|_{M_F}$ plane for $M_F = 1\,\text{TeV}$. The plots are basically symmetric under the interchange $\alpha_{\tilde{\kappa}} \leftrightarrow 2\alpha_\kappa$ as two SM fermion generations couple with κ but

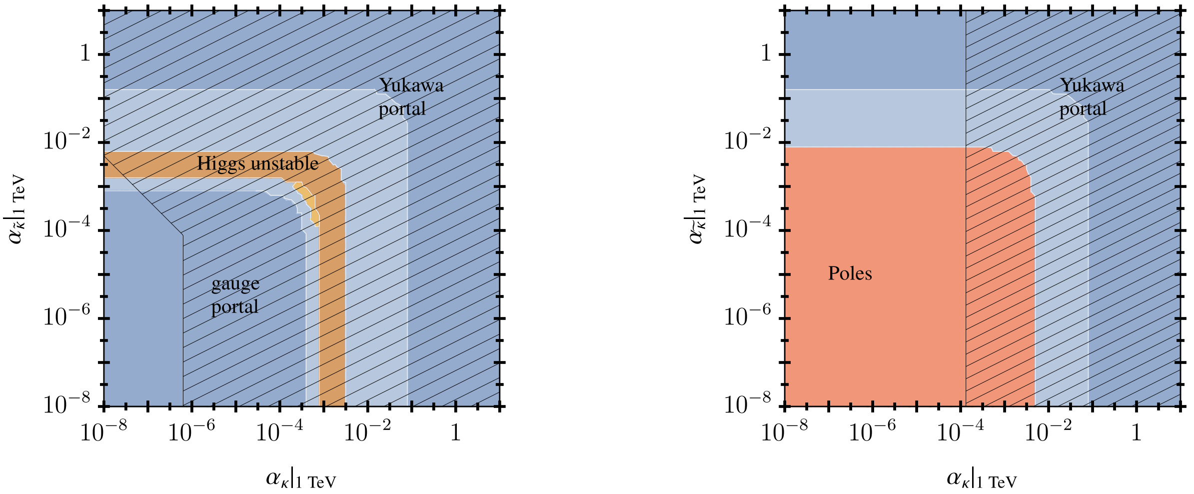

(a) Model M, $M_F = 1\,\text{TeV}$.

(c) Model L, $M_F = 1\,\text{TeV}$.

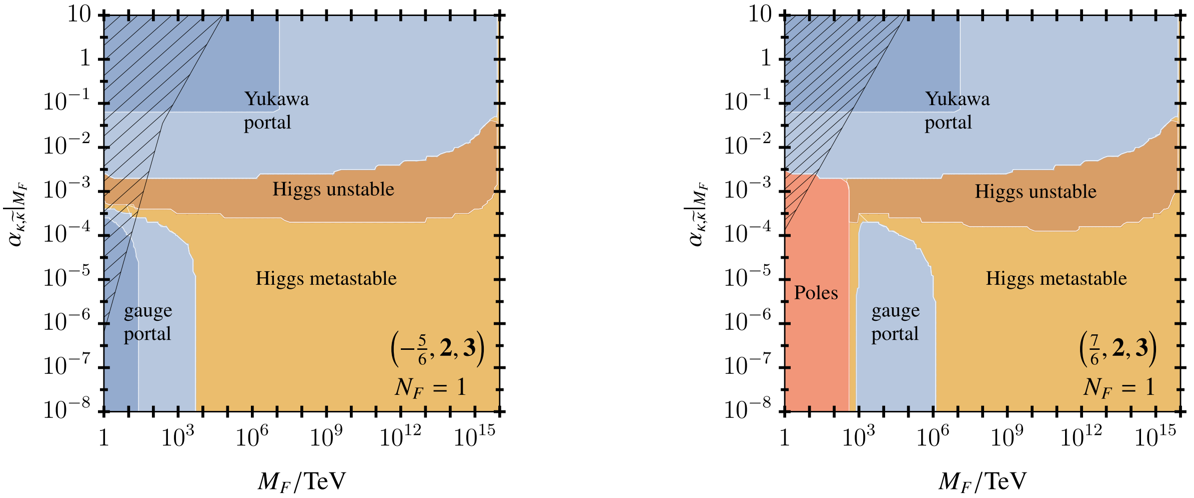

(b) Model M, $\alpha_{\tilde{\kappa}}|_{M_F} = \alpha_{\kappa}|_{M_F}$.

(d) Model L, $\alpha_{\tilde{\kappa}}|_{M_F} = \alpha_{\kappa}|_{M_F}$.

Figure 4.9: BSM critical surfaces for $N_F = 1$ VLF with Yukawa portal couplings to all SM fermion generations. Surfaces are exemplarily given for models M (a,b) and L (c,d) in the $\alpha_{\kappa}|_{M_F} - \alpha_{\tilde{\kappa}}|_{M_F}$ plane with fixed $M_F = 1\,\text{TeV}$ (a,c) and the $M_F - \alpha_{\kappa}|_{M_F}$ plane for $\alpha_{\tilde{\kappa}}|_{M_F} = \alpha_{\kappa}|_{M_F}$ (b,d), respectively. Same color coding as Fig. 4.1. Regions excluded by $\Delta F = 1$ or $\Delta F = 2$ FCNC bounds [179] on α_{κ}/M_F^2 and α_{κ}^2/M_F^2, respectively, are indicated by the black hatched areas. Most stringent FCNC constraints are from $K_L \to \mu\mu$ decays and K-mixing in model M (a,b) as well as 1-loop contributions to D-mixing in model L (c,d). Figures taken from [2].

(a) VLF pair production at colliders (schematic). Figure adapted from [5].

(b) VLF contribution to D-mixing (model L).

Figure 4.10: Phenomenology of VLF models.

just one with $\tilde{\kappa}$. We also learn that for hierarchical Yukawas $\alpha_\kappa \ll \alpha_{\tilde{\kappa}}$ and vice versa the Planck fate is determined by the larger coupling while the influence of the smaller one is of minor importance. While the Yukawa portal dynamics are widely independent of the SM fermion generation(s) and even species the VLF couples to, phenomenological signatures and existing bounds differ severely.

4.2.4 Mass Limits

We briefly examine experimental probes of VLF models A-M featuring a single VLF with Yukawa portal coupling κ. While detailed phenomenological analyses can be found elsewhere [46, 179–181] we focus on the interplay of constraints from phenomenology and PS. A non-vanishing BSM Yukawa coupling $\kappa \neq 0$ induces VLF decay to a SM fermion and a Higgs, W- or Z-boson, depending on the model [179, 180]. This allows for pair and single-production searches at colliders (Fig. 4.10a), see. e.g. [175, 176], which constrain M_F and α_κ as a function of M_F, respectively. Mass bounds from these direct searches typically do not exceed $M_F \lesssim 1.5\,\text{TeV}$ [175] and are not shown in the surface plots for clarity. In addition, bounds on α_κ/M_F^2 can be inferred from global SMEFT fits. They are particularly sensitive to large values of α_κ which are required for the Yukawa portal mechanism. This complementarity often allows to probe higher BSM masses than direct searches.

We exemplarily study the mass bounds arising from the combination of PS and phenomenological constraints for model L, starting with the third generation only scenario. Matching the model to SMEFT induces only two WCs, namely [102]

$$C_{Hu}^{33} = 8\pi^2 \frac{\alpha_\kappa}{M_F^2}, \quad C_{uH}^{33} = 8\pi^2 y_t \frac{\alpha_\kappa}{M_F^2} \tag{4.19}$$

corresponding to the operators

$$Q_{Hu}^{ij} = i\left((H^\dagger D_\mu H) - (D_\mu H)^\dagger H\right)(U_i^R \gamma^\mu U_j^R), \qquad Q_{uH}^{ij} = (H^\dagger H)(\bar{Q}_i H^c U_j)\,. \tag{4.20}$$

From a single operator SMEFT fit [178] we obtain the 90 % c.l. limit $\alpha_\kappa/M_F^2 < 0.01\,\text{TeV}^{-2}$. Recalling that model L does not feature a gauge portal, PS in contrast requires sizeable values of α_κ to achieve PS via the Yukawa portal. Combining both constraints, from Fig. 4.8b we can read off the mass bounds

$$4\,\text{TeV} \lesssim M_F \lesssim 10^7\,\text{TeV}, \qquad (1\,\text{TeV} \lesssim M_F \lesssim 10^{16}\,\text{TeV}) \tag{4.21}$$

for strict (soft) PS, where the lower limit for strict PS is already higher than direct search bounds.

If Yukawa couplings to more than one SM fermion generation are switched on, additional constraints

	Model	**Flavor**	**universal**
	(Y_F, d_2, d_3)	$M_{F,\mathrm{min}}^{\mathrm{soft}}$	$M_{F,\mathrm{min}}^{\mathrm{strict}}$
A	$(-1, \mathbf{1}, \mathbf{1})$	170 TeV	870 TeV
C	$(-\frac{1}{2}, \mathbf{2}, \mathbf{1})$	170 TeV	870 TeV
D	$(-\frac{3}{2}, \mathbf{2}, \mathbf{1})$	X	870 TeV
F	$(\ 0, \mathbf{3}, \mathbf{1})$	X	1400 TeV
G	$(-\frac{1}{3}, \mathbf{1}, \mathbf{3})$	56 TeV	420 TeV
H	$(+\frac{2}{3}, \mathbf{1}, \mathbf{3})$	13 TeV	420 TeV
I	$(-\frac{1}{3}, \mathbf{3}, \mathbf{3})$	29 TeV	29 TeV
J	$(+\frac{2}{3}, \mathbf{3}, \mathbf{3})$	30 TeV	30 TeV
L	$(+\frac{7}{6}, \mathbf{2}, \mathbf{3})$	19 TeV	480 TeV

Table 4.4: Lower VLF mass bounds in models A-M from Tab. 4.1 with $N_F = 1$ from the interplay of strict and soft Planck safety as well as phenomenological FCNC bounds for flavor-universal Yukawa couplings $\kappa_i = (\kappa, \kappa, \kappa)$. While the first in the absence of a gauge portal necessitates large Yukawa couplings $\alpha_\kappa|_{M_F} \gtrsim \mathcal{O}(10^{-3} - 10^{-1})$ the latter restrict $\alpha_\kappa^{(2)}/M_F^2$ to tiny values, which in combination can require quite large M_F of up to a few hundred TeV. The strongest FCNC bounds in VLL and VLQ models typically stem from LFV decays and meson mixing or decays, respectively. For models A, K, M (D, F) no mass bound for (soft) PS can be derived as they feature a gauge portal for strict (soft) PS also for vanishing α_κ. Model E does not induce charged LFV, thus no such mass bounds can be derived.

arise from FCNC processes. In particular, $\varDelta F = 1$ decays are induced at tree-level via fermionic mixing in all models A-M. In addition, $\varDelta F = 2$ contributions to neutral meson mixing arise at 1-loop order from Higgs-VLF box diagrams, e.g. Fig. 4.10b, without CKM or mass suppression in VLQ models G-M. In both cases, the bounds are typically orders of magnitude stronger than the single Yukawa ones.

In model L, the strongest constraint on the flavor-universal scenario arises from D-mixing [179] via Fig. 4.10b and reads $\alpha_\kappa/M_F \lesssim 1.3 \cdot 10^{-4}\,\mathrm{TeV}^{-2}$. From Fig. 4.9d we infer the combined mass bounds

$$480\,\mathrm{TeV} \lesssim M_F \lesssim 10^7\,\mathrm{TeV}, \qquad (19\,\mathrm{TeV} \lesssim M_F \lesssim 10^{16}\,\mathrm{TeV}) \tag{4.22}$$

for strict (soft) PS. In both cases the lower limits are significantly higher than (4.21) and existing collider bounds, impressively demonstrating the predictive power of PS and phenomenological bounds.

The parameter space in the M_F-$\alpha_\kappa|_{M_F}$-plane is qualitatively similar in all models A-M. The only exception is the low M_F and $\alpha_\kappa|_{M_F}$ region, where only some models exhibit a gauge portals. These models allow for arbitrarily small α_κ and are tested in diboson resonance and long lived charged particle searches [174]. In addition, VLQs models are tested in R-hadron and dijet resonance searches [42]. In all other models without low scale gauge portal, similar bounds as (4.21) and (4.22) arise from the interplay of PS and experiments and are summarized in Tab. 4.4. The strongest bounds arise in VLL models from LFV processes such as μ-e-conversion experiments [179] and are of $\mathcal{O}(10^3)$ TeV. However, flavor constraints can always be evaded by keeping just one Yukawa coupling to a single SM fermion generation sizeable and making the other ones feebly small. In this case, the models fall back to those in Subsec. 4.2.2.

4.3 Summary

In this chapter we systematically explored the possibility to cure the Higgs metastability in the SM by extending it with VLFs. We identified the gauge portal mechanism as a minimally invasive way to render the SM Planck-safe. It relies solely on the presence of SM-charged VLFs which enhance the running of gauge couplings. This induces an uplift (4.9) and squeezing (Fig. 4.4) of the RG trajectory of the Higgs quartic that is potentially able to stabilize the Higgs all the way up to the Planck scale. Demanding PS thereby results in constraints on VLF masses and multiplicities. While adding ”too few, too late” is insufficient to cure the metastability, adding ”too many, too soon” results in the breakdown of the model due to subplanckian Landau poles. Notably, for all three gauge interactions and combinations thereof there exists a gauge portal window in between where the model is rendered Planck-safe, see Fig. 4.1, 4.2, 4.3 and 4.5. In particular, the electroweak gauge portals constitute a main novelty of this work. The effects of the gauge portal mechanism are more pronounced for lower VLF masses, as there is more RG time left up to the Planck scale for the mechanism to be operative. Vice versa, for heavier VLFs also higher multiplicities are required for PS before the gauge portal windows finally close for larger masses.

We also studied all 13 VLF representations with renormalizable Yukawa coupling to the Higgs and a SM fermion. For feeble Yukawas some models exhibit a gauge portal window in the TeV range, while others suffer from subplanckian Landau poles or Planck scale metastability, cf. Tab. 4.2. While intermediate values of α_κ tend to destabilize the Higgs [164–169], we find that for $N_F = 1$ and large $\alpha_\kappa \gtrsim \mathcal{O}(10^{-1})$ strict PS can be realized in all models, cf. Tab. 4.3, due to the occurrence of strongly coupled walking regimes, illustrated in Fig. 4.6. This phenomenon is qualitatively similar in all models and for all flavor structures of the Yukawa coupling, yielding similar BSM critical surfaces in all models, see Fig. 4.8 and 4.9.

The VLF models can be experimentally searched for at colliders. Models without or with extremely feeble Yukawas are tested in searches for diboson resonances and long lived charged particles [174] as well as R-hadrons and dijet resonances in case of VLQs [42]. Models with non-feeble Yukawas are constrained by SMEFT fits [178] and if flavorful by severe FCNC bounds. In consequence, in models without a TeV-ish gauge portal the interplay of complementary experimental and PS constraints results in strong lower mass bounds in the flavor-universal case of up to a few hundred TeV, see Tab. 4.4.

Starting from our findings, several interesting directions for future works open up. While the gauge portal mechanism operates at weak coupling, the Yukawa portal mechanism hand appears in the strongly coupled regime with $\alpha_{\kappa,\lambda} \gtrsim 10^{-1}$ close to the perturbativity limit $\alpha_{\kappa,\lambda} \simeq 1$. A crucial future task is therefore to check the persistence of the Yukawa portal at higher orders, i.e. full 3-loop orders as soon as general template scalar 3-loop β-functions are available.

It also appears promising to exploit the identified portal mechanisms for other purposes. In the gauge portal mechanism, the mild enhancement of gauge coupling RG trajectories which is controlled by the VLF representation might allow for coupling unification at or below $M_{\rm Pl}$, motivating a connection to GUTs with a stable ground state (cf. [147] for an example with AS). Moreover, the possibility to achieve (approximate) Higgs criticality at or slightly below the Planck scale renders the gauge portal an interesting tool to connect the SM to quantum gravity in the transplanckian regime [158].

Eventually, Majorana fermions à la model F might enable leptogenesis and generate neutrino masses via the seesaw mechanism while simultaneously stabilizing the electroweak (EW) vacuum [182]. Moreover, it is appealing to investigate the reach of singlet VLFs as dark matter candidates.

5 Scalar Portals into Higgs Stability

In this chapter, we investigate the possibility to induce PS in minimal SM extensions relying solely on BSM singlet scalars, closely following [4]. Such models imply an extended scalar potential featuring additional quartic interactions. It is well know that in this setup Higgs stability can arise due to a renormalizable portal coupling $\sim \delta(H^\dagger H)(S^\dagger S)$ of BSM scalars S and the Higgs [183–191], with minor influence on the gauge and Yukawa sector. At the same time, additional BSM stability conditions constrain the allowed values of BSM quartics. We extend previous studies by investigating this Higgs portal mechanism at full 2-loop accuracy including all quartics and systematically scrutinizing the complete allowed parameter space in minimal scalar extensions with and without flavor. If there is SSB in the BSM sector the Higgs portal induces scalar mixing with crucial consequences for Higgs phenomenology. We investigate the complementarity between PS and phenomenological constraints in this scenario which results in an enhanced predictivity. We also work out prospects for present and future colliders with a focus on Higgs self-couplings which determine the shape of the Higgs potential.

This chapter is structured as follows: We start with unveiling the RG dynamics of the Higgs portal mechanism, in particular focusing on models with a $O(N_S)$ or $SU(N_F) \times SU(N_F)$ flavor symmetry and also explicitly exploring potentially negative BSM quartics in Sec. 5.1. Afterwards, we analyze the phenomenology of Planck-safe models based on scalar mixing in Sec. 5.2 with special emphasis on induced deviations in the couplings of the physical Higgs boson and the corresponding collider reach. In Sec. 5.3 we conclude.

5.1 The Higgs Portal Mechanism

SM extensions with real singlet scalars S_i allow for a renormalizable Higgs portal interaction

$$\mathcal{L} \supset \sum_i \delta_i \, (H^\dagger H)(S_i^T S_i) \tag{5.1}$$

via the dimensionless portal couplings δ_i. It is well known that the Higgs portal directly affects the RG evolution of the Higgs quartic via the 1-loop contribution to its β-function

$$\beta_\lambda = \beta_\lambda^{\text{SM}} + \sum_i 2\, n_i\, \alpha_{\delta_i}^2 \,. \tag{5.2}$$

Here n_i denotes the number of real scalar fields in the component S_i, such that (5.1) is compatible with an $O(n_i)$ symmetry for each S_i. Integrating β_λ (5.2) from the NP scale μ_0 to a scale $\Lambda > \mu_0$ yields an enhancement of the Higgs quartic

$$\alpha_\lambda(\Lambda) - \alpha_\lambda^{\text{SM}}(\Lambda) \propto \sum_i 2\, n_i \alpha_{\delta_i}^2 \,. \tag{5.3}$$

This constitutes the (direct) Higgs portal mechanism. Note that the portal couplings contribute positively to β_λ independent of their signs.

For the sake of simplicity, we now focus on a minimal scenario with a single Higgs portal coupling α_δ. Its RG evolution is then technically natural and given by

$$\beta_\delta = X \alpha_\delta \qquad \text{with} \qquad X = \sum_n X^{(n)}(\alpha(\mu)) \tag{5.4}$$

being a polynomial receiving contributions from both SM and BSM couplings α, cf. (3.12). Hence, α_δ cannot be induced radiatively and the Higgs portal mechanism therefore requires $\alpha_\delta(\mu_0) \neq 0$ at the matching scale. The scalar potential in addition contains quartic couplings α_q between the BSM scalars whose structure is determined by the underlying symmetries. However, they have little direct influence on the running of SM couplings as contributions of α_q to SM β-functions only arise beyond 2-loop order and always involve the portal coupling α_δ [114]. Thus, the leading impact of these pure BSM quartics on α_λ arises indirectly from their 1-loop contributions to the running of the Higgs portal coupling that reads

$$\beta_\delta^{(1)} = X^{(1)}\alpha_\delta \supset \sum_q +H_\delta^{\delta q}\alpha_q\alpha_\delta\,, \tag{5.5}$$

cf. (3.12). As $\sum_q H_\delta^{\delta q}\alpha_q$ is typically positive, this enhances the running of $|\alpha_\delta|$ and thereby fuels the Higgs portal mechanism. Also the SM 1-loop contribution $X^{(1)}(\alpha_{\text{SM}}(\mu_0))$ is positive for $\mu_0 \lesssim 10^{10}$ GeV, rendering the full $X^{(1)} > 0$. Hence, for small $\alpha_\delta \ll 1$ and slowly varying X, (5.4) induces an approximately exponential RG growth of $|\alpha_\delta|$ obeying $\alpha_\delta(\mu) \propto \alpha_\delta(\mu_0)(\mu/\mu_0)^X$. Sizeable BSM quartic values then imply a sizeable X via (5.5) and thereby a fast growth of the portal coupling. Notably, for sufficiently large α_q, this still allows to induce sizeable $\alpha_\delta(\mu)$ in the RG flow which can stabilize the Higgs even when starting with very feeble $\alpha_\delta(\mu_0)$ at the matching scale. This indirect Higgs portal mechanism constitutes one of the main novelties of this work. It demonstrates that vacuum stability from singlet scalars can unexpectedly also be achieved for almost arbitrarily feeble portal couplings.

The maximum values of scalar quartic couplings are however constrained by demanding tree-level perturbative unitarity in scalar 2 → 2 scattering. For the physical SM h and BSM s Higgs modes with a potential

$$V^{(4)}(h,s) = \frac{\lambda}{4}h^4 + \frac{\mathit{\Delta}}{\mathcal{N}^2}s^4 + \frac{\delta}{2\mathcal{N}}h^2s^2\,, \tag{5.6}$$

cf. App. C, these constraints in the limit of vanishing mixing read [192]

$$\alpha_\lambda \lesssim \frac{1}{6\pi}\,, \qquad \mathit{\Delta} \lesssim \frac{\mathcal{N}^2}{24\pi}\,, \qquad \delta \lesssim \frac{\mathcal{N}}{6\pi}\,, \tag{5.7}$$

constraining quartics to rather perturbative values. However, the conditions (5.7) are relaxed when taking into account loop corrections. If there is SSB in the BSM sector additional limits on quartics arise from scalar mixing as discussed in Subsec. 5.2.1.

5.1.1 $O(N_S)$ Scalars

We now focus on the simplest global symmetry group for a SM extension with N_S real BSM scalars, that is $O(N_S)$. The scalar potential reads

$$V_{O(N_S)}(H,S) = -\mu_H^2 H^\dagger H - \frac{\mu_S^2}{2}S^TS + \lambda(H^\dagger H)^2 + v(S^TS)^2 + \delta\,(H^\dagger H)(S^TS)\,, \tag{5.8}$$

where the implicit summation over scalar flavor indices is understood. It features the Higgs portal coupling δ as well as a single BSM scalar self-coupling v and a mass parameter μ_S^2. It is stable at tree-level if

$$\lambda > 0, \qquad v > 0, \qquad \delta > -2\sqrt{\lambda v}\,, \tag{5.9}$$

interestingly also allowing for negative values of the portal coupling. Note that the potential (5.8) also describes the case of $\frac{1}{2}N_S$ complex scalars with a global $U(N_S/2)$ symmetry for $S^T \to S^\dagger$ and an additional factor 2 in the μ_S^2 term, cf. App. C. Additional quartic interactions may arise in the case of more sophisticated global symmetries. Nevertheless, the $O(N_S)$ symmetry can always be restored by setting these additional couplings to zero.

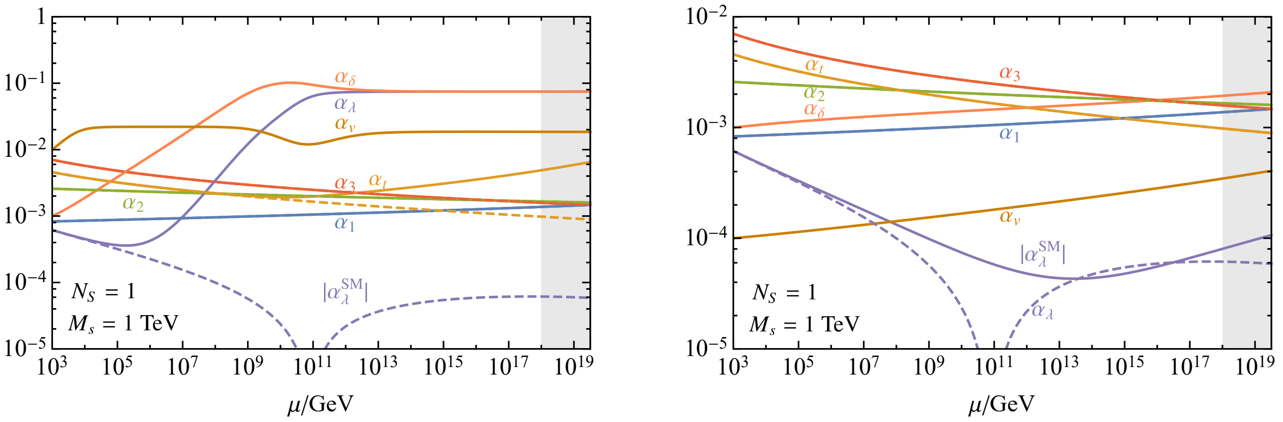

(a) Walking.

(b) Running.

Figure 5.1: Planck-safe 2-loop RG flow in the $O(N_S)$ model (solid) and in the SM (dashed). Exemplarily shown are the RG trajectories of couplings for $N_S = 1$ real BSM scalar singlet of mass $M_s = 1\,\mathrm{TeV}$ with $\alpha_\delta(M_s) = 10^{-3}$, $\alpha_v(M_s) = 10^{-2}$ (a) and $\alpha_\delta(M_s) = 10^{-3}$, $\alpha_v(M_s) = 10^{-4}$ (b), respectively. In (a) the quartic couplings $\alpha_{\lambda,\delta,v}$ enter a walking regime before the Planck scale, whereas in (b) the running to M_{Pl} occurs within a weakly coupled regime without walking. Plots taken from [4].

The Higgs portal mechanism arises at 1-loop in the β-function of the Higgs quartic

$$\beta_\lambda^{(1)} = \beta_\lambda^{(1),\mathrm{SM}} + 2N_S\,\alpha_\delta^2, \tag{5.10}$$

which is enhanced by an inhomogeneous α_δ^2 term in accord with (5.2) for $n_1 = N_S$. Apart from that, RGEs of SM couplings are widely independent of the BSM sector with the leading contributions of α_δ (α_v) to Yukawa and gauge β-functions arising at 2-loop (3-loop) and 3-loop (4-loop), respectively. Recall that the RG evolution of the Higgs portal is technically natural and governed by both SM and BSM couplings, cf. (5.4). Most importantly,

$$\beta_\delta^{(1)} \supset +[(16 + 8N_S)\alpha_v + 8\alpha_\delta]\alpha_\delta \tag{5.11}$$

receives a positive 1-loop contribution from the pure BSM quartic α_v, cf. (5.5)[1]. Hence, sizeable α_v can indirectly fuel the Higgs portal mechanism by accelerating the RG growth of α_δ. The 1-loop β-function of the pure BSM quartic α_v

$$\beta_v^{(1)} = (64 + 8N_S)\alpha_v^2 + 2\alpha_\delta^2 \tag{5.12}$$

depends only on the BSM quartics $\alpha_{\delta,v}$. Importantly, it is not technically natural as it can be radiatively switched on by α_δ. SM coupling contributions on the other hand just arise starting from 2-loop order and are always mediated by the portal coupling, i.e. $\propto \alpha_\delta^2$.

The vacuum stabilization via the Higgs portal mechanism can proceed either in a weakly coupled or a walking regime, see Fig. 5.1, which is determined by the choice of parameters. The occurrence of walking regimes is generically promoted by larger values of α_δ, α_v and N_S. Also the onset of walking occurs at lower energies for larger multiplicities and quartics. Typically the walking regimes capture all quartics at sizeable positive values $\alpha_{\lambda,\delta,v} \simeq \mathcal{O}(10^{-2} - 10^{-1})$ which stabilizes the Higgs, prevents possible subplanckian Landau poles in α_δ and thereby significantly enhances the Planck-safe parameter space.

We now examine the influence of the four free model parameters on vacuum stability, namely the physical

---

[1] We omitted all SM coupling contributions in (5.11) as they are not relevant for demonstrating the portal dynamics.

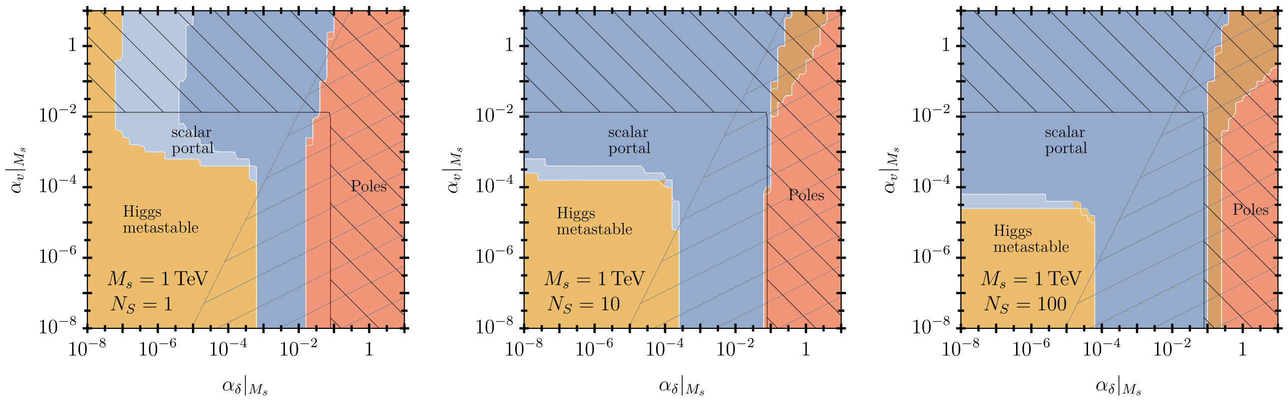

(a) $N_S = 1$.

(b) $N_S = 10$.

(c) $N_S = 100$.

Figure 5.2: The Higgs portal mechanism in the $O(N_S)$ model. Exemplarily shown are the BSM critical surfaces in the $\alpha_\delta(M_s)$-$\alpha_v(M_s)$ plane for $N_S = 1$ (a), $N_S = 10$ (b) and $N_S = 100$ (c) real BSM scalar singlets of mass $M_s = 1\,\text{TeV}$, respectively. PS can be achieved for sufficiently sizeable α_δ or α_v. The minimally required values decrease with increasing N_S. We also indicate bounds from tree-level perturbative unitarity (5.7) (black hatched) and scalar mixing (5.27) (grey hatched). Instabilities of the Higgs potential with $\alpha_\lambda < -10^{-4}$ are indicated in brown, apart from that same color coding as Fig. 4.1a. Plots taken from [4].

BSM scalar mass $M_s \gtrsim 1$ TeV, cf. App. C, as well as N_S, $\alpha_\delta(M_s)$ and $\alpha_v(M_s)$. Starting with the quartics, the BSM critical surface in the $\alpha_\delta(M_s)$-$\alpha_v(M_s)$ plane is shown in Fig. 5.2 for $N_S = 1$, 10, 100 BSM scalars of mass $M_s = 1\,\text{TeV}$. Note that for $N_S = 1$ the scalar symmetry falls back to a $\mathbb{Z}_2$. The metastability of the Higgs potential can be cured if either α_δ or α_v is sufficiently sizeable. However, too large values of α_δ eventually give rise to subplanckian Landau poles in α_δ or instabilities of the potential[2]. For too low $\alpha_{v,\delta}$ on the other hand the effect is too small and the metastability persists. When increasing N_S, the minimal required value of $\alpha_{\delta,v}$ decrease. More precisely, we find the conditions

$$\begin{aligned} 10^{-3}/\sqrt{N_S} \lesssim \alpha_\delta \lesssim \text{few} \times 10^{-2} \\ \text{or} \quad N_S\,\alpha_v \gtrsim 10^{-2} \quad \text{and} \quad \alpha_\delta \gtrsim 10^{-0.16\,N_S - 6.6} \quad (\alpha_\delta \gtrsim 10^{-0.93\,N_S - 6.1}) \end{aligned} \tag{5.13}$$

for strict (soft) PS. While the first condition is for direct stabilization and only depends on α_δ, the latter corresponds to indirect stabilization sourced by the pure BSM quartic α_v, see Fig. 5.3. The scaling of the minimal values of α_δ and α_v can be understood from β_λ (5.10) and β_δ (5.11). The stabilizing contribution to β_λ is $\propto N_S \alpha_\delta^2$ which explains the scaling $\alpha_\delta^{\min} \propto 1/\sqrt{N_S}$ for direct stabilization. In case of indirect stabilization on the other hand the enhancement of β_δ by α_v is in good approximation $\propto N_S \alpha_\delta \alpha_v$ implying a scaling $\alpha_v^{\min} \propto 1/N_S$. Moreover, indirect stabilization requires a minimal value of $\alpha_\delta(M_s) > 0$ as otherwise the mechanism is spoiled by the technical naturalness of α_δ. However, this minimally required value of $\alpha_\delta(M_s)$ exponentially decreases with N_S down to extremely feeble values, see Fig. 5.3a. The reason is that a large $N_S \alpha_v \gtrsim 10^{-2}$ due to (5.11) induces an exponential growth of α_δ over several orders of magnitude as depicted in Fig. 5.3b. There, for $N_S = 10$ a feeble value of $\alpha_\delta(M_s) = 10^{-15}$ is still sufficient to induce soft PS. The PS conditions (5.13) become more strict for larger BSM masses M_s, see Fig. 5.4, as there is less

---

[2] For large N_S and α_δ negative 2-loop contributions $\propto N_S \alpha_\delta^3$ to β_δ become relevant and tame the pole. However, simultaneously negative 2-loop contributions to β_λ also scaling with $N_S \alpha_\delta^3$ spoil the stabilization of the Higgs.

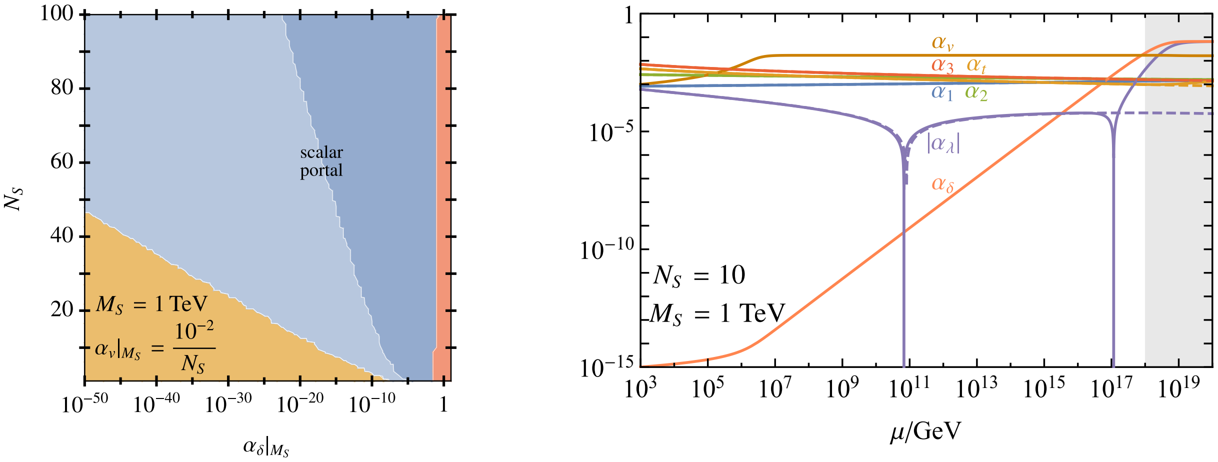

(a) BSM critical surface in the $\alpha_\delta(M_s) - N_S$-plane for fixed $\alpha_v(M_s) = \frac{10^{-2}}{N_S}$ and $M_s = 1\,\text{TeV}$. For larger N_S the minimally required value of $\alpha_\delta(M_s)$ for the indirect portal mechanism significantly reduces down to extremely feeble values. Same color coding as Fig. 5.2.

(b) Exemplary softly Planck-safe RG flow due to the indirect Higgs portal mechanism. We show the RG evolution of couplings at full 2-loop order for $N_S = 10$ BSM scalars (solid lines) with mass $M_s = 1\,\text{TeV}$ and $\alpha_\delta(M_s) = 10^{-15}$, $\alpha_v(M_s) = 10^{-3}$ with SM running (dashed lines) for reference. The portal coupling α_δ exponentially grows over several orders of magnitude, eventually getting sufficiently sizeable to render $\alpha_\lambda(M_{\text{Pl}}) > 0$.

Figure 5.3: The indirect Higgs portal mechanism in the $O(N_S)$ model for feeble portal couplings α_δ. The mechanism is induced by the sizeable $N_S\alpha_v(M_s)$ but still requires $\alpha_\delta > 0$.

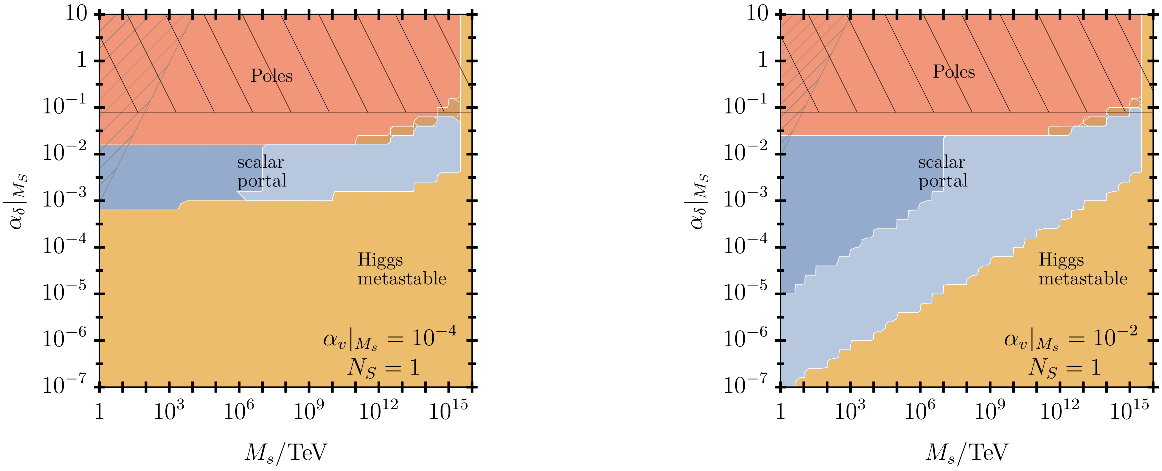

(a) $\alpha_v(M_s) = 10^{-4}$.

(b) $\alpha_v(M_s) = 10^{-2}$.

Figure 5.4: Impact of the BSM mass scale M_s on the Higgs portal mechanism in the $O(N_S)$ model. Exemplarily shown are the BSM critical surfaces in the M_s-$\alpha_\delta(M_s)$ plane for $N_S = 1$ real BSM scalar singlet of mass $M_s = 1\,\text{TeV}$ for fixed $\alpha_v(M_s) = 10^{-4}$ (a) and $\alpha_v(M_s) = 10^{-2}$ (b), respectively. While in the first case there is little influence of M_s on the allowed range of $\alpha_\delta(M_s)$, in the latter the sizeable $\alpha_v(M_s)$ opens up large amounts of parameter space for small $\alpha_\delta(M_s)$ at low M_s due to the indirect Higgs portal mechanism. Same color coding and exclusion regions as Fig. 5.2. Plots taken from [4].

RG time $\ln\frac{\mu}{\mu_0}$ left to stabilize the Higgs. This effect has little impact on the direct Higgs portal mechanism but it is quite important for the indirect stabilization via sizeable $\alpha_v \gtrsim 3\cdot 10^{-3}$, see Fig. 5.4b. There, the strong increase of the minimal required $\alpha_\delta(M_s)$ with M_s nicely illustrates the decreasing effectivity of the indirect stabilization mechanism due to the reduced RG time for which it is active. For TeV-ish M_s and sizeable $\alpha_v(M_s) = 10^{-2}$ however strict (soft) PS can already arise for $\alpha_\delta \gtrsim 10^{-5}\,(10^{-7})$.

5.1.2 Flavorful Scalar Matrix Field

We now study a more sophisticated SM extension by a BSM scalar sector as in the Litim-Sannino model [40]. It features a flavorful, complex BSM scalar matrix singlet field S_{ij} with flavor indices $i,j = 1,\dots,N_F$ which obeys a $SU(N_F)_L \times SU(N_F)_R$ flavor symmetry under which $S \to V^\dagger S U$ and $V, U \subset SU(N_F)_L, SU(N_F)_R$, respectively. The scalar potential of the model reads

$$V_{SU(N_F)^2}(H,S) = -\mu_H^2 H^\dagger H - \mu_S^2 \mathrm{Tr}\left[S^\dagger S\right] + \lambda (H^\dagger H)^2 + u\,\mathrm{Tr}\left[S^\dagger S S^\dagger S\right] + v\left[\mathrm{Tr}\, S^\dagger S\right]^2 + \delta\,(H^\dagger H)\,\mathrm{Tr}\left[S^\dagger S\right]\,, \tag{5.14}$$

where traces are in flavor space. It features the portal coupling δ as well as two pure BSM quartics u, v. The large flavor symmetry severely reduces the number of BSM parameters by preventing the occurrence of a plethora of a priori independent quartics. For $u = 0$ the global flavor symmetry falls back to the $O(2N_F^2)$ case according to the $2N_F^2$ real d.o.f.. Therefore, α_u is technically natural and cannot be switched on radiatively.

The model is interesting for several reasons. First of all, the presented scalar sector has proven to be key for AS in GY theories [40, 42, 45, 46] and also strongly facilitates PS in BSM model building [1, 45, 46]. Moreover, it is possible to connect scalar to SM fermion flavor for $N_F = 3$ [1, 45, 46, 181]. This can give rise to unique, flavorful collider signatures while still evading FCNC limits [181]. In addition, the potential (5.14) exhibits two distinct ground states $V^\pm$

$$V^+ : \quad \begin{cases} \lambda > 0, \quad u > 0, \quad u + N_F v > 0, \\ \delta > -2\sqrt{\lambda\,(u/N_F + v)} \end{cases} \qquad \text{and} \qquad V^- : \quad \begin{cases} \lambda > 0, \quad u < 0, \quad u + v > 0, \\ \delta > -2\sqrt{\lambda\,(u + v)} \end{cases} \tag{5.15}$$

depending on the sign of u. Notably, the ground state V^+ (V^-) allows for negative quartics $\delta, v < 0$ ($\delta, u < 0$). V^- in addition spontaneously breaks flavor universality offering a novel opportunity to address flavor anomalies [45].

We now work out the dynamics of the Higgs portal in this model. The Higgs quartic β-function reads

$$\beta_\lambda^{(1)} = \beta_\lambda^{(1),\mathrm{SM}} + N_F^2 \alpha_\delta^2 \tag{5.16}$$

giving rise to a strong, N_F^2 enhanced Higgs portal. The influence of the BSM quartic self-interactions $\alpha_{u,v}$ on α_λ is as in the $O(N_S)$ case channeled through their contribution to

$$\beta_\delta^{(1)} \supset [8N_F\alpha_u + (4N_F^2 + 4)\alpha_v + 4\alpha_\delta]\alpha_\delta \tag{5.17}$$

enabling the indirect portal mechanism. Their own RG evolution is controlled by

$$\beta_u^{(1)} = (8N_F\alpha_u + 24\alpha_v)\alpha_u\,, \tag{5.18}$$

$$\beta_v^{(1)} = [12\alpha_u^2 + 16N_F\alpha_u\alpha_v + (4N_F^2 + 16)\alpha_v^2 + 2\alpha_\delta^2] \tag{5.19}$$

and largely decoupled from the SM. α_v can be switched on radiatively by both $\alpha_{\delta,u}$, whereas α_u is technically natural. This prevents any RG-induced sign changes of α_u giving rise to vacuum transitions between $V^\pm$.

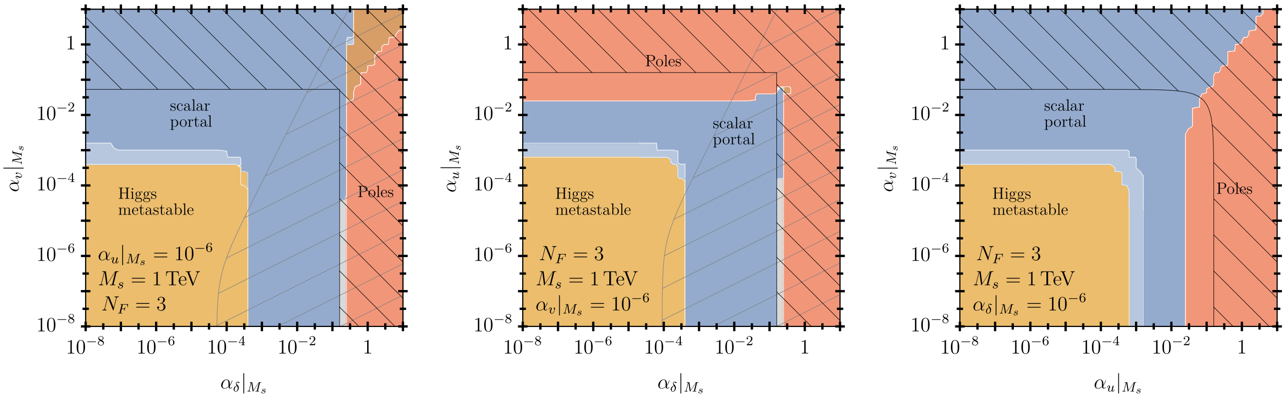

(a) $\alpha_\delta(M_s)$-$\alpha_v(M_s)$ plane. **(b)** $\alpha_\delta(M_s)$-$\alpha_u(M_s)$ plane. **(c)** $\alpha_u(M_s)$-$\alpha_v(M_s)$ plane.

Figure 5.5: The Higgs portal mechanism in the $SU(N_F) \times SU(N_F)$ model. Exemplarily shown are the BSM critical surfaces in the $\alpha_\delta(M_s)$-$\alpha_v(M_s)$ (a), $\alpha_\delta(M_s)$-$\alpha_u(M_s)$ (b) and $\alpha_u(M_s)$-$\alpha_v(M_s)$ (c) plane, respectively, for $N_F = 3$ flavors of complex BSM scalars with a mass $M_s = 1\,\mathrm{TeV}$ and the remaining quartic fixed as $\alpha_{u,v,\delta}(M_s) = 10^{-6}$. The indirect stabilization mechanism is less efficient for α_u, which develops subplanckian Landau poles for too sizeable initial values $\alpha_u(M_s)$. Dark (light) blue corresponds to strict (soft) PS in the vacuum configuration V^+. Apart from that, same color coding and exclusion regions as Fig. 5.2. Plots taken from [4].

For the parameter space analysis we mostly focus on $N_F = 3$ flavors of complex BSM scalars with a mass of $M_s = 1\,\mathrm{TeV}$. The corresponding BSM critical surfaces are shown in Fig. 5.5 in the different planes spanned by the quartic couplings. Qualitatively, the parameter space looks similar to the $O(N_S)$ model Fig. 5.2. Stabilization is possible directly via sizeable $\alpha_\delta(M_s)$ or indirectly via large $\alpha_{u,v}$. However, too sizeable $\alpha_{\delta,u}(M_s)$ give rise to subplanckian Landau poles due to their technical naturalness. If in contrast all quartics are small their impact does not suffice to stabilize the Higgs.

Stability is achieved more easily for larger N_F. This is not surprising, as the contributions to both the direct and indirect mechanisms increase with N_F. The BSM critical surface in the $\alpha_\delta(M_s) - N_F$ plane is exemplarily depicted for tiny $\alpha_{u,v}$ in Fig. 5.6a. The minimally required value of $\alpha_\delta(M_s)$ decreases as $\frac{1}{N_F}$ as expected from (5.16). For lower N_F, an upper limit on α_δ arises due to the occurrence of subplanckian Landau poles. This changes however at larger N_F where the pole is tamed by a negative 2-loop contribution to $\beta_\delta^{(2)} \supset -(N_F^2+10)\alpha_\delta^3$. However, in that case also the Higgs quartic receives a negative 2-loop contribution $\beta_\lambda^{(2)} \supset -4N_F^2\alpha_\delta^3$ which for $\alpha_\delta \gtrsim 0.25$ dominates over the 1-loop uplift (5.17) and causes an instability in the Higgs potential. In combination we obtain the condition

$$\frac{1}{N_F}\,1.4 \cdot 10^{-3} \lesssim \alpha_\delta(M_s) \lesssim \begin{cases} (0.05 \ldots 0.08)\, N_F, & N_F \lesssim 10 \\ 0.25, & N_F \gtrsim 10 \end{cases} \tag{5.20}$$

for PS via the direct portal mechanism, widely independent of $\alpha_{u,v}(M_s)$ and M_s, unless $\alpha_{u,v}(M_s) \simeq \mathcal{O}(1)$ or $M_s \sim M_{\mathrm{Pl}}$. As a novelty w.r.t. the $O(N_S)$ model, we find that indirect stabilization can be achieved via both α_u and α_v. The indirect mechanism via α_u is however less efficient as its contribution to β_δ only scales with N_F whereas the α_v one scales with N_F^2, see (5.17). Accordingly we find the conditions

$$(6 \ldots 8) \cdot 10^{-3} \lesssim N_F^2 \alpha_v(M_s), \qquad 3 \cdot 10^{-3} \lesssim N_F \alpha_u(M_s) \lesssim (6 \ldots 8) \cdot 10^{-2} \tag{5.21}$$

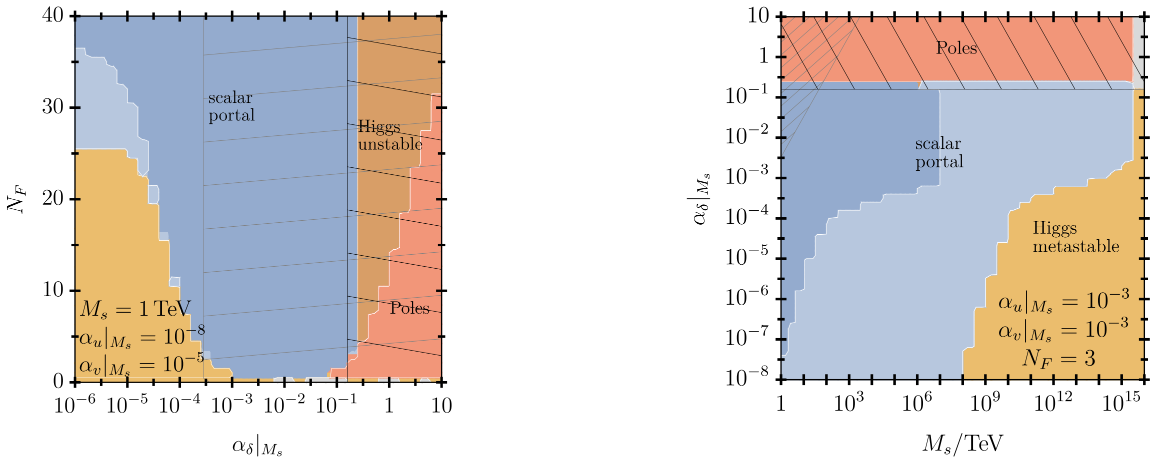

(a) Impact of the number of BSM flavors N_F on the Higgs portal for feeble $\alpha_{u,v}(M_s)$. The minimal required value of $\alpha_\delta(M_s)$ for Higgs stability scales $\propto 1/N_F$ in accord with the contribution to $\beta_\lambda \supset N_F^2 \alpha_\delta^2$ (5.17). Too large, values of α_δ on the other hand destabilize the Higgs due to a sizeable negative 2-loop contribution of α_δ to β_λ. Plot taken from [4].

(b) Impact of the BSM scalar mass M_s on the Higgs portal. For lighter M_s, soft PS can still be realized also for feeble portal couplings $\alpha_\delta(M_s)$ due to the indirect portal mechanism. It is fueled by sizeable $\alpha_{u,v}(M_s) = 10^{-3}$ which induces a fast RG growth of α_δ. For larger M_s also larger $\alpha_\delta(M_s)$ are required to still induce sufficient impact in the reduced RG time left until M_{Pl}.

Figure 5.6: Influence of the number of scalar flavors N_F (a) and the scalar mass M_s (b) on the Higgs portal in the $SU(N_F) \times SU(N_F)$ model. Exemplarily shown are the BSM critical surfaces in the $\alpha_\delta(M_s)$-N_F (a) and M_s-$\alpha_\delta(M_s)$ (b) plane, respectively, with the fixed values of all other parameters indicated in the plots. Same color coding and exclusion regions as Fig. 5.5.

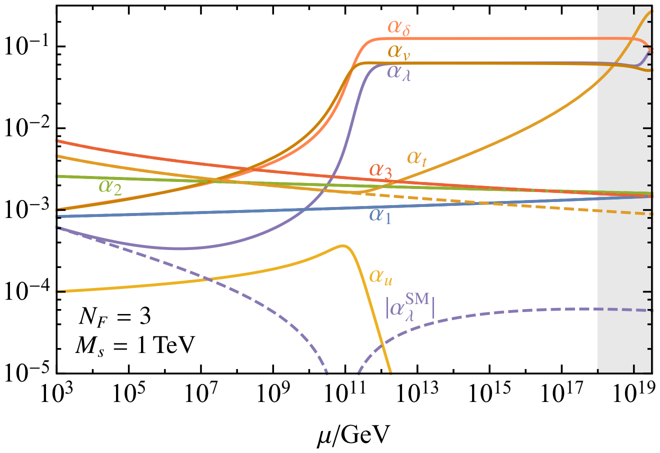

Figure 5.7: Illustration of the Higgs portal mechanism in the $SU(N_F) \times SU(N_F)$ model. Shown is the 2-loop running of couplings for $N_F = 3$ and $M_s = 1\,\mathrm{TeV}$ (solid lines) compared to SM running (dashed line). The quartic couplings $\alpha_{\lambda,\delta,v}$ enter a walking regime at sizeable values around $\mu \simeq 10^{10}\,\mathrm{GeV}$ whereas α_u asymptotically approaches zero, restoring the $O(2N_F^2)$ symmetry. Plot taken from [4].

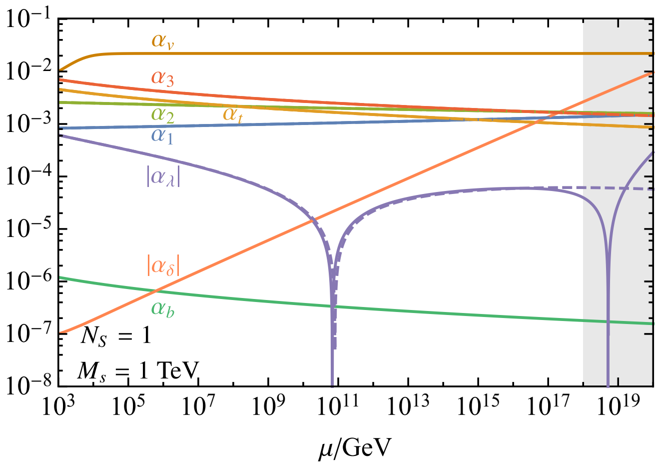

Figure 5.8: Exemplary RG flow for a negative portal coupling $\alpha_\delta(M_s) = -10^{-7}$ in the $O(N_S)$ model. Shown is the 2-loop running of couplings for $N_S = 1$ and $M_s = 1$ TeV compared to SM running (dashed line). The value of $|\alpha_\delta|$ is just sufficient to render $\alpha_\lambda(M_{\text{Pl}}) > 0$, but already violates the BSM stability condition $\alpha_\delta > -2\sqrt{\alpha_\lambda \alpha_v}$ at M_{Pl} spoiling PS.

for small, but not too small $\alpha_\delta(M_s) > 0$ and TeV-ish M_s. The upper bound on α_u arises from demanding the absence of subplanckian Landau poles.

The impact of M_s on stability is shown in Fig. 5.6b. As in the $O(N_S)$ model, for TeV-ish M_s and sizeable $\alpha_{u,v}(M_s)$ PS can also be achieved for tiny $\alpha_\delta(M_s)$ due to the indirect portal mechanism. It is fueled by the pure BSM quartics which induce a fast RG growth of α_δ. For larger M_s there is less RG time left until M_{Pl} for the mechanism to set-in. Hence, also larger $\alpha_\delta(M_s)$ are required to still induce sufficient impact to stabilize the potential.

Larger values of quartics $\alpha_{\delta,u,v}$ and flavors N_F favor the occurrence of walking regimes, see Fig. 5.7, enlarging the PS window. interestingly, the walking regime corresponds to the same pseudo FP as in the $O(2N_F^2)$ case[3]. In accordance, α_u rapidly goes to zero as soon as the other quartics enter the walking regime.

5.1.3 Negative Quartics

Interestingly, the vacuum stability conditions both in the $O(N_S)$ (5.9) and the $SU(N_F) \times SU(N_F)$ (5.15) model explicitly allow for negative values of the portal coupling α_δ. In the $SU(N_F) \times SU(N_F)$ model in addition, negative values of the pure BSM quartics $\alpha_{u,v}$ are compatible with tree-level stability.

A negative portal coupling $\alpha_\delta < 0$ stays negative throughout the RG evolution due to its technical naturalness, cf. (5.5). Notably, this does not spoil the Higgs portal mechanics as the portal contribution to β_λ (5.10), (5.16) scales with α_δ^2. However, we find that PS cannot be realized at all for a negative α_δ in either of the models. This is related to a conflict between the portal stability conditions in (5.9), (5.15) and Higgs stability. While the portal conditions in (5.9), (5.15) are trivially fulfilled for positive quartics, they restrict a negative α_δ not to be excessive compared to the remaining quartics. PS via the Higgs portal mechanism on the other hand requires a sufficiently sizeable α_δ^2 contribution to β_λ at some intermediate scale, which for $\alpha_\delta < 0$ then turns out to generically be in conflict with BSM stability, see Fig. 5.8.

---

[3] Note that the normalization of δ, v differs between $SU(N_F) \times SU(N_F)$ and $O(2N_F^2)$ and therefore they asymptote to different values in Fig. 5.1a and Fig. 5.7.

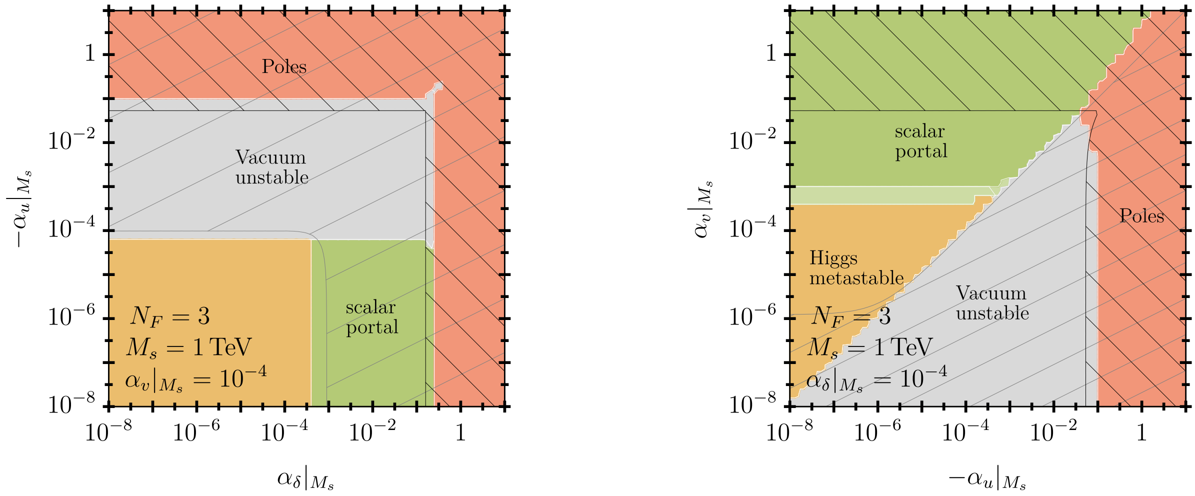

(a) $(\alpha_\delta|_{M_s}, -\alpha_u|_{M_s})$ plane with $\alpha_v|_{M_s} = 10^{-4}$.

(c) $(-\alpha_u|_{M_s}, \alpha_v|_{M_s})$ plane with $\alpha_\delta|_{M_s} = 10^{-4}$.

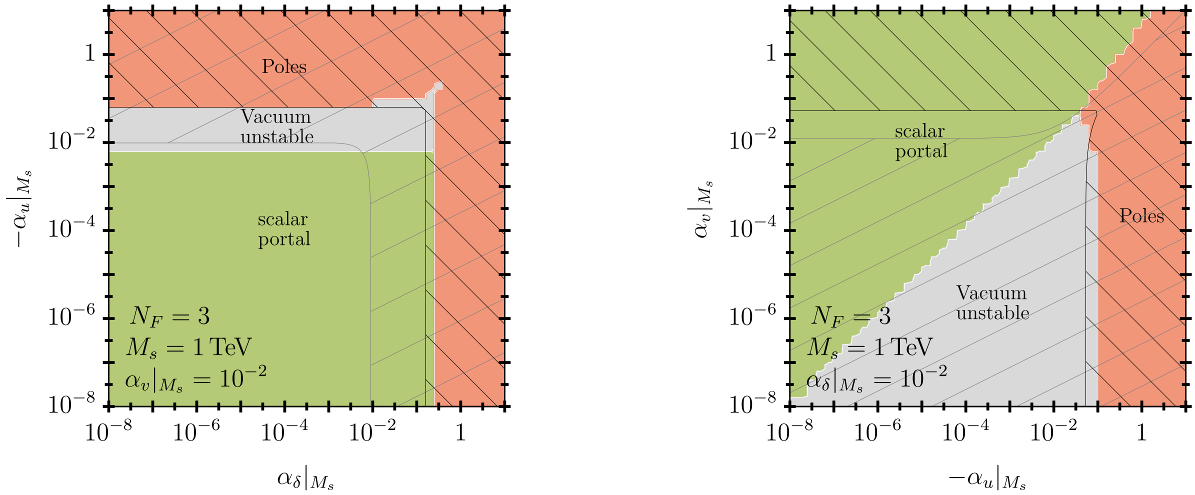

(b) $(\alpha_\delta|_{M_s}, -\alpha_u|_{M_s})$ plane with $\alpha_v|_{M_s} = 10^{-2}$.

(d) $(-\alpha_u|_{M_s}, \alpha_v|_{M_s})$ plane with $\alpha_\delta|_{M_s} = 10^{-2}$

Figure 5.9: BSM critical surfaces in the $SU(N_F) \times SU(N_F)$ model for negative α_u. Surfaces are given in the $(\alpha_\delta(M_s), -\alpha_u(M_s))$ (a,b) and $(-\alpha_u(M_s), \alpha_v(M_s))$ (c,d) plane for $N_F = 3$ and $M_s = 1\,\mathrm{TeV}$ with the remaining quartic fixed as $\alpha_{\delta,v}(M_s) = 10^{-4}$ (a,c) and $\alpha_{\delta,v}(M_s) = 10^{-2}$ (b,d), respectively. Dark (light) green corresponds to strict (soft) PS in the vacuum configuration V^- while gray indicates a violation of the BSM stability conditions in (5.15). Apart from that same color coding and exclusion regions as Fig. 5.2. The stability condition $\alpha_u + N_F\alpha_v > 0$ dictates the most negative allowed value of $\alpha_u|_{M_s}$ for PS giving rise to the border between regions of PS and vacuum instabilities. Plots taken from [4].

A too large $-\alpha_\delta(M_s) > 0$ violates the portal stability condition already at the matching scale. Hence, vacuum stability at $\mu_0 \sim M_s$ implies an upper limit on $-\alpha_\delta(M_s)$ which depends on the value of the pure BSM quartic(s) α_v ($\alpha_{u,v}$). For weakly coupled or tiny $\alpha_v(M_s)$ ($\alpha_{u,v}(M_s)$) also $-\alpha_\delta(M_s)$ has to be small. We find that in this scenario the effect on α_λ is generically to small to induce Higgs stability all the way up

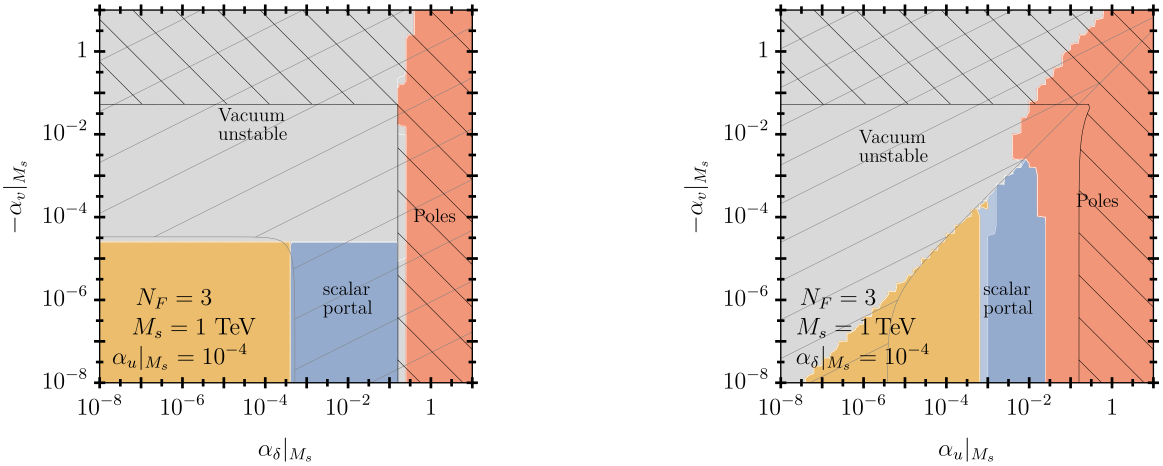

(a) $(\alpha_\delta(M_s), -\alpha_v(M_s))$ plane with $\alpha_u(M_s) = 10^{-4}$.

(c) $(\alpha_u(M_s), -\alpha_v(M_s))$ plane with $\alpha_\delta(M_s) = 10^{-4}$.

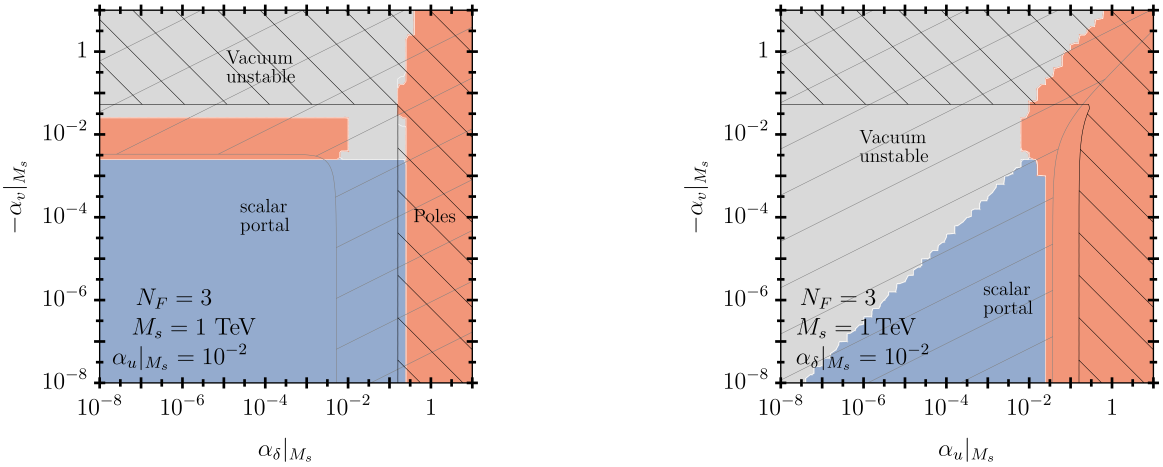

(b) $(\alpha_\delta(M_s), -\alpha_v(M_s))$ plane with $\alpha_u(M_s) = 10^{-2}$.

(d) $(\alpha_u(M_s), -\alpha_v(M_s))$ plane with $\alpha_\delta(M_s) = 10^{-2}$.

Figure 5.10: BSM critical surfaces in the $SU(N_F) \times SU(N_F)$ model for negative α_v. Surfaces are given in the $(\alpha_\delta(M_s), -\alpha_v(M_s))$ (a,b) and $(\alpha_u(M_s), -\alpha_v(M_s))$ (c,d) plane for $N_F = 3$ and $M_s = 1$ TeV with the remaining quartic fixed as $\alpha_{\delta,u}(M_s) = 10^{-4}$ (a,c) and $\alpha_{\delta,u}(M_s) = 10^{-2}$ (b,d), respectively. Same color coding and exclusion regions as Fig. 5.9 with dark (light) blue indicating strict (soft) PS in the vacuum configuration V^+. The stability condition $\alpha_u + \alpha_v > 0$ dictates the most negative allowed value of $\alpha_v(M_s)$ for PS giving rise to the border between regions of PS and vacuum instabilities. Plots taken from [4].

to M_{Pl} via the direct or indirect Higgs portal mechanism. Strongly coupled $\alpha_v(M_s)$ (or $\alpha_u(M_s)$) in contrast induce a quasi-exponential RG growth of $-\alpha_\delta$ via (5.4)[4]. For very feeble $-\alpha_\delta(M_s)$ the indirect portal mechanism is still to weak to render α_λ positive. If in contrast $-\alpha_\delta(M_s)$ is sufficiently large to prevent the sign change of α_λ, this growth invariably results in a RG-induced violation of the portal stability condition

---

[4] The pure BSM quartic terms(s) quickly dominates the RG evolution of the portal coupling independent of $\alpha_{v(,u)}(M_s)$, as sizeable $\alpha_{v(,u)} > 0$ is also always inhomogeneously induced by α_δ itself, cf. (5.12), (5.18), (5.19).

below the Planck scale and potentially even a negative α_δ pole. The deeper reason is the the large separation between the scale of the α_λ sign change in the SM, $\mu \sim 10^{11}$ GeV, and M_{Pl}. Therefore, the above problems cannot be circumvented by increasing the matching scale up to the scale of sign change $M_s \lesssim 10^{11}$ GeV, either. Hence, we find that strict PS cannot be realized for negative portal couplings, which we explicitly verified numerically in extensive parameter scans. In addition, also soft PS with intermediately negative α_λ is inevitably excluded for negative portal couplings as $\alpha_\lambda \lesssim 0$ always violates the portal stability condition[5]. Moreover, we find that restoring Higgs stability at M_{Pl} comes at the price of a simultaneous portal stability violation preventing full Planck scale stability, see Fig. 5.8. Putting it all together, PS is excluded for $\alpha_\delta < 0$.

Vacuum stability in the $SU(N_F) \times SU(N_F)$ model (5.15) also allows for negative values of the pure BSM quartic α_v (V^+) or α_u (V^-). The BSM critical surfaces for negative $\alpha_u(M_s) < 0$ and $\alpha_v(M_s) < 0$ are depicted in Fig. 5.9 and Fig. 5.10, respectively. In both cases, PS can be realized for a vast range of couplings and in the ground state V^- (V^+) for negative α_u (α_v), but without transitions due to the technical naturalness of α_u. Vacuum stability (5.15) at the matching scale in V^+ (V^-) requires $\alpha_v(M_s) > |\alpha_u(M_s)|$ ($\alpha_u(M_s) > N_F|\alpha_v(M_s)|$). These conditions explain several of the borders between regions of PS or Higgs metastability and vacuum instabilities, respectively.

Outside these regions of vacuum instabilities, the BSM critical surfaces exhibit similar patterns as for positive quartics. Stabilization can be achieved directly via a sizeable portal coupling $\alpha_\delta(M_s)$ widely independent of the pure BSM quartics $\alpha_{u,v}(M_s)$. Additionally for sizeable $\alpha_{u,v}(M_s)$ indirect stabilization is operative also for smaller $\alpha_\delta(M_s)$. The BSM critical surfaces are qualitatively similar for negative α_u and α_v, respectively, only differing in their vacuum configuration. However, indirect stabilization via α_u is again a bit less effective than via α_v due to smaller contributions to β_δ (5.17) and the occurrence of subplanckian Landau poles for $|\alpha_u(M_s)| \gtrsim 10^{-2} \dots 10^{-1}$. The identification of sizeable PS parameter space regions for negative $\alpha_{u,v}$ constitutes one of the main novelties in this work and is only possible due to the richer flavor symmetry.

5.2 Higgs Phenomenology

We now work out some crucial implications of our models for Higgs phenomenology at LO. They arise from scalar mass mixing between the SM Higgs and the BSM scalar after SSB via the portal coupling δ, affecting the width and couplings of the physical Higgs. For a more detailed discussion including higher-order effects in the $O(N_S)$ and $SU(N_F) \times SU(N_F)$ model, see e.g. [192, 193] and [46], respectively.

5.2.1 Higgs-BSM Mixing

We start by briefly discussing mixing while relegating the details to App. C. If there occurs SSB in the BSM sector, the BSM scalar S acquires a VEV v_s via

$$O(N_S):\ S_i = (s+v_s)\delta_{i1} + \dots\,, \quad V^+:\ S_{ij} = \frac{\delta_{ij}}{\sqrt{2N_F}}(s+v_s+i\tilde{s}) + \dots\,, \quad V^-:\ S_{ij} = \frac{\delta_{i1}\delta_{j1}}{\sqrt{2}}(s+v_s+i\tilde{s}) + \dots\,, \tag{5.22}$$

where s denotes the BSM Higgs mode, while the pseudoreal singlet $\tilde{s}$ and the remaining scalar components indicated by the dots are irrelevant for the following discussion. Goldstone bosons are assumed to acquire

---

[5] For $\lambda < 0$ the portal stability conditions in (5.9), (5.15) are not well defined. We therefore recall our definition of soft PS in Subsec. 3.2.3: For intermediate, moderate $-10^{-4} \lesssim \alpha_\lambda \lesssim 0$, we conservatively deploy the portal stability condition in the limit $\alpha_\lambda \to 0$, i.e. $\delta > 0$ in both models, when checking for soft PS.

small masses from additional, symmetry breaking mass terms to meet phenomenological constraints [46] but have not been further considered here. From the breaking patterns (5.22) and the unbroken potentials (5.8) and (5.14) we obtain the broken scalar potential of the SM and BSM Higgs modes. It can be expressed as

$$V(h,s) = -\frac{\mu_H^2}{2}(h+v_h)^2 - \frac{1}{2}\mu_S^2(s+v_s)^2 + \frac{\lambda}{4}(h+v_h)^4 + \frac{\Delta}{\mathcal{N}^2}(s+v_s)^4 + \frac{\delta}{2\mathcal{N}}(h+v_h)^2(s+v_s)^2 \quad (5.23)$$

in a model-independent fashion where it holds

$$O(N_S): \ \mathcal{N}=1,\ \Delta = v\,, \qquad V^+: \ \mathcal{N}=2,\ \Delta = \frac{u}{N_F}+v\,, \qquad V^-: \ \mathcal{N}=2,\ \Delta = u+v \quad (5.24)$$

in the different models and vacuum configurations. After EWSB, the portal coupling α_δ induces mixing between the gauge eigenstates h, s into the mass eigenstates h', s' with a mixing angle β given as

$$\tan 2\beta = \frac{\delta}{\sqrt{\lambda\Delta}}\frac{m_h m_s}{m_s^2 - m_h^2}\,, \quad (5.25)$$

where $m_{h,s} \propto v_{h,s}$ are the unrotated masses in the gauge basis. In contrast, we denote the masses of the physical fields as $M_h = m_{h'} = 125$ GeV and $M_s = m_{s'} > M_h$. The scalar mixing and implied phenomenology are very similar in all our models and independent of the multiplicities N_S, N_F as there is always just a single BSM Higgs mode.

There are five (six) additional model parameters μ_H^2, μ_S^2, λ, δ, v (and u) in the $O(N_S)$ ($SU(N_F)\times SU(N_F)$) model which are constrained by two independent observables, namely the physical Higgs mass $M_h = 125$ GeV and VEV $v_h = 246$ GeV obtained from G_F via (2.30). Hence, the models are controlled by (three) four free BSM parameters in addition to the scalar multiplicity N_S, N_F, which we take to be M_s, $\alpha_\delta(M_s)$, $\alpha_v(M_s)$ (and $\alpha_u(M_s)$) as a pleasant choice for the RG analysis. Crucially, this fixes the Higgs quartic $\lambda(M_s)$ to a value deviating from the SM one $\lambda_{\text{SM}} = M_h^2/(2v_h^2)$ depending on the BSM couplings and mass, see (C.25) for the tree-level expression. While this effect has only minor influence on the RG evolution (cf. also Subsec. 3.1.3), it has observable impact on the following phenomenological analysis.

The scalar mixing opens many decay channels of the mass eigenstate s' to SM fermions or gauge bosons. Vice versa, the decay width of the physical Higgs h' to SM final states $\{f\}$ is reduced as

$$\Gamma(h' \to \{f\}) = \cos^2\beta\, \Gamma^{\text{SM}}(h \to \{f\})\,. \quad (5.26)$$

This implies a model-independent bound on the mixing angle at 95% c.l. [192]

$$|\sin\beta| \leq 0.2 \quad (5.27)$$

due to combined Higgs signal strength measurements from ATLAS [194] and CMS [195]. In the limit of small β, we can now approximate (5.25) as

$$\beta \simeq \frac{\delta}{\sqrt{\lambda\Delta}}\frac{m_h}{M_s}\,, \quad (5.28)$$

which is controlled by the size of the portal coupling δ and the scalar mass hierarchy m_h/M_s. We see that the mixing bound (5.27) can be be conveniently fulfilled by choosing the phenomenologically hardly constrained pure BSM quartic α_Δ sufficiently large w.r.t. the portal coupling α_δ or large $M_s \gg m_h$.

5.2.2 Modified Higgs Couplings

The scalar mixing alters the values of the physical Higgs couplings w.r.t. the SM. In particular, we find for the coupling $g_{h'VV}$ of a single Higgs to a pair of electroweak gauge bosons $V = W, Z$

$$\delta g_{hVV} = \frac{g_{h'VV}}{g_{hVV}^{\mathrm{SM}}} - 1 = \cos\beta - 1 \quad \overset{\beta \ll 1}{\simeq} \quad -\frac{\beta^2}{2}\,, \tag{5.29}$$

which in the small mixing angle approximation is suppressed by β^2. The present and future experimental individual sensitivity is generically larger for the Z-coupling [155, 196]. The best individual bounds on δg_{hZZ} are currently at the level of 6% by ATLAS [197] and 7% by CMS [198] while W-bounds are weaker. The currently most stringent combined bound stems from ATLAS [197] assuming $\delta g_{hWW} = \delta g_{hZZ}$ and reads $\delta g_{hVV} \lesssim 0.031$ which still is a slightly weaker constraint than (5.27) from Higgs signal strength. The bound on δg_{hZZ} will be superseded in the near future by HL-LHC with a projected sensitivity of 1.5% [199] and increased by another order of magnitude to 0.16% at FCC-ee [196] and 0.17% at ILC [200] with 1 TeV center of mass energy, respectively. This will also increase the bound on the mixing angle (5.27) to $|\sin\beta| \lesssim 0.17$ (HL-LHC) and $|\sin\beta| \lesssim 0.06$ (ILC, FCC-ee), respectively. Notably, this reasoning can also be turned around. It was argued in [201] that measuring any $\delta g_{hVV} \neq 0$ at the mentioned present or future colliders invariably implies the existence of new bosons within experimental reach, in agreement with our findings.

We now turn to mixing induced deviations in the self-couplings of the physical Higgs boson defined in (2.14). Rotating the cubic terms

$$V^{(3)}(h,s) = \lambda v_h h^3 + \frac{\delta}{\mathcal{N}} v_s h^2 s + \frac{\delta}{\mathcal{N}} v_h h s^2 + \frac{4\Delta}{\mathcal{N}^2} v_s s^3 \tag{5.30}$$

in the broken scalar potential (5.23) to the mass basis we obtain

$$V^{(3)}(h',s') \supset \left(\lambda v_h \cos^3\beta - \frac{\delta v_s}{\mathcal{N}} \cos^2\beta \sin\beta + \frac{\delta v_h}{\mathcal{N}} \cos\beta \sin^2\beta - \frac{4\Delta v_s}{\mathcal{N}^2} \sin^3\beta\right) h'^3\,, \tag{5.31}$$

which fixes the ratio of the trilinear Higgs self-coupling $\kappa_3 h'^3$ w.r.t. its SM value $\kappa_3^{\mathrm{SM}} = \lambda_{\mathrm{SM}} v_h$ as

$$\begin{aligned} \frac{\kappa_3}{\kappa_3^{\mathrm{SM}}} &= \frac{\lambda}{\lambda_{\mathrm{SM}}} \cos^3\beta - \frac{\delta v_s}{\mathcal{N}\lambda_{\mathrm{SM}} v_h} \cos^2\beta \sin\beta + \frac{\delta}{\mathcal{N}\lambda_{\mathrm{SM}}} \cos\beta \sin^2\beta - \frac{4\Delta v_s}{\mathcal{N}^2 \lambda_{\mathrm{SM}} v_h} \sin^3\beta \\ &\overset{\beta \ll 1}{\simeq} 1 - \beta^2 \left(\frac{3}{2}\frac{\lambda}{\lambda_{\mathrm{SM}}} - \frac{\delta}{\mathcal{N}\lambda_{\mathrm{SM}}}\right)\,. \end{aligned} \tag{5.32}$$

Note that in the small angle approximation the $\mathcal{O}(\beta)$ term precisely cancels against the shift in λ (C.25), hence the leading deviation to the SM arises at $\mathcal{O}(\beta^2)$. Currently κ_3 is only poorly constrained by ATLAS $-1.5 < \kappa_3/\kappa_3^{\mathrm{SM}} < 6.7$ [202] and CMS $-1.24 < \kappa_3/\kappa_3^{\mathrm{SM}} < 6.49$ [198]. However, experimental constraints are expected to improve by one order of magnitude to 50% at HL-LHC and another one to 5% at FCC-hh [196]. The projected sensitivity at ILC with 1 TeV center of mass energy is 10% [200].

Proceeding analogously as for κ_3, we obtain for the quartic self-interaction κ_4

$$\frac{\kappa_4}{\kappa_4^{\mathrm{SM}}} = \frac{\lambda}{\lambda_{\mathrm{SM}}} \cos^4\beta + \frac{2\delta}{\mathcal{N}\lambda_{\mathrm{SM}}} \cos^2\beta \sin^2\beta + \frac{4\Delta}{\mathcal{N}^2 \lambda_{\mathrm{SM}}} \sin^4\beta \quad \overset{\beta \ll 1}{\simeq} \quad 1 + \frac{\delta^2}{4\Delta\lambda_{\mathrm{SM}}}\,. \tag{5.33}$$

Notably, the quartic receives a potentially sizeable enhancement which is not suppressed by the mixing

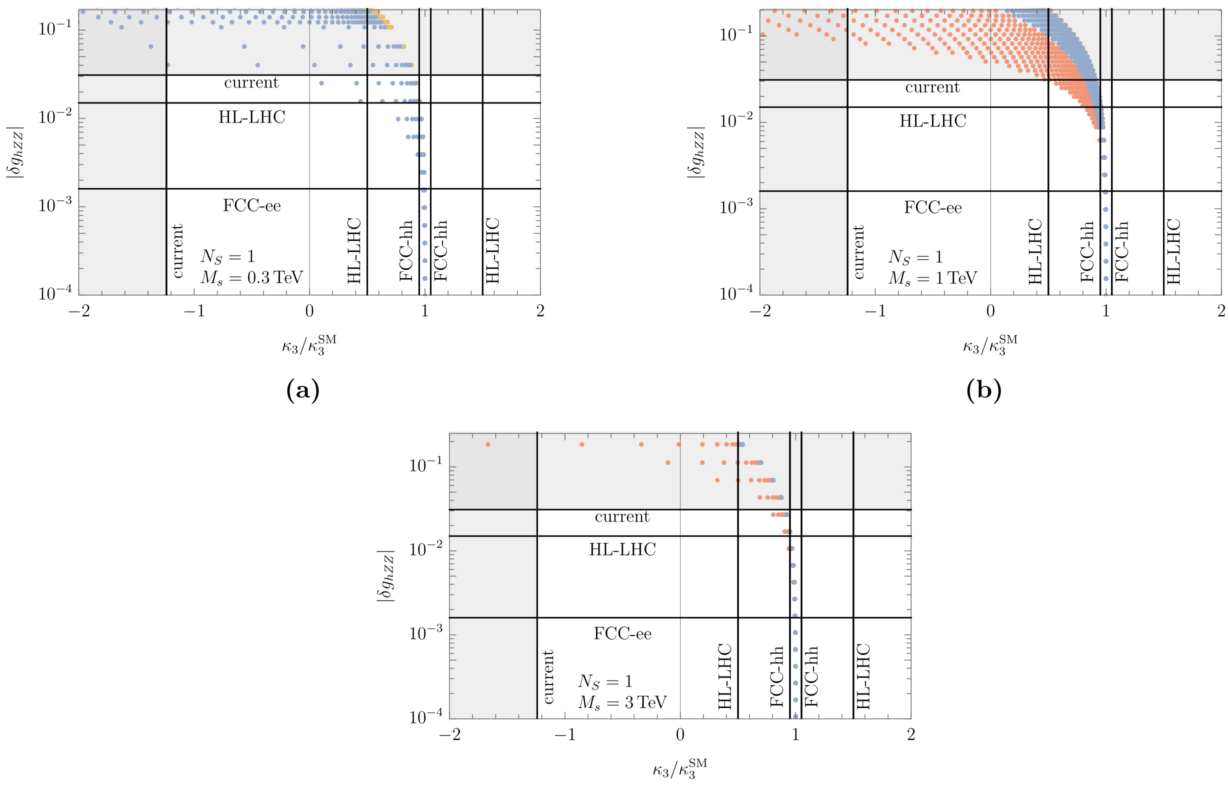

(a) **(b)**

(c)

Figure 5.11: Modified Higgs couplings δg_{hZZ} (5.29) and $\kappa_3/\kappa_3^{\mathrm{SM}}$ (5.32) in the $O(N_S)$ model for $N_S = 1$ and $M_s = 0.3$ TeV (a), and $M_s = 1$ TeV (b) and $M_s = 3$ TeV (c). Scattered dots correspond to different choices of $\alpha_{\delta,v}(M_s)$ from Fig. 5.2 with corresponding color coding indicating the Planck fate. Gray-shaded regions are excluded by direct measurements, whereas black lines indicate projected future sensitivities at current and future colliders. Plots taken from [4].

angle β or scalar mass hierarchy. Hence, for Planck-safe regions with $\delta \sim 2\sqrt{\Delta\lambda_{\mathrm{SM}}}$ (cf. Fig. 5.2 and Fig. 5.5) it can be of order unity and also amount to a factor of a few, even for large BSM masses and smaller β. So far, no constraints on κ_4 are available [155]. However, FCC-hh is expected to constrain the quartic self-interaction for the first time as $-4 \lesssim \kappa_4/\kappa_4^{\mathrm{SM}} \lesssim 10$ for $0 \lesssim \kappa_3/\kappa_3^{\mathrm{SM}} \lesssim 1$ [196]. For now, there exists only the theoretical limit from tree-level perturbative unitarity (5.7) implying $\kappa_4/\kappa_4^{\mathrm{SM}} \lesssim 65$.

5.2.3 Collider Signatures

We now analyze in detail collider signatures and constraints on our model parameters from the modification of Higgs couplings. While we retain the exact analytical expressions for δg_{hZZ} (5.29), κ_3 (5.32) and κ_4 (5.33) the indicated expressions in the small angle approximation allow to qualitatively understand some characteristic features of our analysis results.

We show the modifications of Higgs couplings in the $O(N_S)$ model induced by different values of $\alpha_\delta(M_s)$ and $\alpha_v(M_s)$ in the κ_3-δg_{hZZ} plane and the κ_4-δg_{hZZ} plane in Fig. 5.11 and Fig. 5.12, respectively, for

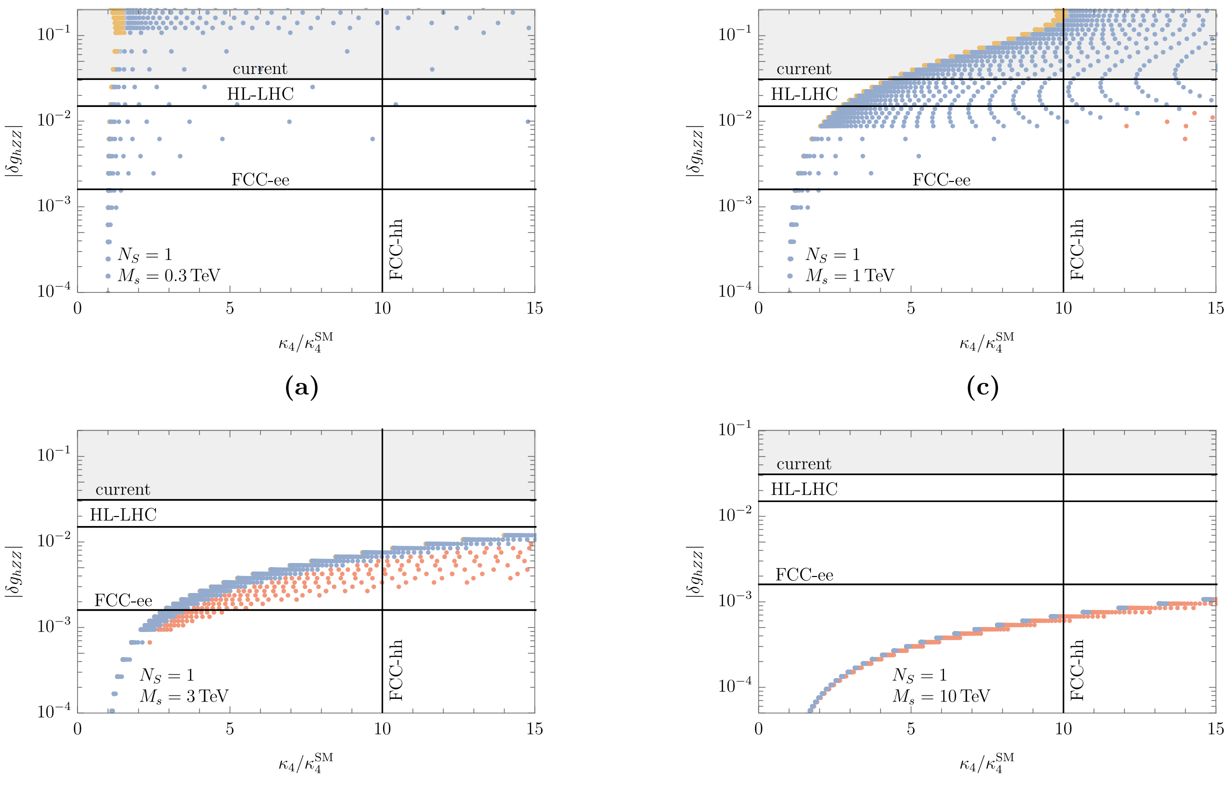

(a)

(c)

(b)

(d)

Figure 5.12: Modified Higgs couplings δg_{hZZ} (5.29) and $\kappa_4/\kappa_4^{\mathrm{SM}}$ (5.33) in the $O(N_S)$ model for $N_S = 1$ and $M_s = 0.3$ TeV (a), $M_s = 1$ TeV (b), $M_s = 3$ TeV (c) and $M_s = 10$ TeV (d). Note the slightly lower $|\delta g_{hZZ}|$ plot range in (d). Same color coding and exclusion regions as Fig. 5.11. Plots taken from [4].

different scalar masses M_s and $N_S = 1$[6] where the color indicates the Planck fate as in Fig. 5.2. We see that some Planck-safe parameter configurations are already ruled out by the existing LHC bounds on δg_{hZZ} and κ_3 (grey area). Generically, experimental bounds on δg_{hZZ} are more stringent than the ones on κ_3. While for lower masses such as $M_s = 0.3$ TeV in Fig. 5.11a the modification of κ_3 could be detectable already at HL-LHC, for TeV-ish or heavier BSM scalars the current (HL-LHC) δg_{hZZ} bound constrains the deviation in the trilinear to less than 20% (10%), see Fig. 5.11a, which is still in reach of FCC-hh. Eventually, the limit on δg_{hZZ} will increase by another order of magnitude at FCC-ee implying deviations in κ_3 to be below the sensitivity of FCC-hh even for low masses. When increasing the BSM mass to more than a few TeV, deviations in both the Z and the trilinear coupling slip out of reach, due to their quadratic suppression with the mixing angle, cf. (5.29), (5.32), and hence the scalar mass ratio due to (5.28).

Turning to the quartic Higgs self-coupling κ_4 in Fig. 5.12 we observe that a large enhancement of a factor larger than ten which is in reach of FCC-hh is implied for some Planck-safe parameters points, independent

---

[6] Recall that fixed $\alpha_{\delta,v}$ and M_s map exactly onto the same point in Higgs coupling space for all N_S. Changing the multiplicity for fixed quartics and mass might only change the Planck-fate of this configuration. In particular, increasing N_S can render RG trajectories Planck-safe for smaller values of $\alpha_{\delta,v}$ as the Higgs portal mechanism is enhanced with N_S. However, the corresponding parameter space points imply only tiny variations in the Higgs couplings and are therefore not visible in Fig. 5.11.

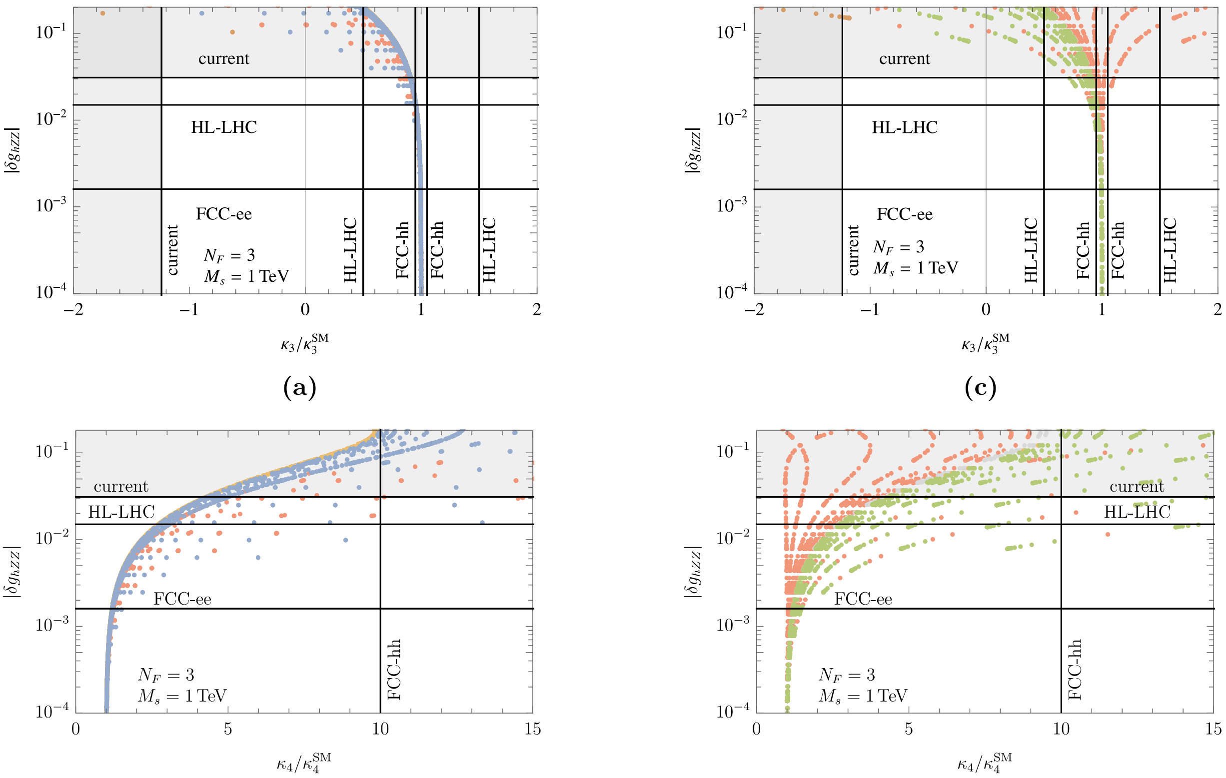

(a) **(c)**

(b) **(d)**

Figure 5.13: Modified Higgs couplings δg_{hZZ} (5.29), $\kappa_3/\kappa_3^{\rm SM}$ (5.32) (a,b) and $\kappa_4/\kappa_4^{\rm SM}$ (5.33) (c,d) in the $SU(N_F) \times SU(N_F)$ model for $N_F = 3$ and $M_s = 1$ TeV in the vacuum configuration V^+ (a,c) and V^- (b,d). Scattered dots correspond to different choices of $\alpha_{\delta,u,v}(M_s)$ from Fig. 5.5, Fig. 5.9 and Fig. 5.10 with corresponding color coding indicating the Planck fate. Gray-shaded regions are excluded by direct measurements, whereas black lines indicate projected future sensitivities at current and future colliders.

of M_s. This reflects the fact that $\kappa_4/\kappa_4^{\rm SM}$ (5.33) is not suppressed by the BSM scalar mass. Hence, for large $M_s \gtrsim 10$ TeV the enhancement of the Higgs quartic is the only signature of the model in reach of FCC, as the sensitivity to δg_{hZZ} and κ_3 is lost, see Fig. 5.12d.

The modifications of Higgs couplings δg_{hZZ}, κ_3 and κ_4 in the $SU(N_F) \times SU(N_F)$ model are shown in Fig. 5.13 for both vacuum configurations V^+ and V^-. As expected from Subsec. 5.2.2, in both vacuum configurations we find the same characteristic patterns as in the $O(N_S)$ model. In particular, effects in δg_{hZZ} and $\kappa_3/\kappa_3^{\rm SM}$ are rather small as they are suppressed by β^2 while the deviation from the SM in κ_4 can be sizeable. We also find a similar dependence on the BSM scalar mass M_s as in the $O(N_S)$ case. We conclude that from the Higgs coupling analysis only it is hardly possible to distinguish the $O(N_S)$ model as well as the different vacuum configurations $V^\pm$ in the $SU(N_F) \times SU(N_F)$ model from each other.

5.3 Summary

In this chapter we studied the possibility to achieve vacuum stability via the Higgs portal mechanism. Therefore, we extended the SM by an additional BSM scalar singlet field S. The core of the stabilization mechanism is the new Higgs portal coupling $\delta(H^\dagger H)(S^\dagger S)$, which contributes positively to β_λ potentially enabling stability, see Fig. 5.2 and Fig. 5.5. The uplift increases with the number of scalars, allowing for PS also for smaller values of the portal coupling, Fig. 5.3a and Fig. 5.6a.

In addition, the potential features quartic BSM scalar self-interactions depending on the scalar symmetry. We studied two models with real and complex BSM scalars featuring an $O(N_S)$ (Subsec. 5.1.1) and a $SU(N_F) \times SU(N_F)$ (Subsec. 5.1.2) flavor symmetry, respectively. In the first case (5.8), there is only one pure BSM quartic v, while in the latter (5.14) there are two, u and v. A main novelty of this work was the finding that independent of the symmetry Higgs stability can also be indirectly achieved for extremely feeble portal couplings via sizeable pure BSM quartics $\alpha_{v(u)}$ (Fig. 5.3). In this case, $\alpha_{v(u)}$ induces a strong RG growth of α_δ (Fig. 5.3b) which enhances the value of the Higgs quartic α_λ. Whether vacuum stability can be achieved also depends on the BSM mass scale M_s, as for larger masses there is less RG time until M_{Pl} left to cause sufficient uplift in the Higgs quartic, see Fig. 5.4 and Fig. 5.6b. The PS parameter space is enhanced by the occurrence of walking regimes (Fig. 5.1a and Fig. 5.7) which capture quartic couplings at sizeable, positive values and thereby enforce stability.

Interestingly, the vacuum stability conditions (5.9), (5.15) also allow for negative values of the portal coupling δ, which equally well fuel the Higgs portal mechanism due to the uplift in β_λ being $\propto \alpha_\delta^2$. However, we find that negative $\alpha_\delta < 0$ are generically excluded due to vacuum instabilities which are invariably induced by the RG dynamics as discussed in Subsec. 5.1.3. In contrast, in the $SU(N_F) \times SU(N_F)$ model stability can be also achieved for negative BSM scalar quartic self-couplings α_u or α_v in the vacuum configuration V^- and V^+, respectively, see Fig. 5.9 and Fig. 5.10.

The main phenomenological signatures of the models in case of a non-trivial BSM ground state arise from scalar mixing between the SM and BSM Higgs modes where the mixing angle is constrained to be small by Higgs signal strength measurements (5.27). The mixing alters the couplings of the physical Higgs bosons and is probed at LHC through measurements of the hZZ and trilinear Higgs self-coupling. The BSM effects are however suppressed by the mixing angle and scalar mass hierarchy, see Fig. 5.11. Existing limits are expected to improve significantly at HL-LHC, ILC and FCC, probing large new parts of Planck-safe parameter space for TeV-ish BSM scalar masses or below. Crucially, the partially significant enhancement of the quartic Higgs self-interaction Fig. 5.12 is unsuppressed by the BSM mass, potentially providing the only detectable signature of our models with multi-TeV scalars at FCC-hh.

There are still several open questions for the future. As soon as scalar template 3-loop β-functions are available it will be crucial to check the perturbative stability of the walking regimes. Furthermore, to ultimately distinguish meta- and instability a full BSM effective potential analysis is desirable. It would also be interesting to explore if a connection can be made to cosmology and in particular to baryogenesis as attempted in [203, 204]. Finally, a possible next step is to analyze the interplay of portals. Naturally, charged scalars allow for the gauge, Higgs and potentially Yukawa portal mechanisms to operate simultaneously. Alternatively, more elaborate models featuring both scalar singlets and VLFs entail the gauge and Higgs portal along with a pure BSM Yukawa interaction. We investigate this possibility in the next chapter.

6 Planck Safety from Vector-like Quarks and Flavorful Scalars

In the previous two chapters we have analyzed mechanisms to render the SM Planck-safe in a minimally invasive manner by adding VLFs or singlet scalars. As a natural next step, in this chapter based on work in progress [7] we investigate whether and how new PS mechanisms can arise in more complex models from the interplay of both presented BSM sectors. The choice of the BSM field content is guided by the template model [40] for AS in GY theories as well as in SM extensions [41, 42], cf. Subsec. 3.2.1. Previous works [44–46, 181] already studied extensions of the SM by VLLs and a flavorful complex singlet scalar matrix field as in Subsec. 5.1.2. Interestingly, it was found that these models did not only allow for PS but also for an explanation of the apparent anomalies in the muon and electron anomalous magnetic moments $(g-2)_{\mu,e}$ [155, 205]. Inspired by this success, we choose a similar setup and study models featuring VLQs and matrix scalars. The RG analysis of these models is much more involved than in minimal VLF and scalar models due to the larger number of parameters but also implies a richer phenomenology.

This chapter is structured as follows: We present our model setup in Sec. 6.1 before turning to the RG analysis in Sec. 6.2. We then discuss SMEFT constraints and collider phenomenology of our models in Sec. 6.3, respectively, before concluding in Sec. 6.4.

6.1 Models

We extend the SM by N_F generations of VLQs as well as a $N_F \times N_F$ complex singlet scalar matrix field $\hat{S}$, cf. Subsec. 5.1.2. In order to make contact with SM flavor we set $N_F = 3$. We focus on the VLQ representations $(Y_F, d_2, d_3) = (\frac{7}{6}, \mathbf{2}, \mathbf{3})$ (model L) and $(Y_F, d_2, d_3) = (-\frac{5}{6}, \mathbf{2}, \mathbf{3})$ (model M), cf. Tab. 4.1, which allow for a mixed SM-BSM Yukawa portal coupling κ_{ij} between the VLQs, the SM Higgs and SM fermions. This choice complements similar studies with VLLs [44–46, 181].

The models a priori exhibit a large BSM flavor symmetry

$$\mathcal{G}_{\mathrm{BSM}} = U(3)_{\psi_L} \times U(3)_{\psi_R} \times U(3)_{\hat{S}_R} \times U(3)_{\hat{S}_L}\,, \tag{6.1}$$

which due to the pure BSM Yukawa interaction

$$-\mathcal{L}^{\mathrm{Y}}_{\mathrm{BSM}} = \hat{y}_{ij}\,\overline{\psi}_{L_i}\,\hat{S}_{ij}\,\psi_{R_j} + \mathrm{h.c.} \tag{6.2}$$

is broken down via $U(3)_{\hat{S}_{L,R}} \sim U(3)_{\psi_{L,R}}$ to $U(N_F)_{\psi_L} \times U(N_F)_{\psi_R}$. $\mathcal{G}_{\mathrm{BSM}}$ is also intertwined with the SM flavor symmetry (2.20) via the portal interactions

$$-\mathcal{L}^{\mathrm{Y}}_{\mathrm{portal}} = \begin{cases} \hat{\kappa}_{ij}\,\overline{\psi}_{L_i} H^c D_j + \mathrm{h.c.} & \text{(model M)} \\ \hat{\kappa}_{ij}\,\overline{\psi}_{L_i} H U_j + \mathrm{h.c.} & \text{(model L)} \end{cases} \tag{6.3}$$

as $U(3)_{\psi_L} \sim U(3)_{U(D)}$ in model L (M). Recall that $\mathcal{G}_{\mathrm{SM}}$ is explicitly broken by SM Yukawas, cf. (2.21). In particular, the sizeable top (bottom) Yukawa couplings y_t (y_b) single out third generation quarks and breaks down $U(3)_{U(D)}$ to the approximate $U(2)_{U(D)}$ symmetry of first and second generation up-type (down-type) quarks. In compliance with these findings, the ansatz

$$\hat{\kappa}_{ij} = \mathrm{diag}(\kappa, \kappa, \tilde{\kappa}) \tag{6.4}$$

suggests that also the BSM flavor symmetry is broken down to $U(2)_{\psi_L} \sim U(2)_{U(D)}$ in model L (M). This constitutes a crucial difference to VLL models [44–46, 181] and leads to a modification

$$-\mathcal{L}^{\rm Y}_{\rm portal} = \begin{cases} \kappa\,\overline{\psi}_{L_i} H\, U_i + \tilde{\kappa}\,\overline{\psi}_{L_3} H\, t_R + \text{h.c.} & \text{(model L)} \\ \kappa\,\overline{\psi}_{L_i} H^c D_i + \tilde{\kappa}\,\overline{\psi}_{L_3} H^c b_R + \text{h.c.} & \text{(model M)} \end{cases} \tag{6.5}$$

of the Yukawa portal couplings in (6.3) with $i = 1, 2$. Moreover, the 3×3 matrix scalar $\hat{S}$ effectively splinters into four independent scalar fields S (2×2), ϕ_L (2×1), ϕ_R (1×2) and φ (1×1) as

$$\hat{S} = \left(\begin{array}{cc|c} S & \cdots & \phi_L \\ \vdots & \ddots & \vdots \\ \hline \phi_R & \cdots & \varphi \end{array} \right) . \tag{6.6}$$

In order to reduce the number of free parameters while retaining the distinction of third generation couplings, we will from now on neglect the scalars $\phi_{L,R}$, i.e. set all their potential couplings to zero. Note that this ansatz is radiatively stable and fully compliant with the flavor structure (6.4). The pure BSM Yukawa Lagrangian is then given by

$$-\mathcal{L}^{\rm Y}_{\rm BSM} = y\,\overline{\psi}_{L_i} S_{ij} \psi_{R_j} + \tilde{y}\,\overline{\psi}_{L_3} \varphi \psi_{R_3} + \text{h.c.}\,. \tag{6.7}$$

The scalar potential for the fields H, S and φ

$$\begin{aligned} V^{(4)} =& \lambda\,(H^\dagger H)^2 + \delta\,(H^\dagger H)\,\mathrm{Tr}(S^\dagger S) + \tilde{\delta}\,(H^\dagger H)(\varphi^\dagger \varphi) \\ &+ u\,\mathrm{Tr}(S^\dagger S S^\dagger S) + v\,\mathrm{Tr}(S^\dagger S)\mathrm{Tr}(S^\dagger S) + s\,(\varphi^\dagger \varphi)^2 + w\,(\varphi^\dagger \varphi)\,\mathrm{Tr}(S^\dagger S) \end{aligned} \tag{6.8}$$

features pure BSM quartics u, v, s as well as portal couplings δ, $\tilde{\delta}$, w. It is stable if [137, 160, 161]

$$\begin{aligned} &\lambda > 0, \quad \mathit{\Delta} > 0, \quad s > 0, \quad \delta' = \delta + 2\sqrt{\lambda \mathit{\Delta}} > 0, \quad \tilde{\delta}' = \tilde{\delta} + 2\sqrt{\lambda s} > 0, \\ &w' = w + 2\sqrt{s \mathit{\Delta}} > 0, \quad 2\sqrt{\lambda \mathit{\Delta} s} + \delta\sqrt{s} + \tilde{\delta}\sqrt{\mathit{\Delta}} + w\sqrt{\lambda} + \sqrt{\delta' \tilde{\delta}' w'} > 0\,, \end{aligned} \tag{6.9}$$

where the parameter

$$\mathit{\Delta} = \begin{cases} \frac{u}{2} + v > 0 & \text{for } u > 0 \quad (V^+) \\ u + v > 0 & \text{for } u < 0 \quad (V^-) \end{cases} \tag{6.10}$$

depends on the vacuum configuration $V^\pm$ of S, cf. Subsec. 5.1.2. For the sake of simplicity, we also define the abbreviated notation

$$\hat{X} = (X, X, \widetilde{X})\,. \tag{6.11}$$

for all fields and parameters that are subject to splitting between the third $\widetilde{X}$ and first two generation X components.

6.2 RG Analysis

In order to study the RG flow of our models we restrict ourselves to scenarios with a NP scale around $\mu_0 \simeq 1\,\text{TeV}$ which is set by the VLF M_F and scalar $M_{\hat{S}}$ masses. A characteristic feature of our models is a sizeable enhancement of all gauge β-functions due to the large multiplicity and charges of the BSM fermions as in Sec. 4.1. As a crucial consequence, the parameter space in both models is dominated by the occurrence of a subplanckian α_1 Landau pole, which for feeble or vanishing BSM couplings appears around

10^9 GeV (10^{14} GeV) in model L (M). The only possibility to push the pole beyond M_{Pl} while keeping $\mu_0 \simeq 1$ TeV are sufficiently sizeable Yukawa couplings. This a priori excludes PS only via the gauge and Higgs portal mechanisms, cf. also Tab. 4.2, and promotes the Yukawa portal mechanism to the key player for PS. Accordingly, Planck-safe RG flows typically exhibit strongly coupled walking regimes, as already seen in Sec. 4.2. In particular, PS generically requires strongly coupled values of $\alpha_y \gtrsim \mathcal{O}(10^{-1})$, whose contribution to β_1 is enhanced by a factor of $(N_F - 1)^2 = 4$. Large values of $\alpha_{\tilde{y},\kappa,\widetilde{\kappa}}$ only on the other hand are typically not sufficient for PS. Moreover, sizeable Yukawa couplings tend to destabilize the Higgs, which implies upper bounds for the Yukawa portal couplings $\alpha_{\kappa,\widetilde{\kappa}}$.

The RGEs in our models are much more interconnected than in the minimal models from Chap. 4 and 5 due to the larger number of couplings. In consequence, the BSM couplings $\alpha_{\delta,\tilde{\delta},u,v,w,s}$ are not technically natural (anymore) and thus can be radiatively induced or change their sign. Crucially, $\alpha_{\delta,u}$ ($\alpha_{\tilde{\delta},s}$) are induced by the typically sizeable BSM Yukawas α_y ($\alpha_{\tilde{y}}$). This has two important consequences: Firstly, RG induced sign changes of α_u enable transitions between the vacuum configurations $V^\pm$ but also instabilities. Secondly, inducing the Higgs portal couplings $\alpha_{\delta,\tilde{\delta}}$ via large $\alpha_{y,\tilde{y}}$ potentially strengthens the Higgs portal mechanism and benefits PS. In spite of this finding, the values of scalar quartics are typically only loosely constrained by PS. An exception are strongly coupled $\gtrsim \mathcal{O}(1)$ values of quartics which tend to induce Landau poles in the scalar sector and therefore disfavor PS, cf. Sec. 5.1. Intermediate values of the Higgs portal couplings $\alpha_{\delta,\tilde{\delta}}$ as well as the pure BSM quartics $\alpha_{u,v,w,s}$ in contrast promote Higgs stability via the direct and indirect Higgs portal mechanism and therefore favor PS. However, this effect is only relevant in the small pole-free subset of the parameter space and therefore of minor importance.

Our models contain in total ten free BSM couplings. Therefore, the complexity of the RG analysis in comparison to the minimal models increases exponentially which prohibits a similarly rigorous scrutinization of the full parameter space. While still scanning the whole parameter space as closely meshed as possible[1], we apply our knowledge from the previous chapter to identify parameter space regions that are particularly promising for PS. Due to their special role in taming the α_1 pole, we especially focus on the BSM Yukawas and the parameter space regions where they are sizeable. In contrast, we scan only coarsely meshed over values of the pure BSM quartic couplings whose impact on the RG evolution of SM couplings at 2-loop order is only indirect and channeled through the Higgs portals. We thereby typically assume feeble, positive values for all pure BSM quartics.

6.2.1 Model M

We find that in model M strict PS can be realized in both vacuum configurations V^+ and V^- at M_{Pl}, whereas the model parameter space hardly exhibits any regions of soft PS or metastable Higgs. The BSM critical surface in the $\alpha_{\kappa,y}|_{\mu_0}$ and $\alpha_{\widetilde{\kappa},\tilde{y}}|_{\mu_0}$ plane is displayed in Fig. 6.1. We see that $\alpha_{\widetilde{\kappa}}|_{\mu_0}$ is crucial to determine which vacuum configuration $V^\pm$ is realized at M_{Pl}. The V^- region in Fig. 6.1 thereby originates from a dynamical, RG induced vacuum transition $V^+ \to V^-$ between the TeV and Planck scale. In total we find that PS requires

$$\alpha_y|_{\mu_0} \gtrsim 10^{-1}, \quad \alpha_{\tilde{y}}|_{\mu_0} \gtrsim 10^{-1}, \quad \alpha_\kappa|_{\mu_0} \lesssim 3\cdot 10^{-3}, \quad \begin{cases} \alpha_{\widetilde{\kappa}}|_{\mu_0} \lesssim 3\cdot 10^{-3} \vee \alpha_{\widetilde{\kappa}}|_{\mu_0} \gtrsim 1 & \text{for } V^+ \\ 3\cdot 10^{-1} \lesssim \alpha_{\widetilde{\kappa}}|_{\mu_0} \lesssim 1 & \text{for } V^- \end{cases}, \tag{6.12}$$

---

[1] The limiting factors are a comparably long CPU time to integrate the large, interconnected system of RGEs for a single configuration of coupling values (~ 3 s on a processor with six cores and a frequency of 2.9 GHz) and the high dimensionality of the coupling space. Due to the 'curse of dimensionality' only scanning three different values per parameter already yields $3^{10} \simeq 60.000$ mesh points and requires a CPU time of roughly two days. Analogously, slightly increasing the number of values per parameter from three to five would require a factor $\frac{5^{10}}{3^{10}} \simeq 165$ larger CPU time of almost a year.

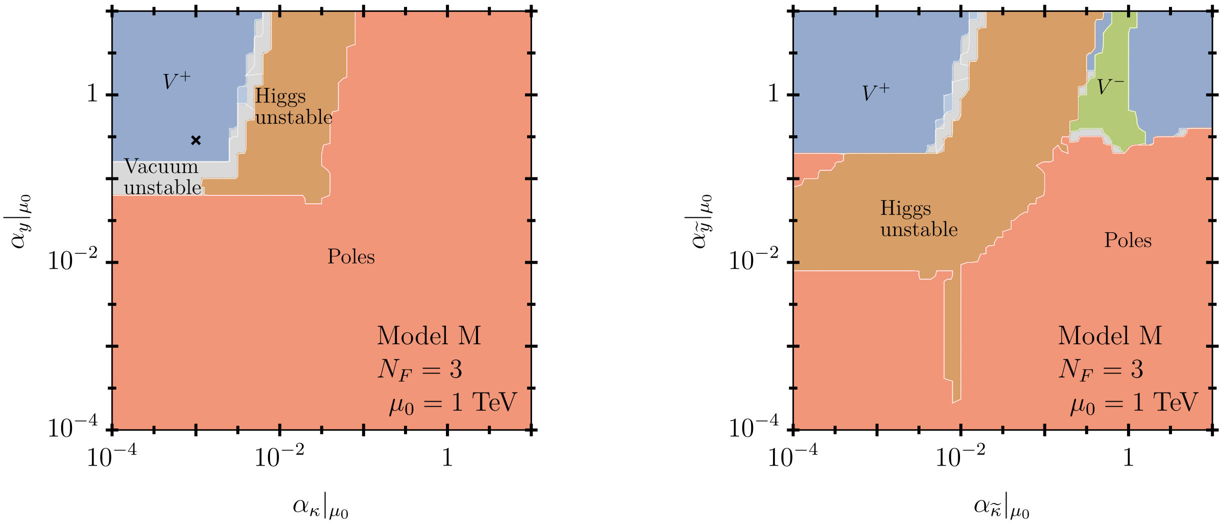

(a) α_y-α_κ-plane for $\{\alpha_{\tilde{\kappa}}, \alpha_{\tilde{y}}\}|_{\mu_0} = \{10^{-3}, 10^{-0.5}\}$.

(b) $\alpha_{\tilde{y}}$-$\alpha_{\tilde{\kappa}}$-plane for $\{\alpha_\kappa, \alpha_y\}|_{\mu_0} = \{10^{-5}, 1\}$.

Figure 6.1: BSM critical surface for model M with $N_F = 3$ and $\mu_0 = 1$ TeV scanning over $\alpha_{y,\kappa}|_{\mu_0}$ (a) and $\alpha_{\tilde{y},\tilde{\kappa}}|_{\mu_0}$ (b). BSM quartics are fixed as $\{\alpha_{\delta,\tilde{\delta}},\, \alpha_u,\, \alpha_v,\, \alpha_w,\, \alpha_s\}|_{\mu_0} = \{10^{-5.5}, 10^{-5}, 10^{-6}, 10^{-7}, 10^{-5}\}$. Same color coding as Fig. 5.9. The black cross indicates the benchmark point for which the RG running is plotted in Fig. 6.2.

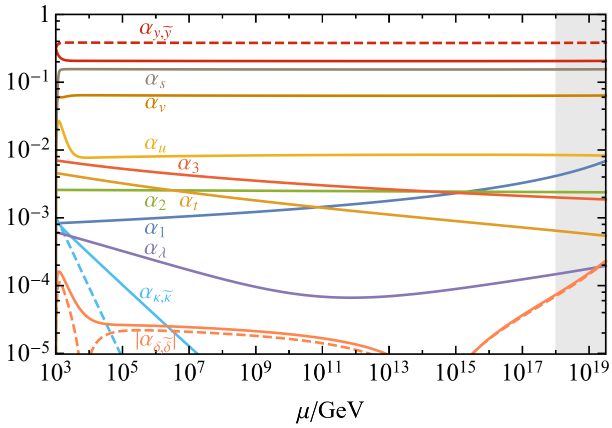

Figure 6.2: Planck-safe RG flow in model M for $N_F = 3$ and $\mu_0 = 1$ TeV. RG trajectories for couplings are indicated by different colors and annotations. Dashed lines with the same color as solid ones correspond to the (tilded) third generation couplings, e.g. $\alpha_{\tilde{y}}$ and α_y. Initial values of BSM couplings are fixed as $\{\alpha_{\kappa,\tilde{\kappa}}, \alpha_{y,\tilde{y}}, \alpha_{\delta,\tilde{\delta}},\, \alpha_u,\, \alpha_v,\, \alpha_w,\, \alpha_s\}|_{\mu_0} = \{10^{-3}, 10^{-0.5}, 10^{-5.5}, 10^{-5}, 10^{-6}, 10^{-7}, 10^{-5}\}$. Note that $\alpha_{b,w}$ stay feeble during the whole RG evolution and are therefore not visible.

which we deduced from extensive parameter scans. Interestingly, this excludes PS for the scenario where the scalar φ is decoupled in a radiatively stable manner by setting $\alpha_{\tilde{y},\tilde{\kappa},\tilde{\delta},w,s} = 0$.

An exemplary Planck-safe RG flow is shown in Fig. 6.2. The sizeable values of $\alpha_{y,\tilde{y}}|_{\mu_0}$ induce a walking

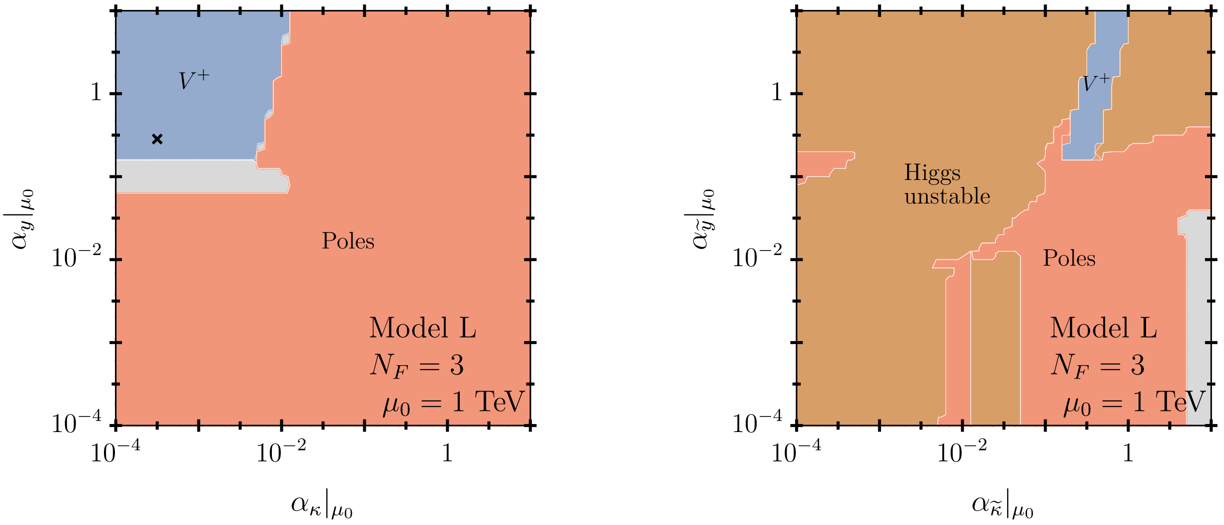

(a) α_y-α_κ-plane for $\{\alpha_{\tilde{\kappa}}, \alpha_{\tilde{y}}\}|_{\mu_0} = \{10^{-0.5}, 10^{-0.5}\}$.

(b) $\alpha_{\tilde{y}}$-$\alpha_{\tilde{\kappa}}$-plane for $\{\alpha_\kappa, \alpha_y\}|_{\mu_0} = \{10^{-5}, 1\}$.

Figure 6.3: BSM critical surface in model L for $N_F = 3$ and $\mu_0 = 1$ TeV scanning over $\alpha_{y,\kappa}|_{\mu_0}$ (a) and $\alpha_{\tilde{y},\tilde{\kappa}}|_{\mu_0}$ (b). BSM quartics are fixed as $\{\alpha_{\delta,\tilde{\delta}},\ \alpha_u,\ \alpha_v,\ \alpha_w,\ \alpha_s\}|_{\mu_0} = \{10^{-5.5}, 10^{-5}, 10^{-6}, 10^{-7}, 10^{-5}\}$. Same color coding as Fig. 5.9. The black cross indicates the benchmark point for which the RG running is plotted in Fig. 6.4.

regime directly above the matching scale that lasts until the transplanckian regime. It quickly captures the quartics $\alpha_{u,v,s}$ at values of $\mathcal{O}(10^{-2} - 10^{-1})$, whereas the Yukawas $\alpha_{y,\tilde{y}}$ are interlocked at $\mathcal{O}(1)$. The portal couplings $\alpha_{\kappa,\tilde{\kappa},\delta,\tilde{\delta},w}$ do not participate in the walking but decrease such that the scalar portals $\alpha_{\delta,\tilde{\delta},w}$ even change sign. The gauge couplings on the other hand although tamed by the Yukawas are enhanced w.r.t. the SM and feed the gauge portal mechanism, cf. Sec. 4.1. In consequence, the Higgs is stabilized at weak coupling all the way up to M_{Pl}. Note also that the initial symmetry between third and the first two generations couplings $\{\alpha_{\tilde{\kappa}}, \alpha_{\tilde{y}}, \alpha_{\tilde{\delta}}\}|_{\mu_0} = \{\alpha_\kappa, \alpha_y, \alpha_\delta\}|_{\mu_0}$ is explicitly broken in the RG evolution as there are sizeable deviations between the running of tilded and the corresponding untilded couplings.

6.2.2 Model L

Planck safety can also be realized in model L. Due to the larger VLQ hypercharge Y_F compared to model M, it is harder to avoid a subplanckian α_1 pole. This results in stricter constraints on the BSM parameters. Accordingly, a smaller BSM critical surface was obtained in the parameter scans, see the corresponding surface plot Fig. 6.3. Moreover and in contrast to model M PS can only be realized in the vacuum configuration V^+ at M_{Pl}. The relevant conditions for a Planck-safe RG flow are

$$\alpha_y|_{\mu_0} \gtrsim 10^{-1}, \quad (\alpha_{\tilde{y}}|_{\mu_0} \gtrsim 10^{-1}), \quad \alpha_\kappa|_{\mu_0} \lesssim 10^{-2}, \quad \alpha_{\tilde{\kappa}}|_{\mu_0} \gtrsim 1.5 \cdot 10^{-1}\,, \tag{6.13}$$

where the $\tilde{y}$ condition in brackets is not strictly necessary but strongly promotes PS. Large values of all Yukawa couplings (except for α_κ) are required at the matching scale to realize PS.

An exemplary Planck-safe RG trajectory is shown in Fig. 6.4. As in model M, the RG flow features a walking regime with onset closely above the matching scale including the pure BSM quartics $\alpha_{u,v,s}$ and Yukawas $\alpha_{y,\tilde{y}}$. Interestingly, also α_λ participates in the walking, resulting in a stabilization of the Higgs at

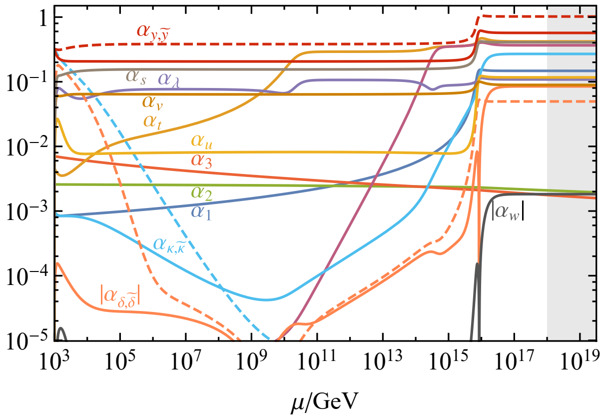

Figure 6.4: Planck-safe RG flow in model L for $N_F = 3$ and $\mu_0 = 1$ TeV. Same labeling as in Fig. 6.2. Initial values of BSM couplings are fixed as $\{\alpha_\kappa, \alpha_{\tilde{\kappa}}, \alpha_{y,\tilde{y}}, \alpha_{\delta,\tilde{\delta}}, \alpha_u, \alpha_v, \alpha_w, \alpha_s\}|_{\mu_0} = \{10^{-3}, 10^{-0.5}, 10^{-0.5}, 10^{-5.5}, 10^{-5}, 10^{-6}, 10^{-7}, 10^{-5}\}$.

strong coupling in contrast to Fig. 6.2. We conclude that here the stabilization is mostly due to the Yukawa rather than the gauge portal mechanism. Around $\mu \simeq 10^{16}$ GeV a transition to a second walking regime occurs in the RG flow. This walking regime attracts not only the former mentioned couplings but also all other quartics and Yukawas as well as most importantly the hypercharge coupling α_1, which prevents a subplanckian pole. Note that in this second walking regime most couplings are locked at sizeable values of $\mathcal{O}(0.1-1)$.

6.3 Phenomenology

We now work out phenomenological bounds on our model parameters and compare them to PS constraints. The isolated phenomenology of BSM models featuring only VLFs or scalars have already been discussed in Chap. 4 and Chap. 5, respectively. Thus, in the following we mainly focus on effects arising from the interplay of the different BSM sectors.

6.3.1 SMEFT Bounds

Matching our models to SMEFT, cf. Subsec. 2.5.1 allows us to derive constraints on our model parameters by comparing induced WCs to results from global fits. Integrating out the BSM fields at tree-level induces the four dimension-6 operators

$$\begin{aligned} Q_{Hq}^{ij} &= i\left((H^\dagger D_\mu H) - (D_\mu H)^\dagger H\right)(q_i^R \gamma^\mu q_j^R), & Q_{qH}^{ij} &= (H^\dagger H)(\bar{Q}_i H^{[c]} q_j^R), \\ Q_{H\Box} &= (H^\dagger H)\partial^\mu \partial_\mu (H^\dagger H), & Q_H &= (H^\dagger H)^3, \end{aligned} \tag{6.14}$$

with flavor indices i, j and $q_{i,j}^R = D_{i,j}\,[U_{i,j}]$ in model M [L]. The scalar WCs $C_{H,H\Box}$ only depend on parameters of the scalar sector which are hardly constrained by PS and are therefore not considered here.

Model	WC	$C/(\Lambda^2[\mathrm{TeV}^2])$	c.l.	Flavor Symmetry	Fit	Constraint on	Numerical Value	Ref.
M	C_{Hd}^{11}	-2.8 ± 1.9	1σ	-	full	$\alpha_{\kappa}/M_F^2[\mathrm{TeV}^2]$	$(\ \ 3.5 \pm 2.4) \cdot 10^{-2}$	[177]
M	C_{Hd}^{22}	-0.6 ± 1.4	1σ	-	full	$\alpha_{\kappa}/M_F^2[\mathrm{TeV}^2]$	$(\ \ 0.7 \pm 1.8) \cdot 10^{-2}$	[177]
M	C_{Hd}^{33}	-0.66 ± 0.22	1σ	-	full	$\alpha_{\widetilde{\kappa}}/M_F^2[\mathrm{TeV}^2]$	$(\ \ 8.4 \pm 2.8) \cdot 10^{-3}$	[177]
M	C_{dH}^{33}	0.018 ± 0.049	1σ	-	full	$\alpha_{\widetilde{\kappa}}/M_F^2[\mathrm{TeV}^2]$	$(\ \ 1.6 \pm 4.5) \cdot 10^{-2}$	[177]
L	$C_{Hu}^{11,22}$	$-0.00^{+0.073}_{-0.075}$	95%	$SU(2)^2 \times SU(3)^3$	single	$\alpha_{\kappa}/M_F^2[\mathrm{TeV}^2]$	$(-0.0^{+9.2}_{-9.5}) \cdot 10^{-4}$	[178]
L	C_{Hu}^{22}	0.11 ± 0.17	1σ	-	full	$\alpha_{\kappa}/M_F^2[\mathrm{TeV}^2]$	$(\ \ 1.4 \pm 2.1) \cdot 10^{-3}$	[177]
L	C_{Hu}^{33}	5.3 ± 7.1	95%	$SU(2)^2 \times SU(3)^3$	full	$\alpha_{\widetilde{\kappa}}/M_F^2[\mathrm{TeV}^2]$	$(\ \ 6.7 \pm 9.0) \cdot 10^{-2}$	[178]
L	C_{Hu}^{33}	0.6 ± 3.5	95%	$SU(2)^2 \times SU(3)^3$	single	$\alpha_{\widetilde{\kappa}}/M_F^2[\mathrm{TeV}^2]$	$(\ \ 0.8 \pm 4.4) \cdot 10^{-2}$	[178]
L	C_{uH}^{33}	-0.10 ± 0.91	95%	$SU(2)^2 \times SU(3)^3$	single	$\alpha_{\widetilde{\kappa}}/M_F^2[\mathrm{TeV}^2]$	$(-0.1 \pm 1.4) \cdot 10^{-2}$	[178]
L	C_{uH}^{33}	-0.28 ± 2.7	1σ	-	full	$\alpha_{\widetilde{\kappa}}/M_F^2[\mathrm{TeV}^2]$	$(-0.4 \pm 4.0) \cdot 10^{-2}$	[177]

Table 6.1: Most stringent limits on fermionic Wilson coefficients $C_{Hd,dH,Hu,uH}$ collected from [177, 178] and corresponding bounds on our model parameters in model L and M. The entries 'full' and 'single' in the column 'Fit' indicate whether the WCs for a whole set of operators or just one single operator are fitted.

The fermionic WCs read[2]

$$C_{Hq}^{ij} = \xi_q\, 8\pi^2 \frac{\alpha_{\hat{\kappa}_i}}{M_F^2}\delta_{ij}, \quad C_{qH}^{ij} = 8\pi^2 Y_q^{ji*}\frac{\alpha_{\hat{\kappa}_j}}{M_F^2}, \tag{6.15}$$

cf. also (4.19), with $\xi_q = -1\,[+1]$ in model M [L]. We see that C_{Hq} and C_{qH} are induced by the Yukawa portal $\alpha_{\hat{\kappa}}$ where C_{qH}^{ij} in comparison to C_{Hq}^{ij} is suppressed by the SM Yukawa matrix element Y_q^{ji*}. Hence, we find that C_{qH}^{33} is the only non-negligible component of C_{qH}^{ij}. Imposing the residual $U(2)^3$ flavor symmetry for the light quarks we also find $C_{Hq}^{11} = C_{Hq}^{22}$. We stress that all induced WCs are insensitive to the pure BSM Yukawa $\alpha_{y,\tilde{y}}$. Hence, the PS requirement of having sizable $\alpha_{y,\tilde{y}}$ in both models is not in conflict with SMEFT bounds. We recall that more dimension six operators than (6.14) are switched on due to RG running [101, 103, 104] between the NP and EW scale, see Sec. 2.5. However, these contributions are neglected due to the loop suppression and the proximity of the NP scale $\mu_0 \simeq 1$ TeV to the electroweak scale.

The most constraining numerical fit results for $C_{Hq,qH}^{ii}$ along with the resulting constraints on our model parameters $\alpha_{\hat{\kappa}}/M_F^2$ are given in Tab. 6.1. In [177] 31 WCs where fitted simultaneously without assuming any BSM flavor symmetry. Thus, the limits are quite robust and can be applied in both models. For model L, in accordance with (6.4) we also take into account the top-specific fit [178] with $SU(2)^2 \times SU(3)^3$ flavor symmetry including 34 WCs.

For model M, comparing limits from [177] with (6.15) yields

$$\frac{\alpha_{\kappa}}{M_F^2[\mathrm{TeV}^2]} \lesssim 3.7 \cdot 10^{-2}, \quad \frac{\alpha_{\widetilde{\kappa}}}{M_F^2[\mathrm{TeV}^2]} \lesssim 1.3 \cdot 10^{-2} \tag{6.16}$$

at 90% c.l.. For the scenario $M_F \simeq \mu_0 \simeq 1$ TeV the constraints presented above are weaker than but in agreement with those from PS (6.12) in large parts of the BSM critical surface. In particular, SMEFT and PS bounds for the vacuum configuration V^+ can always be conveniently fulfilled by imposing sufficiently

---

[2] We computed the WCs using [102]. We also explicitly checked that the expressions (6.15) for $C_{Hq,qH}$ coincide with the ones from [206] in the basis [100], as well as the generalization of the expressions in [178, 207] for one generation of ψ.

small values of $\alpha_{\kappa,\widetilde{\kappa}}(\mu_0)$. On the other hand, for $M_F \simeq \mu_0 \simeq 1$ TeV the fit clearly excludes values of $\alpha_{\widetilde{\kappa}}(\mu_0) \gtrsim 0.3$ which are necessary to realize the vacuum configuration V^- at the Planck scale. However, the bounds (6.16) can still be fulfilled along with the V^- condition in (6.12) by assuming heavier new physics. Combining the PS conditions with the fit bounds yields

$$M_F \gtrsim 4.8 \text{ TeV} \tag{6.17}$$

at 90% c.l. which is well beyond current experimental limits, see Subsec. 6.3.4. Hence, we do not analyze this possibility in more detail.

We now briefly repeat the SMEFT analysis for model L. We obtain the bounds

$$\frac{\alpha_\kappa}{M_F^2[\text{TeV}^2]} \lesssim 1.6 \cdot 10^{-3}\ (7.8 \cdot 10^{-4}), \qquad \frac{\alpha_{\widetilde{\kappa}}}{M_F^2[\text{TeV}^2]} \lesssim 6.2 \cdot 10^{-2}\ (1.0 \cdot 10^{-2}) \tag{6.18}$$

at 90 % c.l., which are extracted from the full [177] (single WC [178]) fit via (6.15). The $\alpha_\kappa(\mu_0)$ condition in (6.18) can always be conveniently fulfilled in accord with the PS bound (6.13) by choosing $\alpha_\kappa(\mu_0)$ sufficiently small. However, for $M_F \simeq \mu_0 \simeq 1$ TeV, the full (single WC) $\alpha_{\widetilde{\kappa}}(\mu_0)$ bound (6.18) is clearly (slightly) excluded by the PS constraint (6.13) requiring $\alpha_{\widetilde{\kappa}}(\mu_0) \gtrsim 0.15$. When allowing for heavier VLQs, the full (single WC) bounds can be fulfilled if

$$M_F \gtrsim 1.6 \text{ TeV } (3.9 \text{ TeV}). \tag{6.19}$$

The full fit mass bound is of the order of current experimental limits which are in the range of 0.9 – 1.5 TeV (see e.g. [208–210] for details) and motivates dedicated searches. However, it constitutes a very optimistic estimate of the minimal VLQ mass scale, as in our model just three out of the 34 WCs included in the fit are induced, so that the single WC fit bound in (6.19) seems actually more realistic. As this is well beyond current limits, we do not consider model L in the following analysis of collider phenomenology.

6.3.2 Fermionic Mixing

After EWSB, the two $SU(2)_L$ components of each VLQ ψ_i in model M are rearranged into two Dirac fermions with different electric charges via $\psi_i = (\psi^{-1/3}, \psi^{-4/3})_i$. The Yukawa portal $\hat{\kappa}$ then induces mass mixing between $\psi^{-1/3}$ and SM down-type quarks d_i. Defining

$$\mathcal{D}_i \equiv (d^{-1/3}, \psi^{-1/3}, \psi^{-4/3})_i \tag{6.20}$$

the relevant mass terms read[3]

$$-\mathcal{L}_{m_\mathcal{D}} = \bar{\mathcal{D}}_{i_L} \mathcal{M}^{\mathcal{D}}_{ij} \mathcal{D}_{j_R} + \text{h.c.}, \qquad \text{with} \qquad \mathcal{M}^{\mathcal{D}}_{ij} = \begin{pmatrix} \frac{v_h}{\sqrt{2}} Y_d & 0 & 0 \\ \frac{v_h}{\sqrt{2}} \hat{\kappa} & M_F & 0 \\ 0 & 0 & M_F \end{pmatrix}_{ij} . \tag{6.21}$$

We assume the CKM rotation to be entirely in the up-sector, hence Y_d is diagonal. This choice naturally avoids inter-generational mixing which is severely constrained by hadronic FCNC processes. After

---

[3] The exotically charged $\psi^{-4/3}$ does not take part in the mixing but is included in $\mathcal{D}$ for later convenience.

diagonalizing $\mathcal{M}^{\mathcal{D}}$ we obtain the rotated mass eigenstates

$$\mathcal{D}'_i = O_{i_{L,R}} \mathcal{D}_i , \qquad \text{with} \qquad O_{i_{L,R}} = \begin{pmatrix} \cos\theta_{i_{L,R}} & -\sin\theta_{i_{L,R}} & 0 \\ \sin\theta_{i_{L,R}} & \cos\theta_{i_{L,R}} & 0 \\ 0 & 0 & 1 \end{pmatrix} , \tag{6.22}$$

which is governed by the six mixing angles

$$\tan\theta_{i_L} = \tfrac{1}{2} y_{d_i} \hat{\kappa}_i \left(\frac{v_h}{M_F}\right)^2 + \mathcal{O}\left(\frac{v_h}{M_F}\right)^4 , \qquad \tan\theta_{i_R} = \frac{1}{\sqrt{2}} \hat{\kappa}_i \left(\frac{v_h}{M_F}\right) + \mathcal{O}\left(\frac{v_h}{M_F}\right)^3 , \tag{6.23}$$

where we assumed universal M_F. The RH mixing angles θ_{i_R} are much more sizable than the LH ones as the latter are suppressed by an additional tiny factor m_{d_i}/M_F. Rotating the weak interaction Lagrangians $\mathcal{L}_Z$ and $\mathcal{L}_W$ to the mass basis gives rise to mixing terms between the VLQs and SM quarks. In particular, one obtains

$$\mathcal{L}_W \supset -\frac{g}{\sqrt{2}} W^-_\mu \bar{\psi}'^{4/3}_i \gamma^\mu \left(\sin\theta_{i_L} P_L + \sin\theta_{i_R} P_R\right) d'_i + \frac{g}{\sqrt{2}} V_{ij} W^-_\mu \left(\bar{\psi}'^{1/3}_i \gamma^\mu \sin\theta_{Li} P_L u'_j\right) , \tag{6.24}$$

$$\mathcal{L}_Z \supset -\frac{g}{2\cos\theta_W} Z_\mu \bar{\psi}'^{1/3}_i \gamma^\mu \left(\sin 2\theta_{i_L} P_L + \frac{\sin 2\theta_{i_R}}{2} P_R\right) d'_i . \tag{6.25}$$

6.3.3 BSM Sector Decay

We now work out the decay modes of the VLQs. The exotically charged $\psi_i^{-4/3}$ can cascade down through the weak interaction via $\psi^{-4/3} \to \psi_i^{-1/3} W^{-*}$ and subsequent W^- decays. The decay is driven by the tiny mass splitting $\Delta M = 0.57$ GeV due to EW gauge boson loops, which is obtained from [211]. The corresponding decay width is heavily suppressed and reads

$$\Gamma(\psi^{-4/3} \to \psi_i^{-1/3} W^{-*} \to \psi_i^{-1/3} \ell^- \bar{\nu}) \simeq \frac{G_F^2}{15\pi^3} (\Delta M)^5 , \tag{6.26}$$

where we expanded in ΔM. If no other decay modes are available, the $\psi^{-4/3}$ is long lived with a lifetime $\tau = \frac{\hbar}{\Gamma}$ of 37 ps corresponding to $c\tau \simeq 1.1$ cm which gives rise to displaced vertex signatures at the LHC. However, for $\hat{\kappa} \neq 0$, fermionic mixing also enables the decay $\psi_i^{-4/3} \to d_i W^-$ with a width of

$$\Gamma(\psi_i^{-4/3} \to d_i W^-) = \frac{\pi\alpha_2}{4} M_F \left(\sin^2\theta_{i_L} + \sin^2\theta_{i_R}\right) \left(1 - \tfrac{m_W^2}{M_F^2}\right)^2 \left(2 + \tfrac{M_F^2}{m_W^2}\right) + \mathcal{O}\left(\frac{m_{d_i}^2}{M_F^2}\right) . \tag{6.27}$$

For TeV-ish VLQs this decay mode is completely dominating and results in a prompt decay unless the Yukawa portal coupling is extremely feeble with $\alpha_{\hat{\kappa}} \lesssim 10^{-14}$.

The $\psi^{-1/3}$ can decay via the $\hat{\kappa}$-Yukawas as $\psi_i^{-1/3} \to d_i h$. Moreover, there are decay modes induced from fermionic mixing as $\psi_i^{-1/3} \to u_j W^-$ and $\psi_i^{-1/3} \to d_i Z$. If kinematically open also $\psi_i^{-1/3} \to d_j \hat{S}_{ij}$ is possible. The respective decay widths are

$$\Gamma(\psi_i^{-1/3} \to d_i h) = \frac{\pi\alpha_{\hat{\kappa}}}{4} M_F \left(1 - \frac{m_h^2}{M_F^2}\right)^2 , \tag{6.28}$$

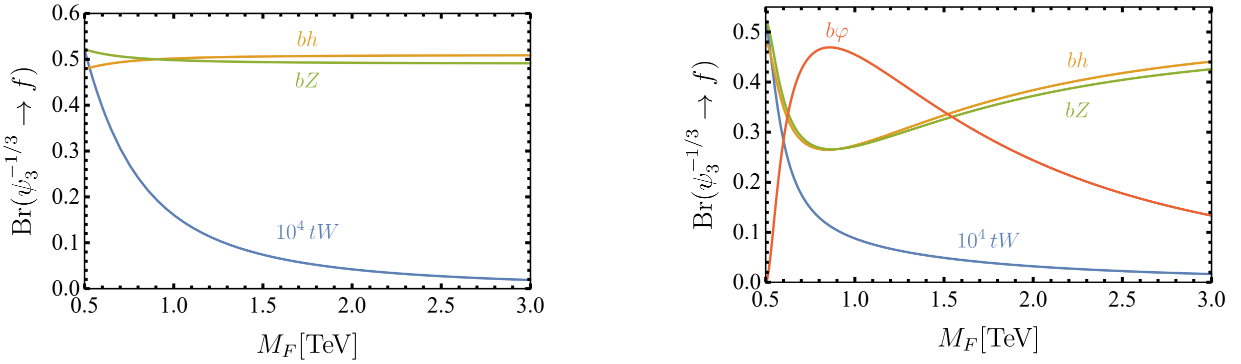

(a) $M_F < M_{\hat{S}}$.

(b) $M_F > M_{\hat{S}}$ for $M_{\hat{S}} = 0.5$ TeV and $\alpha_y = 0.3$.

Figure 6.5: Tree-level branching ratios of the different VLQ $\psi_3^{-1/3}$ decay modes as a function of the BSM fermion mass M_F where the decay $\psi_3^{-1/3} \to b\varphi$ is either kinematically forbidden (a) or open (b). Note that $\mathcal{B}(\psi_3^{-1/3} \to tW^-)$ is rescaled by an additional factor 10^4.

$$\Gamma(\psi_i^{-1/3} \to u_j W^-) = \frac{\pi\alpha_2}{4} M_F |V_{ij}|^2 \sin^2\theta_{i_L} \left(1 - \frac{m_W^2}{M_F^2}\right)^2 \left(2 + \frac{M_F^2}{m_W^2}\right)\,, \tag{6.29}$$

$$\Gamma(\psi_i^{-1/3} \to d_i Z) = \frac{\pi\alpha_2}{8\cos^2\theta_W} M_F \left(\sin^2 2\theta_{i_L} + \frac{\sin^2 2\theta_{i_R}}{4}\right) \left(1 - \frac{m_Z^2}{M_F^2}\right)^2 \left(2 + \frac{M_F^2}{m_Z^2}\right)\,, \tag{6.30}$$

$$\Gamma(\psi_i^{-1/3} \to d_j \hat{S}_{ij}) = \frac{\pi\alpha_{\hat{y}}}{2} M_F \cos^2\theta_{i_L} \sin^2\theta_{j_R} \left(1 - \frac{M_{\hat{S}}^2}{M_F^2}\right)^2\,, \tag{6.31}$$

where in (6.31) there is no summation over j and we made use of (6.24), (6.25). Interestingly, the weak interaction decay rates are kinematically enhanced with $M_F^2/m_{W,Z}^2$. Branching ratios for the different $\psi^{-1/3}$ decay modes are plotted in Fig. 6.5 as a function of M_F. In the small angle approximation (6.23) the branching ratios are independent of $\alpha_{\hat{\kappa}}$. Moreover, to good accuracy it holds $\mathcal{B}(\psi_i^{-1/3} \to d_i Z) \approx \mathcal{B}(\psi_i^{-1/3} \to d_i h) \approx 50\%$. The decay $\psi_i^{-1/3} \to u_j W^-$ in comparison is strongly suppressed with $|V_{ij}|^2 \sin^2\theta_{j_L} / \sin^2\theta_{i_R} \propto |V_{ij}|^2 (m_{d_i}/M_F)^2 \lesssim \mathcal{O}(10^{-4})$ and therefore negligible. Lower- and inter-generational decays of $\psi_i^{-1/3} \to u_j W^-$ are even further CKM- and down-quark mass suppressed. Note that the first two generations can decay as $\psi_i^{-1/3} \to d_j S_{ij}$ with $i,j = 1,2$, i.e. to two different final states involving SM scalars. Hence, the corresponding branching ratio is a factor two larger than $\psi_3^{-1/3} \to b\varphi$.

If kinematically allowed, the BSM scalars $\hat{S}_{ij}$ decay via the sizeable BSM Yukawa $\alpha_{\hat{y}}$ to VLQ pairs $\bar{\psi}_i \psi_j$ and to $\bar{\psi}_i d_j, \bar{d}_i \psi_j, \bar{d}_i d_j$ via fermionic mixing. Rewriting the BSM Yukawa term (6.7) in terms of the (pseudo-)scalar component $\hat{S}_{ij}^{s(p)}$

$$\hat{S}_{ij}^s = \frac{1}{2}\left(\hat{S}_{ij} + \hat{S}_{ji}^*\right) \quad \text{and} \quad \hat{S}_{ij}^p = -\frac{i}{2}\left(\hat{S}_{ij} - \hat{S}_{ji}^*\right)\,, \tag{6.32}$$

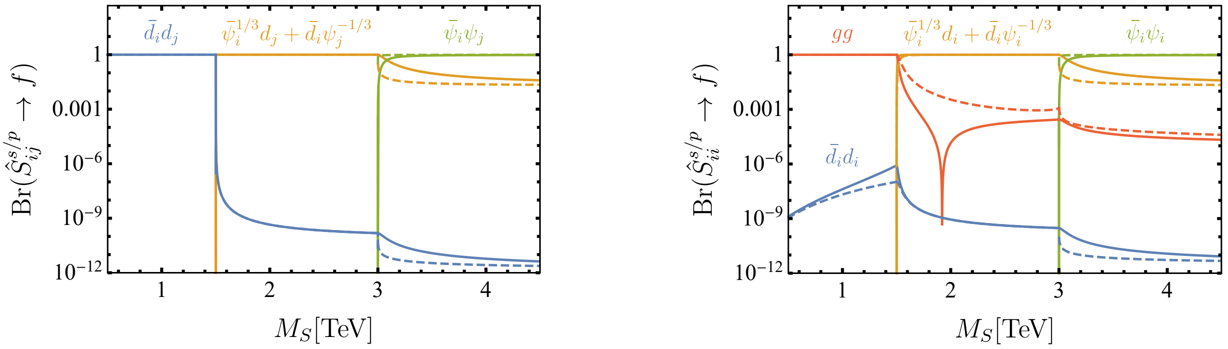

(a) off-diagonal S_{12}.

(b) diagonal S_{22}.

Figure 6.6: Branching ratios for dominant decay modes of off-diagonal (a) and diagonal (b) components of the BSM scalar $\hat S_{ij}$. Solid (dashed) lines correspond to (pseudo-)scalar components $\hat S^s_{ij}$ ($\hat S^p_{ij}$). We fixed $\alpha_\kappa = 0.02$ and $M_F = 1.5$ TeV close to recent bounds. The dependence on $\alpha_{\hat y}$ completely cancels in the branching ratios. It holds $\mathcal{B}(\hat S_{ij}^{s/p}\to \bar d_i\psi_j^{-1/3}) \approx \mathcal{B}(\hat S_{ij}^{s/p}\to \bar\psi_i^{1/3}d_j)$ as well as $\mathcal{B}(\hat S_{ij}^{s/p}\to \bar\psi_i^{1/3}\psi_j^{-1/3}) \approx \mathcal{B}(\hat S_{ij}^{s/p}\to \bar\psi_i^{4/3}\psi_j^{-4/3})$. Note that in the regime $M_S < M_F$ for diagonal components $S_{ii}^{s,p}$ the 1-loop decay to gluons is dominant over the fermionic decay.

as well as the fermions $\mathcal{D}$ (6.20) and rotating to the fermion mass basis via (6.22) yields

$$-\mathcal{L}_Y^{\rm BSM} = \hat y\bar{\mathcal{D}}'_i\Big(\hat S^s_{ij}(X_{ij}P_R+X^\dagger_{ij}P_L)+i\hat S^p_{ij}(X_{ij}P_R-X^\dagger_{ij}P_L)\Big)\mathcal{D}'_j,\quad X_{ij}=\begin{pmatrix} s_{i_L}s_{j_R} & s_{i_L}c_{j_R} & 0\\ c_{i_L}s_{j_R} & c_{i_L}c_{j_R} & 0\\ 0 & 0 & 1\end{pmatrix}, \tag{6.33}$$

where $s_{i_{L,R}} = \sin\theta_{i_{L,R}}$, $c_{i_{L,R}} = \cos\theta_{i_{L,R}}$. The scalar decay width then in agreement with [46] reads

$$\begin{aligned}\Gamma(\hat S_{ij}^{s/p}\to\bar{\mathcal{D}}_i'^{\alpha}\mathcal{D}_j'^{\beta}) =&\pi N_C\alpha_{\hat y}M_{\hat S}\big[(X_{\alpha\beta}^2+X_{\beta\alpha}^2)(1-r_{i,\alpha}^2-r_{j,\beta}^2)-4\xi_{s/p}X_{\alpha\beta}X_{\beta\alpha}r_{i,\alpha}r_{j,\beta}\big]\\ &\cdot\sqrt{1+r_{i,\alpha}^4+r_{j,\beta}^4-2r_{i,\alpha}^2-2r_{j,\beta}^2-2r_{i,\alpha}^2r_{j,\beta}^2}\;\Theta(1-r_{i,\alpha}-r_{j,\beta})\,,\end{aligned} \tag{6.34}$$

where $r_{\alpha,i/\beta,j} = M_{\mathcal{D}'^{\alpha/\beta}_{i/j}}/M_{\hat S}$, $\alpha,\beta = 1,2,3$ are field component indices of $\mathcal{D}$ and $\xi_{s[p]} = +1\,[-1]$. Depending on the BSM mass hierarchy not all decay channels may be kinematically open. The branching ratios for the different fermionic decay modes are plotted in Fig. 6.6. As soon as kinematically allowed, the decays to ψ' rather than d' final state fermions become almost instantly dominant. This is due to the suppression of decays to SM quarks by small mixing angles.

For large $\alpha_y \gtrsim 10^{-1}$ as required for PS and $M_{\hat S} > 2M_F$ the BSM scalars decay promptly. The same holds true for $M_F < M_{\hat S} < 2M_F$ unless κ is very feeble with $\alpha_\kappa \lesssim \mathcal{O}(10^{-13})$. In the scenario where $M_{\hat S} < M_F$ the scalar decay to down-type quarks is doubly mixing suppressed which for weak $\alpha_\kappa \lesssim \mathcal{O}(10^{-4})$ can lead to displaced vertex signatures of off-diagonal components that can be searched for at the LHC.

The diagonal components $\hat S_{ii}$ on the other hand can also decay to pairs of SM gauge bosons via BSM fermion triangle loops. The corresponding decay widths to two electroweak bosons GG' and to gluons gg

read [42, 46]

$$\Gamma(\hat{S}_{ii}^{s/p}\to GG') = \frac{N_C\alpha_e^2\alpha_{\hat{y}}}{16\pi}\frac{M_{\hat{S}}^3}{M_F^2}\left|C_{GG'}A_{s/p}\left(\tfrac{M_{\hat{S}}^2}{4M_F^2}\right)\right|^2, \quad \Gamma(\hat{S}_{ii}^{s/p}\to gg) = \pi\alpha_3^2\alpha_{\hat{y}}\frac{M_{\hat{S}}^3}{M_F^2}\left|2\sqrt{2}A_{s/p}\left(\tfrac{M_{\hat{S}}^2}{4M_F^2}\right)\right|^2 . \tag{6.35}$$

The non-vanishing coefficients $C_{GG'}$ in the limit $M_{\hat{S}} \gg m_{W,Z}$ are given as

$$\begin{aligned} C_{\gamma\gamma} &= \frac{17}{9}, & C_{ZZ} &= \frac{1}{2}\tan^{-2}\theta_W + \frac{25}{18}\tan^2\theta_W, \\ C_{WW} &= \frac{1}{\sqrt{2}\cos^2\theta_W}, & C_{Z\gamma} &= \sqrt{2}\left(\frac{\tan^{-1}\theta_W}{2} - \frac{25}{18}\tan\theta_W\right) \end{aligned} \tag{6.36}$$

and it holds

$$A_{s/p}(\tau) = \frac{2}{\tau^2}(\xi_{s/p}\tau + (\tau - \xi_{s/p})f(\tau)) \quad \text{with} \quad f(\tau) = \begin{cases} \arcsin(\sqrt{\tau}), & \tau \le 1 \\ -\frac{1}{4}\left(\ln\frac{1+\sqrt{1-\tau^{-1}}}{1-\sqrt{1-\tau^{-1}}} - i\pi\right)^2, & \tau > 1 \end{cases}. \tag{6.37}$$

We find that the decay to gluons dominates over decays to EW bosons due to the relative enhancement factor $(4\pi\alpha_3)^2/(N_c\alpha_e^2) \approx 41$ for $M_F \simeq M_{\hat{S}} = 1$ TeV. For the full diboson decay hierarchy we then find $\Gamma_{gg} \gg \Gamma_{ZZ} \gtrsim \Gamma_{\gamma\gamma} > \Gamma_{WW} > \Gamma_{Z\gamma}$. Interestingly, in the regime $M_{\hat{S}} < M_F$, the 1-loop decay to gluons is dominant over the fermionic decay (cf. Fig. 6.6). Furthermore, the diagonal components of $\hat{S}_{ii}$ acquiring a VEV can decay via scalar mixing described in App. C, to all kinematically open final states of a Higgs boson decay. For $M_{\hat{S}} > 2M_H$, also a decay to two Higgs bosons is possible.

6.3.4 Collider Bounds

Our model implies characteristic signatures at colliders which result in bounds on our model parameters. The presence of the $SU(2)_L$ and $U(1)_Y$ charged VLQs modifies the running of $\alpha_{1,2}$ which impacts the EW precision parameters Y, W defined in (4.14). At 1-loop, using LEP data [172] results in the relatively weak mass bound

$$M_F \gtrsim 365 \text{ GeV} . \tag{6.38}$$

In contrast to VLL models [46], bounds can be also derived from the running of α_3. It has been found to be consistent with the SM in various measurements by CMS [212, 213] and ATLAS [171, 214, 215] exploring scales of up to $\mu = 4$ TeV [171, 215]. A fit of the SM running against the latter is found in Fig. 6.7. All data are well contained within the uncertainty, and the central value lies very close to the world average fit [216]. We also show α_3 running in our BSM model with feeble or weak BSM Yukawas for comparison, where the matching was performed such that deviations from the fit band occur at 1.5 TeV or 4 TeV. From the latter we can estimate the minimal NP scale $\mu_0 \sim M_F$ yielding a lower bound

$$M_F \gtrsim 650 \text{ GeV} \tag{6.39}$$

on the VLQ mass, which is still sub-TeV but stronger than (6.38) from $\alpha_{1,2}$ running.

If not too heavy, VLQs and BSM scalars can also be singly and pair produced in various processes at colliders. A selection of corresponding tree-level Feynman diagrams is given in Fig. 6.8. We now briefly summarize the most relevant direct detection bounds on our model from VLQ searches by ATLAS [217–220] and CMS [221–225].

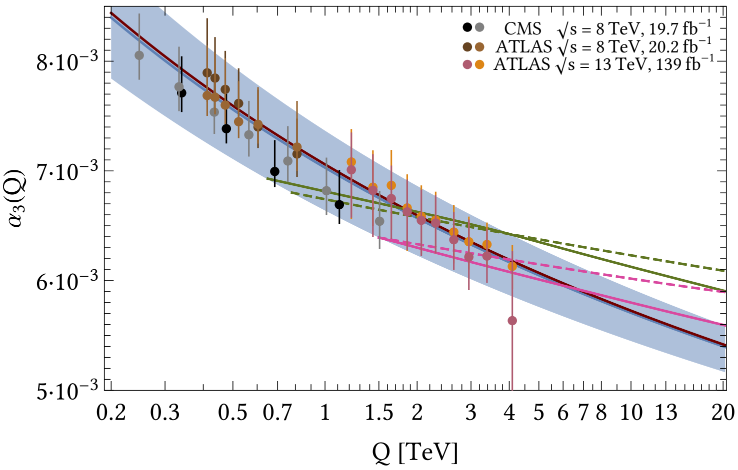

Figure 6.7: Running of the strong coupling constant $\alpha_3(Q)$. Dots correspond to experimental determinations by CMS [212] (black) and [213] (gray) as well as ATLAS [214] (light and dark brown) and [171, 215] (orange and purple). The blue curve and its shaded error region correspond to the SM fitted against the latest ATLAS data [171, 215]. The result is in very good agreement with SM running using the world average [216] (red curve). Green and pink curves represent the running of α_3 in our model for feeble BSM couplings of 10^{-10} (dashed lines) or $\alpha_{\tilde{\kappa}}(Q) = 10^{-4}$ and $\alpha_{\hat{y}}(Q) = 0.2$ (solid lines). The curves are matched to the upper end of the fit uncertainty band at the scale $Q = 4$ TeV (green) and the lower one at $Q = 1.5$ TeV (pink), respectively.

Most analyses [218–221, 223–225] assume only one VLQ generation that mixes exclusively with third generation SM quarks and hence search for final states involving t or b quarks. In these works the VLQ doublet $(\psi^{-1/3}, \psi^{-4/3})$ is denoted by (B, Y). As in our models inter-generational mixing is extremely suppressed (cf. Subsec. 6.3.2), the experimental results are only applicable for $\psi_3^{-1/3}$ and $\psi_3^{-4/3}$, while the properties of $\psi_{1,2}$ are hardly constrained at all. Furthermore, in searches for B it was assumed that $\mathcal{B}(B \to tW) + \mathcal{B}(B \to bh) + \mathcal{B}(B \to bZ) = 100\%$. Hence, the limits on M_B only apply to $\psi_3^{-1/3}$ if $\mathrm{Br}(\psi_3^{-1/3} \to b\hat{S}) = 0$, i.e. if $M_{\hat{S}} > M_{\psi_3^{-1/3}}$[4], and are lowered otherwise. The best limits are $M_Y \geq 1350$ GeV [218] and $M_B \geq 1450$ GeV [225][5]. Recall that in our model the mass splitting within a VLQ doublet is negligible, thus mass bounds for $\psi^{-4/3}$ also apply for $\psi^{-1/3}$ independent of the BSM VLQ to scalar mass hierarchy.

In [220] constraints on the dominant mixing angle θ_{3_R} were derived from single B VLQ production. In our model, these yield upper limits on $\alpha_{\tilde{\kappa}}$ as a function of the VLQ mass, cf. (6.23). For $M_B = 800$ GeV, the upper limit $\alpha_{\tilde{\kappa}} \lesssim 4 \cdot 10^{-3}$ is of order of the V^+ PS bound (6.12). On the other hand, the V^- condition in (6.12) is excluded in the whole analyzed mass range of $800 \leq M_B \leq 1800$ GeV, in agreement with the SMEFT results in Subsec. 6.3.1.

In contrast to the mentioned works, the searches [217, 222] focus on a single VLQ generation that couples only to light quarks. In particular, in [217] a VLQ Q with electric charge $-4/3$ decaying exclusively into a W boson and a light down-type quark d, s was assumed. A lower mass bound $M_Q > 690$ GeV was

---

[4] Note that $\mathcal{B}(\psi_3^{-1/3} \to b\hat{S}) = 0$ can also be achieved by $\alpha_{\tilde{y}} = 0$. This scenario is however excluded from PS.

[5] According to the branching ratio predictions in our model Fig. 6.5 we always quote the bounds on M_B for $\mathcal{B}(B \to bh) = \mathcal{B}(B \to bZ) = 50\%$ assuming $\mathrm{Br}(\psi_3^{-1/3} \to b\hat{S}) = 0$.

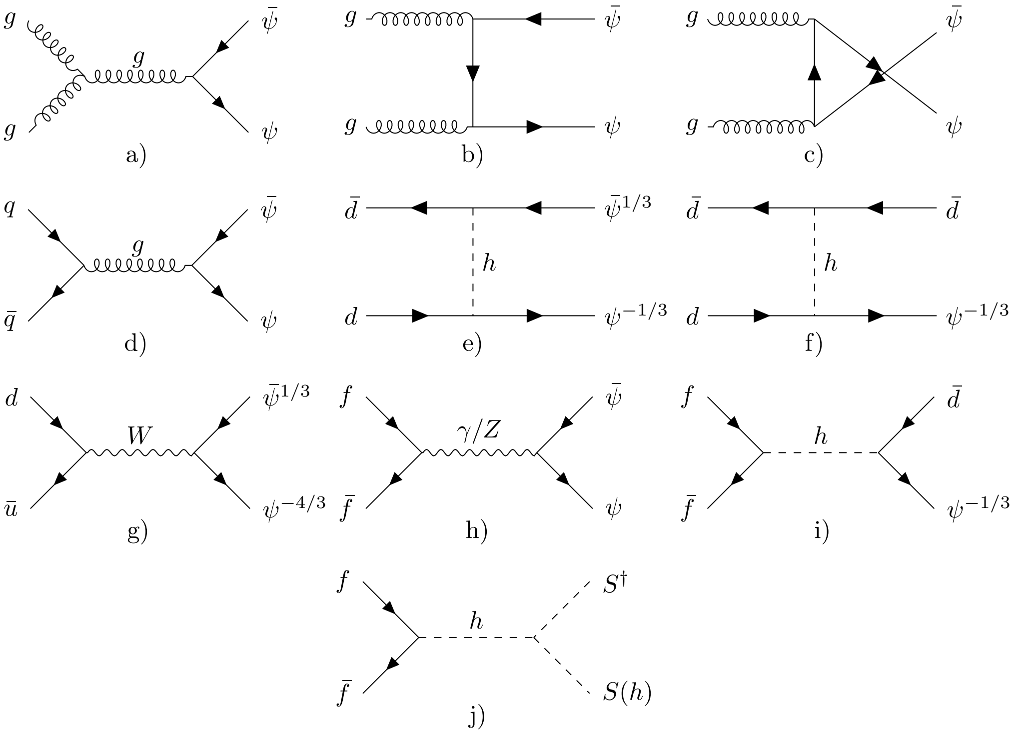

Figure 6.8: Tree-level diagrams for BSM sector production at hadron colliders. For the VLQs ψ, pair production via gluon fusion (diagrams a)-c)) as well as quark anti-quark fusion to an s-channel gluon (diagram d)) are the dominant production mechanisms at hadron machines. Moreover, single and pair production of $\psi^{-1/3}$ via t-channel Higgs (diagrams e)-f)) are possible via the BSM Yukawa coupling $\hat\kappa$. Pair production via s-channel W (diagram g)) is also possible at hadron colliders. At hadronic and leptonic machines, VLQs can finally be pair produced in fermion-antifermion fusion to s-channel γ, Z or Higgs (diagrams h)-i)). The BSM scalars $\hat S_{ij}$ can be singly and pair produced in fermion-antifermion fusion to s-channel Higgs via the portal coupling $\hat\delta$ (diagram j)). Moreover, BSM scalars are produced via scalar mixing with the Higgs and in $\psi^{-1/3}$ decays (not shown).

derived which also applies for $\psi_{1,2}^{-4/3}$. Note however that in our model we have two generations of VLQs coupling (mainly) to the first and second-generation quarks. Hence, for $M_{\psi_1^{-4/3}} = M_{\psi_2^{-4/3}}$ the resulting mass bound is stronger, as the total VLQ production cross section at parton level is enhanced by a factor of two. In [222] a search for a VLQ D was presented with electric charge $-1/3$ decaying into light quarks. Assuming pair production and $\text{Br}(D \to qZ) = \text{Br}(D \to qh) = 50\%$ with $q = d,\, s$ yields a mass bound $M_D > 570$ GeV which is applicable to $\psi_{1,2}^{-1/3}$. Again, the real $M_{\psi_{1,2}^{-1/3}}$ bound is lowered if the decay $\psi_{1,2}^{-1/3} \to qS$ is kinematically allowed but might also be stronger due to the factor two enhanced parton level production cross section.

Putting everything together we finally obtain the combined VLQ mass bounds

$$M_{\psi_{1,2}} \lesssim 690 \text{ GeV}, \qquad M_{\psi_3} \geq \begin{cases} 1450 \text{ GeV}, & M_{\psi_3} \leq M_{\hat S} \\ 1350 \text{ GeV}, & M_{\psi_3} > M_{\hat S} \end{cases}, \tag{6.40}$$

which are dominated by the direct searches.

6.4 Summary

In this chapter we demonstrated that PS can be realized in complex BSM models featuring VLQs and flavorful singlet matrix scalars. We focused on $N_F = 3$ generations of TeV-ish VLQs in the representations $(\mathbf{3}, \mathbf{2}, -\frac{5}{6})$ (model M) and $(\mathbf{3}, \mathbf{2}, \frac{7}{6})$ (model L). To consistently account for sizeable SM Yukawas $y_{t,b}$ in the RG flow, also third generation BSM couplings have to be treated separately from first and second generations ones. This implies a high-dimensional parameter space featuring ten a priori free BSM couplings and gives rise to rather interconnected RG dynamics. We found that large values of the new, pure BSM Yukawa coupling $\alpha_{\hat{y}} \gtrsim \mathcal{O}(10^{-1})$ are key to PS by preventing a subplanckian hypercharge Landau pole. In the pole-free parts of the parameter space, the known gauge and Yukawa portal mechanisms as well as the direct and indirect Higgs portal mechanism can then all together push the Higgs towards stability, where the dominant mechanism is determined by the BSM coupling values. Interestingly, Model M allows for PS in both vacuum configurations $V^{\pm}$, whereas in model L the BSM critical surface is generically tighter and only V^+ is realized at M_{Pl}.

Matching our models to SMEFT implies upper limits on $\alpha_{\hat{\kappa}}/M_F^2$. While PS in V^+ in model M is compatible with SMEFT bounds, for $M_F \simeq 1\,\mathrm{TeV}$ PS is completely excluded in model L as well as for V^- in model M. This demonstrates how PS can guide model building. We then analyzed the collider phenomenology of model M in V^+. Firstly, by comparing BSM running of gauge couplings with LHC measurements we derived VLQ mass bounds of a few 100 GeV. If not too heavy, VLQs are also directly singly and pair produced at hadron machines and decay via the Yukawa portal coupling or fermionic mixing to SM down-type quarks and bosons. Corresponding experimental searches yield lower VLQ mass bounds of up to 1450 GeV. If $M_F > M_{\hat{S}}$, also the decay $\psi^{-1/3} \to dS$ is possible providing novel signatures that can be searched for at LHC. In particular, the subsequent BSM scalar decay via the sizeable BSM Yukawa $\alpha_{\hat{y}}$ to $\bar{d}d$ or gluons provide characteristic triple-jet final states, which are not included in present experimental analyses and invite dedicated study.

Several interesting aspects are still to be analyzed in the future. First of all, it would be desirable to scrutinize the complete high-dimensional model parameter space more rigorously. Moreover, it would be interesting to quantify the impact of our findings from Chap. 4 and Chap. 5 e.g. regarding varying BSM masses and multiplicities on PS. Finally, a full phenomenological analysis based on the scalar mixing between all three scalar fields would be desirable to explore the complex phenomenology of the scalar sector.

7 Interlude: Anomaly-free $U(1)^{\prime}$ Models for Flavor Anomalies

So far, we have restricted our PS analyses to minimal SM extensions by VLFs and flavorful scalars. In the remainder of this theis we want to apply the gained knowledge in the context of a more complex class of BSM models, namely flavorful $U(1)'$ models. In doing so, the main challenge from the RG point of view is the generic Landau pole of the abelian BSM gauge coupling which has to be assured to appear sufficiently far in the UV, c.f. (3.6). Phenomenologically on the other hand flavorful $U(1)'$ models are natural candidates to explain several experimentally observed anomalies in the flavor sector[1] and therefore subject to very active research, e.g. [58–61]. In such models we enlarge the SM gauge group with an additional $U(1)'$ gauge symmetry with generation-dependent charges F_{X_i} for the SM fermions $X = Q, U, D, L, E$ as well as potentially three BSM RH neutrinos $X = \nu$. The $U(1)'$ interaction is then mediated by a massive Z' boson which acquires its mass from a $U(1)'$ breaking SM-singlet scalar ϕ with $U(1)'$ charge $F_\phi \neq 0$.

In this chapter we review some generic features of flavorful $U(1)'$ models. We start with discussing the cancellation of gauge anomalies in Sec. 7.1 as well as gauge kinetic mixing in Sec. 7.2. Afterwards, we focus on the generation of tree-level FCNC couplings from gauge to mass basis rotations in Sec. 7.3 before turning to meson mixing and Z' decays in Sec. 7.4 and Sec. 7.5, respectively.

7.1 Anomaly Cancellation

Fermionic $U(1)'$ charge assignments are constrained by gauge anomaly cancellation conditions (ACCs), see [170] for a comprehensive review. The ACCs assure that triangle diagrams with three external gauge bosons and an internal chiral fermion loop exactly vanish. This is necessary as divergences originating from such diagrams cannot be absorbed in counter-terms in the process of renormalization and hence spoil the consistency of the underlying QFT. In the SM all gauge anomalies cancel generation-wise. In the absence of SM-charged BSM fermions this still holds for all triangle diagrams involving only SM gauge bosons. Demanding anomaly cancellation also in diagrams involving at least one external $U(1)'$ gauge boson on the other hand implies six conditions on the $U(1)'$ charges of SM fermions and RH neutrinos, namely [59]

$$\begin{aligned}
SU(3)_C^2 \times U(1)' : &\quad \sum_{i=1}^{3} \left[2F_{Q_i} - F_{U_i} - F_{D_i}\right] = 0\,,\\
SU(2)_L^2 \times U(1)' : &\quad \sum_{i=1}^{3} \left[3F_{Q_i} + F_{L_i}\right] = 0\,,\\
U(1)_Y^2 \times U(1)' : &\quad \sum_{i=1}^{3} \left[F_{Q_i} + 3F_{L_i} - 8F_{U_i} - 2F_{D_i} - 6F_{E_i}\right] = 0\,,\\
\text{gauge-gravity} : &\quad \sum_{i=1}^{3} \left[6F_{Q_i} + 2F_{L_i} - 3F_{U_i} - 3F_{D_i} - F_{E_i} - F_{\nu_i}\right] = 0\,,\\
U(1)_Y \times U(1)'^2 : &\quad \sum_{i=1}^{3} \left[F_{Q_i}^2 - F_{L_i}^2 - 2F_{U_i}^2 + F_{D_i}^2 + F_{E_i}^2\right] = 0\,,\\
U(1)'^3 : &\quad \sum_{i=1}^{3} \left[6F_{Q_i}^3 + 2F_{L_i}^3 - 3F_{U_i}^3 - 3F_{D_i}^3 - F_{E_i}^3 - F_{\nu_i}^3\right] = 0\,.
\end{aligned} \tag{7.1}$$

---

[1] We focus on two specific flavor anomalies in the next two chapters. In particular we discuss the $b \to s\mu^+\mu^-$ anomalies and the U-Spin-CP anomaly in charm in Subsec. 8.1.1 and Sec. 9.1, respectively.

Here we assumed that the RH neutrinos whose $U(1)'$ charges appear in the gauge-gravity and $U(1)'^3$ ACCs are the only chiral BSM fermions in the theory. Potential vector-like BSM fermions in contrast do not contribute to gauge anomalies. In total, (7.1) imposes six linearly independent conditions on 18 (15) a priori unconstrained fermion charges in models with (without) RH neutrinos, with implications for the RG evolution, cf. Subsec. 8.1.3, and phenomenology [58–60].

Let us briefly comment on some features of the anomaly-free charge assignments studied within this thesis. First of all, we assume all $U(1)'$ charges F_X of fermions and scalars in the model to be rational numbers. Secondly, we stress that $U(1)'$ contributions to physical observables always involve same powers of $U(1)'$ charges F_X and the gauge coupling g_4. Hence all theories that are related via a transformation $F_X \to c\,F_X\ \forall X$, $g_4 \to \frac{g_4}{c}$ for any real constant $c \neq 0$ are equivalent. We make use of this rescaling invariance to fix the largest $U(1)'$ charge as $\max_X |F_X| = 1$ without loss of generality. This choice comes with the advantage that the naive perturbativity limit for the $U(1)'$ coupling $F_X g_4 \lesssim 4\pi$, $\forall X$ simplifies to $\alpha_4 \lesssim 1$ in analogy to the other couplings in the theory. Moreover, we observe that the ACCs (7.1) are invariant under any arbitrary permutation of charge assignments within each individual fermion species. The phenomenology of models in contrast typically changes significantly under such permutations. Hence, in this work we assign the $U(1)'$ charges explicitly for each generation fixed.

7.2 Kinetic Mixing

$U(1)'$ models feature two abelian gauge bosons: the heavy Z' as well as the hypercharge gauge boson. Gauge invariance in this case explicitly allows for the presence of a mixed abelian gauge kinetic term

$$\mathcal{L}_{\text{gauge}} \supset \frac{-1}{4(1-\eta^2)} \begin{pmatrix} B^{\mu\nu} \\ B'^{\mu\nu} \end{pmatrix}^{\top} \begin{pmatrix} 1 & -\eta \\ -\eta & 1 \end{pmatrix} \begin{pmatrix} B_{\mu\nu} \\ B'_{\mu\nu} \end{pmatrix}, \tag{7.2}$$

where $B'^{\mu\nu}$ corresponds to the $U(1)'$ field strength tensor, cf. (2.8). The size of the mixed kinetic term is controlled by the kinetic mixing parameter η, with $|\eta| < 1$, which after EWSB induces Z-Z' mass mixing. If the Higgs was also involved in the $U(1)'$ breaking, additional mixing terms would be generated. However, in this thesis we decouple the electroweak and $U(1)'$ symmetry breaking mechanisms by choosing the Higgs to be uncharged under the $U(1)'$, i.e.

$$F_H = 0\,, \tag{7.3}$$

which evades the presence of further mixing terms.

Kinetic mixing induces corrections to electroweak precision observables such as the ρ parameter

$$\rho = \frac{M_W}{M_Z \cos\theta_W}\,, \tag{7.4}$$

which in the SM at tree-level takes the value $\rho^{\text{SM}} = 1$ due to custodial symmetry. Electroweak precision data on the other hand indicate [155]

$$\frac{\rho - \rho^{\text{SM}}}{\rho} = (3.8 \pm 2.0) \cdot 10^{-4}\,, \tag{7.5}$$

constraining the size of a potential NP contribution. In the presence of kinetic mixing in contrast the modification of the ρ-parameter reads

$$\rho^{-1} = 1 + \frac{\eta^2 \sin^2\theta_W}{1 - z^2} \quad \text{with} \quad z = \left(\frac{M_Z}{M_{Z'}}\right)\Big|_{\eta=0}\,, \tag{7.6}$$

suggesting a deviation from the SM value of opposite sign than the experimental value (7.5). Thus, in absence of cancellations of different origin, kinetic mixing is expected to be subleading at the EW scale $\mu_{\rm EW}$ which roughly translates to the condition

$$|\eta(\mu_{\rm EW})| \lesssim \mathcal{O}(10^{-2})\,. \tag{7.7}$$

Additional constraints arise from corrections of SM fermion X_i couplings to the Z and photon $\propto \eta F_{X_i} g_4$. Again, EW precision data [155] suggest that these corrections are small indicating a small $\eta(\mu_{\rm EW})$ in agreement with (7.7).

The RG evolution of the kinetic mixing parameter is not technically natural. Hence, it is radiatively induced even if set to zero at the NP scale. Nonetheless, its RG growth is diminished in case the 1-loop contribution to its β-function vanishes. This translates to a condition on fermionic $U(1)'$ charges that reads [226]

$$\sum_{i=1}^{3} \sum_{X=Q,U,D,L,E} \left(d_{3,X_i} d_{2,X_i} Y_{X_i} F_{X_i}\right) = \sum_{i=1}^{3} \left(F_{Q_i} - F_{L_i} + 2F_{U_i} - F_{D_i} - F_{E_i}\right) = 0\,. \tag{7.8}$$

7.3 Flavor Rotations

Let us now derive how the Z' couplings to physical fermions are related to the generation-dependent $U(1)'$ charge assignments and the fermionic gauge to mass basis rotations $V^f_{L,R}$ (2.23), see Sec. 2.3 for details. To start, we define the SM fermion $U(1)'$ charge matrices in the gauge basis

$$\mathcal{F}_X = \begin{pmatrix} F_{X_1} & 0 & 0 \\ 0 & F_{X_2} & 0 \\ 0 & 0 & F_{X_3} \end{pmatrix}\,, \tag{7.9}$$

where $X = Q, U, D, L, E$. After EWSB and going to the chiral mass basis we obtain the rotated charge matrices

$$\begin{aligned} \mathcal{F}'_{d_L} &= V_L^{d\dagger} \mathcal{F}_Q V_L^d, & \mathcal{F}'_{d_R} &= V_R^{d\dagger} \mathcal{F}_D V_R^d, \\ \mathcal{F}'_{u_L} &= V_L^{u\dagger} \mathcal{F}_Q V_L^u, & \mathcal{F}'_{u_R} &= V_R^{u\dagger} \mathcal{F}_U V_R^u, \\ \mathcal{F}'_{\ell_L} &= V_L^{\ell\dagger} \mathcal{F}_L V_L^\ell, & \mathcal{F}'_{\ell_R} &= V_R^{\ell\dagger} \mathcal{F}_E V_R^\ell\,, \end{aligned} \tag{7.10}$$

for quarks and charged leptons. Fermion couplings $g^{f_i f_j}_{L,R}$ in the mass basis with $f = u, d, \ell(,\nu)$ are then given by

$$g^{f_i f_j}_{L,R} = g_4 (\mathcal{F}'_{f_{L,R}})_{ij}\,. \tag{7.11}$$

For flavor-universal charge assignments the gauge to mass basis rotations in (7.10) always cancel due to unitarity. Hence, in the SM the rotation matrices $V^f_{L,R}$ are solely constrained by $V_L^{u\dagger} V_L^d = V_{\rm CKM}$ whereas all other rotations are unphysical and therefore arbitrary. However, for generation-dependent charge assignments non-vanishing flavor rotations become observable and induce deviations between the charge matrices in the gauge and mass basis. In particular, the latter can feature tree-level FCNC couplings due to (7.11), which are typically strongly experimentally constrained. In the lepton sector we therefore fix $V^\ell_{L,R} = \mathbb{1}$ which forbids all LFV couplings. In the quark sector in contrast we choose the rotations such that the desired FCNC couplings are induced.

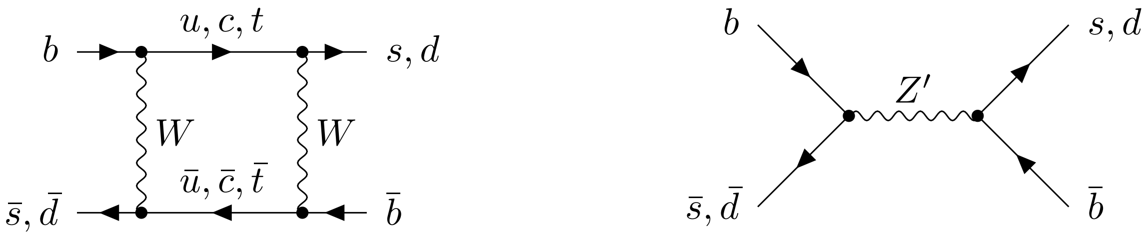

(a) $B_{s,d}$-mixing in the SM. The contribution is small due to loop- and CKM suppression.

(b) Tree-level contribution to $B_{s,d}$-mixing in our Z' model.

Figure 7.1: Leading contributions to $B_{s,d}$-mixing in the SM (a) and Z' models (b). For both diagrams there is also a 90° rotated version contributing which is not shown explicitly. The topology of LO diagrams contributing to D^0- and K^0-mixing is the same as for $B_{s,d}$.

7.4 Meson Mixing

Z'-quark FCNC couplings $g_{L,R}^{qq'} \neq 0$ (7.11) with $qq' = bs, bd, sd, cu$ invariably generate tree-level contributions to the mixing of neutral pseudoscalar mesons $P = B_s, B_d, K^0, D^0$, respectively. In the SM in contrast neutral meson mixing is loop-, CKM and in case of the D^0 also GIM-suppressed promoting it to an excellent test ground for NP. The topology of LO SM and BSM Feynman diagrams contributing to neutral meson mixing is exemplarily depicted for $B_{s,d}$ mesons in Fig. 7.1. Due to the strong SM suppression severe bounds on the FCNC couplings $g_{L,R}^{qq'}$ arise from the experimental determination of neutral meson mass differences ΔM_P, see [155]. Theory predictions on the other hand are typically less precise due to sizeable hadronic uncertainties. For B mesons it has to hold [1, 227]

$$\frac{\Delta M_{B_s}^{\mathrm{SM+NP}}}{\Delta M_{B_s}^{\mathrm{SM}}} \leq 1.156, \qquad \frac{\Delta M_{B_d}^{\mathrm{SM+NP}}}{\Delta M_{B_d}^{\mathrm{SM}}} \leq 1.154 \tag{7.12}$$

at 2.5σ c.l., which leaves room for a NP contribution of up to 15% compared to the SM. The theory prediction for the Z' contribution is given by [1, 227]

$$\frac{\Delta M_{B_q}^{\mathrm{SM+NP}}}{\Delta M_{B_q}^{\mathrm{SM}}} = \left| 1 + 200 \left(\frac{5\,\mathrm{TeV}}{M_{Z'}} \right)^2 \left[(g_L^{bq})^2 + (g_R^{bq})^2 - X_{B_q} g_L^{bq} g_R^{bq} \right] \right| \tag{7.13}$$

for $q = s, d$ and with $X_{B_q} \simeq 10$ for $M_{Z'} \simeq 5\,\mathrm{TeV}$, see [1, 227] for details. Interestingly, the NP contribution to ΔM_{B_q} cancels for $g_L^{bq} = X_{B_q}^{(-1)} g_R^{bq}$. If only one non-vanishing coupling is present the condition (7.12) combined with (7.13) for the B_s-meson simplifies to [228]

$$\frac{g_{L,R}^{bs}}{M_{Z'}^2} \lesssim 1.24 \cdot 10^{-5}\,\mathrm{TeV}^{-2} \equiv I_{\mathrm{max}} \tag{7.14}$$

at 99% c.l.. This constitutes a quite powerful constraint on viable Z' models coupling to b- or s-quarks.

Conversely, for D-mixing no sufficiently controlled SM prediction is available [229]. Conservatively demanding the Z' contribution not to exceed experimental bounds implies the limit [3, 230]

$$\frac{|(g_L^{cu})^2 + (g_R^{cu})^2 + X_{D^0} g_L^{cu} g_R^{cu}|}{{M_{Z'}}^2} \leq 5 \cdot 10^{-7}\,\mathrm{TeV}^{-2} \tag{7.15}$$

at 95% c.l. where we took into account the recent Heavy Flavor Averaging Group (HFLAV) update [231]. Note that RG effects on the right-hand side (RHS) of (7.15) only amount to a few percent for $M_{Z'} \in [10, 10^4]$ GeV and it holds $X_{D_0} \simeq 20$ for $M_{Z'} \simeq 1\,\mathrm{TeV}$, see [3, 230] for details.

Last but not least, the Z' can contribute to neutral kaon oscillations. In order to evade the corresponding strong experimental bounds [155] by construction here and in the following we always assure $g_{L,R}^{sd} = 0$ (cf. (7.11)) via

$$(F_{Q_1} = F_{Q_2}) \quad \text{and} \quad (F_{D_1} = F_{D_2} \quad \text{or} \quad V_L^d = \mathbb{1})\,. \tag{7.16}$$

7.5 Branching Ratios

The Z' decays to pairs of $U(1)'$ charged fermions f or scalars s with mass $m_{f,s} < M_{Z'}/2$, respectively. The corresponding tree-level decay widths read [232]

$$\begin{aligned}
\Gamma(Z' \to f\bar{f}) =& \frac{2\pi N_C^f}{3} \alpha_4 M_{Z'} \left[(F_{f_L}^2 + F_{f_R}^2) - \frac{m_f^2}{M_{Z'}^2} (F_{f_L}^2 - 6 F_{f_L} F_{f_R} + F_{f_R}^2) \right] \sqrt{1 - 4\frac{m_f^2}{M_{Z'}^2}}\, \Theta\left(M_{Z'} - 2m_f\right), \\
\Gamma(Z' \to ss) =& \frac{\pi N_s}{3} \alpha_4 M_{Z'} F_s^2 \sqrt{1 - 4\frac{m_s^2}{M_{Z'}^2}}^{\,3}\, \Theta\left(M_{Z'} - 2m_s\right),
\end{aligned} \tag{7.17}$$

where $N_C^f = 3$ ($N_C^f = 1$) for quarks (leptons), N_s is the number of real components of the scalar s and kinetic mixing has been neglected due to its smallness. Note that for vanishing kinetic mixing the Z' cannot decay to SM gauge bosons at LO. Along with (7.3) we deduce that the Z' typically decays dominantly to fermions.

8 A Planck-Safe $U(1)'$ Explanation for the B Anomalies

In the Chap. 4-6 we have learned that PS can be achieved via a variety of mechanisms in BSM models featuring VLFs, flavorful scalars or both. We now examine whether and how PS can be realized in a similar way in BSM models explaining a set of anomalies in rare $b \to s\mu^+\mu^-$ FCNC transitions coined the B anomalies. Popular tree-level mediators to resolve these anomalies are flavorful Z' bosons or leptoquarks. In this chapter which is based on [1, 233] we explore the reach of heavy, flavorful Z' models introduced in Chap. 7 as candidates for a Planck-safe explanation of the B anomalies.

We start with a brief motivation based on a discussion of the B anomalies and the implied subplanckian Landau poles in generic Z' explanations in Sec. 8.1. We then introduce our model in Sec. 8.2 and analyze various theoretical and experimental constraints. In Sec. 8.3 we explore how the model resolves the B anomalies by matching it to WET before turning to a Planck safety analysis in Sec. 8.4. Afterwards, we work out phenomenological constraints and signatures in Sec. 8.5 before summarizing in Sec. 8.6. Finally, in Sec. 8.7 we briefly comment on attempts to adapt the model to the latest R_K data [234, 235] which were published well after the completion of this project [1, 233].

8.1 Motivation

In this section, we briefly review the B anomalies as well as EFT fits pinning down the structure and size of possible NP contributions. Afterwards we show that Z' explanations of the anomalies generically imply a subplanckian Landau pole.

8.1.1 The B Anomalies

In the past decade, deviations from SM predictions emerged in several observables related to rare $b \to s\mu^+\mu^-$ transitions. They are collectively referred to as (neutral current) B anomalies[1], see [236] for a recent review. These FCNC processes are severely loop- and CKM-suppressed in the SM and therefore especially sensitive to possible NP contributions. However, such observables are also subject to sizeable theoretical and experimental uncertainties. Therefore, deviations in single observables do typically not exceed 2-3 σ. But interestingly, deviations in related observables exhibit characteristic patterns which invites for a joint interpretation as hints for BSM physics.

In particular, measured branching ratios of various decays with underlying $b \to s\mu^+\mu^-$ transitions such as $B \to K^{(*)}\mu^+\mu^-$ [51], $B_s \to \phi\mu^+\mu^-$ [52] as well as the branching ratio of $B_s \to \mu^+\mu^-$ [53, 237] are systematically lower than their SM prediction. Moreover, some optimized angular observables in $B \to K^*\mu^+\mu^-$ decays, most prominently P_5', exhibit a tension between experimental measurements [54, 55] and their SM prediction [238]. Furthermore, several LFU ratios [239]

$$R_H = \frac{\int_{q^2_{\rm min}}^{q^2_{\rm max}} \frac{\mathrm{d}\mathcal{B}(B\to H\mu^+\mu^-)}{\mathrm{d}q^2}\mathrm{d}q^2}{\int_{q^2_{\rm min}}^{q^2_{\rm max}} \frac{\mathrm{d}\mathcal{B}(B\to He^+e^-)}{\mathrm{d}q^2}\mathrm{d}q^2}\,, \tag{8.1}$$

with the dilepton invariant mass squared q^2 and $H = K^{(*)}, K_S, \phi, ...$, were measured below their SM expectation of unity [47–49]. A similar muon-to-electron suppression was seen in the baryonic decay

---

[1] Data also show some anomalies related to charged current $b \to c\tau\nu$ transitions, see e.g. [236]. These are however not considered in this work as they cannot be explained in flavorful Z' models and are less sensitive to NP.

$\Lambda_b^0 \to pK^-\ell^+\ell^-$ [50]. Most prominently,

$$\begin{aligned} R_K^{\text{LHCb'22}}|_{[1.1,6.0]} &= 0.846^{+0.042}_{-0.039}(\text{stat})^{+0.013}_{-0.012}(\text{syst}), \\ R_{K^*}^{\text{LHCb'17}}|_{[0.045,1.1]} &= 0.66^{+0.11}_{-0.07}(\text{stat}) \pm 0.03(\text{syst}), \\ R_{K^*}^{\text{LHCb'17}}|_{[1.1,6.0]} &= 0.69^{+0.11}_{-0.07}(\text{stat}) \pm 0.05(\text{syst}), \end{aligned} \tag{8.2}$$

where the subscript specifies the q^2 bin in units of GeV^2, individually used to deviate from the SM prediction at the level of 3σ [47, 48]. The R_H are both theoretically and experimantaly very clean observables, as hadronic uncertainties as well as many experimental systematics widely cancel in the ratio. Thus, in particular the deviations (8.2) in $R_{K^{(*)}}$ were often interpreted as promising hints for lepton flavor universality violating (LFUV) BSM physics, indicating a different treatment of electrons and muons.

Disclaimer: The $R_{K^{(*)}}$ data (8.2) are not the most recent, but rather reflect the situation at the time this project [1, 233] was carried out. Afterwards, in December 2022 the LHCb collaboration released a new measurement of $R_{K^{(*)}}$ [234, 235] which is compatible with unity and thus in agreement with the SM. We discuss the implications of the new $R_{K^{(*)}}$ data and our attempts to adjust the model accordingly in detail in Sec. 8.7. Until then, we stick with the former data (8.2) from [47, 48] used within [1, 233].

8.1.2 EFT Interpretation and Fits

The correct tool to analyze possible NP indicated by the B anomalies in a model-independent way is WET, introduced in detail in Subsec. 2.5.2. The most general WET Lagrangian inducing tree-level $b \to s\mu^+\mu^-$ transitions is given in (2.34). A plethora of global WET fits for NP WCs[2] to the B anomalies have been performed by various groups, see e.g. [240] and references therein. The individual fits often differ by the considered WCs, their flavor assumptions as well as the included observables. Nevertheless, fit results are widely consistent. In this chapter, we use the results of a fit to $b \to s$ data from [240]. The fit was performed with the tool `flavio` [241] and includes LFU ratios R_H (8.1), (binned) branching ratios as well angular observables such as A_{FB}, F_H and P_i', see [240] for details.

We focus on the fit scenarios summarized in Tab. 8.1 which assume NP only in the semimuonic NP WCs $C_{9,10}^{\mu(\prime)}$, from now on dropping the superscript NP for brevity. In contrast, the (pseudo-)scalar $O_{S,P}^{(\prime)}$, tensor $O_{T,T5}$ and electromagnetic dipole operators $O_7^{(\prime)}$ are not relevant in Z' models and therefore neglected. Note that $C_{9,10}^{(\prime)\ell}$ for $\mu_b \lesssim \mu \lesssim \mu_{\text{EW}}$ do not suffer from sizeable RG effects as they are invariant under QCD [240]. In addition, for $\mu_0 \gtrsim \mu \gtrsim \mu_{\text{EW}}$ the running of corresponding SMEFT operators is rather slow and amounts only to $\lesssim 5\%$ from a scale as high as $\mu_0 = 10\,\text{TeV}$ down to μ_{EW} [240]. Hence, we neglect these small RG effects.

The fit results Tab. 8.1 strongly favor NP contributions to semimuonic WCs $C_{9,10}^{\mu}$ with a pull of $\sim 6\sigma$ from the SM throughout all fit scenarios. Interestingly, the one and two-dimensional fits jointly indicate a pattern

$$-C_9^{\mu} \geq C_{10}^{\mu} \geq 0\,, \tag{8.3}$$

with $-1.3 \lesssim C_9^{\mu} - C_{10}^{\mu} \lesssim -0.8$ mostly fueled by a sizeable negative contribution to C_9^{μ}. In particular, already the 1d fit scenarios C_9^{μ} and $C_9^{\mu} = -C_{10}^{\mu}$ are sufficient to achieve a 6σ pull from the SM. $C_{9,10}^{\prime\mu}$ in contrast are compatible with zero and their inclusion does not significantly increase the pull.

---

[2] Recall that some WCs in WET also receive a non-vanishing SM contribution, see (2.37).

Dim.	Fit for	C_9^μ	C_{10}^μ	$C_9^{\prime\mu}$	$C_{10}^{\prime\mu}$	$\mathrm{Pull}_{\mathrm{SM}}$
1d	C_9^μ	-0.83 ± 0.14	-	-	-	$6.0\,\sigma$
1d	$C_9^\mu = -C_{10}^\mu$	-0.41 ± 0.07	$-C_9$	-	-	$6.0\,\sigma$
2d	$C_{9,10}^\mu$	-0.71 ± 0.17	0.20 ± 0.13	-	-	$5.9\,\sigma$
4d	$C_{9,10}^{(\prime)\mu}$	-1.07 ± 0.17	0.18 ± 0.15	0.27 ± 0.32	-0.28 ± 0.19	$6.5\,\sigma$

Table 8.1: Best fit values for the semimuonic NP WCs $C_{9,10}^{(\prime)\mu}$ in different NP scenarios and their respective pull from the SM hypothesis. Table adapted from [1], entries taken from [240].

8.1.3 Landau Poles in Flavorful Z' Explanations

A tremendous effort in model building in the past decade has resulted in a vast number of different BSM explanations for the B anomalies, see e.g. [236] for an overview. A simple and popular ansatz to resolve the anomalies are flavorful Z' models as introduced in Chap. 7. However, these models are typically not Planck-safe due to a generic, subplanckian Landau pole in the $U(1)'$ gauge coupling entailing a loss of predictivity much below M_{Pl}. We carefully derive this finding in the following.

Minimal $U(1)'$ charge assignments to induce the favored C_9^μ contribution in Tab. 8.1 to $b \to s\mu^+\mu^-$ transitions are to LH muons (F_{L_2}) and LH b- (F_{Q_3}) or s-quarks (F_{Q_2}). Moreover, inducing the bs-coupling of the Z' requires quark flavor mixing. Assuming the mixing to be CKM induced from $V_{ts}^* V_{tb} \simeq -0.04$ by a rotation in the down sector with $V_L^d \simeq V_{\mathrm{CKM}}$ and $V_L^u \simeq \mathbb{1}$ (cf. Sec. 2.3) the Z' contribution to $b \to s\mu^+\mu^-$ transitions is

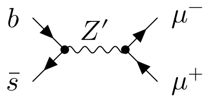

$$\sim V_{ts}^* V_{tb} F_{Q_3} F_{L_2} \frac{g_4^2(M_{Z'})}{M_{Z'}^2} \simeq \frac{1}{\Lambda^2}\,, \tag{8.4}$$

see Sec. 8.3 for details. Here, g_4 and $M_{Z'}$ denote the $U(1)'$ gauge coupling and the Z' mass, respectively. Inducing sufficiently sizeable NP contributions to explain the B anomalies as in Tab. 8.1 points to a NP scale of $\Lambda \simeq 40\,\mathrm{TeV}$ [242]. Generic mass bounds for a flavorful Z' in comparison are in the ballpark of $5\,\mathrm{TeV}$ [243]. As the Z' contribution scales as $\frac{g_4^2}{M_{Z'}^2}$ the Z' mass suppression has to be compensated by larger values of g_4. More precisely, $M_{Z'} \simeq 5$ TeV together with (8.4) yields

$$\alpha_4(\mu_0 = 5\,\mathrm{TeV}) \sim \frac{1}{(4\pi)^2} \frac{(5\,\mathrm{TeV}/40\,\mathrm{TeV})^2}{V_{tb} V_{ts}^* F_{L_2} F_{Q_3}} \sim \frac{1}{40\pi^2} \frac{1}{F_{L_2} F_{Q_3}} \tag{8.5}$$

as required value of the $U(1)'$ coupling $\alpha_4 = \frac{g_4^2}{16\pi^2}$. The leading order RG evolution of the $U(1)'$ coupling is then given by (3.5) and governed by the 1-loop coefficient B_4 defined in (3.7), see Subsec. 3.1.1 for details. It implies a Landau pole at

$$\ln \frac{\mu_{\mathrm{LP}}}{\mu_0} = \frac{1}{B_4 \alpha_4(\mu_0)}\,, \tag{8.6}$$

cf. (3.6). Assigning the required non-zero $U(1)'$ charges F_{L_2} and F_{Q_3} to LH muons and b quarks, respectively, as well as the minimal amount of extra charges to avoid gauge anomalies (see Sec. 7.1) we find

$$B_4 \geq \frac{16}{3}(F_{L_2}^2 + 3F_{Q_3}^2)\,. \tag{8.7}$$

Plugging this and (8.5) into (8.6) we obtain

$$\ln\frac{\mu_{\mathrm{LP}}}{\mu_0}=\frac{1}{B_4\alpha_4(\mu_0)}=\frac{15\pi^2}{2}\frac{F_{L_2}F_{Q_3}}{F_{L_2}^2+3F_{Q_3}^2}\lesssim\frac{15\pi^2}{4\sqrt{3}}\,,\tag{8.8}$$

irrespective of the charge assignments F_{L_2,Q_3}. Hence, for $\mu_0\simeq M_{Z'}\simeq 5\,\mathrm{TeV}$ the Landau pole appears at

$$\mu_{\mathrm{LP}}\lesssim 10^{10}\,\mathrm{TeV}\ll M_{\mathrm{Pl}}\tag{8.9}$$

well below the Planck scale. We stress that in realistic models B_4 is typically larger than (8.7) due to contributions from additional $U(1)'$ charges. This translates to an exponentially lower scale for the Landau pole, see Fig. 8.2 for an example. Note that demanding anomaly cancellation was crucial for this derivation and that our findings are not altered when including kinetic mixing below the experimental limit (7.7).

We briefly comment on exceptions to the generic bound (8.9). One possibility is to impose sizeable flavor rotations $V_L^{u,d}$ in the up- and down-sector that largely cancel as $V_L^{u\dagger}V_L^d=V_{\mathrm{CKM}}$, see e.g. [244, 245]. Thereby, the required $Z'bs$-coupling can be generated by α_4 lower than (8.5) which pushes the Landau pole to higher energies. However, in these scenario potentially sizeable contributions to several FCNCs transitions are induced in the down- and up-sector but severely constrained experimentally. Hence, they prevent the rotations $V_L^{u,d}$ to become arbitrarily large which limits the reach of this mechanism to lower the required value of α_4.

Secondly, one could choose all first- and second-generation quarks to be uncharged under the $U(1)'$ gauge symmetry as e.g. in third generation hypercharge or B_3-L_2 models, see [237, 246]. In that case Z' production in pp collisions is severely suppressed and the corresponding LHC mass bounds are lowered. As the Z' contribution to $b\to s\mu^+\mu^-$ (8.4) scales with $\frac{\alpha_4}{M_{Z'}^2}$ this also allows for lower values of α_4. However, even in this scenario contributions to Z' production from $b\bar{b}$ fusion typically still result in mass bounds well above a TeV and thus might not allow for a sufficiently low α_4 to avoid a subplanckian Landau pole. Moreover, in order to achieve PS in both scenarios the Higgs metastability still needs to be cured. As they are also rather fine tuned we do not consider them in this work. Instead, our goal in this chapter is to develop a Planck-safe Z' model explaining the B anomalies with the help of an enlarged BSM sector via the mechanisms discussed in Chap. 4, Chap. 5 and in particular Chap. 6.

8.2 $Z^{'}$ Model Set-Up

We extend the SM with a heavy flavorful Z', a $U(1)'$ breaking SM singlet scalar ϕ as well as three BSM RH neutrinos ν. Moreover, we include N_F generations of universally charged BSM fermions $\psi_{L,R}$ as well as a $N_F\times N_F$ SM singlet scalar matrix field S_{ij}.

For the sake of simplicity and in order to reduce the number of free parameters we promote the BSM fermions $\psi_{L,R}$ to vector-like SM singlets coming in three generations and assume the matrix scalar to be uncharged also under the $U(1)'$ gauge interaction. Hence, we fix

$$N_F=3,\quad Y_{\psi_{L/R,i}}=0,\quad d_{2,\psi_{L/R,i}}=\mathbf{1},\quad d_{3,\psi_{L/R,i}}=\mathbf{1},\quad F_{\psi_{L/R,i}}=F_\psi,\quad F_S=0\,.\tag{8.10}$$

8.2.1 Yukawa Sector

The Yukawa sector of our model

$$-\mathcal{L}_{\mathrm{Yukawa}}=Y_{ij}^d\,\overline{Q}_iHD_j+Y_{ij}^u\,\overline{Q}_i\widetilde{H}U_j+Y_{ij}^\ell\,\overline{L}_iHE_j+Y_{ij}^\nu\,\overline{L}_i\widetilde{H}\nu_j+y\,\overline{\psi}_{Li}\,S_{ij}\,\psi_{Rj}+\text{h.c.}\tag{8.11}$$

contains the SM Yukawa matrices $Y^{u,d,\ell}$, a similar BSM Yukawa Y^ν for neutrinos as well as the single pure BSM Yukawa coupling y as in Chap. 6. It is protected by the only softly broken $SU(N_F)_{\psi_L} \times SU(N_F)_{\psi_R}$ flavor symmetry. It also forbids any additional Yukawa interactions involving $\psi_{L,R}$ or S_{ij} and in particular a Yukawa portal coupling κ à la Model E in Tab. 4.1. We restrict ourselves to charge assignments with $F_\phi \neq \pm 2F_\nu$, which by construction forbid a potential Majorana-like Yukawa interactions of the RH neutrinos and the scalar ϕ.

While gauge invariance of the BSM Yukawa y is already ensured by (8.10), for the SM and neutrino Yukawa matrices it requires

$$\begin{aligned} Y^u_{ij}: &\quad 0 = F_{Q_i} + F_H - F_{U_j}, & Y^d_{ij}: &\quad 0 = F_{Q_i} - F_H - F_{D_j}, \\ Y^\ell_{ij}: &\quad 0 = F_{L_i} - F_H - F_{E_j}, & Y^\nu_{ij}: &\quad 0 = F_{L_i} + F_H - F_{\nu_j}, \end{aligned} \tag{8.12}$$

for $i,j = 1,2,3$. Fulfilling all conditions (8.12) invariably implies flavor-universal $U(1)'$ charges for all quarks and leptons. This forbids non-universal $F_{Q_2} \neq F_{Q_3}$ which is however required to induce a tree-level LH $Z'bs$ coupling in order to explain the B anomalies, see (8.4).

In the following we therefore pursue a different path that allows us to explain the B anomalies in a radiatively stable and Planck-safe manner. We mitigate the conditions (8.12) by only demanding invariance of diagonal quark Yukawa couplings via

$$Y^u_{ii}: \quad 0 = F_{Q_i} + F_H - F_{U_i}\,, \qquad Y^d_{ii}: \quad 0 = F_{Q_i} - F_H - F_{D_i}\,, \tag{8.13}$$

which allows for the corresponding mass terms. Thereby, we explicitly assure gauge invariance of the most sizeable top (and bottom) Yukawa coupling(s) while only neglecting Yukawa couplings that are numerically small and of negligible impact for the RG analysis. This includes the lepton and neutrino Yukawas $Y^{\ell,\nu}_{ij}$. We stress that solving the flavor puzzle, i.e. explaining the observed patterns in fermion masses as well as CKM and PMNS mixing is beyond the scope of this work.

8.2.2 Scalar Sector

The scalar potential

$$\begin{aligned} V^{(4)} =& \lambda\,(H^\dagger H)^2 + s\,(\phi^\dagger\phi)^2 + u\,\mathrm{Tr}(S^\dagger S S^\dagger S) + v\,\mathrm{Tr}(S^\dagger S)\mathrm{Tr}(S^\dagger S) \\ &+ \delta\,(H^\dagger H)\,\mathrm{Tr}(S^\dagger S) + \tilde\delta\,(H^\dagger H)(\phi^\dagger\phi) + w\,(\phi^\dagger\phi)\,\mathrm{Tr}(S^\dagger S) \end{aligned} \tag{8.14}$$

is structurally equivalent to (6.8). It contains Higgs (λ) and BSM (u, v, s) quartic self interactions as well as portal couplings ($\delta, \tilde\delta, w$) among the different scalar fields. The potential (8.14) exhibits the two distinct ground states $V^\pm$ with stability criteria

$$\begin{aligned} &\lambda > 0, \quad \varDelta > 0, \quad s > 0, \delta' = \delta + 2\sqrt{\lambda\varDelta} > 0, \quad \tilde\delta' = \tilde\delta + 2\sqrt{\lambda s} > 0, \\ &w' = w + 2\sqrt{s\varDelta} > 0, \quad 2\sqrt{\lambda\varDelta s} + \delta\sqrt{s} + \tilde\delta\sqrt{\varDelta} + w\sqrt{\lambda} + \sqrt{\delta'\tilde\delta' w'} > 0\,, \end{aligned} \tag{8.15}$$

cf. (6.9) and (6.10), which are distinguished by the parameter

$$\varDelta = \begin{cases} \frac{u}{3} + v > 0 & \text{for } u > 0 \quad (V^+) \\ u + v > 0 & \text{for } u < 0 \quad (V^-) \end{cases}. \tag{8.16}$$

After spontaneous breaking of the $U(1)'$ symmetry, the scalar ϕ acquires a VEV $\langle\phi\rangle = v_\varphi/\sqrt{2} > 0$ which generates a mass term for the Z' boson

$$M_{Z'} = |F_\phi| g_4 v_\varphi \,, \tag{8.17}$$

where additional contributions from the Higgs are prevented by (7.3). Moreover, after EWSB

$$H = \frac{1}{\sqrt{2}}\begin{pmatrix} 0 \\ v_h + h \end{pmatrix}, \qquad \phi = \frac{1}{\sqrt{2}}(v_\varphi + \varphi), \tag{8.18}$$

the surviving real scalar modes h and φ mix, see Subsec. 5.2.1 and App. C for details. The scalar mixing angle β is constrained to be small by Higgs signal strength measurements (5.27). Applying (8.17) in the limit $\beta \ll 1$ results in a bound

$$|F_\phi| g_4 \frac{\tilde{\delta}}{s} \lesssim 0.81\, M_{Z'}[\,\mathrm{TeV}]\,, \tag{8.19}$$

which can be easily fulfilled by $\tilde{\delta} \lesssim s$ as typically $|F_\phi| g_4 \lesssim \mathcal{O}(1)$ in our models as outlined in Subsec. 8.3.3. For a more detailed phenomenological discussion of the $U(1)'$ breaking scalar ϕ we refer to [247]. If in addition the scalar S acquires a VEV it also participates in the mixing. However, this effect can be regulated by the size of the portal couplings $|\delta|$ and $|w|$, and is therefore not further analyzed in this work.

8.3 Viable $Z^{'}$ Models Explaining the B Anomalies

We now match the minimal Z' model for $b \to s\mu^+\mu^-$ transitions to the low energy description in WET, briefly discuss important phenomenological constraints and derive viable benchmark models (BMs).

8.3.1 EFT Matching

In order to generate the required contributions to the semileptonic $b \to s\mu^+\mu^-$ transitions via (8.4) the Z' has to couple to b- and s-quarks as well as muons with $g^{bs}_{L/R}$ and $g^{\mu\mu}_{L/R}$, respectively, cf. (7.11). The requisite minimal Lagrangian in the mass basis reads

$$\mathcal{L}_{Z'} \supset \left(g^{bs}_L\, \bar{s}_L \gamma^\mu b_L Z'_\mu + g^{bs}_R\, \bar{s}_R \gamma^\mu b_R Z'_\mu + \text{h.c.}\right) + g^{\mu\mu}_L \bar{\mu}_L \gamma^\mu \mu_L Z'_\mu + g^{\mu\mu}_R \bar{\mu}_R \gamma^\mu \mu_R Z'_\mu \,. \tag{8.20}$$

Integrating out the Z' at tree level yields the effective Lagrangian

$$-\mathcal{L}^{\text{eff}}_{Z'} \supset \frac{1}{2M^2_{Z'}} \Big[\left(g^{bs}_L (\bar{s}_L \gamma^\mu b_L) + g^{bs}_R (\bar{s}_R \gamma^\mu b_R) + \text{h.c.}\,\right) + g^{\mu\mu}_L (\bar{\mu}_L \gamma^\mu \mu_L) + g^{\mu\mu}_R (\bar{\mu}_R \gamma^\mu \mu_R) \Big]^2 \tag{8.21}$$

and comparing to the WET Lagrangian (2.34) we can read off the Z' contributions to semimuonic WCs

$$\begin{aligned} C^{(\prime)\mu}_9 &= \left(-\frac{\sqrt{2}\, G_F\, \alpha_e}{\pi}\, V_{tb}\, V^*_{ts}\right)^{-1} \frac{g^{bs}_{L(R)}(g^{\mu\mu}_R + g^{\mu\mu}_L)}{M^2_{Z'}}\,, \\ C^{(\prime)\mu}_{10} &= \left(-\frac{\sqrt{2}\, G_F\, \alpha_e}{\pi}\, V_{tb}\, V^*_{ts}\right)^{-1} \frac{g^{bs}_{L(R)}(g^{\mu\mu}_R - g^{\mu\mu}_L)}{M^2_{Z'}}\,. \end{aligned} \tag{8.22}$$

Here, we have neglected the numerically small running of $C^{(\prime)\ell}_{9,10}$ enabling us to directly match our Z' model to WET at the NP scale $\mu_0 \simeq M_{Z'}$.

The requisite couplings $g_{L,R}^{bs,\mu\mu}$ are determined by (7.11). In order to induce the required FCNC coupling $g_L^{bs} \neq 0$ we choose the CKM rotation to be entirely in the down-sector, i.e. $V_L^d = V_{\mathrm{CKM}}$ which yields

$$g_L^{bs} = g_4(\mathcal{F}'_{d_L})_{23} = g_4 V_{tb}\, V_{ts}^* \left(F_{Q_3} - F_{Q_2}\right) + V_{ub}\, V_{us}^* \left(F_{Q_1} - F_{Q_2}\right) \simeq g_4 V_{tb}\, V_{ts}^* \left(F_{Q_3} - F_{Q_2}\right) , \tag{8.23}$$

where we made use of CKM unitarity and hierarchy. This choice also implies $V_L^u = \mathbb{1}$ which along with $V_R^u = \mathbb{1}$ evades any potential FCNC couplings in the up-sector. Also in the RH down sector unless stated otherwise we choose $V_R^d = \mathbb{1}$ resulting in $g_R^{bs} = 0$ and hence $C_{9,10}^{\prime\ell} = 0$ in accord with the fit results Tab. 8.1. In the lepton sector we fix $V_{L,R}^\ell = \mathbb{1}$ which forbids all LFV couplings and with $i = 1,2,3 \leftrightarrow \ell = e,\mu,\tau$ simply gives

$$g_L^{\ell\ell} = g_4 F_{L_i}, \qquad g_R^{\ell\ell} = g_4 F_{E_i} \,. \tag{8.24}$$

8.3.2 Phenomenological Constraints

To avoid severe experimental constraints from LEP-II [248, 249] and other EW precision measurements [58] we demand electrons to be uncharged under the $U(1)'$, i.e.

$$F_{L_1} = 0, \qquad F_{E_1} = 0\,, \tag{8.25}$$

such that they do not couple to the Z'. Moreover, to avoid contributions to kaon mixing we choose

$$F_{Q_1} = F_{Q_2}, \qquad F_{D_1} = F_{D_2}\,, \tag{8.26}$$

which yields $g_{L,R}^{sd} = 0$, c.f. (7.16). The required Z' coupling $g_L^{bs} \neq 0$ in contrast invariably generates tree-level contributions to B_s-mixing, c.f. Fig. 7.1, which is strongly bounded by (7.14). Using $I_{\max} = 1.24{\cdot}10^{-5}\ \mathrm{TeV}^{-2}$ from (7.14) we define the ratio

$$r_{B_s} = \frac{1}{I_{\max}} \frac{|g_L^{bs}|^2}{M_{Z'}^2} \tag{8.27}$$

for future reference which has to be $r_{B_s} < 1$ in viable models. This bound implies

$$\left| \frac{g_L^{bs}}{g_R^{\mu\mu} + g_L^{\mu\mu}} \right| \lesssim \frac{8 \cdot 10^{-3}}{|C_9^\mu|}\,, \tag{8.28}$$

which means that the Z' couples much more strongly to muons than bs and results in a charge hierarchy

$$\frac{F_{E_2} + F_{L_2}}{F_{Q_3} - F_{Q_1}} \gtrsim -5.1\, C_9^\mu \,. \tag{8.29}$$

Constraints on $|g_L^{bd}|^2/M_{Z'}^2$ from B_d-mixing analogous to (7.14) are of the same order but less stringent due to the stronger CKM suppression of g_L^{bd}, cf. (8.23). In order to realize the favored pattern for the values of WCs (8.3) the involved $U(1)'$ charges have to obey

$$(F_{Q_3} > F_{Q_2} \quad \text{and} \quad F_{L_2} \geq F_{E_2} \geq 0) \quad \text{or} \quad (F_{Q_3} < F_{Q_2} \quad \text{and} \quad F_{L_2} \leq F_{E_2} \leq 0)\,. \tag{8.30}$$

From (8.22) we can moreover deduce that the scenario $C_9^\mu = -C_{10}^\mu$ requires $F_{E_2} = 0$, whereas $C_{10}^\mu = 0$ necessitates vector-like muon charges $F_{L_2} = F_{E_2}$.

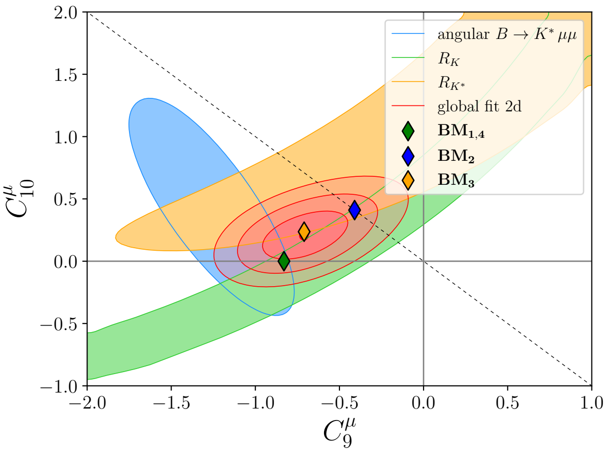

Figure 8.1: 2d fit to the B anomalies in the C_9^μ-C_{10}^μ-plane from [240], cf. Tab. 8.1. Indicated are the overall 1-3$\,\sigma$ best fit regions (red) along with 1σ contours for fits to subsets of observables, namely only R_K (green), only R_{K^*} (yellow) and $B \to K^* \mu^+ \mu^-$ angular observables (blue). Our four benchmark models in Tab. 8.2 are indicated by diamond-shaped symbols, the dashed black line corresponds to $C_9^\mu = -C_{10}^\mu$. Note that BM1 and BM4 generate the same values for $C_{9,10}^\mu$. Plot taken from [1].

Model	F_{Q_i}			F_{U_i}			F_{D_i}			F_{L_i}			F_{E_i}			F_{ν_i}			F_H	F_ψ	F_S	F_ϕ
BM1	$\frac{1}{20}$	$\frac{1}{20}$	$-\frac{1}{10}$	$\frac{1}{20}$	$\frac{1}{20}$	$-\frac{1}{10}$	$\frac{1}{20}$	$\frac{1}{20}$	$-\frac{1}{10}$	0	$-\frac{9}{10}$	$\frac{9}{10}$	0	$-\frac{9}{10}$	$\frac{9}{10}$	0	0	0	0	1	0	$\frac{1}{5}$
BM2	$-\frac{1}{4}$	$-\frac{1}{4}$	$\frac{1}{6}$	$-\frac{1}{4}$	$-\frac{1}{4}$	$\frac{1}{6}$	$-\frac{1}{4}$	$-\frac{1}{4}$	$\frac{1}{6}$	0	1	0	0	0	1	$\frac{1}{12}$	$-\frac{1}{12}$	1	0	$\frac{11}{12}$	0	$\frac{1}{9}$
BM3	$-\frac{1}{8}$	$-\frac{1}{8}$	0	$-\frac{1}{8}$	$-\frac{1}{8}$	0	$-\frac{1}{8}$	$-\frac{1}{8}$	0	0	$\frac{1}{2}$	$\frac{1}{4}$	0	$\frac{1}{4}$	$\frac{1}{2}$	0	$\frac{1}{4}$	$\frac{1}{2}$	0	1	0	$\frac{1}{8}$
BM4	0	0	$\frac{1}{9}$	0	0	$\frac{1}{9}$	0	0	$\frac{1}{9}$	0	$\frac{1}{3}$	$-\frac{2}{3}$	0	$\frac{1}{3}$	$-\frac{2}{3}$	0	$\frac{1}{3}$	$-\frac{2}{3}$	0	1	0	$\frac{1}{6}$

Table 8.2: $U(1)'$ charge assignments F_X with $X = Q_i, U_i, D_i, L_i, E_i, \nu_i, \psi, H, S, \phi$ in our four benchmark models. Table adapted from [1].

8.3.3 Benchmark Models

We now work out viable Z' BMs charge assignments fulfilling all relevant constraints from Chap. 7. The number of a priori free $U(1)'$ charges is reduced by choosing the scalar S to be a complete gauge singlet (8.10), cancellation of gauge anomalies (7.1), decoupling EW from $U(1)'$ symmetry breaking (7.3), gauge invariance of quark mass terms (8.13) as well as electron (8.25) and kaon bounds (8.26). Moreover, to evade the B_s-mixing bound (7.14) $U(1)'$ charges have to fulfill (8.29). In order to match the patterns of WCs in (8.3) favored in the fits, cf. Tab. 8.1 and Fig. 8.1, $U(1)'$ charges in addition have to fulfill (8.30).

We identified four different BMs fulfilling all these requirements, with the corresponding charge assignments given in Tab. 8.2. The BMs induce different NP scenarios in the WCs $C_{9,10}^\mu$:

$$\text{BM1,4: } C_9^\mu < 0 \text{ and } C_{10}^\mu = 0, \qquad \text{BM2: } C_9^\mu = -C_{10}^\mu < 0, \qquad \text{BM3: } -C_9^\mu \gg C_{10}^\mu > 0, \tag{8.31}$$

see also Fig. 8.1 where the corresponding values of WCs are indicated in the C_9^μ-C_{10}^μ-plane. For BM1-BM3 we assume the Z' mass to be $M_{Z'} \simeq 5\,\text{TeV}$. In BM4 in contrast a lower value $M_{Z'} \simeq 3\,\text{TeV}$ is considered.

We now discuss the characteristics of each BM in more detail. BM1 belongs to a class of models with

$$F_{q_3} = -2F_{q_2} = -2F_{q_1}, \qquad F_{\ell_1} = 0, \qquad F_{\ell_3} = -F_{\ell_2}, \qquad F_{\nu_1} = 0, \qquad F_{\nu_3} = -F_{\nu_2}, \tag{8.32}$$

where $q = Q, U, D$ and $\ell = L, E$, controlled by only three free parameters $F_{q_3}, F_{\ell_3}, F_{\nu_3}$, for chiral fermions. Interestingly, we can choose $F_{\nu_3} = 0$ and obtain a model without RH neutrinos. This is not possible in models with $C_{10}^{\mu} \neq 0$ as in this case anomaly cancellation in combination with the other constraints invariably requires some non-vanishing $F_{\nu_i} \neq 0$. Moreover, in BM1 diagonal lepton Yukawas Y_{ii}^{ℓ} and corresponding mass terms are allowed by gauge invariance. BM1 also fulfills (7.8) so that the kinetic mixing parameter η is not induced at 1-loop. In order to obtain the best fit value $C_9^{\mu} = -0.83$ we fix the $U(1)'$ gauge coupling as $\alpha_4(\mu_0) = 1.87 \cdot 10^{-2}$.

For BM2, in order to obtain $C_{10}^{\mu} = -C_9^{\mu} = -0.41$ we set $F_{E_2} = 0$ and fix $\alpha_4(\mu_0) = 5.97 \cdot 10^{-3}$. Note that the model is rather close to the B_s-mixing bound (7.14) with $r_{B_s} \simeq 0.86$, cf. (8.27).

In BM3, the charge assignment along with $\alpha_4(\mu_0) = 4.60 \cdot 10^{-2}$ generates hierarchical $C_9^{\mu} = -0.71$, $C_{10}^{\mu} = +0.24$ in excellent agreement with the 2d scenario in Tab. 8.1. This is highly nontrivial, as only the value of the gauge coupling could be adjusted in order to generate the required values for both WCs. Interestingly, in this BM third-generation quarks are uncharged and the coupling g_L^{bs} is generated only from F_{Q_2} after the gauge to mass basis rotation.

Finally, in BM4 first- and second-generation quarks are uncharged under the $U(1)'$. Hence, a lighter Z' of $M_{Z'} = 3\,\text{TeV}$ is still compatible with collider bounds, due to the double b-quark parton distribution function (PDF) suppression in Z' production. Fixing $\alpha_4(\mu_0) = 2.45 \cdot 10^{-2}$ we obtain $C_9^{\mu} = -0.83$, $C_{10}^{\mu} = 0$ as in BM1. BM4 can be considered more minimal as fewer fields are $U(1)'$ charged than in the other BM models.

8.4 Planck Safety Analysis

The RG analysis of our BM models is rather complex due to the large number of different couplings and their interplay. Whereas $\alpha_4(\mu_0)$ for $\mu_0 \sim M_{Z',\psi,S}$ is fixed by explaining the B anomalies, the set of mostly a priori free BSM couplings

$$\{\eta, \alpha_y, \alpha_u, \alpha_v, \alpha_s, \alpha_\delta, \alpha_{\tilde{\delta}}, \alpha_w\}|_{\mu_0} \tag{8.33}$$

is only loosely constrained by kinetic (7.7) as well as scalar mixing (8.19) and spans an eight dimensional parameter space to be scrutinized. Luckily, we can make use of our findings from the previous chapters to identify subsets of this parameter space which are likely to give rise to a Planck-safe RG flow.

The required value of $U(1)'$ gauge coupling to explain the B anomalies with a heavy Z' is typically rather large with $\alpha_4(\mu_0) \simeq \mathcal{O}(10^{-2})$, cf. (8.4). In addition, many particles are charged under the $U(1)'$ which accelerates the RG growth of α_4. This growth if not tamed results in a Landau pole much below the estimate (8.9) and only a few orders of magnitude above the TeV scale[3], see for instance Fig. 8.2. Hence, large parts of the BSM parameter space exhibit subplanckian poles. However, the BSM Yukawa α_y slows down the growth of α_4 via

$$\beta_4 \supset -4\, N_F^2\, d_{2,\psi}\, d_{3,\psi}\, F_\psi^2\, \alpha_4^2 \alpha_y\,, \tag{8.34}$$

which is enhanced by N_F^2. This allows to prevent subplanckian Landau poles in our BMs for

$$F_\psi^2 \alpha_y(\mu_0) \gtrsim \mathcal{O}(10^{-1})\,. \tag{8.35}$$

---

[3] In fact, we also analyzed many more phenomenologically viable charge assignments than our BMs. However, for the majority of them the $U(1)'$ Landau pole could not be pushed beyond $M_{\rm Pl}$ preventing us from achieving PS.

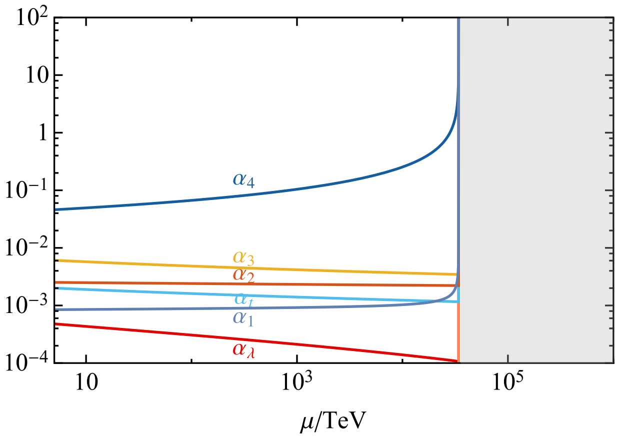

Figure 8.2: 2-loop running of couplings in a realistic heavy Z' model explaining the B anomalies. The RG flow exhibits an α_4 Landau pole already a few order of magnitude above the TeV scale. The $U(1)'$ charges and coupling in this plot are the same as in BM 3 of Tab. 8.2, but without any of the BSM fields ψ, S and ϕ, see Sec. 8.3 for details. Plot taken from [1].

Exploiting this mechanism implies an upper limit on the mass of the BSM fields ψ, S interacting via the Yukawa coupling y. If their mass is close to or above the naive Landau pole estimate (8.6), the fields do not become dynamical before the pole is reached and the theory falls apart before the slow-down by α_y sets in. In (8.35) we moreover heavily profit from the absence of stringent phenomenological bounds on α_y as well as some patterns in our BM charge assignments. All $U(1)'$ charged fields X contribute to $B_4 \supset\propto d_{2,X} d_{3,X} F_X^2$ which drives the RG growth of α_4 with their color and isospin multiplicity, cf. (3.7). Hence, we benefit from small quark charges $|F_{q_i}|/|F_\psi| \ll 1$ with $q = Q, U, D$ which for $F_{Q_{2,3}}$ is incidentally in accord with requirements from B_s-mixing bounds (7.14). Moreover, opposite-signed $F_{Q_{2,3}}$ in combination with large muon charges F_{L_2,E_2} allow to account for the B anomalies with still comparably low values of $\alpha_4(\mu_0)$.

Unluckily, large Yukawa coupling values also tend to destabilize the Higgs potential, cf. Sec. 4.2. Nonetheless, if one of the portal couplings $\delta, \tilde{\delta}$ is sufficiently sizeable with roughly

$$10^{-3} \lesssim \alpha_{\delta/\tilde{\delta}}(\mu_0) \lesssim 10^{-1}, \tag{8.36}$$

stability can still be achieved via the Higgs portal mechanism, see Sec. 5.1 for details. As previously, strongly coupled walking regimes which are induced by the rather large $\alpha_{y,\delta,\tilde{\delta}}(\mu_0)$ are key to achieve PS as they mutually tame the $U(1)'$ Landau pole and stabilize the Higgs. Interestingly, quartic couplings are not technically natural and can thus change signs, cf. Sec. 6.2, in particular allowing for transitions between the vacua $V^\pm$ by sign changes of α_u.

Notably, we also find some fine-tuned Planck-safe trajectories with both Higgs portal couplings tiny at the matching scale. The reason is a sizeable, inhomogeneous 2-loop contribution $\propto \alpha_4^2 \alpha_t$ to $\beta_{\tilde{\delta}}$. This constitutes a qualitatively new mechanism w.r.t. Chap. 6 as it is based on the non-vanishing scalar $U(1)'$ charge $F_\phi \neq 0$. It allows to induce sizeable $\alpha_{\tilde{\delta}}$ promoting Higgs stability, similarly to the indirect Higgs portal mechanism in Chap. 5. However, this effect can easily be spoiled by the contributions of other couplings in the interconnected RG flow.

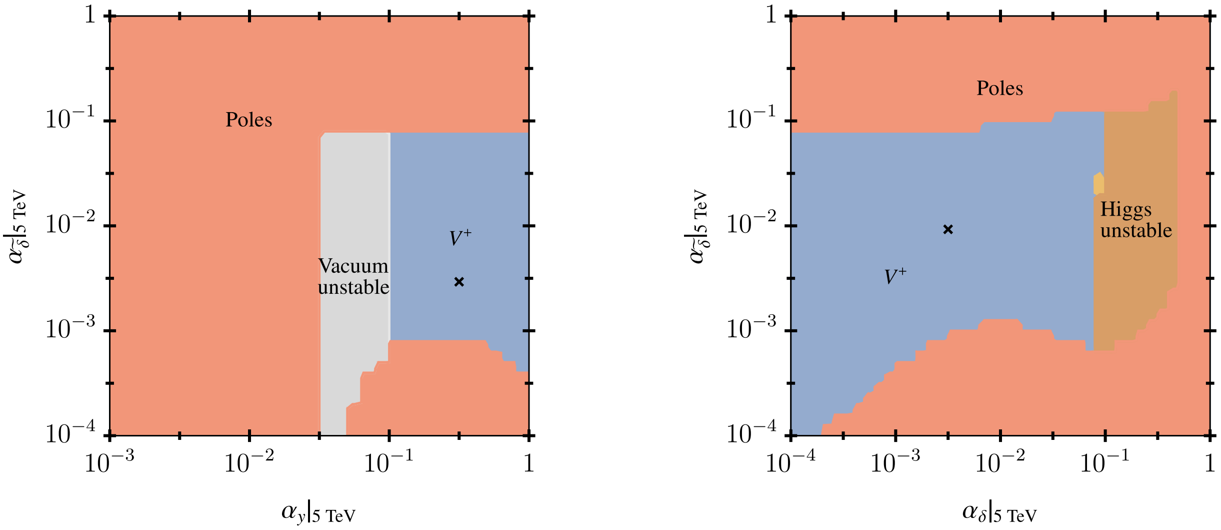

(a) $\alpha_y(\mu_0)$-$\alpha_{\tilde{\delta}}(\mu_0)$-plane for $\alpha_\delta(\mu_0) = 10^{-2.5}$.

(b) $\alpha_\delta(\mu_0)$-$\alpha_{\tilde{\delta}}(\mu_0)$-plane for $\alpha_y(\mu_0) = 10^{-0.5}$.

Figure 8.3: BSM critical surface of BM1 in the $\alpha_y(\mu_0)$-$\alpha_{\tilde{\delta}}(\mu_0)$- (a) and $\alpha_\delta(\mu_0)$-$\alpha_{\tilde{\delta}}(\mu_0)$-plane (b) for $\mu_0 = 5$ TeV. The remaining BSM couplings are fixed as $\{\alpha_4, \eta, \alpha_u, \alpha_v, \alpha_w, \alpha_s\}|_{\mu_0} = \{1.87 \cdot 10^{-2}, 0, 10^{-4}, 10^{-5}, 10^{-6}, 10^{-2}\}$. Same color coding as Fig. 4.1a. Plots taken from [1].

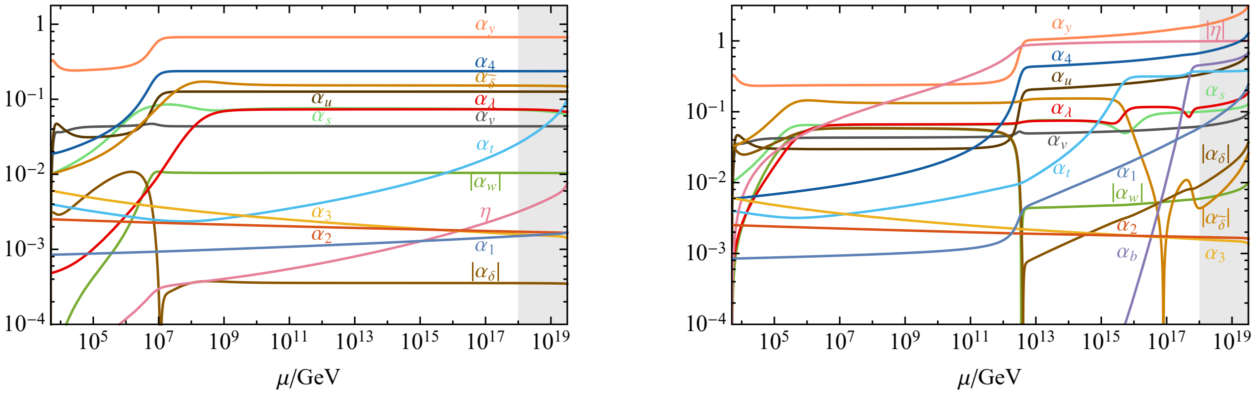

(a) BM1

(b) BM2

Figure 8.4: Exemplary Planck-safe RG trajectories in BM1 (a) and BM2 (b) for the parameter configurations indicated by the black crosses in Fig. 8.3 and Fig. 8.5, respectively. Plots taken from [1].

Model	μ_0	$\alpha_4(\mu_0)$	μ_{LP}	$\alpha_y(\mu_0)$	$\alpha_\delta(\mu_0)$	$\alpha_{\tilde\delta}(\mu_0)$
BM1	5 TeV	$1.87 \cdot 10^{-2}$	110 TeV	$\gtrsim 10^{-1.25}$	$10^{-4} \lesssim \alpha_\delta(\mu_0) \lesssim 10^{-0.75}$	$10^{-5} \lesssim \alpha_{\tilde\delta}(\mu_0) \lesssim 10^{-0.75}$
BM2	5 TeV	$5.97 \cdot 10^{-3}$	$2 \cdot 10^5$ TeV	$\gtrsim 10^{-1.75}$	$10^{-6} \lesssim \alpha_\delta(\mu_0) \lesssim 10^{-1}$	$10^{-5} \lesssim \alpha_{\tilde\delta}(\mu_0) \lesssim 10^{-0.5}$
BM3	5 TeV	$4.60 \cdot 10^{-2}$	25 TeV	$\gtrsim 10^{-1}$	$10^{-4} \lesssim \alpha_\delta(\mu_0) \lesssim 10^{-1}$	$10^{-2.5} \lesssim \alpha_{\tilde\delta}(\mu_0) \lesssim 10^{-1}$
BM4	3 TeV	$2.46 \cdot 10^{-2}$	60 TeV	$\gtrsim 10^{-1.25}$	$10^{-4} \lesssim \alpha_\delta(\mu_0) \lesssim 10^{-1}$	$10^{-4} \lesssim \alpha_{\tilde\delta}(\mu_0) \lesssim 10^{-1}$

Table 8.3: RG characteristics of our BMs. Indicated are the NP scale $\mu_0 \simeq M_{Z'}$, the required value of $\alpha_4(\mu_0)$ to obtain the best fit WCs Tab. 8.1 and the scale of the naive Landau pole μ_{LP} when setting all BSM couplings to zero that dictates an upper mass limit for the BSM fields ψ and S of $M_{S,\psi} < \mu_{\mathrm{LP}}$. Moreover, we give the preferred parameter ranges in $\alpha_{y,\delta,\tilde\delta}$ which give rise to a Planck-safe RG evolution.

8.4.1 Individual Benchmarks

The discussed RG characteristics are qualitatively rather similar in the individual BMs. Some quantitative features are therefore jointly collected in Tab. 8.3, indicating also the naive Landau pole estimate, and precise Planck-safe ranges for the BSM Yukawa and Higgs portal couplings.

An exemplary Planck-safe RG flow in BM1 is illustrated in Fig. 8.4a. We observe that $\alpha_{4,y}$ and some quartic couplings enter a walking regime around $\mu \sim 10^7$ GeV. The Higgs portal couplings $\alpha_{\delta,\tilde\delta}$ and the Higgs quartic α_λ join the walking around 10^8 GeV and 10^9 GeV, respectively. Within the walking regime, most couplings take sizeable values of $\mathcal{O}(10^{-1})$, except for the portal couplings $\alpha_{\delta,w}$ which are locked at negative values of lower magnitude. The SM gauge couplings do not participate in the walking but run moderately, similar as in the SM. The top Yukawa α_t and kinetic mixing parameter η grow more strongly, but stay well perturbative all the way up to M_{Pl}. The BSM parameter space Fig. 8.3 in BM1 is widely dominated by poles. PS can however be realized if poles are prevented by a large BSM Yukawa in accord with the estimate (8.35) as well as at least one sizeable Higgs portal coupling $\alpha_{\delta,\tilde\delta}$ promoting vacuum stability, cf (8.36) and Tab. 8.3. The remaining BSM couplings stay widely unconstrained. However, we observe a slight tendency for larger $\alpha_{u,v,s}(\mu_0)$ to enlarge the viable ranges for $\alpha_{\delta,\tilde\delta}(\mu_0)$ due to the indirect Higgs portal mechanism as long as they are still small enough to evade interference with the walking regime and Landau poles in quartic couplings. Stability at the Planck scale is always realized in the vacuum configuration V^+ although some RG trajectories feature intermediate transitions to V^-. We also examined the possibility to include RH neutrinos with $F_{\nu_3} = -F_{\nu_2} \neq 0$ in the model. The impact on the RG evolution is however small and of minor relevance. We conclude that including $U(1)'$-charged RH neutrinos in the model is possible from the view of PS. We now discuss the RG evolution of BM2-BM4 more briefly, focusing mostly on individual characteristics and differences w.r.t. the other BMs.

For BM2, the BSM critical surfaces are depicted in Fig. 8.5. Interestingly, due to the low value of $\alpha_4(\mu_0)$ compared to the other BMs already lower values of $\alpha_y \gtrsim 10^{-1.75}$ allow to tame the $U(1)'$ Landau pole and induce PS. This is also reflected in the higher scale of the naive Landau pole in Tab. 8.3. Accordingly, also the allowed ranges of the Higgs portal couplings $\alpha_{\delta,\tilde\delta}$ are wider. The reason is the lower value of the destabilizing α_y contribution to β_λ, enabling Higgs stability already for smaller values of the portal couplings $\alpha_{\delta,\tilde\delta}$. Turning to an exemplary Planck-safe RG flow in Fig. 8.4b, we notice that stabilization entails a crossover between two different walking regimes. The first walking regime appears already around 10^5 GeV capturing most quartics including the Higgs at values of $\lesssim 10^{-1}$ while gauge and Yukawa couplings except for α_y keep running at weakly coupled values. Around 10^{12} GeV the situation however changes. In particular, α_4 and η start to participate in the walking, the portal coupling $\alpha_{\delta,\tilde\delta,w}$ change sign and several couplings are now locked at borderline perturbative values of $\mathcal{O}(1)$.

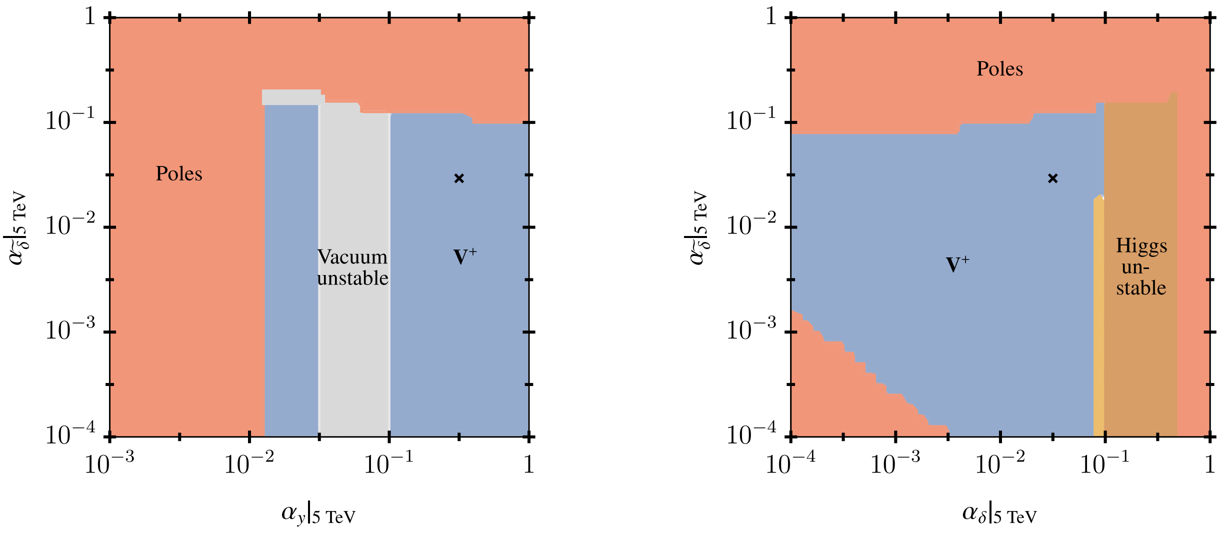

(a) $\alpha_y(\mu_0)$-$\alpha_{\tilde{\delta}}(\mu_0)$-plane for $\alpha_\delta(\mu_0) = 10^{-1.5}$.

(b) $\alpha_\delta(\mu_0)$-$\alpha_{\tilde{\delta}}(\mu_0)$-plane for $\alpha_y(\mu_0) = 10^{-0.5}$.

Figure 8.5: BSM critical surface of BM2 in the $\alpha_y(\mu_0)$-$\alpha_{\tilde{\delta}}(\mu_0)$- (a) and $\alpha_\delta(\mu_0)$-$\alpha_{\tilde{\delta}}(\mu_0)$-plane (b) for $\mu_0 = 5$ TeV. The remaining BSM couplings are fixed as $\{\alpha_4, \eta, \alpha_u, \alpha_v, \alpha_w, \alpha_s\}|_{\mu_0} = \{5.97 \cdot 10^{-3}, 0, 10^{-4}, 10^{-5}, 10^{-6}, 10^{-2}\}$. Same color coding as Fig. 4.1a. Plots taken from [1].

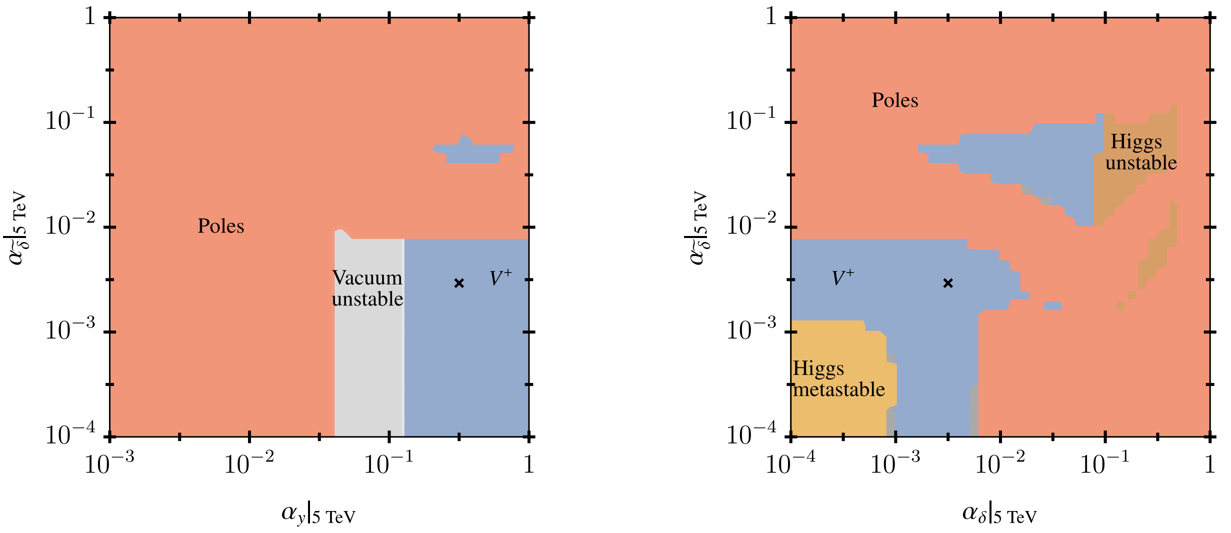

(a) $\alpha_y(\mu_0)$-$\alpha_{\tilde{\delta}}(\mu_0)$-plane for $\alpha_\delta(\mu_0) = 10^{-1.5}$.

(b) $\alpha_\delta(\mu_0)$-$\alpha_{\tilde{\delta}}(\mu_0)$-plane for $\alpha_y(\mu_0) = 10^{-0.5}$.

Figure 8.6: BSM critical surface of BM3 in the $\alpha_y(\mu_0)$-$\alpha_{\tilde{\delta}}(\mu_0)$- (a) and $\alpha_\delta(\mu_0)$-$\alpha_{\tilde{\delta}}(\mu_0)$-plane (b) at $\mu_0 = 5$ TeV. The remaining BSM couplings are fixed as $\{\alpha_4, \eta, \alpha_u, \alpha_v, \alpha_w, \alpha_s\}|_{\mu_0} = \{4.60 \cdot 10^{-2}, 0, 10^{-4}, 10^{-5}, 10^{-6}, 10^{-3.5}\}$. Same color coding as Fig. 4.1a. Plot taken from [1].

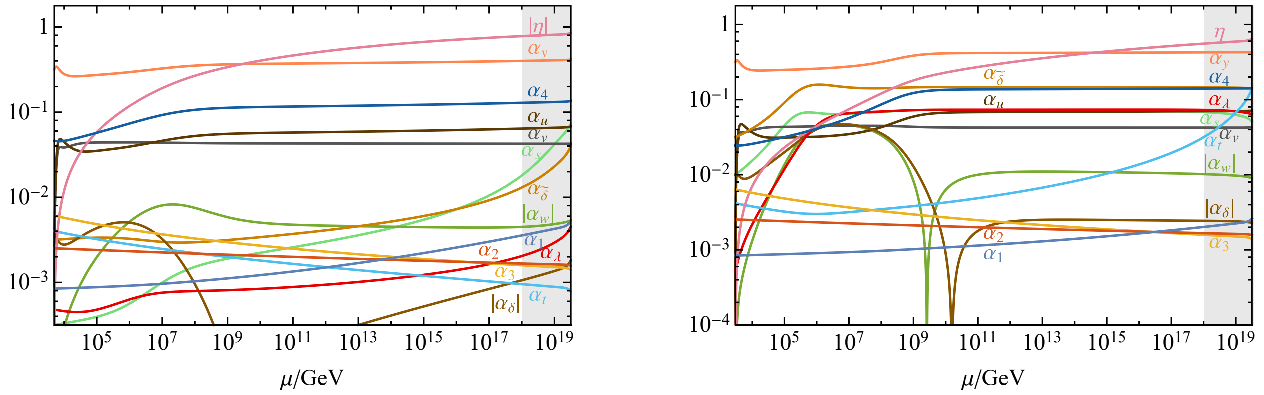

(a) BM3 **(b)** BM4

Figure 8.7: Exemplary Planck-safe RG trajectories in BM3 (a) and BM4 (b) from the NP scale $\mu_0 = 5$ TeV (a) and $\mu_0 = 3$ TeV (b) up to the Planck scale, for the parameter configurations indicated by the black crosses in Fig. 8.6 (a) and Fig. 8.8 (b), respectively. Plots taken from [1].

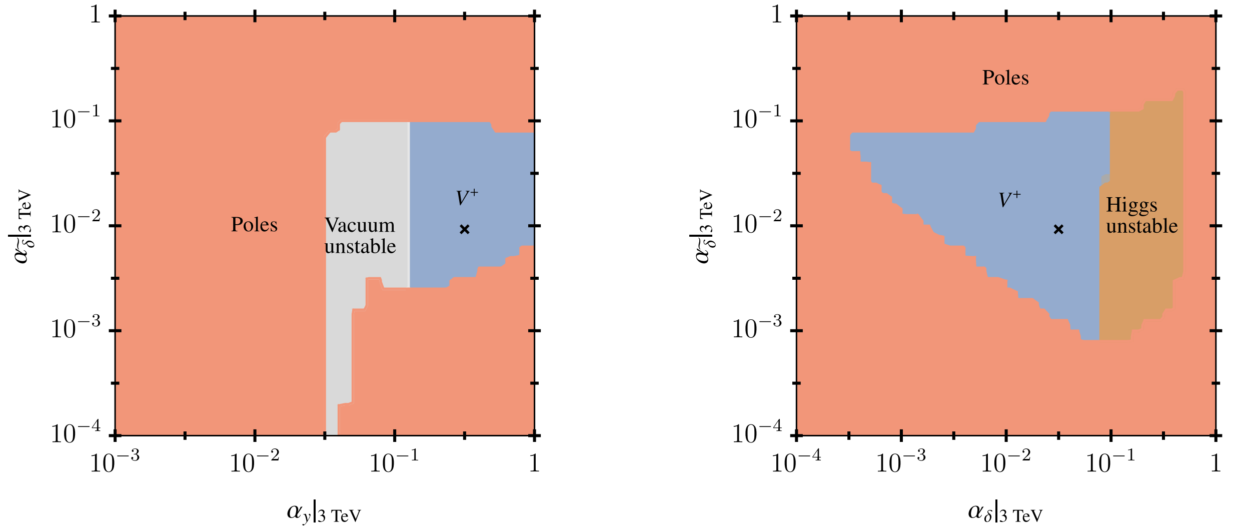

(a) $\alpha_y(\mu_0)$-$\alpha_{\tilde{\delta}}(\mu_0)$-plane for $\alpha_\delta(\mu_0) = 10^{-1.5}$. **(b)** $\alpha_\delta(\mu_0)$-$\alpha_{\tilde{\delta}}(\mu_0)$-plane for $\alpha_y(\mu_0) = 10^{-0.5}$.

Figure 8.8: BSM critical surface of BM4 in the $\alpha_y(\mu_0)$-$\alpha_{\tilde{\delta}}(\mu_0)$- (a) and $\alpha_\delta(\mu_0)$-$\alpha_{\tilde{\delta}}(\mu_0)$-plane (b) for $\mu_0 = 5$ TeV. The remaining BSM couplings are fixed as $\{\alpha_4, \eta, \alpha_u, \alpha_v, \alpha_w, \alpha_s\}|_{\mu_0} = \{2.45 \cdot 10^{-2}, 0, 10^{-4}, 10^{-5}, 10^{-6}, 10^{-2}\}$. Same color coding as Fig. 4.1a. Plots taken from [1].

PS is comparably harder to achieve in BM3 due to the lowest scale of the naive Landau pole resulting in the strictest constraints on $\alpha_{y,\delta,\tilde{\delta}}$, cf. Tab. 8.3. This can also be seen from the BSM critical surface in Fig. 8.6. Notably, in contrast to the other BMs it consists of two isolated pieces which are separated by the occurrence of Landau poles. While the first features sizeable $\mathcal{O}(10^{-1})$ values of both Higgs portal couplings $\alpha_{\delta,\tilde{\delta}}$, the latter requires one portal to be comparably small and both not to exceed values of $\sim 10^{-2}$. A Planck-safe RG flow in the latter piece is depicted in Fig. 8.7a. We find that it is overall more perturbative than in the other BMs with values of most couplings at the Planck scale $\lesssim 10^{-1}$ and the majority even $\lesssim 10^{-2}$. The reason is that only $\alpha_{y,4,u,v}$ and hence much less couplings than in the other BMs enter a walking regime.

We show the BSM critical surface and an exemplary Planck-safe RG flow of BM4 in Fig. 8.8 and Fig. 8.7b, respectively. Recall, that BM4 features a lower NP scale than the other BMs of $\mu_0 = 3$ TeV. As expected, also here we find a parameter space region giving rise to Planck-safe trajectories characterized by large α_y and moderate $\alpha_{\delta,\tilde{\delta}}$, cf. Tab. 8.3. PS is thereby enforced by a characteristic walking regime capturing $\alpha_{y,4}$ and the BSM quartics at strongly coupled values until beyond the Planck scale.

8.5 Phenomenological Implications

We now derive predictions for Z'-induced dineutrino branching ratios, work out collider signatures and discuss consequences of potential Z'-mediatedRH quark currents.

8.5.1 Predictions for $B \to K^{(*)}\nu\bar{\nu}$

The Z' couples to neutrinos due to the charges F_{L_i,ν_i} and hence contributes to decays $B \to H\nu\bar{\nu}$, $H = K, K^*, \ldots$ at tree-level. In absence of RH quark currents the effect on the corresponding branching ratios is universal and given by [240][4]

$$\frac{\mathcal{B}\,(B \to H\nu\bar{\nu})}{\mathcal{B}\,(B \to H\nu\bar{\nu})_{\text{SM}}} = \frac{1}{3}\left(\sum_i |1 + F_{L_i}a|^2 + |F_{\nu_i}a|^2\right) \qquad \text{where} \qquad a = \frac{-\sqrt{2}\pi(F_{Q_3} - F_{Q_2})g_4^2}{G_F\,\alpha_e\,M_{Z'}^2\,X_{\text{SM}}}, \tag{8.37}$$

with $X_{\text{SM}} = -12.64$ [250] encoding the SM contribution. From the BM charge assignments Tab. 8.2 and employing (8.37) we obtain the ratios 1.003, 1.05, 1.08 and 0.97 in BM1, BM2, BM3 and BM4, respectively. Since $|a| \ll 1$, the leading BSM effect stems from the interference of the LH Z' contribution with the SM. For RH neutrinos there is no such interference [251] and their contribution is only at the permille level. This explains the smallness of the BSM contribution in BM1, where the interference terms cancel due to $\sum_i F_{L_i} = 0$. As expected, the B anomalies generically point towards enhanced $\mathcal{B}\,(B \to H\nu\bar{\nu})$ [240]. An exception is BM4, where $a > 0$ along with $\sum_i F_{L_i} < 0$ results in a mild suppression due to a negative sum of interference terms. However, in all BMs the BSM effect on $b \to s$ dineutrino branching ratios only amounts to $\lesssim 10\%$ which is too small to be distinguished from the SM within present precision. In particular, it is not sufficient to explain the excess in $\mathcal{B}(B^+ \to K^+\nu\bar{\nu})$ hinted by the Belle II experiment [81, 82]. Moreover, while Belle II is expected to observe $\mathcal{B}(B \to K^{(*)}\nu\bar{\nu})$ at the SM level [252] and thus in all BMs, the projected sensitivity is insufficient to distinguish between our BMs and the SM.

8.5.2 Collider Signatures

From the partial Z' decay widths (7.17) and assuming negligible kinematic suppression of the decays $Z' \to \bar{\psi}\psi, \phi\phi$ we compute the total Z' widths in our models. They are in the ballpark of $\Gamma_{Z'}^{\text{tot}} = \text{few} \times 0.1\, M_{Z'}$ in all BMs, indicating a broad Z' due to large α_4. The precise values for the Z' widths and (tree-level) branching ratios in our BMs are summarized in Tab. 8.4.

If kinematically allowed, in all models the dominant Z' decay mode is $Z' \to \bar{\psi}_i\psi_i$ with flavor-summed BM specific branching ratios of $\sim 50\% - 80\%$. If the dominant decay $Z' \to \bar{\psi}\psi$ is kinematically forbidden, the total Z' width is reduced by a factor 2 (4-5) in BM1 and BM2 (BM3 and BM4) while all other branching

---

[4] Neutrinos are experimentally only indirectly detected as missing energy. Thus, we give the branching ratio prediction summing over neutrino flavors.

Model	jets	b	t	e	μ	τ	$\nu_{e,\mu,\tau}$	h	$\psi_{1,2,3}$	ϕ	$\Gamma_{Z'}^{\text{tot}}$
BM 1	0.5	0.5	0.5	0	15	15	15	0	54	0.2	$0.43\, M_{Z'}$
BM 2	14	1.5	1.5	0	9	9	18	0	46	0.1	$0.14\, M_{Z'}$
BM 3	5	0	0	0	4	4	8	0	79	0.1	$0.73\, M_{Z'}$
BM 4	0	0.9	0.9	0	3	11	14	0	72	0.2	$0.43\, M_{Z'}$

Table 8.4: Total Z' widths and branching ratios of different fermionic and scalar $Z' \to \bar{f}f, ss$ decays at tree-level in %. Numerical values are given neglecting fermionic, scalar as well as kinetic mixing and assuming $Z' \to \psi_i\bar{\psi}_i, \phi\phi$ to be kinematically open with negligible phase space suppression. If the dominant decay to $\psi\psi$ is forbidden (kinematically significantly suppressed), the other branching ratios increase by a factor of (up to) 2, 4 and 5 in BM1 and BM2, BM3 as well as BM4, respectively. Table adapted from [1].

ratios are correspondingly enhanced. Keeping in mind that ψ is a SM singlet and in combination with sizeable branching ratios of $\gtrsim 10\%$ to (LH and RH) neutrinos $\bar{\nu}_i\nu_i$, we learn that the Z' decays dominantly to invisibles with a total branching ratio of 65%-85%. This provides a smoking-gun signature of our model class. Moreover, all benchmarks feature sizeable branching ratios in muons and taus which differ among the individual benchmarks and range between 3% and 15%. BM2 and BM3 also exhibit sizeable branching ratios of 15% and 5% to jets, respectively, whereas this decay mode is negligible in BM1 and BM4. In combination, measuring Z' branching ratios at the level of 10% would allow to distinguish between the different benchmarks. Decays $Z' \to \bar{t}t, \bar{b}b, e^+e^-, hh, \phi\phi$ have negligible branching ratios of $\lesssim 1\%$ in all BMs.

The Z' can be produced at a hadron machine in $q\bar{q}$-fusion. A clean signal are high-energy Drell-Yan processes. The corresponding cross section reads [155, 253]

$$\sigma(pp \to Z'X \to f\bar{f}X) \simeq \frac{\pi}{6s} \sum_q c_q^f w_q(s, {M_{Z'}}^2)\,, \tag{8.38}$$

where $q = u, d, s, c, b$ and interference with the SM has been neglected. The model-independent functions $w_q(s, {M_{Z'}}^2)$ encode all necessary information on proton PDFs and QCD corrections. The coefficients

$$c_q^f = 16\pi^2\alpha_4\, (F_{q_L}^2 + F_{q_R}^2)\, \mathcal{B}(Z' \to f\bar{f}) \tag{8.39}$$

on the other hand are BM specific and depend on quark $U(1)'$ charges as well as the Z' branching ratios. We now deploy the results of a CMS search [243] for high p_T dileptons which gives Z' mass limits as a function of $c_{u,d}^\ell$ with $\ell = e, \mu$ and obtain

$$M_{Z'}^{\text{BM1}} \gtrsim 5.0 \text{ TeV}(5.4 \text{ TeV})\,, \quad M_{Z'}^{\text{BM2}} \gtrsim 5.9 \text{ TeV}(6.3 \text{ TeV})\,, \quad M_{Z'}^{\text{BM3}} \gtrsim 5.8 \text{ TeV}(6.8 \text{ TeV}) \tag{8.40}$$

at 95% c.l. for $2M_\psi \ll M_{Z'}$ ($2M_\psi > M_{Z'}$). The results however have to be taken with a grain of salt as the muon and electron channels were combined, whereas in our BMs the Z' does not decay to electrons. Moreover, s, c and b contributions to the production cross sections were not taken into account. For this reason we cannot derive a mass limit for BM4 where first-generation quarks are uncharged under the $U(1)'$. However, mass bounds as low as $M_{Z'} \gtrsim 1.2\,\text{TeV}$ have been obtained in similar models without couplings to light quarks [244, 254, 255], which serves as a ballpark estimate.

All our BMs can also be searched for at a future muon collider, where the large muon coupling $F_{L_2}g_4$ strongly enhances s-channel Z' production. We find for the corresponding LO BSM cross section with subsequent invisible Z' decay

$$\sigma(\mu^+\mu^- \to Z' \to \psi\bar{\psi}, \nu\bar{\nu}) = \frac{16\pi^3}{3} \frac{\alpha_4^2 \left(F_{L_2}^2 + F_{E_2}^2\right) s}{\left(M_{Z'}^2 - s\right)^2 + M_{Z'}^2 \Gamma_{Z'}^2} \left[2N_F F_\psi^2 + \sum_i (F_{L_i}^2 + F_{\nu_i}^2)\right] . \tag{8.41}$$

For $\sqrt{s} = 3\,\text{TeV}$ [256], it is enhanced w.r.t. the LO SM cross section

$$\sigma(\mu^+\mu^- \to Z \to \nu\bar{\nu}) = \frac{3\,s\,\left(g_Z^{\nu_L}\right)^2 \left[\left(g_Z^{\mu_L}\right)^2 + \left(g_Z^{\mu_R}\right)^2\right]}{48\pi \left(M_Z^2 - s\right)^2} \tag{8.42}$$

by a factor of 880, 72, 560 and 4800 in BM1-BM4[5], respectively, where the SM Z couplings $g_Z^{\mu_{L,R},\nu_{L,R}}$ can be read off from (2.18). The large enhancement in BM4 is due to resonant Z' production with $M_{Z'} = \sqrt{s}$. For a detailed muon collider study of Z' models for the B anomalies see [257].

8.5.3 Right-handed Quark Currents

Thus far, we focused on models with only LH FCNC quark couplings g_L^{bs} inducing $C_{9,10}^\mu$ which suffices to explain the B anomalies, c.f. Tab. 8.1, but always implies $R_{K^*} \simeq R_K$ [258]. However, LHCb data [47, 48] given in (8.2) indicate $R_{K^+} > R_{K^{*0}}$ at the 1σ level. If confirmed, $R_{K^*} \neq R_K$ hints at a non-vanishing RH coupling $g_R^{bs} \neq 0$ as at LO [258]

$$\frac{R_{K^*}}{R_K} \simeq 1 - 0.41\,(C_9'^\mu - C_{10}'^\mu), \tag{8.43}$$

c.f. also (8.22). $C_9'^\mu - C_{10}'^\mu \neq 0$ can be induced by assuming RH bs mixing in V_R^d by a small angle θ_d resulting in $g_R^{bs} \simeq (F_{D_3} - F_{D_2}) \sin\theta_d g_4$, see (7.11). We then obtain

$$\frac{C_9'^\mu}{C_9^\mu} = \frac{C_{10}'^\mu}{C_{10}^\mu} = \frac{g_R^{bs}}{g_L^{bs}} \equiv r, \tag{8.44}$$

with the fit in Tab. 8.1 suggesting $r \lesssim 0$. $r < 0$ ($r > 0$) then implies $R_{K^*} < R_K$ ($R_{K^*} > R_K$) where the B_s-mixing bound (7.12) currently allows for a deviation of the order $\sim 10\%$ ($\sim 20\%$) at the 2σ level in all BMs. Note that a potential cancellation between LH and RH contributions to B_s-mixing (7.13) requires positive $r = X_{B_s}$ or $r = X_{B_s}^{-1}$ which is disfavored by the data.

8.6 Summary

In this chapter we studied flavorful Z' models which can explain the B anomalies in a Planck-safe manner. We identified four viable BM models which fulfill all relevant theoretical and phenomenological constraints, most prominently from anomaly cancellation, Yukawa gauge invariance, EW precision data and neutral meson mixing. The main features of the individual BM models are summarized in Tab. 8.5. The BMs correspond to different global fit scenarios to experimental data (Tab. 8.1 and Fig. 8.1) and all induce NP in $b \to s\mu^+\mu^-$ transitions with $C_9^\mu - C_{10}^\mu \sim -1$ as favored by data. Potential subleading contributions to RH WCs $C_{9,10}'^\mu$ could also be realized in all BMs, see Subsec. 8.5.3.

Z' models explaining the B anomalies are generically plagued by the occurrence of subplanckian Landau poles, see Subsec. 8.1.3. While the $U(1)'$ gauge interaction is responsible for accommodating $b \to s\mu^+\mu^-$

---

[5] In this estimate we neglected subleading SM-BSM interference terms as well as SM contributions to the $\bar{\nu}_\mu \nu_\mu$ final state from t-channel W-exchange.

Model	μ_0	$\alpha_4(\mu_0)$	C_9^μ	C_{10}^μ	$Y_{ii}^{u,d}$	Y_{ii}^ℓ	Y_{ii}^ν	r_{B_s}	$\mathcal{B}(Z' \to \text{inv.})$	ν_R
BM 1	5 TeV	$1.87 \cdot 10^{-2}$	-0.83	0	✓	✓	X	0.35	73%	X
BM 2	5 TeV	$5.97 \cdot 10^{-3}$	-0.41	$-C_9^\mu$	✓	X	X	0.86	64%	✓
BM 3	5 TeV	$4.60 \cdot 10^{-2}$	-0.71	$+0.24$	✓	X	X	0.60	87%	✓
BM 4	3 TeV	$2.46 \cdot 10^{-2}$	-0.83	0	✓	✓	✓	0.70	86%	✓

Table 8.5: Overview of the characteristics of Planck-safeBM models from Tab. 8.2. We show the values of the NP scale $\mu_0 = M_{Z'}$, induced semimuonic WCs $C_{9,10}^\mu$ as well as the $U(1)'$ gauge coupling $\alpha_4(\mu_0)$ and indicate which diagonal fermion Yukawa couplings ($Y_{ii}^{u,d,e,\nu}$) are allowed by gauge invariance as well as whether RH neutrinos ν_R are included in the model. Furthermore, we give the branching ratio of invisible Z' decays $Z' \to \nu\bar{\nu}, \psi\psi$ and the room left by the B_s-mixing constraint $r_{B_s} \leq 1$. Table adapted from [1].

data, a large value of the BSM Yukawa α_y is key to push the notorious $U(1)'$ Landau pole beyond the Planck scale by inducing strongly coupled walking regimes as discussed in Sec. 8.4. Simultaneously, sizeable BSM quartics are able to stabilize the scalar potential via the (indirect) Higgs portal mechanism. Hence, the enlarged BSM sector with VLFs and matrix scalars S_{ij} is indispensable to achieve PS in our models. Moreover, the combination of phenomenological and theoretical constraints from B data and PS, respectively, greatly enhances the predictivity of the models and guides further model building.

The Z' is quite broad and decays dominantly to invisibles, which provides a smoking-gun signature of our model. Model specific branching ratios to dimuons, ditaus and jet of $\sim 0-20\%$ allow to distinguish between different BMs. Effects of the Z' on dineutrino branching ratios $B \to K^{(*)}\bar{\nu}\nu$ on the other hand do not exceed a few % in all BMs which is still within present theoretical uncertainties. Our models can be probed at hadron machines in Drell-Yan production of dimuons and ditaus as well as at future muon colliders. As of now, corresponding LHC searches generically imply mass bounds of $M_{Z'} \gtrsim 5$ TeV for a Z' explaining the B anomalies and coupling to light quarks.

8.7 Addendum: Implications of the Latest LHCb Measurement $R_{K^{(*)}} \simeq 1$

At the time this project [1, 233] was carried out data pointed to $R_{K^{(*)}} < 1$ at the 3σ level. However, the most recent LHCb data for $R_{K^{(*)}}$ [234, 235] of December 2022

$$\begin{aligned} R_K|_{[0.1,1.1]} &= 0.994^{+0.090}_{-0.082}(\text{stat})^{+0.029}_{-0.027}(\text{syst}), & R_K|_{[1.1,6.0]} &= 0.949^{+0.042}_{-0.041}(\text{stat})^{+0.022}_{-0.022}(\text{syst}), \\ R_{K^*}|_{[0.1,1.1]} &= 0.927^{+0.093}_{-0.087}(\text{stat})^{+0.036}_{-0.035}(\text{syst}), & R_{K^*}|_{[1.1,6.0]} &= 1.027^{+0.072}_{-0.068}(\text{stat})^{+0.027}_{-0.026}(\text{syst}) \end{aligned} \tag{8.45}$$

are in agreement with the SM within 1σ. Hence, $R_{K^{(*)}}$ now support LFU in rare B decays and the former experimental hints for μ-e universality violation disappeared. The origin of the deviation w.r.t. the previous result (8.2) was an intricate experimental problem related to electron misidentification in the former measurements [47, 48] that was just resolved in the latest update [234, 235]. Purely muonic observables such as angular observables and branching ratios discussed in Subsec. 8.1.1 were however not affected by electron misidentification and the tension of $b \to s\mu^+\mu^-$ data with the SM still persists. We now briefly discuss consequences of (8.45) for EFT fits to rare B decay data in Subsec. 8.7.1 and possible attempts to accommodate them in Z' in Subsec. 8.7.2, respectively.

Fit for	value	Pull$_{\text{SM}}$
C_9^μ	$-0.42^{+0.13}_{-0.14}$	$3.2\,\sigma$
$C_9^\mu = -C_{10}^\mu$	$-0.17^{+0.06}_{-0.06}$	$2.7\,\sigma$
C_9^ℓ	$-0.78^{+0.21}_{-0.21}$	$3.7\,\sigma$
$C_9^\ell = -C_{10}^\ell$	$-0.40^{+0.11}_{-0.11}$	$3.5\,\sigma$

Table 8.6: Results of the WET fit [259] to rare B decay data, including the new $R_K^{(*)}$ data [234, 235] of December 2022 (8.45). Given are the values of semileptonic WCs $C_{9,10}^{\ell(\mu)}$ in different LFU (muon-specific) 1d NP fit scenarios and their respective pull from the SM hypothesis. Table entries taken from [259].

8.7.1 Updated Fit Results

The new $R_{K^{(*)}}$ measurement (8.45) changes the overall picture of the $b \to s\mu^+\mu^-$ anomalies. This is seen in recent EFT fits to rare B decays [238, 259–261] including the new LHCb data, see [262] for a comprehensive overview. In particular, the overall pull from the SM is reduced, as $R_{K^{(*)}}$ ceased to be a key driver of the B anomalies. While the preferred patterns in the Dirac structure of semileptonic operators remain unchanged, i.e. NP scenarios with $C_9 \lesssim -C_{10} \lesssim 0$, the fits now unsurprisingly favor μ-e-universal rather than muon-specific NP. However, also muon-specific scenarios still increase the compatibility with data compared to the SM. The best fit is achieved for a sizeable μ-e-universal contribution and a small, muon-specific correction. These patterns are observed in all fits [238, 259, 261]. Despite using different statistical methods, hadronic parametrizations and software tools, the fit results are numerically in good agreement demonstrating the robustness of the results.

We exemplarily discuss the results from [259] in detail. Best fit values for the most favored 1d NP scenarios from [259] together with their pull from the SM are given in Tab. 8.6. The SM-pulls of 2.7-3.7σ are still significant but roughly halved compared to the old fit in Tab. 8.1 with $\sim 6\sigma$. The best fit result is obtained for a μ-e-universal $C_9^\ell \simeq -0.8$ very close to the former, muon-specific best-fit value of C_9^μ. Analogously, $C_9^\ell = -C_{10}^\ell \simeq -0.4$ is basically identical to the old best fit value of $C_9^\mu = -C_{10}^\mu$ in Tab. 8.1. This can be understood as electronic $b \to se^+e^-$ branching ratios and angular observables generically are experimentally less constrained than muonic ones. NP effects in semielectronic operators of the same magnitude as favored for semimuonic ones are typically allowed within experimental uncertainties. Hence, μ-e-universal scenarios are favored as simultaneously compatible with both $R_{K^{(*)}} = 1$ and $b \to s\mu^+\mu^-$ data. Muon-specific scenarios in comparison are slightly less favored with pulls of $\sim 3\sigma$. Moreover, the best fit values of $C_9^\mu \simeq -0.4$, $C_9 = -C_{10}^\mu \simeq -0.2$ are only roughly half as large as in the old fit Tab. 8.1 due to the generically induced tension with $R_{K^{(*)}}$. Hence, a LFU contribution is preferred by the data.

However, fit results for LFU NP in C_9^ℓ have to be taken with a grain of salt. The reason are potentially sizeable LFU contributions to $b \to s\ell^+\ell^-$ transitions from electroweak penguins with non-local charm loops. Those contributions can mimic a NP contribution to $C_{7,9}$ as they are coupled identically to the leptonic vector current [236, 262] which introduces an intrinsic bias in the fit. The magnitude and therefore relevance of such non-local charm contributions is theoretically hard to predict and therefore subject of an ongoing debate. One group even claims that $b \to s\mu^+\mu^-$ data can be entirely explained in the SM that way [260], in contrast to [238, 259, 261]. This disagreement arises due to the very general parametrization of the charm contributions in [260], which by construction allows to absorb any potential NP in C_9^ℓ in hadronic free parameters. Deploying a more sophisticated parametrization based on the analyticity of the amplitude and deriving dispersive bounds from unitarity constraints in contrast allows to control the uncertainty of the non-local charm contribution [109, 263]. The theory predictions of [109, 263] for $B \to K\mu^+\mu^-$,

$B \to K^*\mu^+\mu^-$ and $B \to \phi\mu^+\mu^-$ still exhibit sizeable tensions between data and the SM hinting that charm contributions are too small to explain the anomaly. This result is in agreement with the finding of [238] that there is now evidence for an explicit dependence of the best fit value for C_9^ℓ on the dilepton invariant mass squared q^2, as it would be caused by a loop contribution.

In conclusion, the new LHCb measurements of $R_{K^{(*)}}$ [234, 235] (8.45) in contrast to before now point towards μ-e universality. However, the $b \to s\mu^+\mu^-$ anomalies in several angular observables and branching ratios still persist, hinting the presence of NP. This is reflected in updated EFT fits such as [259]. While the overall pull from the SM is reduced, one-parameter fits for LFU NP in C_9^ℓ or $C_9^\ell = -C_9^\ell$ still exhibit a sizeable pull of $\gtrsim 3.5\sigma$ from the SM hypothesis. While these findings are still subject to uncertainties due to non-local charm loops there is increasing evidence that these contributions are too small to explain the anomalies in the SM. We conclude that strong hints for LFU NP in rare B decays remain to be present.

8.7.2 Attempts to Accommodate the New Data in Z' Models

In spite of the new LHCb LFU data [234, 235], our BMs presented in this chapter are still valid BSM models as they reduce the overall tension between theory predictions and data w.r.t. the SM. The reason is that they still resolve the $b \to s\mu^+\mu^-$ anomalies while being in tension with the latest $R_{K^{(*)}}$ data (8.45) only at the 2σ level, cf. [237]. Consequently, the pull of our BMs from the SM in recent fits is reduced from $\sim 6\sigma$ to $\sim 3\sigma$ [259]. In order to improve compatibility with data, we explored several different ansätze to modify our Z' models such that we obtain $R_{K^{(*)}} \simeq 1$ while still explaining the $b \to s\mu^+\mu^-$ anomalies.

The most natural strategy is to assume LFU Z' couplings $g_{L,R}^{ee} = g_{L,R}^{\mu\mu}$ to electrons and muons resulting in $R_{K^{(*)}} \simeq 1$ due to $C_{9,10}^e = C_{9,10}^\mu$ as favored by fits [259]. In this case the Z' contributes to $e^+e^- \to e^+e^-$ scattering at tree level. The induced SMEFT WCs $C_{ll,le,ee}^{1111}$ of the corresponding four-electron operators

$$Q_{ll}^{ijkl} = (\bar{L}\gamma_\mu L)(\bar{L}\gamma^\mu L), \qquad Q_{le}^{ijkl} = (\bar{L}\gamma_\mu L)(\bar{E}\gamma^\mu E), \qquad Q_{ee}^{ijkl} = (\bar{E}\gamma_\mu E)(\bar{E}\gamma^\mu E), \tag{8.46}$$

with $i,j,k,l = 1,2,3 \leftrightarrow e,\mu,\tau$ are however severely constrained by LEP-II data [248, 249, 264]. While

$$C_{ll}^{1111} = -\frac{g_4^2 F_{L_1}^2}{M_{Z'}^2}, \qquad C_{le}^{1111} = -\frac{g_4^2 F_{L_1} F_{E_1}}{M_{Z'}^2}, \qquad C_{ee}^{1111} = -\frac{g_4^2 F_{E_1}^2}{M_{Z'}^2} \tag{8.47}$$

induced in viable Z' models are always negative[6], LEP-II data [248] indicate positive $C_{ll,le,ee}^{1111}$. Generating $C_9^\ell \sim -0.8 \pm 0.2$ [259] while accommodating the charge hierarchy (8.29) dictated by the B_s-mixing bound (7.14) implies a lower limit on the absolute values of $C_{ll,le,ee}^{1111}$ resulting in a pull of at least $4.0\sigma, 2.5\sigma$ and 2.7σ from LEP-II data, respectively. Hence LFU Z' couplings are evidently disfavored. The tension with electron data can be slightly reduced in Z' models with moderate lepton flavor universality violation (LFUV), e.g. from a gauged $3B_3 - 2L_\mu - L_e$ symmetry [245]. However, this in turn causes increasing tension with $R_{K^{(*)}}$ (8.45) again, preventing a relevant overall increase of compatibility with data.

Another possibility to accommodate the new data on an EFT level is to assume complex WCs $C_{9,10}^\mu$. Neglecting $C_{9,10}'^\mu$, in this case we obtain [258]

$$R_K = \left(1 + 2\mathrm{Re}\frac{C_9^\mu - C_{10}^\mu}{C_9^{\mathrm{SM}} - C_{10}^{\mathrm{SM}}} + \frac{|C_9^\mu - C_{10}^\mu|^2 + |C_9^\mu + C_{10}^\mu|^2}{|C_9^{\mathrm{SM}} - C_{10}^{\mathrm{SM}}|^2}\right) / (\mu \to e)\,, \tag{8.48}$$

---

[6] Demanding $\mu - e$ universality with $F_{L_1,E_1} = F_{L_2,E_2}$ in combination with the previous constraints always yields models with $F_{L_1} = F_{E_1}$ and thus also $C_{le}^{1111} < 0$.

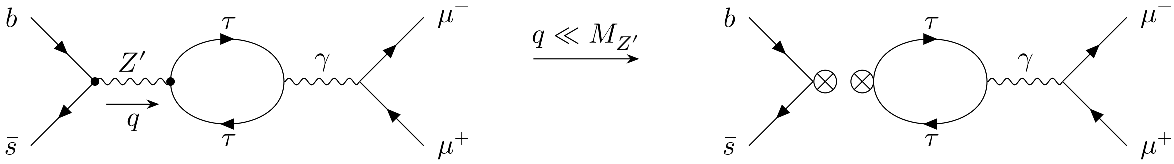

Figure 8.9: Dominant τ-loop induced BSM contribution to $C_9^{\mu,\mathrm{eff}}(q^2)$ in a $U(1)'$ model (left) and WET (right), respectively.

where the interference term with the SM vanishes for purely imaginary $C^\mu_{9,10}$, approximately yielding $R_K \simeq 1$. Such a scenario with complex $C^\mu_{9,10}$ was analyzed in detail in [265]. Inducing complex $C^\mu_{9,10}$ in a Z' model requires a complex g_L^{bs}, which can be induced by phases in the gauge to mass basis rotation V_L^d. However, complex values of g_L^{bs} are experimentally strongly constrained from CP violation. In particular, the Z'-contribution to B_s-mixing also induces a BSM contribution to the CP asymmetry $A_{CP}^{\mathrm{mix}}(B_s \to J/\psi\phi)$ via the interference of mixing and decay[7], see [227, 266] for details. Additional CP asymmetries arise in angular observables in $b \to s\mu^+\mu^-$ transitions [227, 266]. Whereas $A_{CP}^{\mathrm{mix}}(B_s \to J/\psi\phi)$ allows for either mostly real or mostly imaginary g_L^{bs}, semimuonic observables indicate a sizeable $\mathrm{Re}(g_L^{bs})$ [227, 266]. Hence, fits show that all complex values of g_L^{bs} with sizeable imaginary part are in strong tension with at least one of the experimental constraints from $A_{CP}^{\mathrm{mix}}(B_s \to J/\psi\phi)$, angular $b \to s\mu^+\mu^-$ observables or B_s-mixing, c.f. [266] Fig. 4 and [227] Fig. 6. This rules out a mostly imaginary g_L^{bs} to avoid large BSM effects in $R_{K^{(*)}}$.

A more sophisticated ansatz is to assume that NP in $b \to s\mu^-\mu^+$ is not induced at tree-level but rather from τ-loops, see Fig. 8.9. In this scenario, the light leptons are uncharged under the $U(1)'$ such that μ-e-universality is conserved while simultaneously tree-level contributions to WCs of four-electron operators (8.46) constrained by LEP-II [248] are evaded. The τ-loop contribution in Fig. 8.9 to $b \to s\mu^+\mu^-$ processes can be encoded in the effective WC [83, 267, 268]

$$C_9^{\mu,\mathrm{eff}}(q^2) = C_9^\mu + Y_{\mathrm{SM}}(q^2) + Y_{\tau\bar{\tau}}(q^2)\,, \tag{8.49}$$

which exhibits a dependence on the dilepton invariant mass squared q^2 and contains well-known SM loop contributions $Y^{\mathrm{SM}}(q^2)$ [83, 267, 268][8] as well as the BSM Z' contribution $Y_{\tau\bar{\tau}}(q^2) \propto -\frac{\alpha_e}{2\pi} C_9^\tau$ from the τ-loop, see [269] for details and a definition of $Y_{\tau\bar{\tau}}(q^2)$. Due to the loop and α_e suppression this scenario requires huge C_9^τ in order to generate the necessary $C_9^\ell \simeq -0.8$. However, C_9^τ is constrained by rare B decays [240, 269] and Drell-Yan processes [240]. In particular, we obtain $C_9^\tau < 510\,(910)$ for $C_9^\tau = C_{10}^\tau$ ($C_{10}^\tau = 0$) [269] from the BaBar bound $\mathcal{B}(B^+ \to K^+\tau^+\tau^-) < 2.25 \cdot 10^{-3}$ at 90% c.l. [270]. Saturating this bound for $C_{10}^\tau = 0$ we find that the allowed average contribution to C_9^μ is $-C_9^{\mu,\mathrm{eff}}(q^2) \lesssim 0.18$ for $q^2 \in [1.1\,\mathrm{GeV}^2, 6\,\mathrm{GeV}^2]$ which is only $\lesssim 20\%$ of the required value to account for the $b \to s\mu^+\mu^-$ anomalies. Moreover, assuring perturbativity of the Z'-τ-coupling, i.e. $g_L^{\tau\tau} < 4\pi$, and simultaneously evading the B_s-mixing bound (7.14) in this case requires $g_L^{bs}/g_L^{\tau\tau} \lesssim 10^{-5}$ and $M_{Z'} < 60\,\mathrm{GeV}$ which clearly rules out a heavy Z' of a few TeV as required by muon Drell-Yan searches [243, 244, 254, 255].

---

[7] Note that bounds from $A_{CP}^{\mathrm{mix}}(B_s \to J/\psi\phi)$ and δM_{B_s} have not been considered in [265] where only the effects of semileptonic WCs $C^\mu_{9,10}$ were investigated. In Z' models on the other hand, contributions to these observables are invariably generated by a complex g_L^{bs}.

[8] The SM contribution $Y_{\mathrm{SM}}(q^2)$ is typically already taken into account in fits such as [259].

Integrating out the Z' also generates the WCs $C_{3,5}$ of the four-quark operators

$$O_3 = (\bar{s}_L \gamma_\mu b_L) \sum_q (\bar{q}_L \gamma^\mu q_L), \qquad O_5 = (\bar{s}_L \gamma_\mu b_L) \sum_q (\bar{q}_R \gamma^\mu q_R) \tag{8.50}$$

at tree level which can contribute to $C_9^{\ell,\text{eff}}(q^2)$ via quark loops with the same topology as Fig. 8.9. However, $g_L^{bs}/g_L^{\tau\tau} \lesssim 10^{-5}$ from perturbativity together with B_s-mixing generically implies $|C_{3,5}(m_W)| \lesssim \mathcal{O}(10^{-3})$ which is of the same order as α_s-corrections to the WET matching [83] and has negligible impact on $C_9^{\ell,\text{eff}}(q^2)$ at the b mass scale μ_b. Hence, loop-induced μ-e-universal Z' contributions to $C_9^{\ell,\text{eff}}$ are also disfavored as an explanation for the $b \to s\mu^+\mu^-$ anomalies, in agreement with the analysis in [238].[9]

The last ansatz we discuss are LFU 3-3-1 models, see [272, 273] for a detailed introduction. The models feature a $SU(3)_C \times SU(3)_L \times U(1)_X$ gauge group which is broken to $SU(3)_C \times SU(2)_L \times U(1)_Y$, where the Z' corresponds to the gauge boson of $U(1)_X$. In this models, the hypercharge is given by [273]

$$Y = \beta T^8 + X\,, \tag{8.51}$$

where T^8 and X denote the corresponding generator of $SU(3)_L$ and the $U(1)_X$ charge, respectively. β is a free parameter, but only integer multiples of $\sqrt{3}, 1/\sqrt{3}$ yield integer charges for the gauge bosons. The models are very predictive and completely controlled by the free parameters β and $M_{Z'}$. The relevant Z' couplings read [273]

$$\begin{aligned} g_L^{bs} &= g_X V_{tb} V_{ts}^* \frac{\cos\theta_W}{\sqrt{3}\sqrt{1-(1+\beta^2)\sin^2\theta_W}}\,, \\ g_L^{\ell\ell} &= g_X \frac{-1+\sin^2\theta_W+\sqrt{3}\beta\sin^2\theta_W}{2\sqrt{3}\cos\theta_W\sqrt{1-(1+\beta^2)\sin^2\theta_W}}\,, \qquad g_R^{\ell\ell} = \begin{cases} -g_X \frac{\beta\sin^2\theta_W}{\cos\theta_W\sqrt{1-(1+\beta^2)\sin^2\theta_W}}\,, & \beta \neq \sqrt{3} \\ g_X \frac{\sqrt{1-4\sin^2\theta_W}}{\sqrt{3}\cos\theta_W}\,, & \beta = \sqrt{3} \end{cases}\,, \end{aligned} \tag{8.52}$$

with $U(1)_X$ gauge coupling g_X and $|\beta| < \sqrt{(1-\sin^2\theta_W)/\sin^2\theta_W} \simeq 1.82$ to avoid diverging or imaginary couplings. Moreover, for fixed β the B_s-mixing bound (7.14) implies a lower limit on $M_{Z'}$, which translates to an upper limit $-C_9^\ell \lesssim -0.01, -0.18, -0.03, -0.34, -0.09$ at 99% c.l. for the allowed values $\beta = 1/\sqrt{3}, -1/\sqrt{3}, \sqrt{3}, -\sqrt{3}, 0$, respectively[10]. Hence, even if saturating the 99% c.l. B_s-mixing bound and in the best scenario $\beta = -\sqrt{3}$ only $\sim 40\%$ of the value $C_9^\ell \simeq -0.8$ indicated by fits to B data can be accommodated. Thus, also 3-3-1 models do not offer a satisfactory explanation for the $b \to s\mu^+\mu^-$ anomalies.

In conclusion it seems rather hard to simultaneously accommodate all relevant experimental data from rare B decays, B_s-mixing and electroweak precision observables in models with a single Z' as new mediator. A possible loop-hole are models containing several Z's, e.g. [274, 275]. Clearly, future measurements are needed to further constrain NP effects in $b \to s\ell^+\ell^-$ and direct model building. In particular, the expected LHCb angular analysis of the $B \to K^* e^+e^-$ decay will hopefully shed new light on the B anomalies.

---

[9] Beyond Z' models, BSM charm-loop contributions to $C_9^{\ell,\text{eff}}$ via the charged-current four-quark operators $O_{1,2}^c$ (2.38) can potentially account for the B anomalies, see [271] for details.

[10] Note that β fixes the ratios $g_L^{bs}/(g_L^{\ell\ell}+g_R^{\ell\ell})$ and C_9^ℓ/C_{10}^ℓ.

9 A $U(1)^{\prime}$ Explanation to the *U*-Spin-*CP* Anomaly in Charm

In the previous chapter we have established Planck-safe Z' models as an explanation for the anomalies observed in rare $b \to s\mu^+\mu^-$ transitions. In this chapter, which is based on [3, 6], we explore in a similar manner the reach of flavorful $U(1)'$ models to address another flavor anomaly, namely the U-Spin-CP anomaly in charm. Interestingly, in this case data point to a subelectroweak, leptophobic Z' with a different phenomenology and RG behavior than the heavy Z' models for the B anomalies.

We introduce the U-Spin-CP-anomaly in charm in Sec. 9.1. Afterwards, in Sec. 9.2 we present our models, discuss constraints from charm data and work out the implied Z' mass scale. We then analyze the light Z' phenomenology in Sec. 9.3, before turning to the RG evolution in Sec. 9.4. In Sec. 9.5 we conclude.

9.1 The *U*-Spin-*CP* Anomaly in Charm

In 2019, the LHCb determination of [56]

$$\Delta A_{CP} = A_{CP}(K^+K^-) - A_{CP}(\pi^+\pi^-) = (-15.4 \pm 2.9) \cdot 10^{-4} \tag{9.1}$$

in $D^0 \to K^+K^-, \pi^+\pi^-$ decays with the CP asymmetries

$$A_{CP}(f) = \frac{\Gamma(D^0 \to f) - \Gamma(\bar{D}^0 \to f)}{\Gamma(D^0 \to f) + \Gamma(\bar{D}^0 \to f)} \tag{9.2}$$

provided the first observation of CP violation in charm. Recently, LHCb also directly measured [57]

$$A_{CP}(D_0 \to K^+K^-) = (6.8 \pm 5.4(\text{stat}) \pm 1.6(\text{syst})) \cdot 10^{-4}\ . \tag{9.3}$$

This allowed for the first time to fit the direct CP asymmetries in $D^0 \to K^+K^-, \pi^+\pi^-$ decays to

$$a^{d,\text{exp}}_{K^-K^+} = (7.7 \pm 5.7) \cdot 10^{-4}\ , \qquad a^{d,\text{exp}}_{\pi^-\pi^+} = (23.2 \pm 6.1) \cdot 10^{-4}\ , \tag{9.4}$$

providing a $3.8\,\sigma$ evidence of CP violation in $D^0 \to \pi^+\pi^-$. These results are puzzling for two reasons: Firstly, $a^d_{\pi^-\pi^+}$ is quite large, while in the SM CP violation is CKM suppressed, cf. (2.27). Applying CKM unitarity to parametrize the SM amplitude as

$$\begin{aligned} \mathcal{A} =& \mathcal{A}^{\text{SM}}(D^0 \to \pi^+\pi^-) = \lambda_d t + \lambda_b h e^{i\delta}\,, \\ \bar{\mathcal{A}} =& \mathcal{A}^{\text{SM}}(\bar{D}^0 \to \pi^+\pi^-) = \lambda_d^* t + \lambda_b^* h e^{i\delta} \end{aligned} \tag{9.5}$$

in terms of CKM factors $\lambda_q = V^*_{cq} V_{uq}$ and the relative strong phase δ yields

$$a^{d,\,\text{SM}}_{\pi^-\pi^+} = \frac{|\mathcal{A}|^2 - |\bar{\mathcal{A}}|^2}{|\mathcal{A}|^2 + |\bar{\mathcal{A}}|^2} \simeq 2 \cdot \text{Im}\left(\frac{\lambda_b}{\lambda_d}\right) \frac{h}{t} \sin\delta \lesssim 1.2 \cdot 10^{-3}\,\frac{h}{t}\,, \tag{9.6}$$

where we neglected contributions of higher powers in the CKM ratio $\lambda_b/\lambda_d \sim 10^{-3}$. A SM explanation of $a^{d,\text{exp}}_{\pi^+\pi^-}$ in (9.4) would thus require higher-order contributions h to be enhanced over the tree-level one by a factor of $\frac{h}{t} \gtrsim 2$ to compensate the CKM suppression. This required enhancement is significantly larger than theoretical estimations [276, 277] which however suffer from sizeable uncertainties due to hadronic final-state interactions. Notably, in the same manner the theoretical upper limit $|\Delta A^d_{CP}| \lesssim 2.4 \cdot 10^{-4}$ [278] on direct CP violation in ΔA_{CP} is a factor six lower than the measured value (9.1). Secondly, (9.4) implies a 2.7σ violation of the approximate SM $SU(2)$ U-spin symmetry rotating d and s quarks [279],

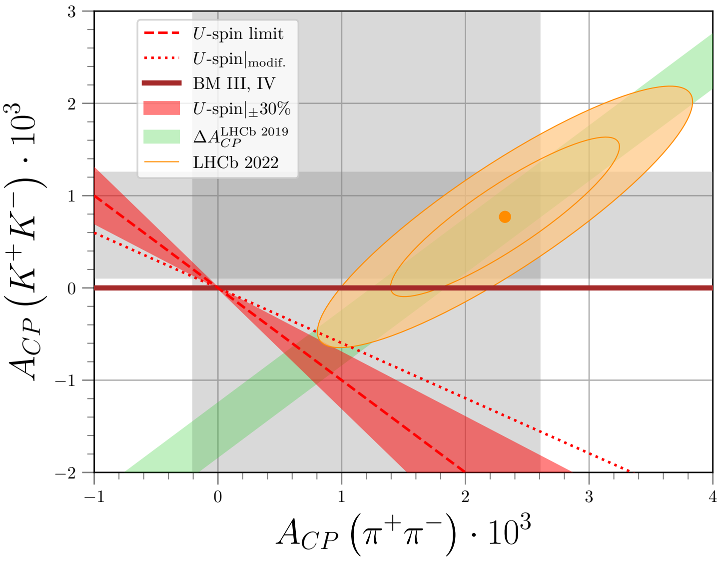

Figure 9.1: The U-spin-CP anomaly in charm. Shown are LHCb bounds on ΔA_{CP} (9.1) (green) and $A_{CP}(K^+K^-)$ (9.3) (grey), as well as $A_{CP}(\pi^+\pi^-) = (12 \pm 14)\cdot 10^{-4}$ from HFLAV [231] (grey). The best fit values $a^d_{K^+K^-,\pi^-\pi^+}$ (9.4) are shown including their correlation at 1σ and 2σ c.l. (orange). The U-spin limit (red dashed line) including $\lesssim 30\%$ SM-like U-spin breaking (red cones) and the modified U-spin relation (9.7) (red dotted line) are also indicated. In addition we show the predictions in our BM models BM III (for $G = 0$) and BM IV (both thick brown line), see Tab. 9.1. Figure adapted from [3].

which predicts $a^d_{\pi^-\pi^+} = -a^d_{K^-K^+}$. SM U-spin breaking is only of $\mathcal{O}\left(\frac{m_s - m_d}{\Lambda_{\text{QCD}}}\right) \simeq 30\%$ and thereby insufficient to explain the data by a factor ~ 4. This constitutes the U-Spin-CP anomaly in charm which is further illustrated in Fig. 9.1. Note that a SM-like 30% U-spin breaking contribution of opposite signs is more than enough to explain the enhancement of $\mathcal{B}(D \to K^+K^-)/\mathcal{B}(D \to \pi^+\pi^-) \simeq 2.8$ [155]. This suggests a modified U-spin relation

$$\frac{a^d_{K^-K^+}}{a^d_{\pi^-\pi^+}} = -\sqrt{\frac{\mathcal{B}(D \to \pi^+\pi^-)}{\mathcal{B}(D \to K^+K^-)}} \simeq -0.60\,, \tag{9.7}$$

also shown in Fig. 9.1 but only slightly alleviates the tension with data. Hence, the anomaly still remains.

9.2 Models

We now aim at explaining the U-Spin-CP anomaly in charm with flavorful Z' models. The Z' contributes to the decays $D^0 \to \pi^+\pi^-, K^+K^-$ at tree-level via the diagram shown in Fig. 9.2. The corresponding contribution to the direct CP asymmetries arises from interference with the SM and reads [280]

$$a^d_{\pi^-\pi^+,K^-K^+} = \frac{g_4^2}{M_{Z'}^2}\Delta\tilde{F}_R\left[c_{\pi,K}F_{Q_{1,2}} + d_{\pi,K}F_{D_{1,2}}\right], \tag{9.8}$$

where we assumed maximal relative strong and weak phases. The hadronic parameters $c_{\pi,K}$, $d_{\pi,K}$ include the LO RG running of WET WCs from the Z' to the charm mass scale as well as the hadronic matrix

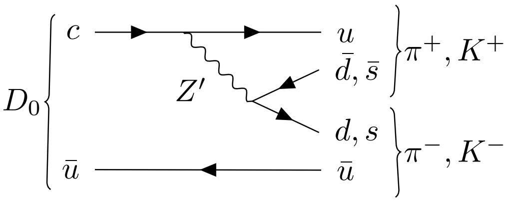

Figure 9.2: Leading Z' contributions to $D^0 \to \pi^+\pi^-, K^+K^-$ decay amplitudes. Figure adapted from [3].

Model	F_{Q_i}			F_{U_i}			F_{D_i}			F_{L_i}			F_{E_i}			F_{ν_i}		
BM III	0	0	0	G	-F	0	F	-G	0	0	0	0	0	-G	F	0	G	-F
BM IV	0	0	0	-F_u	F_u	0	F_d	0	-F_d	0	0	0	F_e	0	-F_e	F_ν	-F_ν	0

Table 9.1: Flavorful Z' BM charge assignments for the U-spin-CP anomaly in charm. Interestingly, swapping charges in the RH up sector of BM III, i.e. $F_{U_1} = -F, F_{U_2} = G$, yields an equally viable model to which we refer as BM III-s. In BM III(-s), (9.11) and (9.25) imply $|G/F| \ll 1$ also allowing for $G = 0$. In BM IV, F_e, F_u, F_d are related by anomaly cancellation while RH neutrinos can also be decoupled by setting $F_\nu = 0$. Unless stated otherwise we use the specific charge assignment (9.12). Table adapted from [3].

elements, see [3, 280] for details. Note that the latter suffer from sizeable uncertainties. The quantity

$$\Delta\tilde{F}_R = e^{i\phi_R}(\mathcal{F}'_{u_R})_{21} = \sin\theta_u \cos\theta_u \,(F_{U_2} - F_{U_1}) \tag{9.9}$$

relates to the RH $c \to u$ FCNC coupling g_R^{uc} and is obtained following Sec. 7.3. Here, we assumed RH c-u mixing by

$$V_R^u = \begin{pmatrix} \cos\theta_u & -e^{i\phi_R}\sin\theta_u & 0 \\ e^{-i\phi_R}\sin\theta_u & \cos\theta_u & 0 \\ 0 & 0 & 1 \end{pmatrix} , \tag{9.10}$$

with a mixing angle $\theta_u \neq 0$ and phase $\phi_R \neq 0$ as well as $F_{U_2} \neq F_{U_1}$. In contrast, we set $V_R^d = \mathbb{1}$ and $F_{Q_{1,2}} = 0$, in order to avoid kaon constraints according to (7.16). Moreover, applying (9.8) and (9.4) we demand

$$\frac{F_{D_2}}{F_{D_1}} = \frac{d_\pi \, a^{d,\mathrm{exp}}_{K^-K^+}}{d_K \, a^{d,\mathrm{exp}}_{\pi^-\pi^+}} \simeq -0.42^{+0.83}_{-0.13} , \tag{9.11}$$

i.e. explicit U-Spin breaking with a hierarchy $|F_{D_2}| \ll |F_{D_1}|$ to accommodate the data. In addition, we demand the cancellation of gauge anomalies according to (7.1) as well as gauge invariance of the top Yukawa coupling (cf. (8.12)) and prefer the absence 1-loop induced kinetic mixing via (7.8). The first typically requires the addition of RH neutrinos ν_R.

Applying this selection criteria results in the BM charge assignments BM III and BM IV in Tab. 9.1 with their characteristic patterns[1]. BM III features two independent charges F and G, where (9.11) implies $|G/F| \ll 1$ and we fix $F = 1$ without loss of generality. BM III-s, a variant of BM III with $F_{U_1} \leftrightarrow F_{U_2}$ is equally viable and exhibits a different phenomenology due to the suppressed charm coupling. In BM IV, the

---

[1] Note that we do not include BM I, II from [3] in this chapter, as they are clearly ruled out by the lepton bounds in Subsec. 9.3.2, see [3] for details.

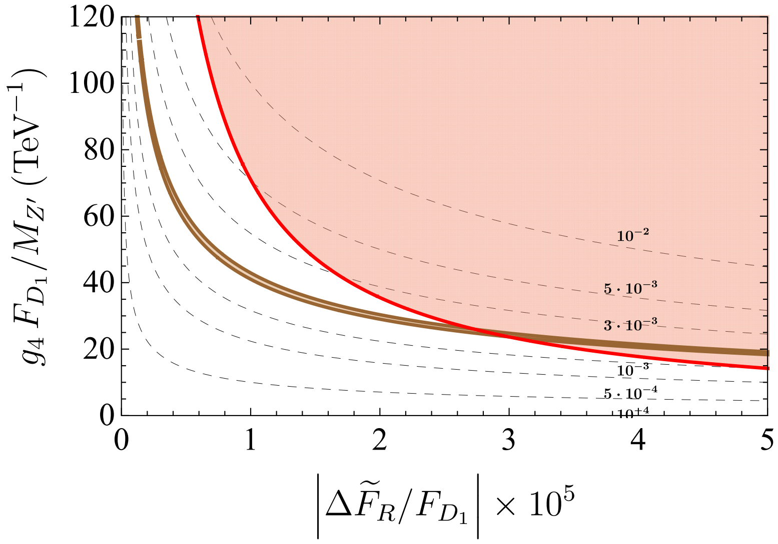

Figure 9.3: D-mixing constraints on our Z' models BM III (with $G=0$) and BM IV from Tab. 9.1. Shown are the parameter regions for $g_4\,F_{D_1}/M_{Z'}$ as a function of $\Delta\widetilde{F}_R/F_{D_1}$ with $d_\pi \simeq 0.1\ \mathrm{TeV}^2$, that allow to explain ΔA_{CP} (9.1) and $a^d_{\pi^-\pi^+}$ (9.4) at 1σ including additional 30% of hadronic uncertainty (brown). The regions are identical in both BMs and can be expressed semi-analytically as $g_4 F_{D_1}/M_{Z'} = c\,(\Delta\widetilde{F}_R/F_{D_1})^{-1/2}$ with factor $c = 0.133 \pm 0.003\,\mathrm{TeV}^{-1}$, see (9.15). Parameter regions excluded by D-mixing (9.14) are indicated in red. Moreover, curves corresponding to different values of $a^d_{\pi^-\pi^+}$ (dashed lines) are shown for comparison. Figure adapted from [3].

charges F_e, F_u, F_d are not independent but related by anomaly cancellation (7.1). Rational, anomaly free charges assignments obeying the hierarchy $|F_e| \ll |F_u|, |F_d|$ that will turn out to be required from lepton bounds (9.25) can be systematically derived by a Diophantine construction, see [3] for details. Neutrino charges F_ν on the other hand can be freely adjusted, allowing also to decouple them completely. Unless stated otherwise, in this work we set

$$F_d = 1, \qquad F_u = \frac{985}{1393}, \qquad F_e = \frac{1}{1393}, \qquad F_\nu = 0\,. \tag{9.12}$$

9.2.1 Charm Phenomenology and Constraints

Z' models contributing to ΔA_{CP} also invariably induce CP asymmetries in $D^{0,+} \to \pi^0\pi^{0,+}$ decays [280], where $D^+ \to \pi^0\pi^+$ explicitly requires isospin violation. In our BMs where $|F_{D_2}| \ll |F_{D_1}|$ all CP asymmetries involving pions are correlated as [280]

$$A_{CP}(\pi^+\pi^0) \simeq \frac{d_{\pi'}}{d_{\pi^0}} A_{CP}(\pi^0\pi^0) \simeq -\frac{d_{\pi'}}{d_\pi}\left(1 - \frac{F_{U_1}}{F_{D_1}}\right)\Delta A_{CP}\,. \tag{9.13}$$

As the hadronic parameters d_π, $d_{\pi'}$, d_{π^0} are all of similar size and $|F_{U_1}| < |F_{D_1}|$ in our models $A_{CP}(\pi^{0,+}\pi^0)$ are both of opposite sign and similar magnitude as $\Delta A_{CP} \sim 10^{-3}$, hence sizeable. More precisely, we find that the relative factor $1 - F_{U_1}/F_{D_1}$ equals 1 in BM III (with $G=0$) whereas in BM III-s (with $G=0$) and BM IV with the charge assignment (9.12) it generates an enhancement of 2 and 1.7 w.r.t. $|\Delta A_{CP}|$, respectively, due to the opposite signs of F_{U_1} and F_{D_1}.

Lepton	Observable	Ref.	Charge Constraint
e	Drell-Yan	[282]	$\sqrt{F_{L_1}^2+F_{E_1}^2}\lesssim 2.3\,\lvert F_{D_1}\rvert$
μ	$\mathcal{B}(D^0\to\mu^+\mu^-)$	[283]	$\lvert F_{L_2}-F_{E_2}\rvert\lesssim 0.8\,\lvert F_{D_1}\rvert$
	$\mathcal{B}(D^0\to\pi^0\mu^+\mu^-)$	[284]	$\sqrt{F_{L_2}^2+F_{E_2}^2}\lesssim 0.8\,\lvert F_{D_1}\rvert$
τ	Drell-Yan	[282]	$\sqrt{F_{L_3}^2+F_{E_3}^2}\lesssim 4.7\,\lvert F_{D_1}\rvert$
ν	$\mathcal{B}(D^0\to\pi^0+\text{inv.})$	[285]	$\lvert F_\nu\rvert\lesssim 110\,\lvert F_{D_1}\rvert$

Table 9.2: Most stringent bounds on lepton charges from charming dilepton processes. Indicated is the most constraining experimental observable, the corresponding reference as well as the resulting constraint on the $U(1)'$ charges for charged leptons and neutrinos using (9.15). Note that the bound for neutrinos gets more strict if more than one neutrino generation is charged. Moreover, the same bound applies for the charge F_ψ of a potential singlet VLFs ψ if $D^0\to\pi^0\bar\psi\psi$ is kinematically allowed.

We now discuss constraints on model parameters from D-mixing, Drell-Yan data as well as branching ratios of (semi-)leptonic or invisible D-decays[2]. The Z' contributes to D-mixing at tree-level, cf. Sec. 7.4. The experimental limit (7.15) for $g_L^{uc}=0$ yields the bound

$$\frac{g_4\,\Delta\tilde F_R}{M_{Z'}} < 7.1\cdot 10^{-4}\,\text{TeV}^{-1} \tag{9.14}$$

at 95 % c.l. in our BMs. The bound severely constrains the available parameter space, which is illustrated in $g_4F_{D_1}/M_{Z'}-\Delta\tilde F_R/F_{D_1}$ space in Fig. 9.3 (red). Curves explaining $a^d_{\pi^-\pi^+}$ (9.4) at 1σ and including additional 30% hadronic uncertainty are also shown for BM III and IV (brown). They are roughly given by

$$\frac{g_4\,F_{D_1}}{M_{Z'}}\sqrt{\frac{\Delta\tilde F_R}{F_{D_1}}}\simeq 0.13\,\text{TeV}^{-1}\ . \tag{9.15}$$

We see that D-mixing constrains $\Delta\tilde F_R/F_{D_1}\lesssim 3\cdot10^{-5}$. Hence large hierarchies $|\Delta\tilde F_R|\ll|F_{D_1}|$ are necessary to generate a sizeable $a^d_{\pi^+\pi^-}$ while simultaneously evading constraints from D-mixing (9.14), which can be achieved by adjusting the mixing angle to small values $\sin\theta_u\ll1$. D-mixing also implies a lower limit of 30 TeV^{-1} on $F_{D_1}g_4/M_{Z'}$, cf. Fig. 9.3, suggesting a low NP scale. More precisely, combining (9.4), (9.8) and (9.14) we find

$$\frac{g_4F_{D_1}}{M_{Z'}}\simeq\frac{1}{0.025\ \text{TeV}}\times\frac{|a^d_{\pi^+\pi^-}|}{0.002}\,, \tag{9.16}$$

indicating a light, subelectroweak Z', with significantly lower mass than in Chap. 8. This constitutes a central finding of our analysis with consequences for phenomenology.

The main constraints from dilepton processes in charm are summarized in Tab. 9.2. $U(1)'$ charges of electrons and muons are constrained by branching ratio measurements of rare (semi-)leptonic $D\to(\pi)\ell^+\ell^-$ decays with $\ell=\mu,e$, see [283, 284]. These turn out to give the strongest available constraints for muons. For $\ell=e,\tau$ in cotrast Drell-Yan constraints [282] are most stringent. From these bounds and applying (9.15) we learn that $U(1)'$ charges of charged leptons should not be excessive compared to the quark ones,

---

[2] The Z' contribution to four-quark operators $\bar cu\bar qq$ with $q=d,s$ is roughly 2-3 orders of magnitude smaller than the SM tree-level one from W exchange [3, 281]. Hence, the Z' contribution to $D\to\pi^+\pi^-$, K^+K^- branching ratios is negligible.

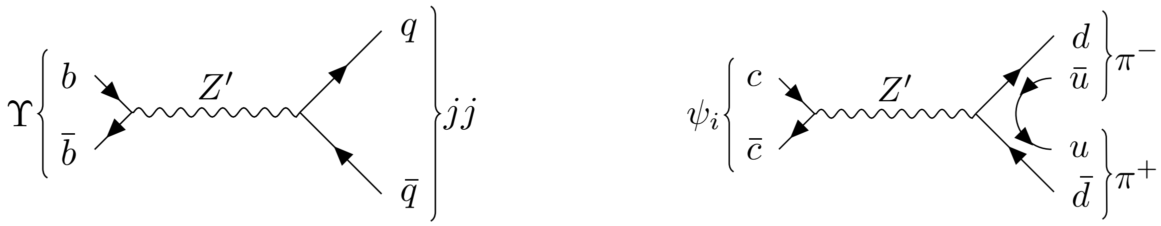

(a) $\Upsilon \to jj$. **(b)** $\psi_i \to \pi^+\pi^-$. Figure adapted from [3].

Figure 9.4: Tree-level Z' contribution to hadronic quarkonia decay amplitudes.

i.e. $F_{L_i,E_i} \lesssim (1...2) \cdot F_{D_1}$.

The Z' couplings to RH neutrinos are probed in (semi-)invisible decays. Following [286] and again applying (9.15) the most stringent bound is obtained from the BESIII upper limit $\mathcal{B}(D^0 \to \pi^0 + \text{inv.}) < 2.1 \cdot 10^{-4}$ at 90% c.l. [285]. We find that RH neutrino charges are only poorly constrained with $|F_{\nu_i}| \lesssim 110|F_{D_1}|$. This bound also constrains $U(1)'$ charges of potential light singlet VLFs ψ with $M_\psi < m_D/2$. Note that the constraint gets stricter if several flavors contribute to the decay.

Overall, we find that both BM III(-s) and BM IV from Tab. 9.1 pass all relevant charm constraints. All models exhibit explicit U-spin breaking $|F_{D_2}| \ll |F_{D_1}|$ and fulfill the bounds in Tab. 9.2 on lepton charges. Most importantly, explaining $a^d_{\pi^+\pi^-}$ while evading D-mixing constraints implies a subelectroweak Z' mass scale (9.16).

9.3 A Hadrophilic Z' of $\mathcal{O}(10\text{ GeV})$?

Constraints on couplings of a light Z' to quarks arise from low mass dijets. For $10\text{ GeV} \lesssim M_{Z'} \lesssim 50\text{ GeV}$ the strongest constraint stems from CMS [287] and their search for dijets in association with initial state radiation (ISR) [288], which approximately results in the limit $g_4 F_{D_1} \lesssim 0.5$. In combination with the constraints from charm (9.4) and (9.16) this yields the allowed mass range

$$10\text{ GeV} \lesssim M_{Z'} \lesssim 20\text{ GeV}\,. \tag{9.17}$$

Around and below 10 GeV constraints become model dependent due to quarkonia constraints.

9.3.1 Quarkonium Constraints

Around 10 GeV, severe constraints arise from $\Upsilon \to jj$ decays [289], cf. Fig. 9.4a, which apply to models with non-vanishing b-quark $U(1)'$ charges, i.e. our BM IV. Using [290] as well as the charge assignment (9.12) we find that explaining CP data (9.4) via (9.16) while accommodating bounds from $\Upsilon(1s)$ decays implies the mass limits

$$M_{Z'} \lesssim 7\text{ GeV} \qquad \text{or} \qquad M_{Z'} \gtrsim 15\text{ GeV} \qquad \text{(BM IV)}. \tag{9.18}$$

In BM III(-s) in contrast no constraints arise as the b quark is uncharged under the $U(1)'$.

Charm couplings of a GeV-ish Z' are probed in charmonium decays, cf. Fig. 9.4b, which provide additional constraints in BM III and IV. BM III-s in contrast evades all charmonium constraints as the charm quark is uncharged under the $U(1)'$ (for $G = 0$). The model can however be probed in hadronic processes involving first-generation quarks and invisibles. Potential Z' masses below a GeV would then due

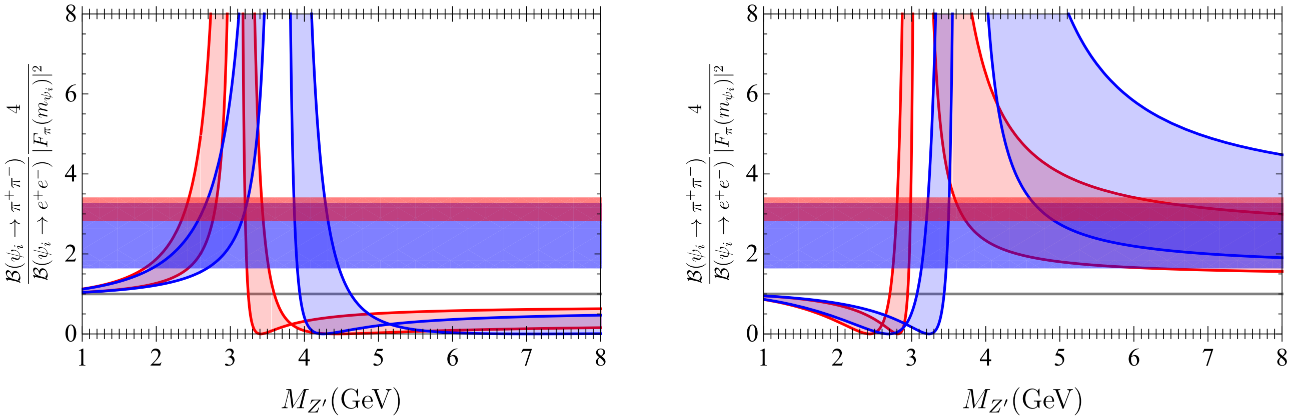

(a) BM III with $G = 0$.

(b) BM IV with charge assignment (9.12).

Figure 9.5: Z' mass constraints from charmonium decays in BM III (a) and BM IV (b). Horizontal red (blue) bands correspond to the experimental determination of the LHS of (9.19), using 1σ ranges of $J/\psi\,(\psi')$ data [155] and values of the pion form factor $|F_\pi(m_{J/\psi})| = 0.056$ ($|F_\pi(m_{\psi'})| = 0.04$) from $e^+e^- \to \pi^+\pi^-$ data [293]. Colored curves represent the corresponding predictions of the RHS of (9.19) in our BM models using (9.16) including experimental uncertainties from (9.4). The SM prediction for photon-exchange is also shown (grey). Figures taken from [3].

to (9.16) imply a feebly interacting Z', which could be searched for at forward facilities [291].

In BM III and IV, following [292] we find for the $\psi_i = J/\psi, \psi'$ pion-to-electron ratio of branching ratios

$$\frac{\mathcal{B}(\psi_i \to \pi^+\pi^-)}{\mathcal{B}(\psi_i \to e^+e^-)}\frac{4}{|F_\pi(m_{\psi_i})|^2} = \left|1+\frac{A_{Z'}}{A_\gamma}\right|^2, \quad \frac{A_{Z'}}{A_\gamma} = \frac{m_{\psi_i}^2}{m_{\psi_i}^2 - M_{Z'}^2 + iM_{Z'}\Gamma_{Z'}}\frac{3g_4^2 F_{U_2}(F_{U_1} - F_{D_1})}{8\pi\alpha_e}\,. \tag{9.19}$$

Here, $A_{Z'}$ and A_γ correspond to the Z'-induced and SM photon amplitude contributing to the pionic decay, respectively, and we neglected the numerically small SM Z contribution. F_π denotes the pion form factor which is extracted from $e^+e^- \to \pi^+\pi^-$ and pion-electron scattering data to $|F_\pi(m_{J/\psi})| = 0.056$ and $|F_\pi(m_{\psi'})| = 0.04$ [293]. As the Z' is (quasi-)electrophobic in our BMs its effect in this F_π determination method is negligible. The total Z' width $\Gamma_{Z'}$ is obtained from (7.17) and selected numerical values are given in Tab. 9.3. The normalization of the left-hand side (LHS) of (9.19) is chosen such that it equals one in the SM.

The constraints from (9.19) on BM III and IV as a function of $M_{Z'}$ are shown in Fig. 9.5. The experimental determination of the pion-to-electron ratio via the LHS of (9.19) from $J/\Psi(\psi')$ data [155] including 1σ uncertainties and using F_π from [293] is illustrated as red (blue) horizontal band. Crucially, the experimentally determined values are enhanced w.r.t. the SM (grey) roughly by a factor ~ 3, corresponding to a deviation of 7σ and $1.8\,\sigma$ from the SM, respectively. The theoretical prediction of the pion-to-electron-ratio via the RHS of (9.19) is indicated by red (blue) curves for $J/\psi\,(\psi')$ and assumes (9.16) to accommodate CP data (9.4) within their experimental uncertainty. The curves exhibit the expected resonance structure with peaks around $m_{J/\psi,\psi'}$ and only slowly decoupling NP contributions due to (9.16). The main difference between the two BM models originates from the $Z' - \gamma$ interference term in (9.19), which is of similar size but opposite sign. As a consequence, favored Z' mass regions in BM III are in the resonant region, whereas in BM IV they occur in the tails. More precisely,

$$\begin{aligned} &\text{BM III:} \quad 2.3\text{ GeV} \lesssim M_{Z'} \lesssim 2.8\,\text{GeV} \quad \text{or} \quad 3.2\text{ GeV} \lesssim M_{Z'} \lesssim 3.3\,\text{GeV}\,, \\ &\text{BM IV:} \quad 4.6\text{ GeV} \lesssim M_{Z'} \lesssim 7\,\text{GeV} \end{aligned} \tag{9.20}$$

allow to simultaneously accommodate $J/\psi, \psi', \Upsilon$ and charm CP data. In this scenario, our models also offer an explanation for the longstanding discrepancy between F_π extractions from $J/\psi \to \pi^+\pi^-$ decays and QCD estimates, see e.g. [294]. Hence, our Z' models can resolve two anomalies at once.

However, recall that our results are subject to sizeable uncertainties from several sources. That is first of all the uncertainty from the evaluation of hadronic matrix elements, cf. [3]. Moreover, if the Z' is light with a mass close to the charm scale sizeable corrections arise to tree-level WET matching, i.e. simply integrating out the Z'. The proper framework for charm physics in this case would rather be a 'WET+Z'' EFT including the Z' as dynamical d.o.f., cf. Sec. 2.5. We also neglect G-parity violating SM contributions to quarkonia decays, see [295] for details, noting that the tension of 7σ tension for J/ψ data is significant. Therefore in our analysis we also consider Z' masses in wider ranges than (9.20).

BM III also features sizeable Z' couplings to taus and RH neutrinos, which contribute to charmonium decays. In particular, the measurement of $\mathcal{B}(\psi' \to \tau^+\tau^-) = (3.1 \pm 0.4) \cdot 10^{-4}$ implies the allowed Z' mass ranges $M_{Z'} \lesssim 2.2$ GeV and 4.0 GeV $\lesssim M_{Z'} \lesssim 4.8$ GeV, very close to the mass window (9.20) from the pion form factor. $\mathcal{B}(J/\psi \to \text{inv.}) < 7 \cdot 10^{-4}$ [155] on the other hand requires either a very light Z' with $M_{Z'} < 0.7$ GeV or the BSM neutrino coupling to the Z' to be heavier than $\frac{m_{J/\psi}}{2}$ to kinematically forbid the corresponding decay. This might be achieved via the Dirac inverse see-saw mechanism, see [296], but is not investigated here.

9.3.2 Leptonic Constraints

We now work out constraints from light Z' decays in dileptons. In particular, we focus on dark photon searches via kinetic mixing (cf. Sec. 7.2), which provide severe constraints on electron and muon couplings [297] in the mass range of 1-100 GeV. A subelectroweak Z' mixes with the photon via

$$\mathcal{L}_\text{gauge} \supset \frac{-1}{4} \begin{pmatrix} F^{\mu\nu} \\ B'^{\mu\nu} \end{pmatrix}^\top \begin{pmatrix} 1 & \eta' \\ \eta' & 1 \end{pmatrix} \begin{pmatrix} F_{\mu\nu} \\ B'_{\mu\nu} \end{pmatrix}, \tag{9.21}$$

where the photon kinetic mixing parameter η' can be related to the hypercharge one η in (7.2) via $\eta' = \eta \cos\Theta_W$. It induces a coupling of the Z' to the electromagnetic current J^μ which reads

$$\mathcal{L}_\epsilon = -\epsilon e J^\mu Z'_\mu \qquad \text{with} \qquad \epsilon = -\frac{\eta'}{\sqrt{1-\eta'^2}}. \tag{9.22}$$

Experimental search limits on ϵ in (9.22) read

$$|\epsilon(M_{Z'})| \lesssim 10^{-3} \tag{9.23}$$

in both electrons and muons [298, 299]. This can be translated to a bound on Z' lepton couplings via

$$g_4 F_{L_{1,2},E_{1,2}} = \sqrt{8\pi\alpha_e}\epsilon \lesssim 4 \cdot 10^{-4}. \tag{9.24}$$

Along with the required Z' coupling strength to d-quarks from (9.16) this implies a severe suppression of electron and muon charges

$$\frac{F_{L_{1,2},E_{1,2}}}{F_{D_1}} \lesssim \frac{1}{750} \tag{9.25}$$

for $M_{Z'} \simeq 10$ GeV, significantly stronger than the D-decay and Drell-Yan constraints in Tab. 9.2.

Moreover, the kinetic mixing induced correction to the ρ parameter (7.4) in terms of ϵ reads

$$\frac{\rho - \rho^{\rm SM}}{\rho} = -\frac{\epsilon^2 \tan^2\theta_W}{2(1+\epsilon^2)}\frac{M_{Z'}^2}{M_Z^2} + \mathcal{O}\left(\frac{M_{Z'}}{M_Z}\right) . \tag{9.26}$$

It has the opposite sign than the experimental determination (7.5) but is within the 2σ region if

$$|\epsilon(M_Z)| \lesssim 4 \cdot 10^{-1}\ (7 \cdot 10^{-2}) \tag{9.27}$$

for $M_{Z'} \gtrsim 3\,\text{GeV}$ ($M_{Z'} \gtrsim 15\,\text{GeV}$). As the kinetic mixing parameter ϵ is not technically natural, simultaneously evading the dark photon bound (9.23) at $M_{Z'}$ and the ρ-parameter bound (9.27) at M_Z yields additional constraints on model parameters. In BM IV, the kinetic mixing fulfills (7.8) and becomes effectively natural as the leading naturalness breaking term arises only at 2-loop order and is suppressed by small α_b[3]. Hence, for tiny or vanishing ϵ both constraints are fulfilled. In BM III in contrast the RG evolution [3]

$$\epsilon(\mu) = \epsilon(\mu_0) - \delta_\epsilon \ln\left(\frac{\mu}{\mu_0}\right) + \text{2-loop}\,, \qquad \text{with} \qquad \delta_\epsilon = \frac{eFg_4}{3\pi^2} + \mathcal{O}(\epsilon) \tag{9.28}$$

along with $\frac{Fg_4}{M_{Z'}} \gtrsim 30\,\text{TeV}^{-1}$ from (9.16) implies a running

$$|\epsilon(M_Z) - \epsilon(M_{Z'})| \gtrsim \frac{10\,e}{\pi^2}\frac{M_{Z'}}{\text{TeV}} \ln\left(\frac{M_Z}{M_{Z'}}\right) \simeq 10^{-3} \tag{9.29}$$

between M_Z and $M_{Z'}$, where in the last step we used $M_{Z'} \simeq 3$ GeV. Hence, dilepton and ρ-parameter bounds can be avoided if $|\epsilon(M_Z)| \simeq \mathcal{O}(10^{-2})$, i.e. by tuning the contribution at the matching scale (9.27) at the level of 10%, see [3] for details.

In summary, dark photon bounds on light lepton $U(1)'$ charges (9.25) as well as dark photon and ρ-parameter bounds on kinetic mixing itself can be simultaneously avoided in both BMs. The key is a large charge hierarchy $|G/F| \lesssim 10^{-3}$ and $|F_e/F_d| \lesssim 10^{-3}$, retrospectively motivating the charge assignment (9.12), in BM III and IV, respectively, and small $\epsilon(M_{Z'})$.

9.3.3 Z' Decay

Z' branching ratios and total widths obtained from (7.17) are summarized in Tab. 9.3. We learn that the Z' decays promptly in all BMs with the largest branching ratio to light quarks. For low $M_{Z'}$ the results are however not accurate, as rather hadronic than partonic final states have to be considered. Decays to pairs of electroweak gauge or Higgs bosons are kinematically forbidden. In the same manner, also $\mathcal{B}(Z' \to \bar{b}b, \bar{c}c, \tau^+\tau^-)$ are kinematically suppressed or forbidden for a GeV-ish Z', while they can be sizeable for $M_{Z'} > 2m_f$ with $f = c, b, \tau$. Moreover, all models are muon- and electrophobic. In BM III(-s) the invisible decay to neutrinos can have a branching ratio in the ballpark of 10%-20%. Z' decays to pairs of charged particles receive contributions from kinetic mixing. Generically, the corresponding decay width are

---

[3] Recall that the top-quark is uncharged under the $U(1)'$ in BM IV.

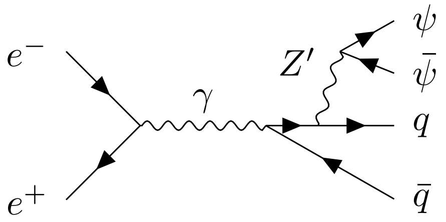

Figure 9.6: Production of hadrons in association with missing energy at e^+e^- machines in our BM models. A $q\bar{q}$-pair is produced via a s-channel photon and radiates off a Z' which decays invisibly to $\bar{\psi}\psi$ or $\bar{\nu}\nu$. This process constitutes a smoking-gun signature for the scenario $|F_{\psi/\nu}| \gtrsim |F_X|$ with $X = Q$, U, D, L, E. Figure adapted from [3].

Model	light quarks	b	c	e	μ	τ	ν	$\Gamma_{Z'}$ [GeV]
BM III$\vert_{M_{Z'}=2.5\text{ GeV}}$	75	0	0	0	0	0	25	$2 \cdot 10^{-3}$
BM III$\vert_{M_{Z'}=15\text{ GeV}}$	38	0	37	0	0	12	13	0.8
BM III-s$\vert_{M_{Z'}=2.5\text{ GeV}}$	86	0	0	0	0	0	14	$3 \cdot 10^{-3}$
BM III-s$\vert_{M_{Z'}=15\text{ GeV}}$	75	0	0	0	0	12	13	0.8
BM IV$\vert_{M_{Z'}=5\text{ GeV}}$	79	0	21	0	0	0	0	$2 \cdot 10^{-2}$
BM IV$\vert_{M_{Z'}=15\text{ GeV}}$	54	28	18	0	0	0	0	0.8

Table 9.3: Fermionic $Z' \to \bar{f}f$ branching ratios and total widths $\Gamma_{Z'}$ at tree-level for heavier and lighter Z' masses according to (9.17) and (9.20), respectively. Results for BM III(-s) and BM IV are given for $G \ll F$ and the charge assignment (9.12), respectively. Branching ratios differ between the indicated Z' masses, as the decays $Z' \to b\bar{b}$, $c\bar{c}$, $\tau^+\tau^-$ are kinematically forbidden or suppressed for a GeV-ish Z'. Kinetic mixing induced corrections to branching ratios via (9.30) are generically $\lesssim 10^{-7}$. Table adapted from [3].

suppressed w.r.t. unmixed ones by a tiny factor κ that reads

$$\kappa \sim \frac{\sum_f (2N_C^f q_f^2)\epsilon^2 e^2}{\sum_f N_C^f (F_{f_L}^2 + F_{f_R}^2) g_4^2} \propto \frac{\epsilon^2 e^2}{g_4^2}\,, \tag{9.30}$$

where q_f denotes the fermion electric charge. In combination with (9.27) and for $g_4 = \mathcal{O}(1)$ we obtain $\kappa \sim 10^{-7}$. This provides an order of magnitude estimate for kinetic mixing corrections to Z' branching ratios, which are negligible for our purposes.

Branching ratios to quarks and leptons can be suppressed by large $|F_\nu| \gg |F_{u,d,e}|$ in BM IV, cf. Tab. 9.2, yielding a mainly invisibly decaying Z'. The same can be achieved in all models by adding a SM singlet VLF ψ with $M_\psi < M_{Z'}/2$ and $|F_\psi| \gg |F_X|$ where $X = Q, U, D, L, E$ promoting $Z' \to \bar{\psi}\psi$ to the main decay mode, in analogy to our approach in Chap. 8 for a heavy Z'. This scenario implies characteristic signals involving quarks and invisibles. More precisely, the production of hadrons in association with missing energy from an invisibly decaying Z' radiated off final-state hadrons constitutes a smoking-gun signature of this scenario at e^+e^- machines, see Fig. 9.6. Unluckily, to our knowledge no experimental search for this process is available to date. Existing searches for $e^+e^- \to \gamma_{\text{ISR}} + (Z' \to \psi\bar{\psi})$ [300–302] are

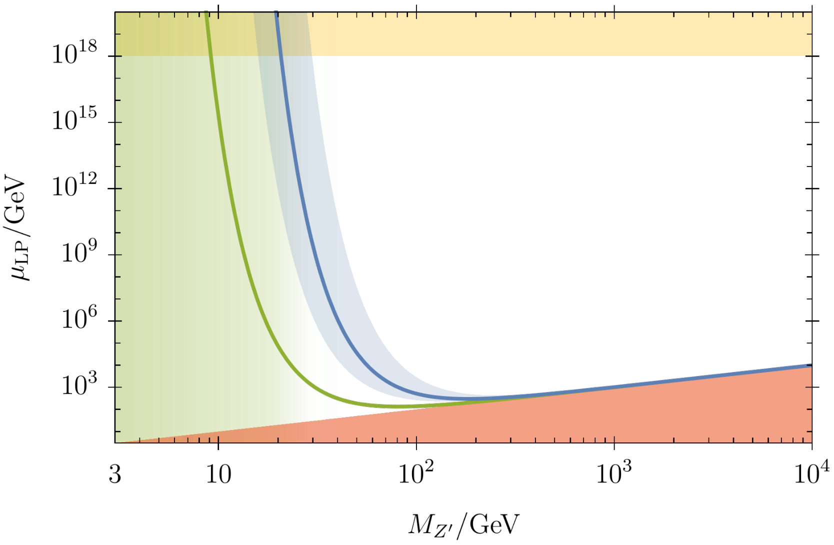

Figure 9.7: Scale μ_{LP} of the $U(1)'$ Landau pole as a function of $M_{Z'}$ in BM III (blue line) following (9.32) and including 30% uncertainty in $a^d_{\pi^+\pi^-}$ in (9.16) (blue band). The preferred Z' mass range is shaded in green. In the presence of a dark VLF, the pole is systematically shifted towards lower scales (green line). The red shaded area is excluded, as $\mu_{\mathrm{LP}} \leq M_{Z'}$. The Planckian regime is indicated in yellow. Figure taken from [3].

significantly less constraining as the corresponding cross sections are strongly suppressed by ϵ^2 or $F^2_{E_1}$ even for $\mathcal{B}(Z' \to \psi\bar{\psi}) \simeq 100\%$. Note however that $F_{\nu,\psi}$ cannot be arbitrarily large due to the occurrence of Landau Poles close to the electroweak scale, which is detailed in the next subsection.

9.4 RG Evolution

We now examine the consequences of the required size of the NP contribution in (9.16) on the RG evolution of our models. Perturbativity of all $U(1)'$ fermion couplings, i.e. $F_X^2\alpha_4 \lesssim 1 \Leftrightarrow F_X g_4 \lesssim 4\pi$, results in an upper bound

$$M_{Z'} \lesssim 400 \text{ GeV} \tag{9.31}$$

on the Z' mass. However, much stricter constraints arise from demanding the scale μ_{LP} of the notorious $U(1)'$ to be above a certain minimal scale μ_{min}. The location of the pole is approximately given by

$$\mu_{\mathrm{LP}} \simeq M_{Z'} \exp\left(\frac{(4\pi)^2 \Lambda^2}{M^2_{Z'}}\right), \tag{9.32}$$

cf. (3.6), with the NP scale $\mu_0 \simeq M_{Z'}$ and a characteristic scale Λ. (9.32) implies $\mu_{\mathrm{LP}} \simeq M_{Z'}$ for $M_{Z'} \gtrsim 4\pi\Lambda$. Hence, avoiding Landau poles close to $M_{Z'}$ requires $M_{Z'} \ll 4\pi\Lambda$. With (3.6), we find for Λ

$$\frac{1}{\sqrt{B_4}\Lambda} = \frac{g_4(M_{Z'})}{M_{Z'}} \simeq \frac{1}{30 \text{ GeV}}, \tag{9.33}$$

where B_4 is the $U(1)'$ 1-loop coefficient (3.7) and we applied (9.16) in the last step. Note again that in this case the characteristic scale is three orders of magnitude lower than for the B anomalies, where $\sqrt{B_4}\Lambda \simeq 40$ TeV, cf. Subsec. 8.1.3 for details. Ideally, in the spirit of PS we would now like to demand the Landau pole (9.32) to only occur beyond $\mu_{\text{min}} = M_{\text{Pl}}$. Due to the low characteristic scale dictated by (9.33) we find that this option implies quite stringent bounds on the Z' mass. The location of the Landau pole as a function of $M_{Z'}$ is illustrated in more detail in Fig. 9.7 for BM III, where from $B_4 = \frac{32}{3}F^2$ and (9.33) we obtain $\Lambda \simeq 10$ GeV. Here, avoiding Landau poles below $\mu_{\text{min}} = M_{\text{Pl}}$ ($\mu_{\text{min}} = 1\,\text{TeV}$) requires light, subelectroweak

$$M_{Z'} \lesssim 20\,\text{GeV}\ (81\ \text{GeV})\,, \tag{9.34}$$

in agreement with mass constraints from dijets (9.17) and quarkonium data (9.20). The Landau pole appears significantly lower in the presence of a dark VLF ψ, which is shown exemplarily for $F_\psi = 4F$.

It is not clear whether PS might still be achievable for a very light, GeV-ish Z' that pushes the Landau pole beyond M_{Pl}. The reason are sizeable uncertainties in our analysis presented above from several sources. Firstly, we only use the naive 1-loop Landau pole estimate (9.32) in (9.34), which generically gets more strict when taking into account higher loop orders. Moreover, we so far completely neglected the $U(1)'$ breaking scalar ϕ which is necessary to generate the Z' mass. While sizeable phenomenological effects at low energies can be avoided by choosing a large BSM scalar mass, its quartic couplings might be crucial to cure the notorious Higgs metastability via the direct or indirect Higgs portal mechanism, cf. Sec. 5.1. At the same time, its $U(1)'$ charge $F_\phi \neq 0$ enhances the running of α_4 and thereby aggravates the Landau pole problem. This effect can however be kept under control by choosing a small $|F_\phi| \ll 1$. Eventually, a sizeable uncertainty arises when deploying the running in the full UV model all the way from the EW scale down to GeV-ish energies as it is potentially subject to large logarithmic corrections, cf. Sec. 2.5. Deriving a reliable RG flow for a GeV-ish Z' would therefore rather require to compute the RG flow between the Z' and EW scale in a 'WET+Z'' EFT, match it to the full BSM model at the EW scale and then deploy the full BSM RGEs up to M_{Pl}.

9.5 Summary

Recent LHCb charm data (9.3) along with ΔA_{CP} (9.1) hint at a sizeable violation of two approximate symmetries of the SM: CP and U-spin, see Fig. 9.1. While hadronic uncertainties in the corresponding $D^0 \to K^+K^-$, $\pi^+\pi^-$ decays are still large, the direct CP asymmetries (9.4) taken at face value can be interpreted as a hint for NP.

In this chapter we explored the reach of flavorful $U(1)'$ models as a BSM explanation for charm CP data. The shape of viable models is severely narrowed down by various experimental and theoretical constraints. Nevertheless, we identified three BMs Tab. 9.1 which fulfill all relevant constraints, most importantly from D-mixing, rare D decays, dijets and dark photon searches. In consequence, the BMs exhibit very characteristic patterns: they feature a light, subelectroweak Z' of $\lesssim 20$ GeV, which is muon- and electrophobic and couples only to $SU(2)_L$ singlet fermions. Moreover, they imply specific signals such as sizeable $A_{CP}(\pi^{+,0}\pi^0)$ and enhanced $\pi^+\pi^-$, $\bar{D}D$ (, $\tau^+\tau^-$, $\bar{\nu}\nu$) production. The models might also be able to address the large isospin breaking in $\psi(3770) \to D^+D^-, \bar{D}^0D^0$ decays [155] and in case of BM IV potentially the U-spin puzzle in hadronic B decays [303]. This has however to be clarified by future investigations.

BM III and IV can be further probed in charmonium decays. Interestingly, a very light Z' of $M_{Z'} \simeq 3$ GeV in BM III or $M_{Z'} \simeq 4-7$ GeV in BM IV also allows to explain the measured enhancement of $J/\psi, \psi' \to \pi^+\pi^-$ branching ratios and to thereby resolve the longstanding pion formfactor discrepancy between extraction from e^+e^- data and $J/\psi, \psi'$ decays, see Fig. 9.5. Models may also feature large couplings to neutrinos or dark VLFs. This scenario can be tested at e^+e^- machines in final states involving hadrons and missing energy, cf. Fig. 9.6, but is also constrained by demanding a controlled RG evolution.

The presented $U(1)'$ BM models are generically plagued by a low energy $U(1)'$ Landau pole close above the matching scale, which prevents us from establishing PS in our BMs. The reason for this is the in comparison to the B anomalies discussed in Chap. 8 very low characteristic scale (9.33) implied by data. Nearby poles can therefore only be avoided if the Z' is quite light with $M_{Z'} \lesssim$ few × 10 GeV, see Fig. 9.7.

It remains as a future task to rigorously check whether PS might be achievable for a very light Z' in the GeV range. Recall that the accuracy of our our RG analysis in Sec. 9.4 for this scenario was quite limited. A robust PS analysis would in contrast be rather complex and require to compute the RG flow up to full 2-loop order, explicitly including the full scalar sector and in a 'WET+Z'' EFT. It would then have to be matched onto the full UV model at the EW scale and evolved further to the Planck scale using full BSM RGEs.

10 Conclusion and Outlook

In this thesis we demonstrated the power of the RG based concept of Planck safety as a guideline for BSM model building. In particular, we worked out several fundamental RG mechanisms towards PS in minimal models at full 2-loop accuracy and systematically scrutinized their complete BSM parameter spaces. We also investigated the interplay and complementarity between Planck safety and BSM phenomenology. Thereby, we pointed out corresponding synergies in both minimal and more sophisticated models, such as $U(1)'$ extensions addressing flavor anomalies in the beauty and charm sector.

After revisiting the full 2-loop RGEs of gauge-Yukawa theories and especially the SM we introduced the notion of PS as bottom-up counterpart to AS in Chap. 3. Planck-safe models by definition exhibit a well behaved RG evolution of couplings without any Landau poles or vacuum instabilities all the way up to the Planck scale $M_{\text{Pl}} \simeq 10^{19}$ GeV where quantum gravity effects are expected to set in. In particular, PS requires to cure the notorious SM Higgs metastability. Demanding PS then results in bounds on BSM model parameters which are widely independent of and complementary to experimental constraints. Thereby, PS greatly enhances the predictivity of BSM models which also motivates its application in phenomenologically driven model building.

To start with, we investigated PS in SM extensions featuring BSM vector-like fermions, singlet scalars or both in Chap. 4, Chap. 5 and Chap. 6, respectively. In particular, we worked out the basic, underlying RG mechanisms for PS in these models taking into account higher loop effects and systematically scanned the complete available parameter spaces spanned by BSM masses, multiplicities, charges and couplings.

In VLF models (Chap. 4) we identified the strong and novel electroweak gauge portal mechanisms as minimal pathways to PS. They are based on the presence of SM charged BSM matter that enhances the running of gauge couplings. This results in an uplift of the Higgs quartic, which in wide ranges of masses and multiplicities allows to achieve vacuum stability without inducing subplanckian Landau poles. Moreover, for thirteen suitable VLF representations ψ renormalizable mixed SM-BSM Yukawa portals à la $\kappa\bar{\psi}Hf_{\text{SM}}$ are available. If sizeable, they offer a unique way to tame potential poles in the gauge sector and induce PS in strongly coupled walking via the newly established Yukawa portal mechanism. While VLF models without Yukawa portal are hardly experimentally constrained, the portal coupling induces fermionic mixing, VLF decays and if flavorful FCNCs, which can result in mass bounds of up to a few 100 TeV.

In Chap. 5 we then turned to SM extensions based on singlet scalars S. Generically, the models feature a more complex scalar potential, exhibiting a Higgs portal coupling $\delta(H^\dagger H)(S^\dagger S)$ as well as pure BSM quartics. The portal coupling enhances the running of the Higgs quartic α_λ and promotes Higgs stability via the direct Higgs portal mechanism. Notably, we demonstrated that stability can also be achieved for tiny values of the portal coupling via the indirect Higgs portal mechanism. In this case, sizeable pure BSM quartics induce a fast RG growth of the portal coupling and thereby eventually also of α_λ. BSM vacuum stability conditions interestingly also allow for negative values of BSM quartics. While negative portal couplings although allowed by stability are found to be entirely excluded by PS, pure BSM couplings of flavorful $SU(N_F) \times SU(N_F)$ matrix scalars are compatible with PS, enabling also the flavor-asymmetric vacuum configuration V^-. After SSB, the Higgs portal induces mass mixing between the SM and BSM Higgs mode. This generically results in a reduction of most Higgs couplings, such as the triple Higgs or hZZ coupling, which is however controlled by the small mixing angle. Crucially, the mixing also induces an unsuppressed enhancement of the Higgs quartic self-interaction of a factor a few or even larger, providing a novel smoking gun signatures of our models with experimental prospects at future hadron machines even for very heavy BSM scalars.

Combining the presented minimal BSM sectors in Chap. 6 we afterwards focused on a more complex model featuring VLQs and matrix scalars. Here, key to PS is a large value of the new BSM Yukawa coupling $y\bar{\psi}_i S_{ij}\psi_j$ which induces walking regimes and allows to push the notorious hypercharge pole beyond the Planck scale. In the pole free parts of the parameter space, vacuum stability can then arise through the interplay of the gauge, Yukawa and Higgs portal mechanisms. Phenomenologically, the models are probed in direct and indirect searches. Crucially, SMEFT fits for some models and vacuum configurations allow to completely exclude PS from TeV-ish NP. In particular, combined mass bounds can exceed those from measuring the running of gauge couplings and from direct searches. If not too heavy, BSM particles are singly and pair produced at colliders. This implies novel characteristic signals such as resonant $\psi \to dS \to d\bar{d}d, dgg$ decays to three-jet final states.

In the remainder of this thesis we aimed at achieving PS in flavorful Z' models addressing flavor anomalies which we introduced in Chap. 7. The Z' can induce FCNC couplings via generation dependent charges but is subject to various experimental and theoretical constraints from anomaly cancellation, EW precision observables and meson mixing. Moreover, Z' models for flavor anomalies generically feature subplanckian, low energy Landau poles, that have to be tamed by an extended BSM Yukawa sector.

In Chap. 8 we constructed four Planck-safe Z' models explaining the ongoing anomalies observed in $b \to s\mu^+\mu^-$ transitions. While the heavy Z' is key to explain the flavor data by inducing WET WCs $C_9^\mu - C_{10}^\mu \simeq -1$, PS is achieved via the inclusion of singlet VLFs and a matrix scalar featuring a large BSM Yukawa coupling α_y. Strong bounds on model parameters arise in particular from B_s-mixing and dimuon Drell-Yan searches which typically imply a heavy Z' of $M_{Z'} \gtrsim 5\,\text{TeV}$. Interestingly, Planck-safe Z' explanations predict a dominantly invisibly decaying Z', providing a characteristic signature at colliders. We also tried to modify our models in order to accommodate the latest LHCb measurement of $R_{K^{(*)}} \simeq 1$ [234, 235] which now to good accuracy suggest μ-e-universality in rare B decays. In particular, we analyzed scenarios with μ-e-universal charge assignments, imaginary semileptonic WCs, τ-loop induced $b \to s\ell^+\ell^-$ transitions as well as 3-3-1 models. However, it turned out that each ansatz was excluded by different constraints, respectively, showing that simultaneously accommodating all relevant experimental data in BSM models based on a single Z' is a rather involved task.

Moving to charm physics, in Chap. 9 we exploited the possibility to explain the sizeable violations of U-spin and CP in $D^0 \to K^+K^-, \pi^+\pi^-$ decays indicated by LHCb [56, 57] in a Z' model. Surprisingly, charm CP asymmetries in combination with D-mixing bounds suggest a subelectroweak Z' while the large required coupling generically excludes PS due to low-energy Landau poles. The models are severely constrained by rare D-decays, dijets and dark photon searches which imply a light, leptophobic Z' of $\lesssim 20$ GeV. A GeV-ish Z' is further probed in Υ and charmonium decays. Notably, it also allows to resolve the longstanding pion formfactor discrepancy between extraction from $e^+e^- \to \pi^+\pi^-$ and $J/\psi \to \pi^+\pi^-$ data.

By and large, in this thesis we demonstrated that Planck safety is a powerful and well-motivated tool for BSM model building. To date, the overall number of anomalies in particle physics is small and decreasing. Hence, the possibility of a great desert without NP up to energies possibly as high as the Planck scale has to be taken for real. This calls for novel directions in model building. The core focus on a safe RG evolution up to highest energies therefore promotes Planck safety to a prime candidate to cross the desert. The implied characteristic links between the UV fate and the low-energy phenomenology of BSM models thereby further augment the rich future prospects of Planck safety.

In order to fully exploit the potential of Planck safety, several open questions remain to be addressed in future works. Most importantly, the generically large coupling values in walking regimes sourced by the Yukawa or Higgs portal mechanism call for a dedicated analysis at higher loop orders in order to infer their perturbative persistence and stability. Moreover, minimal BSM models featuring charged scalars such as leptoquarks provide ideal natural laboratories to further investigate the interplay of the gauge, Yukawa and Higgs portal mechanisms and invite future studies. Finally, the successful projects presented in this thesis motivate the application of Planck safety also in other areas of phenomenologically driven model building such as cosmology, dark matter or neutrino physics. We are looking forward to further pursue this exciting endeavor in the future.

A Notations, Conventions and Parameters

Within this thesis we work in natural units, i.e. we set $\hbar = c = 1$, where $\hbar$ denotes the reduced Planck constant and c is the speed of light. Hence, all physical observables have dimensions of (inverse) powers of energy, typically given in powers of electron volt (eV).

A.1 Chiral Fermion Fields

Chiral fermion fields

$$\psi = \psi_L + \psi_R, \qquad \bar{\psi} = \overline{\psi_L} + \overline{\psi_R} \tag{A.1}$$

consist of a LH $\psi_L = P_L\psi$ and RH $\psi_R = P_R\psi$ component with the chirality projectors

$$P_L = \frac{1-\gamma^5}{2}, \qquad P_R = \frac{1+\gamma^5}{2}\,. \tag{A.2}$$

where the fifth Dirac matrix is defined as

$$\gamma^5 = \mathrm{i}\gamma^0\gamma^1\gamma^2\gamma^3 = \frac{\mathrm{i}}{4!}\epsilon^{\mu\nu\rho\sigma}\gamma_\mu\gamma_\nu\gamma_\rho\gamma_\sigma \tag{A.3}$$

and $\epsilon^{\mu\nu\rho\sigma}$ denotes the totally anti-symmetric tensor of rank four obeying $\epsilon_{0123} = 1$. Furthermore, it holds

$$\overline{\psi_{L,R}} = \psi^\dagger_{L,R}\gamma^0 = \bar{\psi}_{R,L} \tag{A.4}$$

A detailed overview of the Dirac algebra as well as explicit expressions for Dirac matrices and fermion spinors can be found in [64, 65].

A.2 Experimental Input Parameters

In this section we give all relevant experimental input parameters that have been used in this thesis, which were mostly taken from the PDG [155].

The SM gauge, Yukawa and quartic couplings

$$\alpha_i = \frac{g_i^2}{16\pi^2}\,, \qquad \alpha_{t,b} = \frac{y_{t,b}^2}{16\pi^2}\,, \qquad \alpha_\lambda = \frac{\lambda}{16\pi^2}\,, \tag{A.5}$$

were extracted with great accuracy at $\mu_{\text{ref}} = 200\,\text{GeV}$ in the $\overline{\text{MS}}$-scheme in [162] and read

$$\begin{aligned} \alpha_1(\mu_{\text{ref}}) &= 8.15474\cdot 10^{-4}, & \alpha_2(\mu_{\text{ref}}) &= 2.64950\cdot 10^{-3}, & \alpha_3(\mu_{\text{ref}}) &= 8.41148\cdot 10^{-3},\\ \alpha_t(\mu_{\text{ref}}) &= 5.40400\cdot 10^{-3}, & \alpha_b(\mu_{\text{ref}}) &= 1.48916\cdot 10^{-6}, & \alpha_\lambda(\mu_{\text{ref}}) &= 7.82285\cdot 10^{-4}, \end{aligned} \tag{A.6}$$

where we neglected all other fermion Yukawa couplings due to their numerical smallness.

The Fermi constant G_F (2.30) and weak mixing angle in the $\overline{\text{MS}}$-scheme at the Z-boson mass are given as [155]

$$G_F = 1.1663788(6)\times 10^{-5}\ \text{GeV}^{-2}, \qquad \sin^2\theta_W(M_Z) = 0.23121(4)\,, \tag{A.7}$$

respectively.

We now turn to the masses of SM particles. The electroweak and Higgs boson masses read [155]

$$M_W = 80.377 \pm 0.012\,\text{GeV}, \quad M_Z = 91.1876 \pm 0.0021\,\text{GeV}, \quad M_h = 125.25 \pm 0.17\,\text{GeV}\,. \tag{A.8}$$

The SM lepton masses are determined to

$$m_e = 511.0\,\text{keV}, \quad m_\mu = 105.66\,\text{MeV}, \quad m_\tau = 1.777\,\text{GeV}, \tag{A.9}$$

with negligible errors [155]. Furthermore, the quark masses in the $\overline{\text{MS}}$-scheme are given as

$$\begin{aligned} m_u(2\,\text{GeV}) &= 2.16^{+0.49}_{-0.26}\,\text{MeV}, & m_d(2\,\text{GeV}) &= 4.67^{+0.48}_{-0.17}\,\text{MeV}, & m_s(2\,\text{GeV}) &= 93.4^{+8.6}_{-3.4}\,\text{MeV}, \\ m_c(m_c) &= 1.27 \pm 0.02\,\text{GeV}, & m_b(m_b) &= 4.18^{+0.03}_{-0.02}\,\text{GeV} & m_t(m_t), &= 162.5^{+2.1}_{-1.5}\,\text{GeV}\,. \end{aligned} \tag{A.10}$$

The absolute values of CKM matrix elements numerically are [155]

$$|V_\text{CKM}| = \begin{pmatrix} 0.97435 \pm 0.00016 & 0.22500 \pm 0.00067 & 0.00369 \pm 0.00011 \\ 0.22486 \pm 0.00067 & 0.97349 \pm 0.00016 & 0.04182^{+0.00085}_{-0.00074} \\ 0.00857^{+0.00020}_{-0.00018} & 0.04110^{+0.00083}_{-0.00072} & 0.999118^{+0.000031}_{-0.000036} \end{pmatrix}. \tag{A.11}$$

Equivalently, they can be obtained in the Wolfenstein parametrization (2.27) from the parameters [155]

$$\lambda = 0.22500 \pm 0.00067, \qquad A = 0.826^{+0.018}_{-0.015}, \qquad \rho = 0.159 \pm 0.010, \qquad \eta = 0.348 \pm 0.010\,. \tag{A.12}$$

Furthermore we make use of the following meson and quarkonium masses [155]

$$\begin{aligned} m_{B^0} &= 5.27965(12)\,\text{GeV}\,, & m_{B^\pm} &= 5.27934(12)\,\text{GeV}\,, & m_{B_s^0} &= 5.36688(14)\,\text{GeV}\,, \\ m_{D^0} &= 1.86484(5)\,\text{GeV}\,, & m_{D^\pm} &= 1.86966(5)\,\text{GeV}\,, & & \\ m_{K^0} &= 497.611(13)\,\text{MeV}\,, & m_{K^\pm} &= 493.677(16)\,\text{MeV}\,, & m_{K^*} &= 845(17)\,\text{MeV}\,, \\ m_{\pi^0} &= 134.9768(5)\,\text{MeV}\,, & m_{\pi^\pm} &= 139.57039(18)\,\text{MeV}\,, & & \\ m_{J/\psi} &= 3.096900(6)\,\text{GeV}\,, & m_{\psi'} &= 3.68610(6)\,\text{GeV}\,, & m_{\Upsilon(1s)} &= 9.46040(10)\,\text{GeV}\,. \end{aligned} \tag{A.13}$$

B Details on Planck Safety in Minimal VLF Models

In this appendix we give some additional surface plots illustrating Planck safety in minimal VLF models.

B.1 Gauge Portal

B.1.1 Higher Loop Orders

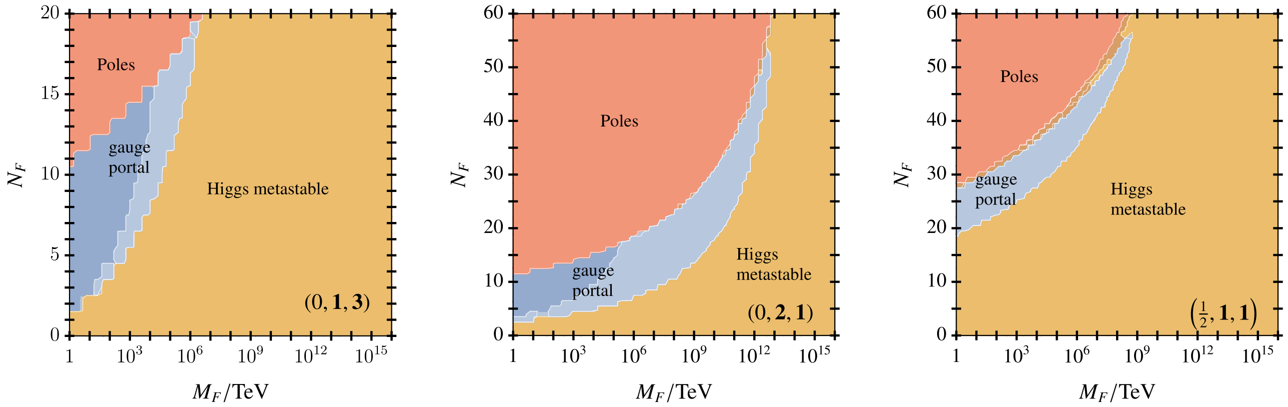

(a) The strong gauge portal at 222 loop order, same as Fig. 4.1a.

(c) The weak gauge portal at 222 loop order, same as Fig. 4.2a.

(e) The hypercharge portal at 222 loop order, same as Fig. 4.3a.

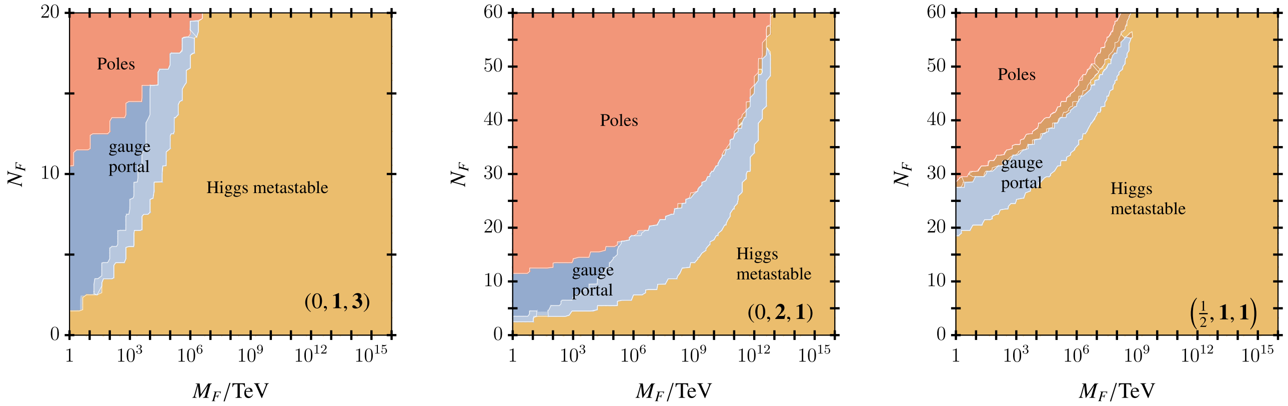

(b) The strong gauge portal at 432 loop order.

(d) The weak gauge portal at 432 loop order.

(f) The hypercharge portal at 432 loop order.

Figure B.1: Gauge portals at different loop orders. Shown are the BSM critical surfaces in the (N_F, M_F) plane for the strong (a, b), weak (c, d) and hypercharge (e, f) portal with indicated VLF representations at loop order 222 and 432 in the gauge, Yukawa and scalar sector, respectively. While the first ansatz takes into account the same loop order for all couplings, the latter applies the highest available loop order in each sector. The BSM critical surfaces are for all portals basically identical in both scenarios. Same color coding as Fig. 4.1a.

B.1.2 Higher Representations

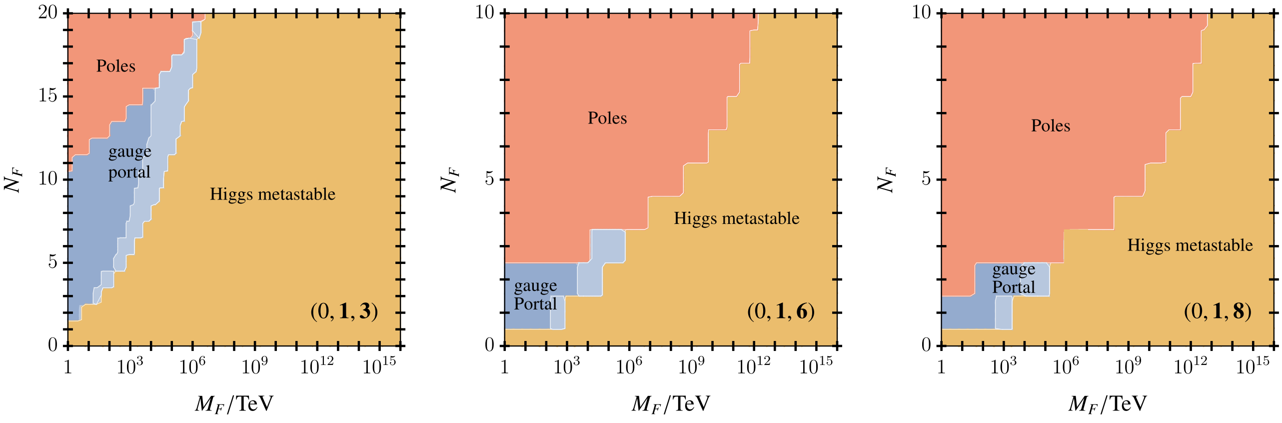

(a) $d_3 = \mathbf{3}$, same as Fig. 4.1a.

(b) $d_3 = \mathbf{6}$.

(c) $d_3 = \mathbf{8}$.

Figure B.2: The strong gauge portal at full 2-loop order for VLFs charged as $(0, \mathbf{1}, d_3)$ for $d_3 = \mathbf{3}$ (a) and higher representations $d_3 = \mathbf{6}$, $\mathbf{8}$ (b, c) under $SU(3)_C$. Shown is the BSM critical surface in the (N_F, M_F) plane. Same color coding as Fig. 4.1. For higher d_3 the Planck safety window is systematically shifted towards lower N_F and shrinks (Note the different scaling of the N_F-axes).

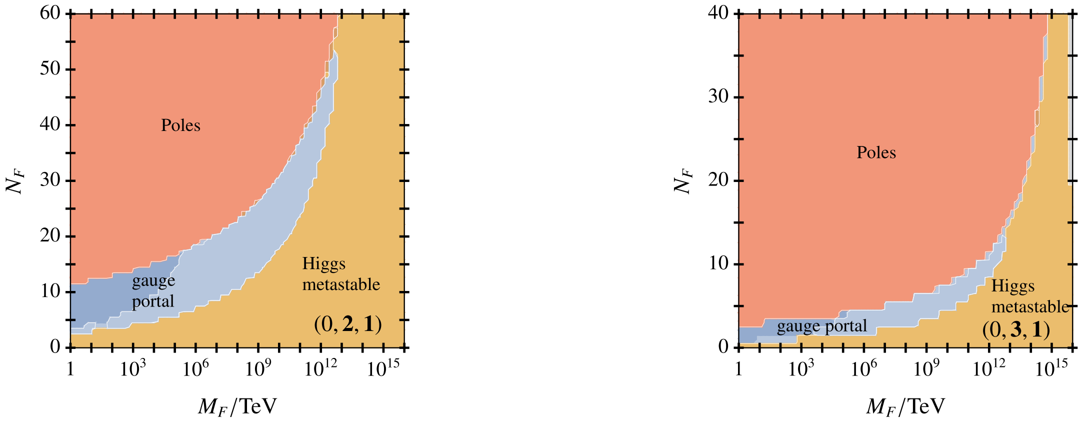

(a) $d_2 = \mathbf{2}$, same as Fig. 4.2a.

(b) $d_2 = \mathbf{3}$.

Figure B.3: Weak portal at full 2-loop order for a SM extensions with VLLs charged as $(0, d_2, \mathbf{1})$ under the SM. Shown is the BSM critical surface of the in the (N_F, M_F) plane for $d_2 = \mathbf{2}$ (a) and $d_2 = \mathbf{3}$ (b). The stability window shrinks for higher representations (Note the different scaling of the N_F-axes). Same color coding as Fig. 4.1.

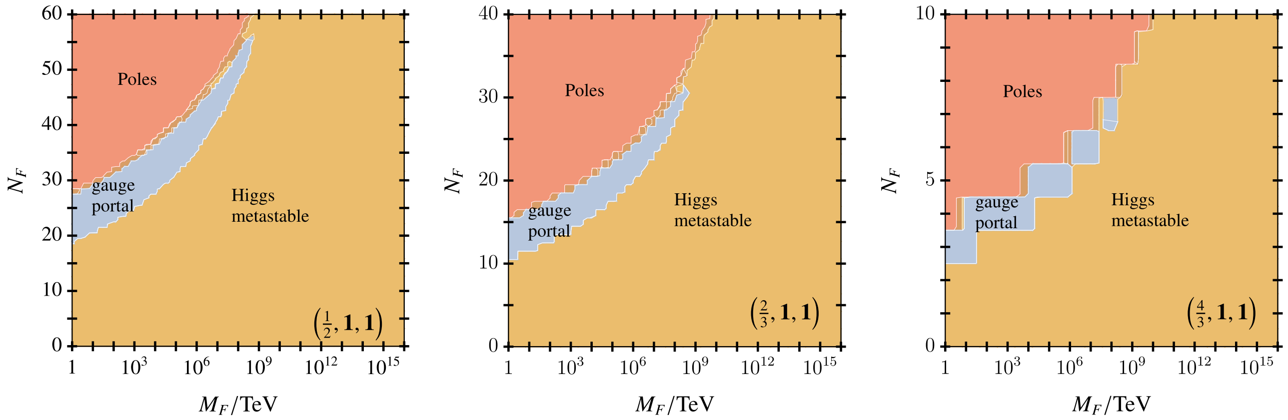

(a) $Y_F = \frac{1}{2}$, same as Fig. 4.3a.

(b) $Y_F = \frac{2}{3}$.

(c) $Y_F = \frac{4}{3}$.

Figure B.4: Hypercharge portal at full 2-loop order for a SM extensions with VLLs charged as $(Y_F, \mathbf{1}, \mathbf{1})$ under the SM. Shown is the BSM critical surface of the in the (N_F, M_F) plane for $Y_F = \frac{1}{2}$ (a), $Y_F = \frac{2}{3}$ (b) and $Y_F = \frac{4}{3}$ (c). The stability window in N_F is significantly reduced for higher Y_F (note the different scaling of the N_F-axes). Same color coding as Fig. 4.1.

B.2 Yukawa Portal

B.2.1 Higher Loop Orders

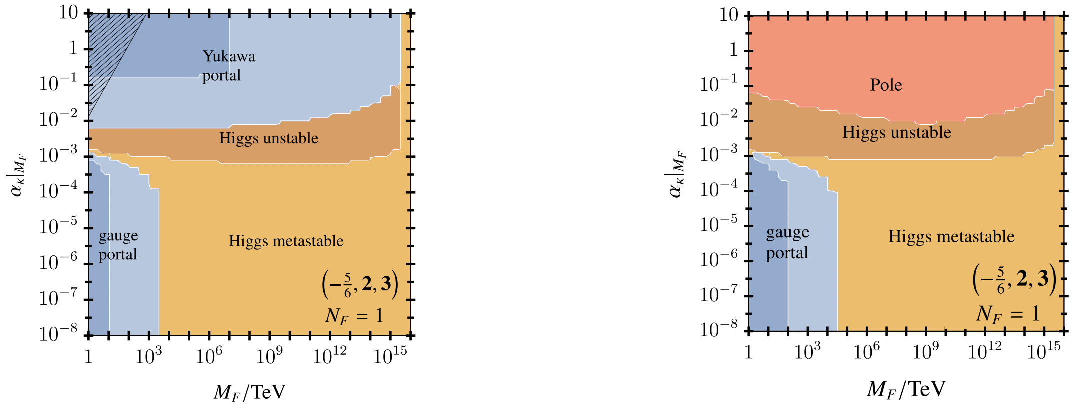

(a) The Yukawa portal at 222 loop order, as Fig. 4.8a.

(b) The Yukawa portal at 432 loop order.

Figure B.5: The Yukawa portal at different loop orders. Exemplarily shown are the BSM critical surfaces in the (N_F, M_F) plane in model M featuring $N_F = 1$ VLF charged as $(\frac{5}{6}, \mathbf{2}, \mathbf{3})$ under the SM at loop order 222 (a) and 432 (b) in the gauge, Yukawa and scalar sector, respectively. While the first ansatz takes into account the same loop order for all couplings, the latter applies the highest available loop order in each sector. At order 432 the Yukawa portal disappears due to Landau poles in the Yukawa sector. However, walking regimes sourcing the Yukawa portal mechanism at 222 typically also attract the Higgs quartic at similarly sizeable values as the Yukawas $\alpha_\lambda \simeq \mathcal{O}(10^{-1})$. Therefore the 432 approximation seems inconsistent. Same color coding as Fig. 4.1a.

C Scalar Mixing

In this appendix we discuss in detail scalar mass mixing in BSM models with additional singlet scalars. The canonically normalized kinetic and mass terms for a single, free scalar field S read

$$\mathcal{L}_S = \frac{\mathcal{N}}{2}(\partial_\mu S)^\dagger \partial^\mu S - \frac{\mathcal{N}}{2} m_S^2 S^\dagger S \tag{C.1}$$

where $\mathcal{N} = 2$ ($\mathcal{N} = 1$) for a complex (real) scalar field. If there is SSB in the BSM sector, a VEV v_s and a real BSM Higgs mode s emerge as

$$S = \frac{1}{\sqrt{\mathcal{N}}}(s + v_s) + \dots \tag{C.2}$$

together with additional components indicated by $(\dots)$ depending on the details of the scalar sector. In the $O(N_S)$ model, SSB yields an additional scalar field ϕ in the fundamental representation of the remaining $O(N_S - 1)$ symmetry:

$$O(N_S): \quad S = (v_s + s,\, \phi^1,\, \dots,\, \phi^{N_S - 1})^T\,. \tag{C.3}$$

In the $SU(N_F)_L \times SU(N_F)_R$ model in contrast after SSB we always additionally obtain a pseudo-real singlet $\tilde{s}$ as the scalar field is complex valued. In the vacuum configuration V^- the scalar symmetry is broken as $SU(N_F)_L \times SU(N_F)_R \to SU(N_F - 1)_L \times SU(N_F - 1)_R$, which gives rise to additional fields $\phi_{L,R}$ and Φ in the decomposition

$$S = \begin{pmatrix} \frac{1}{\sqrt{2}}(v_s + s + i\tilde{s}) & \phi_R^1 & \dots & \phi_R^{N_F - 1} \\ \phi_L^1 & \Phi^{1,1} & \dots & \Phi^{1,N_F-1} \\ \vdots & \vdots & & \vdots \\ \phi_L^{N_F-1} & \Phi^{N_F-1,1} & \dots & \Phi^{N_F-1,N_F-1} \end{pmatrix}. \tag{C.4}$$

Here, $\phi_{L,R}$ are in the fundamental and singlet representation under $SU(N_F - 1)_{L,R}$ and $SU(N_F - 1)_{R,L}$, respectively, whereas Φ is bifundamental. In V^+ on the other hand, the breaking proceeds as $SU(N_F)_L \times SU(N_F)_R \to SU(N_F)_V$. This yields the pseudoreal adjoints R and I, respectively, and implies the decomposition

$$S_{ij} = \frac{\delta_{ij}}{\sqrt{2N_F}}(v_s + s + i\tilde{s}) + (R^a + iI^a)\, t^a_{ij}\,, \tag{C.5}$$

where t^a_{ij} denote the (traceless) generators of $SU(N_F)_V$. Expressing the unbroken scalar potentials

$$V_{O(N_S)}(H,S) = -\mu_H^2 H^\dagger H - \frac{1}{2}\mu_S^2 S^T S + \lambda (H^\dagger H)^2 + v (S^T S)^2 + \delta\, (H^\dagger H)(S^T S), \tag{C.6}$$

$$V_{SU(N_F)^2}(H,S) = -\mu_H^2 H^\dagger H - \mu_S^2 \operatorname{Tr}[S^\dagger S] + \lambda (H^\dagger H)^2 + u \operatorname{Tr}[S^\dagger S S^\dagger S] + v \left[\operatorname{Tr} S^\dagger S\right]^2 + \delta\, (H^\dagger H) \operatorname{Tr}[S^\dagger S]\,, \tag{C.7}$$

cf. (5.8) and (5.14), through the scalar field components after SSB yields very long expressions. However, mixing with the SM Higgs boson solely arises from the part of the potential depending on the SM h and BSM s Higgs modes. It can be model-independently parametrized as (5.23)

$$V(h,s) = -\frac{\mu_H^2}{2}(h + v_h)^2 - \frac{1}{2}\mu_S^2 (s + v_s)^2 + \frac{\lambda}{4}(h + v_h)^4 + \frac{\Delta}{\mathcal{N}^2}(s + v_s)^4 + \frac{\delta}{2\mathcal{N}}(h + v_h)^2 (s + v_s)^2 \tag{C.8}$$

which falls back to the model-specific expressions for

$$O(N_S): \quad \mathcal{N} = 1,\ \Delta = v\,, \qquad V^+: \quad \mathcal{N} = 2,\ \Delta = \frac{u}{N_F} + v\,, \qquad V^-: \quad \mathcal{N} = 2,\ \Delta = u + v\,. \tag{C.9}$$

Minimizing the potential (C.8) via $\mathrm{d}V(h,s)/\mathrm{d}h = \mathrm{d}V(h,s)/\mathrm{d}s = 0$ implies the conditions

$$\mu_H^2 = \lambda v_h^2 + \frac{\delta}{\mathcal{N}} v_s^2, \qquad \mu_S^2 = \frac{4\Delta}{\mathcal{N}^2} v_s^2 + \frac{\delta}{\mathcal{N}} v_h^2 \,. \tag{C.10}$$

The quadratic terms in the broken potential (C.8) then correspond to mass terms for the real scalars h and s according to

$$V(h,s) \subset +\frac{1}{2} m_h^2 h^2 + \frac{1}{2} m_{hs}^2 hs + \frac{1}{2} m_s^2 s^2 \,. \tag{C.11}$$

Reading off the explicit expressions for the mass terms

$$m_h^2 = \left.\frac{\mathrm{d}^2 V(h,s)}{\mathrm{d}h^2}\right|_{h,s=0} = 2\lambda v_h^2, \quad m_{hs}^2 = 2\left.\frac{\mathrm{d}^2 V(h,s)}{\mathrm{d}h\mathrm{d}s}\right|_{h,s=0} = \frac{4}{\mathcal{N}} \delta v_h v_s, \quad m_s^2 = \left.\frac{\mathrm{d}^2 V(h,s)}{\mathrm{d}s^2}\right|_{h,s=0} = \frac{8}{\mathcal{N}^2} \Delta v_s^2 \tag{C.12}$$

additionally yields

$$v_h^2 = \frac{m_h^2}{2\lambda}, \quad v_s^2 = \frac{\mathcal{N}^2 m_s^2}{8\Delta}, \quad m_{hs}^2 = \frac{\delta}{\sqrt{\lambda\Delta}} m_h m_s \,. \tag{C.13}$$

Moreover, we define the mass matrix

$$M^2 = \begin{pmatrix} m_s^2 & m_{hs}^2/2 \\ m_{hs}^2/2 & m_h^2 \end{pmatrix} = \begin{pmatrix} \frac{8}{\mathcal{N}^2}\Delta v_s^2 & \frac{2}{\mathcal{N}}\delta v_h v_s \\ \frac{2}{\mathcal{N}}\delta v_h v_s & 2\lambda v_h^2 \end{pmatrix} \tag{C.14}$$

such that

$$\frac{1}{2}(s,h) M^2 \begin{pmatrix} s \\ h \end{pmatrix} = \frac{1}{2} m_s^2 s^2 + \frac{1}{2} m_{hs}^2 hs + \frac{1}{2} m_h^2 h^2 = \frac{4}{\mathcal{N}^2}\Delta v_s^2 s^2 + \frac{2}{\mathcal{N}}\delta v_h v_s sh + \lambda v_h^2 h^2. \tag{C.15}$$

The scalars h and s now mix into mass eigenstates h' and s' via

$$\begin{pmatrix} s' \\ h' \end{pmatrix} = O \begin{pmatrix} s \\ h \end{pmatrix} \tag{C.16}$$

with the orthogonal mixing matrix

$$O = \begin{pmatrix} \cos\beta & \sin\beta \\ -\sin\beta & \cos\beta \end{pmatrix} \,. \tag{C.17}$$

Demanding the (1,2) element of the diagonalized mass matrix

$$M'^2 = O M^2 O^T \tag{C.18}$$

to vanish, we obtain the relation

$$\tan 2\beta = \frac{m_{hs}^2}{m_s^2 - m_h^2} = \frac{\frac{4}{\mathcal{N}}\delta v_h v_s}{\left(\frac{8}{\mathcal{N}^2}\Delta v_s^2 - 2\lambda v_h^2\right)} = \frac{\delta}{\sqrt{\lambda\Delta}} \frac{m_h m_s}{m_s^2 - m_h^2}. \tag{C.19}$$

for the mixing angle β. From the other components of (C.18) we obtain the additional relations

$$m_s^2 = \cos^2\beta\, m_{s'}^2 + \sin^2\beta\, m_{h'}^2, \qquad m_h^2 = \cos^2\beta\, m_{h'}^2 + \sin^2\beta\, m_{s'}^2, \qquad \sin 2\beta = \frac{m_{hs}^2}{m_{s'}^2 - m_{h'}^2} \,, \tag{C.20}$$

where in the main part of this thesis we denote the physical scalar masses as

$$m_{h'} = M_h = 125 \text{ GeV} \,, \qquad m_{s'} = M_s . \tag{C.21}$$

We see that for $m_{s'} > m_{h'}$ as well as $\delta > 0$ (and thus $m_{hs}^2 > 0$) as required by PS we always obtain a positive mixing angle $\beta > 0$. Moreover, for $m_{s'} > m_{h'}$ it holds $m_{h'}^2 \leq m_s^2, m_h^2 \leq m_{s'}^2$, where $m'_s \simeq m_s$, $m'_h \simeq m_h$ in the small angle approximation $0 < \beta \ll 1$. Note that this approximation works well for m'_s but breaks down for m'_h as soon as $\beta m'_s \gtrsim m'_h$.

Alternatively, from explicitly diagonalizing M^2 we obtain for the masses of the physical scalars h', s'

$$m_{s',h'}^2 = \frac{m_s^2 + m_h^2}{2} \mp \frac{m_s^2 - m_h^2}{2} \sqrt{1 + \frac{m_{hs}^4}{(m_s^2 - m_h^2)^2}} = \frac{m_s^2 + m_h^2}{2} \mp \frac{m_s^2 - m_h^2}{2} \sqrt{1 + \frac{\delta^2}{\lambda \Delta} \frac{m_h^2 m_s^2}{(m_s^2 - m_h^2)^2}} \tag{C.22}$$

where $m_{s'}^2 > m_s^2$ and $m_{h'}^2 < m_h^2$. Vice versa, we can express

$$m_{s,h}^2 = \frac{m_{s'}^2 + m_{h'}^2}{2} \mp \frac{m_{s'}^2 - m_{h'}^2}{2} \sqrt{1 - \frac{4\delta^2}{4\lambda\Delta - \delta^2} \frac{m_{h'}^2 m_{s'}^2}{(m_{s'}^2 - m_{h'}^2)^2}} \tag{C.23}$$

Note that demanding $m_s^2, m_h^2 > 0$[1] with (C.20) implies the condition

$$|\delta| < 4\sqrt{\lambda\Delta}\, \frac{m_{s'}^2 - m_{h'}^2}{m_{s'}^2 + m_{h'}^2} \,. \tag{C.24}$$

Note also that equating the unrotated m_h^2 in (C.12) and (C.23) fixes λ as

$$\begin{aligned} \lambda =& \lambda_{\text{SM}} + \frac{1}{4v_h^2} \left(m_{s'}^2 - m_{h'}^2 + \frac{\delta^2}{2\Delta} v_h^2 - \sqrt{(m_{s'}^2 - m_{h'}^2)^2 - 2(m_{s'}^2 + m_{h'}^2) \frac{\delta^2}{2\Delta} v_h^2 + \left(\frac{\delta^2}{2\Delta} v_h^2 \right)^2} \right) \\ =& \lambda_{\text{SM}} + \frac{\delta^2}{4\Delta} \left(1 + \frac{m_{h'}^2}{m_{s'}^2} + \mathcal{O}\left(\frac{m_{h'}^4}{m_{s'}^4} \right) \right) \end{aligned} \tag{C.25}$$

where $\lambda_{\text{SM}} = \frac{m_{h'}^2}{2v_h^2}$.

We briefly comment on a possible contribution $-\mu_{det}(det(S) + det(S^\dagger))$ to the scalar potential (C.7) in the $SU(N_F) \times SU(N_F)$ model, which is explicitly allowed by the global symmetries. For $N_F = 3$ μ_{det} is dimensionful and therefore negligible in the RG flow. Nevertheless, in V^+ it gives rise to an additional term $-\mu_{det}(s + v_s)^3 / (\sqrt{2}\sqrt{N_F}^3)$ in the broken potential $V(h, s)$ (C.8) that contributes to the trilinear Higgs coupling κ_3 as $\mu_{det} \sin^3 \beta / (\sqrt{2}\sqrt{N_F}^3)$. Due to the strong suppression by the small mixing angle (and the multiplicity N_F) this contribution is negligible for the phenomenological analysis. However, the presence of μ_{det} changes the BSM minimization condition in (C.10) to $\mu_S^2 = \Delta v_s^2 + \frac{\delta}{2} v_h^2 - \frac{v_s \mu_{det}}{\sqrt{2N_F}}$. This alters the relation (C.12) between the BSM scalar mass and VEV to $m_s^2 = 2\Delta v_s^2 - \frac{v_s \mu_{det}}{\sqrt{2N_F}}$, introducing a dependence of v_s on μ_{det} for a fixed BSM mass. This does not change the sign of the mixing angle but complicates the parameter space analysis by adding another d.o.f.. Hence, we neglect μ_{det} for the purpose of this work. We also stress that no such contribution to the broken potential arises in V^-.

---

[1] By this choice we avoid spontaneous CP violation from complex VEVs.

Bibliography

[1] R. Bause, G. Hiller, T. Höhne, D. F. Litim, and T. Steudtner. “B-anomalies from flavorful U(1)′ extensions, safely”. In: *Eur. Phys. J. C* 82.1 (2022), p. 42. DOI: `10.1140/epjc/s10052-021-09957-1`. arXiv: `2109.06201 [hep-ph]`.

[2] G. Hiller, T. Höhne, D. F. Litim, and T. Steudtner. “Portals into Higgs vacuum stability”. In: *Phys. Rev. D* 106.11 (2022), p. 115004. DOI: `10.1103/PhysRevD.106.115004`. arXiv: `2207.07737 [hep-ph]`.

[3] R. Bause, H. Gisbert, G. Hiller, T. Höhne, D. F. Litim, and T. Steudtner. “U-spin-CP anomaly in charm”. In: *Phys. Rev. D* 108.3 (2023), p. 035005. DOI: `10.1103/PhysRevD.108.035005`. arXiv: `2210.16330 [hep-ph]`.

[4] G. Hiller, T. Höhne, D. F. Litim, and T. Steudtner. “Vacuum Stability in the Standard Model and Beyond”. In: (Jan. 2024). arXiv: `2401.08811 [hep-ph]`.

[5] G. Hiller, T. Höhne, D. F. Litim, and T. Steudtner. “Vacuum Stability as a Guide for Model Bulding”. In: *57th Rencontres de Moriond on Electroweak Interactions and Unified Theories*. May 2023. arXiv: `2305.18520 [hep-ph]`.

[6] R. Bause, H. Gisbert, G. Hiller, T. Höhne, D. F. Litim, and T. Steudtner. “Old and new anomalies in charm”. In: *21st International Conference on B-Physics at Frontier Machines*. Sept. 2023. arXiv: `2309.04513 [hep-ph]`.

[7] G. Hiller, T. Höhne, D. F. Litim, and T. Steudtner. *Planck Safety from Vector-like Quarks and Flavorful Scalars*. (in preparation).

[8] G. Aad et al. “Observation of a new particle in the search for the Standard Model Higgs boson with the ATLAS detector at the LHC”. In: *Phys. Lett. B* 716 (2012), pp. 1–29. DOI: `10.1016/j.physletb.2012.08.020`. arXiv: `1207.7214 [hep-ex]`.

[9] S. Chatrchyan et al. “Observation of a New Boson at a Mass of 125 GeV with the CMS Experiment at the LHC”. In: *Phys. Lett. B* 716 (2012), pp. 30–61. DOI: `10.1016/j.physletb.2012.08.021`. arXiv: `1207.7235 [hep-ex]`.

[10] P. W. Anderson. “Plasmons, Gauge Invariance, and Mass”. In: *Phys. Rev.* 130 (1963). Ed. by J. C. Taylor, pp. 439–442. DOI: `10.1103/PhysRev.130.439`.

[11] P. W. Higgs. “Broken Symmetries and the Masses of Gauge Bosons”. In: *Phys. Rev. Lett.* 13 (1964). Ed. by J. C. Taylor, pp. 508–509. DOI: `10.1103/PhysRevLett.13.508`.

[12] F. Englert and R. Brout. “Broken Symmetry and the Mass of Gauge Vector Mesons”. In: *Phys. Rev. Lett.* 13 (1964). Ed. by J. C. Taylor, pp. 321–323. DOI: `10.1103/PhysRevLett.13.321`.

[13] G. S. Guralnik, C. R. Hagen, and T. W. B. Kibble. “Global Conservation Laws and Massless Particles”. In: *Phys. Rev. Lett.* 13 (1964). Ed. by J. C. Taylor, pp. 585–587. DOI: `10.1103/PhysRevLett.13.585`.

[14] N. Aghanim et al. “Planck 2018 results. VI. Cosmological parameters”. In: *Astron. Astrophys.* 641 (2020). [Erratum: Astron.Astrophys. 652, C4 (2021)], A6. DOI: `10.1051/0004-6361/201833910`. arXiv: `1807.06209 [astro-ph.CO]`.

[15] B. D. Fields, K. A. Olive, T.-H. Yeh, and C. Young. “Big-Bang Nucleosynthesis after Planck”. In: *JCAP* 03 (2020). [Erratum: JCAP 11, E02 (2020)], p. 010. DOI: `10.1088/1475-7516/2020/03/010`. arXiv: `1912.01132 [astro-ph.CO]`.

[16] Y. Fukuda et al. “Evidence for oscillation of atmospheric neutrinos”. In: *Phys. Rev. Lett.* 81 (1998), pp. 1562–1567. DOI: `10.1103/PhysRevLett.81.1562`. arXiv: `hep-ex/9807003`.

[17] Q. R. Ahmad et al. “Measurement of the rate of $\nu_e + d \to p + p + e^-$ interactions produced by ^{8}B solar neutrinos at the Sudbury Neutrino Observatory”. In: *Phys. Rev. Lett.* 87 (2001), p. 071301. DOI: `10.1103/PhysRevLett.87.071301`. arXiv: `nucl-ex/0106015`.

[18] E. C. G. Stueckelberg de Breidenbach and A. Petermann. “Normalization of constants in the quanta theory”. In: *Helv. Phys. Acta* 26 (1953), pp. 499–520. DOI: 10.5169/seals-112426.

[19] M. Gell-Mann and F. E. Low. “Quantum electrodynamics at small distances”. In: *Phys. Rev.* 95 (1954), pp. 1300–1312. DOI: 10.1103/PhysRev.95.1300.

[20] K. Symanzik. “Small distance behavior in field theory and power counting”. In: *Commun. Math. Phys.* 18 (1970), pp. 227–246. DOI: 10.1007/BF01649434.

[21] C. G. Callan Jr. “Broken scale invariance in scalar field theory”. In: *Phys. Rev. D* 2 (1970), pp. 1541–1547. DOI: 10.1103/PhysRevD.2.1541.

[22] K. G. Wilson. “Renormalization group and critical phenomena. 1. Renormalization group and the Kadanoff scaling picture”. In: *Phys. Rev. B* 4 (1971), pp. 3174–3183. DOI: 10.1103/PhysRevB.4.3174.

[23] K. G. Wilson. “Renormalization group and critical phenomena. 2. Phase space cell analysis of critical behavior”. In: *Phys. Rev. B* 4 (1971), pp. 3184–3205. DOI: 10.1103/PhysRevB.4.3184.

[24] D. J. Gross and F. Wilczek. “Ultraviolet Behavior of Nonabelian Gauge Theories”. In: *Phys. Rev. Lett.* 30 (1973). Ed. by J. C. Taylor, pp. 1343–1346. DOI: 10.1103/PhysRevLett.30.1343.

[25] H. D. Politzer. “Reliable Perturbative Results for Strong Interactions?” In: *Phys. Rev. Lett.* 30 (1973). Ed. by J. C. Taylor, pp. 1346–1349. DOI: 10.1103/PhysRevLett.30.1346.

[26] A. Bednyakov and A. Pikelner. “Four-Loop Gauge and Three-Loop Yukawa Beta Functions in a General Renormalizable Theory”. In: *Phys. Rev. Lett.* 127.4 (2021), p. 041801. DOI: 10.1103/PhysRevLett.127.041801. arXiv: 2105.09918 [hep-ph].

[27] J. Davies, F. Herren, and A. E. Thomsen. “General gauge-Yukawa-quartic β-functions at 4-3-2-loop order”. In: *JHEP* 01 (2022), p. 051. DOI: 10.1007/JHEP01(2022)051. arXiv: 2110.05496 [hep-ph].

[28] C. Poole and A. E. Thomsen. “Constraints on 3- and 4-loop β-functions in a general four-dimensional Quantum Field Theory”. In: *JHEP* 09 (2019), p. 055. DOI: 10.1007/JHEP09(2019)055. arXiv: 1906.04625 [hep-th].

[29] T. Steudtner. “General scalar renormalisation group equations at three-loop order”. In: *JHEP* 12 (2020), p. 012. DOI: 10.1007/JHEP12(2020)012. arXiv: 2007.06591 [hep-th].

[30] T. Steudtner. “Towards general scalar-Yukawa renormalisation group equations at three-loop order”. In: *JHEP* 05 (2021), p. 060. DOI: 10.1007/JHEP05(2021)060. arXiv: 2101.05823 [hep-th].

[31] I. Jack, H. Osborn, and T. Steudtner. “Explorations in Scalar Fermion Theories: β-functions, Supersymmetry and Fixed Points”. In: (Jan. 2023). arXiv: 2301.10903 [hep-th].

[32] D. F. Litim and T. Steudtner. “ARGES – Advanced Renormalisation Group Equation Simplifier”. In: (Dec. 2020). arXiv: 2012.12955 [hep-ph].

[33] T. Steudtner. *ForGER*. (to appear).

[34] L. Sartore and I. Schienbein. “PyR@TE 3”. In: *Comput. Phys. Commun.* 261 (2021), p. 107819. DOI: 10.1016/j.cpc.2020.107819. arXiv: 2007.12700 [hep-ph].

[35] A. E. Thomsen. “Introducing RGBeta: a Mathematica package for the evaluation of renormalization group β-functions”. In: *Eur. Phys. J. C* 81.5 (2021), p. 408. DOI: 10.1140/epjc/s10052-021-09142-4. arXiv: 2101.08265 [hep-ph].

[36] F. Bezrukov, M. Y. Kalmykov, B. A. Kniehl, and M. Shaposhnikov. “Higgs Boson Mass and New Physics”. In: *JHEP* 10 (2012). Ed. by G. Moortgat-Pick, p. 140. DOI: 10.1007/JHEP10(2012)140. arXiv: 1205.2893 [hep-ph].

[37] G. Degrassi et al. "Higgs mass and vacuum stability in the Standard Model at NNLO". In: *JHEP* 08 (2012), p. 098. DOI: 10.1007/JHEP08(2012)098. arXiv: 1205.6497 [hep-ph].

[38] D. Buttazzo et al. "Investigating the near-criticality of the Higgs boson". In: *JHEP* 12 (2013), p. 089. DOI: 10.1007/JHEP12(2013)089. arXiv: 1307.3536 [hep-ph].

[39] S. Weinberg. "ULTRAVIOLET DIVERGENCES IN QUANTUM THEORIES OF GRAVITATION". In: *General Relativity: An Einstein Centenary Survey.* 1980, pp. 790–831.

[40] D. F. Litim and F. Sannino. "Asymptotic safety guaranteed". In: *JHEP* 12 (2014), p. 178. DOI: 10.1007/JHEP12(2014)178. arXiv: 1406.2337 [hep-th].

[41] K. Kowalska, A. Bond, G. Hiller, and D. Litim. "Towards an asymptotically safe completion of the Standard Model". In: *PoS* EPS-HEP2017 (2017). Ed. by P. Checchia et al., p. 542. DOI: 10.22323/1.314.0542.

[42] A. D. Bond, G. Hiller, K. Kowalska, and D. F. Litim. "Directions for model building from asymptotic safety". In: *JHEP* 08 (2017), p. 004. DOI: 10.1007/JHEP08(2017)004. arXiv: 1702.01727 [hep-ph].

[43] D. Barducci, M. Fabbrichesi, C. M. Nieto, R. Percacci, and V. Skrinjar. "In search of a UV completion of the standard model — 378,000 models that don't work". In: *JHEP* 11 (2018), p. 057. DOI: 10.1007/JHEP11(2018)057. arXiv: 1807.05584 [hep-ph].

[44] G. Hiller, C. Hormigos-Feliu, D. F. Litim, and T. Steudtner. "Asymptotically safe extensions of the Standard Model with flavour phenomenology". In: *54th Rencontres de Moriond on Electroweak Interactions and Unified Theories.* 2019, pp. 415–418. arXiv: 1905.11020 [hep-ph].

[45] G. Hiller, C. Hormigos-Feliu, D. F. Litim, and T. Steudtner. "Anomalous magnetic moments from asymptotic safety". In: *Phys. Rev. D* 102.7 (2020), p. 071901. DOI: 10.1103/PhysRevD.102.071901. arXiv: 1910.14062 [hep-ph].

[46] G. Hiller, C. Hormigos-Feliu, D. F. Litim, and T. Steudtner. "Model Building from Asymptotic Safety with Higgs and Flavor Portals". In: *Phys. Rev. D* 102.9 (2020), p. 095023. DOI: 10.1103/PhysRevD.102.095023. arXiv: 2008.08606 [hep-ph].

[47] R. Aaij et al. "Test of lepton universality with $B^0 \to K^{*0}\ell^+\ell^-$ decays". In: *JHEP* 08 (2017), p. 055. DOI: 10.1007/JHEP08(2017)055. arXiv: 1705.05802 [hep-ex].

[48] R. Aaij et al. "Test of lepton universality in beauty-quark decays". In: *Nature Phys.* 18.3 (2022), pp. 277–282. DOI: 10.1038/s41567-021-01478-8. arXiv: 2103.11769 [hep-ex].

[49] R. Aaij et al. "Tests of lepton universality using $B^0 \to K^0_S\ell^+\ell^-$ and $B^+ \to K^{*+}\ell^+\ell^-$ decays". In: *Phys. Rev. Lett.* 128.19 (2022), p. 191802. DOI: 10.1103/PhysRevLett.128.191802. arXiv: 2110.09501 [hep-ex].

[50] R. Aaij et al. "Test of lepton universality with $\Lambda^0_b \to pK^{-+-}$ decays". In: *JHEP* 05 (2020), p. 040. DOI: 10.1007/JHEP05(2020)040. arXiv: 1912.08139 [hep-ex].

[51] R. Aaij et al. "Differential branching fractions and isospin asymmetries of $B \to K^{(*)}\mu^+\mu^-$ decays". In: *JHEP* 06 (2014), p. 133. DOI: 10.1007/JHEP06(2014)133. arXiv: 1403.8044 [hep-ex].

[52] R. Aaij et al. "Branching Fraction Measurements of the Rare $B^0_s \to \phi\mu^+\mu^-$ and $B^0_s \to f_2'(1525)\mu^+\mu^-$-Decays". In: *Phys. Rev. Lett.* 127.15 (2021), p. 151801. DOI: 10.1103/PhysRevLett.127.151801. arXiv: 2105.14007 [hep-ex].

[53] R. Aaij et al. "Analysis of Neutral B-Meson Decays into Two Muons". In: *Phys. Rev. Lett.* 128.4 (2022), p. 041801. DOI: 10.1103/PhysRevLett.128.041801. arXiv: 2108.09284 [hep-ex].

[54] R. Aaij et al. "Angular Analysis of the $B^+ \to K^{*+}\mu^+\mu^-$ Decay". In: *Phys. Rev. Lett.* 126.16 (2021), p. 161802. DOI: 10.1103/PhysRevLett.126.161802. arXiv: 2012.13241 [hep-ex].

[55] R. Aaij et al. “Measurement of CP-Averaged Observables in the $B^0 \to K^{*0}\mu^+\mu^-$ Decay”. In: *Phys. Rev. Lett.* 125.1 (2020), p. 011802. DOI: 10.1103/PhysRevLett.125.011802. arXiv: 2003.04831 [hep-ex].

[56] R. Aaij et al. “Observation of CP Violation in Charm Decays”. In: *Phys. Rev. Lett.* 122.21 (2019), p. 211803. DOI: 10.1103/PhysRevLett.122.211803. arXiv: 1903.08726 [hep-ex].

[57] R. Aaij et al. “Measurement of the Time-Integrated CP Asymmetry in D0→K-K+ Decays”. In: *Phys. Rev. Lett.* 131.9 (2023), p. 091802. DOI: 10.1103/PhysRevLett.131.091802. arXiv: 2209.03179 [hep-ex].

[58] J. Ellis, M. Fairbairn, and P. Tunney. “Anomaly-Free Models for Flavour Anomalies”. In: *Eur. Phys. J. C* 78.3 (2018), p. 238. DOI: 10.1140/epjc/s10052-018-5725-0. arXiv: 1705.03447 [hep-ph].

[59] B. C. Allanach, J. Davighi, and S. Melville. “An Anomaly-free Atlas: charting the space of flavour-dependent gauged $U(1)$ extensions of the Standard Model”. In: *JHEP* 02 (2019). [Erratum: JHEP 08, 064 (2019)], p. 082. DOI: 10.1007/JHEP02(2019)082. arXiv: 1812.04602 [hep-ph].

[60] J. Aebischer, A. J. Buras, M. Cerdà-Sevilla, and F. De Fazio. “Quark-lepton connections in Z’ mediated FCNC processes: gauge anomaly cancellations at work”. In: *JHEP* 02 (2020), p. 183. DOI: 10.1007/JHEP02(2020)183. arXiv: 1912.09308 [hep-ph].

[61] W. Altmannshofer, J. Davighi, and M. Nardecchia. “Gauging the accidental symmetries of the standard model, and implications for the flavor anomalies”. In: *Phys. Rev. D* 101.1 (2020), p. 015004. DOI: 10.1103/PhysRevD.101.015004. arXiv: 1909.02021 [hep-ph].

[62] J. Ellis. “TikZ-Feynman: Feynman diagrams with TikZ”. In: *Comput. Phys. Commun.* 210 (2017), pp. 103–123. DOI: 10.1016/j.cpc.2016.08.019. arXiv: 1601.05437 [hep-ph].

[63] Wolfram Research Inc. *Mathematica, Version 13.2*. Champaign, IL, 2022.

[64] M. E. Peskin and D. V. Schroeder. *An Introduction to quantum field theory*. Reading, USA: Addison-Wesley, 1995.

[65] M. D. Schwartz. *Quantum Field Theory and the Standard Model*. Cambridge University Press, Mar. 2014.

[66] Y. Grossman and P. Tanedo. “Just a Taste: Lectures on Flavor Physics”. In: *Theoretical Advanced Study Institute in Elementary Particle Physics: Anticipating the Next Discoveries in Particle Physics*. 2018, pp. 109–295. DOI: 10.1142/9789813233348_0004. arXiv: 1711.03624 [hep-ph].

[67] G. ’t Hooft and M. J. G. Veltman. “Regularization and Renormalization of Gauge Fields”. In: *Nucl. Phys. B* 44 (1972), pp. 189–213. DOI: 10.1016/0550-3213(72)90279-9.

[68] H. Fritzsch, M. Gell-Mann, and H. Leutwyler. “Advantages of the Color Octet Gluon Picture”. In: *Phys. Lett. B* 47 (1973), pp. 365–368. DOI: 10.1016/0370-2693(73)90625-4.

[69] S. Weinberg. “Nonabelian Gauge Theories of the Strong Interactions”. In: *Phys. Rev. Lett.* 31 (1973), pp. 494–497. DOI: 10.1103/PhysRevLett.31.494.

[70] S. L. Glashow. “Partial Symmetries of Weak Interactions”. In: *Nucl. Phys.* 22 (1961), pp. 579–588. DOI: 10.1016/0029-5582(61)90469-2.

[71] S. Weinberg. “A Model of Leptons”. In: *Phys. Rev. Lett.* 19 (1967), pp. 1264–1266. DOI: 10.1103/PhysRevLett.19.1264.

[72] A. Salam. “Weak and Electromagnetic Interactions”. In: *Conf. Proc. C* 680519 (1968), pp. 367–377. DOI: 10.1142/9789812795915_0034.

[73] J. M. Pendlebury et al. “Revised experimental upper limit on the electric dipole moment of the neutron”. In: *Phys. Rev. D* 92.9 (2015), p. 092003. DOI: `10.1103/PhysRevD.92.092003`. arXiv: `1509.04411 [hep-ex]`.

[74] A. Hook. “TASI Lectures on the Strong CP Problem and Axions”. In: *PoS* TASI2018 (2019), p. 004. arXiv: `1812.02669 [hep-ph]`.

[75] J. Goldstone, A. Salam, and S. Weinberg. “Broken Symmetries”. In: *Phys. Rev.* 127 (1962), pp. 965–970. DOI: `10.1103/PhysRev.127.965`.

[76] Y. Nir. “Probing new physics with flavor physics (and probing flavor physics with new physics)”. In: *2nd Workshop on Monte Carlo Tools for Beyond the Standard Model Physics*. Aug. 2007. arXiv: `0708.1872 [hep-ph]`.

[77] N. Cabibbo. “Unitary Symmetry and Leptonic Decays”. In: *Phys. Rev. Lett.* 10 (1963), pp. 531–533. DOI: `10.1103/PhysRevLett.10.531`.

[78] M. Kobayashi and T. Maskawa. “CP Violation in the Renormalizable Theory of Weak Interaction”. In: *Prog. Theor. Phys.* 49 (1973), pp. 652–657. DOI: `10.1143/PTP.49.652`.

[79] L. Wolfenstein. “Parametrization of the Kobayashi-Maskawa Matrix”. In: *Phys. Rev. Lett.* 51 (1983), p. 1945. DOI: `10.1103/PhysRevLett.51.1945`.

[80] A. D. Sakharov. “Violation of CP Invariance, C asymmetry, and baryon asymmetry of the universe”. In: *Pisma Zh. Eksp. Teor. Fiz.* 5 (1967), pp. 32–35. DOI: `10.1070/PU1991v034n05ABEH002497`.

[81] I. Adachi et al. “Evidence for $B^+ \to K^+ \nu\bar{\nu}$ Decays”. In: (Nov. 2023). arXiv: `2311.14647 [hep-ex]`.

[82] R. Bause, H. Gisbert, and G. Hiller. “Implications of an enhanced $B \to K\nu\bar{\nu}$ branching ratio”. In: (Aug. 2023). arXiv: `2309.00075 [hep-ph]`.

[83] A. J. Buras. “Weak Hamiltonian, CP violation and rare decays”. In: *Les Houches Summer School in Theoretical Physics, Session 68: Probing the Standard Model of Particle Interactions*. June 1998, pp. 281–539. arXiv: `hep-ph/9806471`.

[84] G. Buchalla, A. J. Buras, and M. E. Lautenbacher. “Weak decays beyond leading logarithms”. In: *Rev. Mod. Phys.* 68 (1996), pp. 1125–1144. DOI: `10.1103/RevModPhys.68.1125`. arXiv: `hep-ph/9512380`.

[85] A. Pich. “Effective field theory: Course”. In: *Les Houches Summer School in Theoretical Physics, Session 68: Probing the Standard Model of Particle Interactions*. June 1998, pp. 949–1049. arXiv: `hep-ph/9806303`.

[86] M. Neubert. “Effective field theory and heavy quark physics”. In: *Theoretical Advanced Study Institute in Elementary Particle Physics: Physics in* $D \geqq 4$. Dec. 2005, pp. 149–194. DOI: `10.1142/9789812773579_0004`. arXiv: `hep-ph/0512222`.

[87] M. Neubert. “Renormalization Theory and Effective Field Theories”. In: (Jan. 2019). Ed. by S. Davidson, P. Gambino, M. Laine, M. Neubert, and C. Salomon. DOI: `10.1093/oso/9780198855743.003.0001`. arXiv: `1901.06573 [hep-ph]`.

[88] A. V. Manohar. “Effective field theories”. In: *Lect. Notes Phys.* 479 (1997). Ed. by H. Latal and W. Schweiger, pp. 311–362. DOI: `10.1007/BFb0104294`. arXiv: `hep-ph/9606222`.

[89] T. Appelquist and J. Carazzone. “Infrared Singularities and Massive Fields”. In: *Phys. Rev. D* 11 (1975), p. 2856. DOI: `10.1103/PhysRevD.11.2856`.

[90] K. G. Wilson. “Nonlagrangian models of current algebra”. In: *Phys. Rev.* 179 (1969), pp. 1499–1512. DOI: `10.1103/PhysRev.179.1499`.

[91] E. Fermi. "An attempt of a theory of beta radiation. 1." In: *Z. Phys.* 88 (1934), pp. 161–177. DOI: 10.1007/BF01351864.

[92] I. Brivio and M. Trott. "The Standard Model as an Effective Field Theory". In: *Phys. Rept.* 793 (2019), pp. 1–98. DOI: 10.1016/j.physrep.2018.11.002. arXiv: 1706.08945 [hep-ph].

[93] I. Brivio, J. Gonzalez-Fraile, M. C. Gonzalez-Garcia, and L. Merlo. "The complete HEFT Lagrangian after the LHC Run I". In: *Eur. Phys. J. C* 76.7 (2016), p. 416. DOI: 10.1140/epjc/s10052-016-4211-9. arXiv: 1604.06801 [hep-ph].

[94] S. Weinberg. "Baryon and Lepton Nonconserving Processes". In: *Phys. Rev. Lett.* 43 (1979), pp. 1566–1570. DOI: 10.1103/PhysRevLett.43.1566.

[95] B. Grzadkowski, M. Iskrzynski, M. Misiak, and J. Rosiek. "Dimension-Six Terms in the Standard Model Lagrangian". In: *JHEP* 10 (2010), p. 085. DOI: 10.1007/JHEP10(2010)085. arXiv: 1008.4884 [hep-ph].

[96] L. Lehman. "Extending the Standard Model Effective Field Theory with the Complete Set of Dimension-7 Operators". In: *Phys. Rev. D* 90.12 (2014), p. 125023. DOI: 10.1103/PhysRevD.90.125023. arXiv: 1410.4193 [hep-ph].

[97] B. Henning, X. Lu, T. Melia, and H. Murayama. "2, 84, 30, 993, 560, 15456, 11962, 261485, ...: Higher dimension operators in the SM EFT". In: *JHEP* 08 (2017). [Erratum: JHEP 09, 019 (2019)], p. 016. DOI: 10.1007/JHEP08(2017)016. arXiv: 1512.03433 [hep-ph].

[98] L. Lehman and A. Martin. "Hilbert Series for Constructing Lagrangians: expanding the phenomenologist's toolbox". In: *Phys. Rev. D* 91 (2015), p. 105014. DOI: 10.1103/PhysRevD.91.105014. arXiv: 1503.07537 [hep-ph].

[99] A. Kobach. "Baryon Number, Lepton Number, and Operator Dimension in the Standard Model". In: *Phys. Lett. B* 758 (2016), pp. 455–457. DOI: 10.1016/j.physletb.2016.05.050. arXiv: 1604.05726 [hep-ph].

[100] W. Buchmuller and D. Wyler. "Effective Lagrangian Analysis of New Interactions and Flavor Conservation". In: *Nucl. Phys. B* 268 (1986), pp. 621–653. DOI: 10.1016/0550-3213(86)90262-2.

[101] R. Alonso, E. E. Jenkins, A. V. Manohar, and M. Trott. "Renormalization Group Evolution of the Standard Model Dimension Six Operators III: Gauge Coupling Dependence and Phenomenology". In: *JHEP* 04 (2014), p. 159. DOI: 10.1007/JHEP04(2014)159. arXiv: 1312.2014 [hep-ph].

[102] J. de Blas, J. C. Criado, M. Perez-Victoria, and J. Santiago. "Effective description of general extensions of the Standard Model: the complete tree-level dictionary". In: *JHEP* 03 (2018), p. 109. DOI: 10.1007/JHEP03(2018)109. arXiv: 1711.10391 [hep-ph].

[103] E. E. Jenkins, A. V. Manohar, and M. Trott. "Renormalization Group Evolution of the Standard Model Dimension Six Operators I: Formalism and lambda Dependence". In: *JHEP* 10 (2013), p. 087. DOI: 10.1007/JHEP10(2013)087. arXiv: 1308.2627 [hep-ph].

[104] E. E. Jenkins, A. V. Manohar, and M. Trott. "Renormalization Group Evolution of the Standard Model Dimension Six Operators II: Yukawa Dependence". In: *JHEP* 01 (2014), p. 035. DOI: 10.1007/JHEP01(2014)035. arXiv: 1310.4838 [hep-ph].

[105] Z. Bern, J. Parra-Martinez, and E. Sawyer. "Structure of two-loop SMEFT anomalous dimensions via on-shell methods". In: *JHEP* 10 (2020), p. 211. DOI: 10.1007/JHEP10(2020)211. arXiv: 2005.12917 [hep-ph].

[106] W. Dekens and P. Stoffer. "Low-energy effective field theory below the electroweak scale: matching at one loop". In: *JHEP* 10 (2019). [Erratum: JHEP 11, 148 (2022)], p. 197. DOI: 10.1007/JHEP10(2019)197. arXiv: 1908.05295 [hep-ph].

[107] K. G. Chetyrkin, M. Misiak, and M. Munz. “Weak radiative B meson decay beyond leading logarithms”. In: *Phys. Lett. B* 400 (1997). [Erratum: Phys.Lett.B 425, 414 (1998)], pp. 206–219. DOI: 10.1016/S0370-2693(97)00324-9. arXiv: hep-ph/9612313.

[108] S. Descotes-Genon, T. Hurth, J. Matias, and J. Virto. “Optimizing the basis of $B \to K^*ll$ observables in the full kinematic range”. In: *JHEP* 05 (2013), p. 137. DOI: 10.1007/JHEP05(2013)137. arXiv: 1303.5794 [hep-ph].

[109] N. Gubernari, M. Reboud, D. van Dyk, and J. Virto. “Improved theory predictions and global analysis of exclusive $b \to s\mu^+\mu^-$ processes”. In: *JHEP* 09 (2022), p. 133. DOI: 10.1007/JHEP09(2022)133. arXiv: 2206.03797 [hep-ph].

[110] C. G. Bollini and J. J. Giambiagi. “Dimensional Renormalization: The Number of Dimensions as a Regularizing Parameter”. In: *Nuovo Cim. B* 12 (1972), pp. 20–26. DOI: 10.1007/BF02895558.

[111] G. ’t Hooft. “Dimensional regularization and the renormalization group”. In: *Nucl. Phys. B* 61 (1973), pp. 455–468. DOI: 10.1016/0550-3213(73)90376-3.

[112] M. E. Machacek and M. T. Vaughn. “Two Loop Renormalization Group Equations in a General Quantum Field Theory. 1. Wave Function Renormalization”. In: *Nucl. Phys. B* 222 (1983), pp. 83–103. DOI: 10.1016/0550-3213(83)90610-7.

[113] M. E. Machacek and M. T. Vaughn. “Two Loop Renormalization Group Equations in a General Quantum Field Theory. 2. Yukawa Couplings”. In: *Nucl. Phys. B* 236 (1984), pp. 221–232. DOI: 10.1016/0550-3213(84)90533-9.

[114] M. E. Machacek and M. T. Vaughn. “Two Loop Renormalization Group Equations in a General Quantum Field Theory. 3. Scalar Quartic Couplings”. In: *Nucl. Phys. B* 249 (1985), pp. 70–92. DOI: 10.1016/0550-3213(85)90040-9.

[115] M.-x. Luo, H.-w. Wang, and Y. Xiao. “Two loop renormalization group equations in general gauge field theories”. In: *Phys. Rev. D* 67 (2003), p. 065019. DOI: 10.1103/PhysRevD.67.065019. arXiv: hep-ph/0211440.

[116] I. Schienbein, F. Staub, T. Steudtner, and K. Svirina. “Revisiting RGEs for general gauge theories”. In: *Nucl. Phys. B* 939 (2019). [Erratum: Nucl.Phys.B 966, 115339 (2021)], pp. 1–48. DOI: 10.1016/j.nuclphysb.2018.12.001. arXiv: 1809.06797 [hep-ph].

[117] L. Mihaila. “Three-loop gauge beta function in non-simple gauge groups”. In: *PoS* RADCOR2013 (2013), p. 060. DOI: 10.22323/1.197.0060.

[118] F. Jegerlehner. “Facts of life with gamma(5)”. In: *Eur. Phys. J. C* 18 (2001), pp. 673–679. DOI: 10.1007/s100520100573. arXiv: hep-th/0005255.

[119] K. G. Chetyrkin and M. F. Zoller. “Three-loop \beta-functions for top-Yukawa and the Higgs self-interaction in the Standard Model”. In: *JHEP* 06 (2012), p. 033. DOI: 10.1007/JHEP06(2012)033. arXiv: 1205.2892 [hep-ph].

[120] K. G. Chetyrkin and M. F. Zoller. “β-function for the Higgs self-interaction in the Standard Model at three-loop level”. In: *JHEP* 04 (2013). [Erratum: JHEP 09, 155 (2013)], p. 091. DOI: 10.1007/JHEP04(2013)091. arXiv: 1303.2890 [hep-ph].

[121] P. A. Baikov, K. G. Chetyrkin, and J. H. Kühn. “Five-Loop Running of the QCD coupling constant”. In: *Phys. Rev. Lett.* 118.8 (2017), p. 082002. DOI: 10.1103/PhysRevLett.118.082002. arXiv: 1606.08659 [hep-ph].

[122] F. Herzog, B. Ruijl, T. Ueda, J. A. M. Vermaseren, and A. Vogt. “The five-loop beta function of Yang-Mills theory with fermions”. In: *JHEP* 02 (2017), p. 090. DOI: 10.1007/JHEP02(2017)090. arXiv: 1701.01404 [hep-ph].

[123] T. Luthe, A. Maier, P. Marquard, and Y. Schroder. "The five-loop Beta function for a general gauge group and anomalous dimensions beyond Feynman gauge". In: *JHEP* 10 (2017), p. 166. DOI: `10.1007/JHEP10(2017)166`. arXiv: `1709.07718 [hep-ph]`.

[124] K. G. Chetyrkin, G. Falcioni, F. Herzog, and J. A. M. Vermaseren. "Five-loop renormalisation of QCD in covariant gauges". In: *JHEP* 10 (2017). [Addendum: JHEP 12, 006 (2017)], p. 179. DOI: `10.1007/JHEP10(2017)179`. arXiv: `1709.08541 [hep-ph]`.

[125] A. Bednyakov and A. Pikelner. "Six-loop beta functions in general scalar theory". In: *JHEP* 04 (2021), p. 233. DOI: `10.1007/JHEP04(2021)233`. arXiv: `2102.12832 [hep-ph]`.

[126] E. Mølgaard. "Decrypting gauge-Yukawa cookbooks". In: *Eur. Phys. J. Plus* 129 (2014), p. 159. DOI: `10.1140/epjp/i2014-14159-2`. arXiv: `1404.5550 [hep-th]`.

[127] M.-x. Luo and Y. Xiao. "Renormalization group equations in gauge theories with multiple U(1) groups". In: *Phys. Lett. B* 555 (2003), pp. 279–286. DOI: `10.1016/S0370-2693(03)00076-5`. arXiv: `hep-ph/0212152`.

[128] A. D. Bond and D. F. Litim. "Theorems for Asymptotic Safety of Gauge Theories". In: *Eur. Phys. J. C* 77.6 (2017). [Erratum: Eur.Phys.J.C 77, 525 (2017)], p. 429. DOI: `10.1140/epjc/s10052-017-4976-5`. arXiv: `1608.00519 [hep-th]`.

[129] A. G. M. Pickering, J. A. Gracey, and D. R. T. Jones. "Three loop gauge beta function for the most general single gauge coupling theory". In: *Phys. Lett. B* 510 (2001). [Erratum: Phys.Lett.B 535, 377 (2002)], pp. 347–354. DOI: `10.1016/S0370-2693(01)00624-4`. arXiv: `hep-ph/0104247`.

[130] A. V. Bednyakov, A. F. Pikelner, and V. N. Velizhanin. "Yukawa coupling beta-functions in the Standard Model at three loops". In: *Phys. Lett. B* 722 (2013), pp. 336–340. DOI: `10.1016/j.physletb.2013.04.038`. arXiv: `1212.6829 [hep-ph]`.

[131] A. V. Bednyakov, A. F. Pikelner, and V. N. Velizhanin. "Three-loop SM beta-functions for matrix Yukawa couplings". In: *Phys. Lett. B* 737 (2014), pp. 129–134. DOI: `10.1016/j.physletb.2014.08.049`. arXiv: `1406.7171 [hep-ph]`.

[132] L. N. Mihaila, J. Salomon, and M. Steinhauser. "Renormalization constants and beta functions for the gauge couplings of the Standard Model to three-loop order". In: *Phys. Rev. D* 86 (2012), p. 096008. DOI: `10.1103/PhysRevD.86.096008`. arXiv: `1208.3357 [hep-ph]`.

[133] A. V. Bednyakov, A. F. Pikelner, and V. N. Velizhanin. "Anomalous dimensions of gauge fields and gauge coupling beta-functions in the Standard Model at three loops". In: *JHEP* 01 (2013), p. 017. DOI: `10.1007/JHEP01(2013)017`. arXiv: `1210.6873 [hep-ph]`.

[134] T. Steudtner. "Asymptotic safety: from perturbatively exact models to particle physics". PhD thesis. Sussex U., 2020.

[135] G. Veneziano. "U(1) Without Instantons". In: *Nucl. Phys. B* 159 (1979), pp. 213–224. DOI: `10.1016/0550-3213(79)90332-8`.

[136] A. D. Bond and D. F. Litim. "Price of Asymptotic Safety". In: *Phys. Rev. Lett.* 122.21 (2019), p. 211601. DOI: `10.1103/PhysRevLett.122.211601`. arXiv: `1801.08527 [hep-th]`.

[137] D. F. Litim, M. Mojaza, and F. Sannino. "Vacuum stability of asymptotically safe gauge-Yukawa theories". In: *JHEP* 01 (2016), p. 081. DOI: `10.1007/JHEP01(2016)081`. arXiv: `1501.03061 [hep-th]`.

[138] A. D. Bond, D. F. Litim, G. Medina Vazquez, and T. Steudtner. "UV conformal window for asymptotic safety". In: *Phys. Rev. D* 97.3 (2018), p. 036019. DOI: `10.1103/PhysRevD.97.036019`. arXiv: `1710.07615 [hep-th]`.

[139] A. D. Bond and D. F. Litim. "Asymptotic safety guaranteed for strongly coupled gauge theories". In: *Phys. Rev. D* 105.10 (2022), p. 105005. DOI: `10.1103/PhysRevD.105.105005`. arXiv: `2202.08223 [hep-th]`.

[140] A. D. Bond and D. F. Litim. "Asymptotic safety guaranteed in supersymmetry". In: *Phys. Rev. Lett.* 119.21 (2017), p. 211601. DOI: `10.1103/PhysRevLett.119.211601`. arXiv: `1709.06953 [hep-th]`.

[141] A. D. Bond, D. F. Litim, and G. M. Vázquez. "Conformal Windows Beyond Asymptotic Freedom". In: (July 2021). arXiv: `2107.13020 [hep-th]`.

[142] T. Buyukbese and D. F. Litim. "Asymptotic Safety of Gauge Theories Beyond Marginal Interactions". In: *PoS* LATTICE2016 (2017), p. 233. DOI: `10.22323/1.256.0233`.

[143] A. D. Bond, D. F. Litim, and T. Steudtner. "Asymptotic safety with Majorana fermions and new large N equivalences". In: *Phys. Rev. D* 101.4 (2020), p. 045006. DOI: `10.1103/PhysRevD.101.045006`. arXiv: `1911.11168 [hep-th]`.

[144] A. D. Bond and D. F. Litim. "More asymptotic safety guaranteed". In: *Phys. Rev. D* 97.8 (2018), p. 085008. DOI: `10.1103/PhysRevD.97.085008`. arXiv: `1707.04217 [hep-th]`.

[145] P. Schuh. "Vacuum Stability of Asymptotically Safe Two Higgs Doublet Models". In: *Eur. Phys. J. C* 79.11 (2019), p. 909. DOI: `10.1140/epjc/s10052-019-7426-8`. arXiv: `1810.07664 [hep-ph]`.

[146] J. McDowall and D. J. Miller. "High Scale Boundary Conditions in Models with Two Higgs Doublets". In: *Phys. Rev. D* 100.1 (2019), p. 015018. DOI: `10.1103/PhysRevD.100.015018`. arXiv: `1810.04518 [hep-ph]`.

[147] M. Fabbrichesi, C. M. Nieto, A. Tonero, and A. Ugolotti. "Asymptotically safe SU(5) GUT". In: *Phys. Rev. D* 103.9 (2021), p. 095026. DOI: `10.1103/PhysRevD.103.095026`. arXiv: `2012.03987 [hep-ph]`.

[148] R. Alkofer, A. Eichhorn, A. Held, C. M. Nieto, R. Percacci, and M. Schröfl. "Quark masses and mixings in minimally parameterized UV completions of the Standard Model". In: *Annals Phys.* 421 (2020), p. 168282. DOI: `10.1016/j.aop.2020.168282`. arXiv: `2003.08401 [hep-ph]`.

[149] G. Hiller, D. F. Litim, and K. Moch. "Fixed points in supersymmetric extensions of the standard model". In: *Eur. Phys. J. C* 82.10 (2022), p. 952. DOI: `10.1140/epjc/s10052-022-10885-x`. arXiv: `2202.01264 [hep-ph]`.

[150] D. F. Litim, N. Riyaz, E. Stamou, and T. Steudtner. "Asymptotic safety guaranteed at four-loop order". In: *Phys. Rev. D* 108.7 (2023), p. 076006. DOI: `10.1103/PhysRevD.108.076006`. arXiv: `2307.08747 [hep-th]`.

[151] T. Steudtner. "Effective Potential and Vacuum Stability in the Litim-Sannino Model". In: (Feb. 2024). arXiv: `2402.16950 [hep-th]`.

[152] A. G. Cohen and H. Georgi. "Walking Beyond the Rainbow". In: *Nucl. Phys. B* 314 (1989), pp. 7–24. DOI: `10.1016/0550-3213(89)90109-0`.

[153] G. Cacciapaglia, C. Pica, and F. Sannino. "Fundamental Composite Dynamics: A Review". In: *Phys. Rept.* 877 (2020), pp. 1–70. DOI: `10.1016/j.physrep.2020.07.002`. arXiv: `2002.04914 [hep-ph]`.

[154] S. R. Coleman and E. J. Weinberg. "Radiative Corrections as the Origin of Spontaneous Symmetry Breaking". In: *Phys. Rev. D* 7 (1973), pp. 1888–1910. DOI: `10.1103/PhysRevD.7.1888`.

[155] R. L. Workman et al. "Review of Particle Physics". In: *PTEP* 2022 (2022), p. 083C01. DOI: `10.1093/ptep/ptac097`.

[156] A. H. Hoang. "What is the Top Quark Mass?" In: *Ann. Rev. Nucl. Part. Sci.* 70 (2020), pp. 225–255. DOI: `10.1146/annurev-nucl-101918-023530`. arXiv: `2004.12915 [hep-ph]`.

[157] A. M. Sirunyan et al. “Measurement of $\mathrm{t\bar{t}}$ normalised multi-differential cross sections in pp collisions at $\sqrt{s} = 13$ TeV, and simultaneous determination of the strong coupling strength, top quark pole mass, and parton distribution functions”. In: *Eur. Phys. J. C* 80.7 (2020), p. 658. DOI: 10.1140/epjc/s10052-020-7917-7. arXiv: 1904.05237 [hep-ex].

[158] M. Shaposhnikov and C. Wetterich. “Asymptotic safety of gravity and the Higgs boson mass”. In: *Phys. Lett. B* 683 (2010), pp. 196–200. DOI: 10.1016/j.physletb.2009.12.022. arXiv: 0912.0208 [hep-th].

[159] A. Eichhorn and M. Schiffer. “Asymptotic safety of gravity with matter”. In: (Dec. 2022). arXiv: 2212.07456 [hep-th].

[160] K. Kannike. “Vacuum Stability Conditions From Copositivity Criteria”. In: *Eur. Phys. J. C* 72 (2012), p. 2093. DOI: 10.1140/epjc/s10052-012-2093-z. arXiv: 1205.3781 [hep-ph].

[161] A. J. Paterson. “{Coleman-Weinberg} Symmetry Breaking in the Chiral SU(N) X SU(N) Linear Sigma Model”. In: *Nucl. Phys. B* 190 (1981), pp. 188–204. DOI: 10.1016/0550-3213(81)90489-2.

[162] Z. Alam and S. P. Martin. “Standard model at 200 GeV”. In: *Phys. Rev. D* 107.1 (2023), p. 013010. DOI: 10.1103/PhysRevD.107.013010. arXiv: 2211.08576 [hep-ph].

[163] A. V. Manohar. “Introduction to Effective Field Theories”. In: (Apr. 2018). Ed. by S. Davidson, P. Gambino, M. Laine, M. Neubert, and C. Salomon. DOI: 10.1093/oso/9780198855743.003.0002. arXiv: 1804.05863 [hep-ph].

[164] N. Arkani-Hamed, K. Blum, R. T. D’Agnolo, and J. Fan. “2:1 for Naturalness at the LHC?” In: *JHEP* 01 (2013), p. 149. DOI: 10.1007/JHEP01(2013)149. arXiv: 1207.4482 [hep-ph].

[165] A. Joglekar, P. Schwaller, and C. E. M. Wagner. “Dark Matter and Enhanced Higgs to Di-photon Rate from Vector-like Leptons”. In: *JHEP* 12 (2012), p. 064. DOI: 10.1007/JHEP12(2012)064. arXiv: 1207.4235 [hep-ph].

[166] M. Fairbairn and P. Grothaus. “Baryogenesis and Dark Matter with Vector-like Fermions”. In: *JHEP* 10 (2013), p. 176. DOI: 10.1007/JHEP10(2013)176. arXiv: 1307.8011 [hep-ph].

[167] K. Blum, R. T. D’Agnolo, and J. Fan. “Vacuum stability bounds on Higgs coupling deviations in the absence of new bosons”. In: *JHEP* 03 (2015), p. 166. DOI: 10.1007/JHEP03(2015)166. arXiv: 1502.01045 [hep-ph].

[168] W. Altmannshofer, M. Bauer, and M. Carena. “Exotic Leptons: Higgs, Flavor and Collider Phenomenology”. In: *JHEP* 01 (2014), p. 060. DOI: 10.1007/JHEP01(2014)060. arXiv: 1308.1987 [hep-ph].

[169] S. Gopalakrishna and A. Velusamy. “Higgs vacuum stability with vectorlike fermions”. In: *Phys. Rev. D* 99.11 (2019), p. 115020. DOI: 10.1103/PhysRevD.99.115020. arXiv: 1812.11303 [hep-ph].

[170] A. Bilal. “Lectures on Anomalies”. In: (Feb. 2008). arXiv: 0802.0634 [hep-th].

[171] ATLAS collaboration. “Determination of the strong coupling constant and test of asymptotic freedom from Transverse Energy-Energy Correlations in multijet events at $\sqrt{s}$=13 TeV with the ATLAS detector”. In: *ATLAS-CONF-2020-025* (July 2020).

[172] M. Farina, G. Panico, D. Pappadopulo, J. T. Ruderman, R. Torre, and A. Wulzer. “Energy helps accuracy: electroweak precision tests at hadron colliders”. In: *Phys. Lett. B* 772 (2017), pp. 210–215. DOI: 10.1016/j.physletb.2017.06.043. arXiv: 1609.08157 [hep-ph].

[173] D. S. M. Alves, J. Galloway, J. T. Ruderman, and J. R. Walsh. “Running Electroweak Couplings as a Probe of New Physics”. In: *JHEP* 02 (2015), p. 007. DOI: 10.1007/JHEP02(2015)007. arXiv: 1410.6810 [hep-ph].

[174] M. M. Altakach, P. Lamba, R. Masełek, V. A. Mitsou, and K. Sakurai. “Discovery prospects for long-lived multiply charged particles at the LHC”. In: (Apr. 2022). arXiv: `2204.03667 [hep-ph]`.

[175] M. Aaboud et al. “Combination of the searches for pair-produced vector-like partners of the third-generation quarks at $\sqrt{s} = 13$ TeV with the ATLAS detector”. In: *Phys. Rev. Lett.* 121.21 (2018), p. 211801. DOI: `10.1103/PhysRevLett.121.211801`. arXiv: `1808.02343 [hep-ex]`.

[176] J. Erdmann. “Overview of searches for single production of vector-like top and bottom quarks with the ATLAS experiment at 13 TeV”. In: *11th International Workshop on Top Quark Physics*. Nov. 2018. arXiv: `1811.11496 [hep-ex]`.

[177] A. Falkowski and D. Straub. “Flavourful SMEFT likelihood for Higgs and electroweak data”. In: *JHEP* 04 (2020), p. 066. DOI: `10.1007/JHEP04(2020)066`. arXiv: `1911.07866 [hep-ph]`.

[178] J. Ellis, M. Madigan, K. Mimasu, V. Sanz, and T. You. “Top, Higgs, Diboson and Electroweak Fit to the Standard Model Effective Field Theory”. In: (Dec. 2020). arXiv: `2012.02779 [hep-ph]`.

[179] K. Ishiwata, Z. Ligeti, and M. B. Wise. “New Vector-Like Fermions and Flavor Physics”. In: *JHEP* 10 (2015), p. 027. DOI: `10.1007/JHEP10(2015)027`. arXiv: `1506.03484 [hep-ph]`.

[180] J. A. Aguilar-Saavedra, R. Benbrik, S. Heinemeyer, and M. Pérez-Victoria. “Handbook of vectorlike quarks: Mixing and single production”. In: *Phys. Rev. D* 88.9 (2013), p. 094010. DOI: `10.1103/PhysRevD.88.094010`. arXiv: `1306.0572 [hep-ph]`.

[181] S. Bißmann, G. Hiller, C. Hormigos-Feliu, and D. F. Litim. “Multi-lepton signatures of vector-like leptons with flavor”. In: *Eur. Phys. J. C* 81.2 (2021), p. 101. DOI: `10.1140/epjc/s10052-021-08886-3`. arXiv: `2011.12964 [hep-ph]`.

[182] G. Hiller, T. Höhne, D. F. Litim, K. J. Spychala, and T. Steudtner. *Planck Safety with Majorana Fermions*. (in preparation).

[183] A. Falkowski, C. Gross, and O. Lebedev. “A second Higgs from the Higgs portal”. In: *JHEP* 05 (2015), p. 057. DOI: `10.1007/JHEP05(2015)057`. arXiv: `1502.01361 [hep-ph]`.

[184] N. Khan and S. Rakshit. “Study of electroweak vacuum metastability with a singlet scalar dark matter”. In: *Phys. Rev. D* 90.11 (2014), p. 113008. DOI: `10.1103/PhysRevD.90.113008`. arXiv: `1407.6015 [hep-ph]`.

[185] H. Han and S. Zheng. “New Constraints on Higgs-portal Scalar Dark Matter”. In: *JHEP* 12 (2015), p. 044. DOI: `10.1007/JHEP12(2015)044`. arXiv: `1509.01765 [hep-ph]`.

[186] I. Garg, S. Goswami, K. N. Vishnudath, and N. Khan. “Electroweak vacuum stability in presence of singlet scalar dark matter in TeV scale seesaw models”. In: *Phys. Rev. D* 96.5 (2017), p. 055020. DOI: `10.1103/PhysRevD.96.055020`. arXiv: `1706.08851 [hep-ph]`.

[187] E. Gabrielli, M. Heikinheimo, K. Kannike, A. Racioppi, M. Raidal, and C. Spethmann. “Towards Completing the Standard Model: Vacuum Stability, EWSB and Dark Matter”. In: *Phys. Rev. D* 89.1 (2014), p. 015017. DOI: `10.1103/PhysRevD.89.015017`. arXiv: `1309.6632 [hep-ph]`.

[188] J. Elias-Miro, J. R. Espinosa, G. F. Giudice, H. M. Lee, and A. Strumia. “Stabilization of the Electroweak Vacuum by a Scalar Threshold Effect”. In: *JHEP* 06 (2012), p. 031. DOI: `10.1007/JHEP06(2012)031`. arXiv: `1203.0237 [hep-ph]`.

[189] M. Gonderinger, H. Lim, and M. J. Ramsey-Musolf. “Complex Scalar Singlet Dark Matter: Vacuum Stability and Phenomenology”. In: *Phys. Rev. D* 86 (2012), p. 043511. DOI: `10.1103/PhysRevD.86.043511`. arXiv: `1202.1316 [hep-ph]`.

[190] R. Costa, A. P. Morais, M. O. P. Sampaio, and R. Santos. "Two-loop stability of a complex singlet extended Standard Model". In: *Phys. Rev. D* 92 (2015), p. 025024. DOI: `10.1103/PhysRevD.92.025024`. arXiv: `1411.4048 [hep-ph]`.

[191] V. V. Khoze, C. McCabe, and G. Ro. "Higgs vacuum stability from the dark matter portal". In: *JHEP* 08 (2014), p. 026. DOI: `10.1007/JHEP08(2014)026`. arXiv: `1403.4953 [hep-ph]`.

[192] S. Dawson, P. P. Giardino, and S. Homiller. "Uncovering the High Scale Higgs Singlet Model". In: *Phys. Rev. D* 103.7 (2021), p. 075016. DOI: `10.1103/PhysRevD.103.075016`. arXiv: `2102.02823 [hep-ph]`.

[193] P. Huang, A. J. Long, and L.-T. Wang. "Probing the Electroweak Phase Transition with Higgs Factories and Gravitational Waves". In: *Phys. Rev. D* 94.7 (2016), p. 075008. DOI: `10.1103/PhysRevD.94.075008`. arXiv: `1608.06619 [hep-ph]`.

[194] G. Aad et al. "Combined measurements of Higgs boson production and decay using up to 80 fb^{-1} of proton-proton collision data at $\sqrt{s} = 13$ TeV collected with the ATLAS experiment". In: *Phys. Rev. D* 101.1 (2020), p. 012002. DOI: `10.1103/PhysRevD.101.012002`. arXiv: `1909.02845 [hep-ex]`.

[195] "Combined Higgs boson production and decay measurements with up to 137 fb^{-1} of proton-proton collision data at $\sqrt{s} = 13$ TeV". In: (2020).

[196] A. Abada et al. "FCC Physics Opportunities: Future Circular Collider Conceptual Design Report Volume 1". In: *Eur. Phys. J. C* 79.6 (2019), p. 474. DOI: `10.1140/epjc/s10052-019-6904-3`.

[197] G. Aad et al. "A detailed map of Higgs boson interactions by the ATLAS experiment ten years after the discovery". In: *Nature* 607.7917 (2022). [Erratum: Nature 612, E24 (2022)], pp. 52–59. DOI: `10.1038/s41586-022-04893-w`. arXiv: `2207.00092 [hep-ex]`.

[198] A. Tumasyan et al. "A portrait of the Higgs boson by the CMS experiment ten years after the discovery." In: *Nature* 607.7917 (2022), pp. 60–68. DOI: `10.1038/s41586-022-04892-x`. arXiv: `2207.00043 [hep-ex]`.

[199] M. Cepeda et al. "Report from Working Group 2: Higgs Physics at the HL-LHC and HE-LHC". In: *CERN Yellow Rep. Monogr.* 7 (2019). Ed. by A. Dainese, M. Mangano, A. B. Meyer, A. Nisati, G. Salam, and M. A. Vesterinen, pp. 221–584. DOI: `10.23731/CYRM-2019-007.221`. arXiv: `1902.00134 [hep-ph]`.

[200] H. Aihara et al. "The International Linear Collider. A Global Project". In: (Jan. 2019). arXiv: `1901.09829 [hep-ex]`.

[201] R. T. D'Agnolo, F. Nortier, G. Rigo, and P. Sesma. "The two scales of new physics in Higgs couplings". In: *JHEP* 08 (2023), p. 019. DOI: `10.1007/JHEP08(2023)019`. arXiv: `2305.19325 [hep-ph]`.

[202] "Search for Higgs boson pair production in the two bottom quarks plus two photons final state in pp collisions at $\sqrt{s} = 13$ TeV with the ATLAS detector". In: (Mar. 2021).

[203] J. Ellis, M. Lewicki, M. Merchand, J. M. No, and M. Zych. "The scalar singlet extension of the Standard Model: gravitational waves versus baryogenesis". In: *JHEP* 01 (2023), p. 093. DOI: `10.1007/JHEP01(2023)093`. arXiv: `2210.16305 [hep-ph]`.

[204] E. Fernández-Martínez, J. López-Pavón, J. M. No, T. Ota, and S. Rosauro-Alcaraz. "ν Electroweak Baryogenesis: The Scalar Singlet Strikes Back". In: (Oct. 2022). arXiv: `2210.16279 [hep-ph]`.

[205] G. Colangelo et al. "Prospects for precise predictions of a_μ in the Standard Model". In: (Mar. 2022). arXiv: `2203.15810 [hep-ph]`.

[206] F. del Aguila, M. Perez-Victoria, and J. Santiago. “Observable contributions of new exotic quarks to quark mixing”. In: *JHEP* 09 (2000), p. 011. DOI: 10.1088/1126-6708/2000/09/011. arXiv: hep-ph/0007316.

[207] C. Bobeth, A. J. Buras, A. Celis, and M. Jung. “Patterns of Flavour Violation in Models with Vector-Like Quarks”. In: *JHEP* 04 (2017), p. 079. DOI: 10.1007/JHEP04(2017)079. arXiv: 1609.04783 [hep-ph].

[208] M. Chala. “Direct bounds on heavy toplike quarks with standard and exotic decays”. In: *Phys. Rev. D* 96.1 (2017), p. 015028. DOI: 10.1103/PhysRevD.96.015028. arXiv: 1705.03013 [hep-ph].

[209] M. Aaboud et al. “Search for pair production of heavy vector-like quarks decaying into high-p_T W bosons and top quarks in the lepton-plus-jets final state in pp collisions at $\sqrt{s} = 13$ TeV with the ATLAS detector”. In: *JHEP* 08 (2018), p. 048. DOI: 10.1007/JHEP08(2018)048. arXiv: 1806.01762 [hep-ex].

[210] M. Aaboud et al. “Search for new phenomena in events with same-charge leptons and b-jets in pp collisions at $\sqrt{s} = 13$ TeV with the ATLAS detector”. In: *JHEP* 12 (2018), p. 039. DOI: 10.1007/JHEP12(2018)039. arXiv: 1807.11883 [hep-ex].

[211] M. Cirelli, N. Fornengo, and A. Strumia. “Minimal dark matter”. In: *Nucl. Phys. B* 753 (2006), pp. 178–194. DOI: 10.1016/j.nuclphysb.2006.07.012. arXiv: hep-ph/0512090.

[212] CMS collaboration. “Determination of the strong coupling constant from the measurement of inclusive multijet event cross sections in pp collisions at $\sqrt{s}$=8 TeV”. In: *CMS-PAS-SMP-16-008* (Feb. 2017).

[213] V. Khachatryan et al. “Measurement and QCD analysis of double-differential inclusive jet cross sections in pp collisions at $\sqrt{s} = 8$ TeV and cross section ratios to 2.76 and 7 TeV”. In: *JHEP* 03 (2017), p. 156. DOI: 10.1007/JHEP03(2017)156. arXiv: 1609.05331 [hep-ex].

[214] M. Aaboud et al. “Determination of the strong coupling constant α_s from transverse energy-energy correlations in multijet events at $\sqrt{s}$=8TeV using the ATLAS detector”. In: *Eur. Phys. J. C* 77.12 (2017), p. 872. DOI: 10.1140/epjc/s10052-017-5442-0. arXiv: 1707.02562 [hep-ex].

[215] P. Loch. “Inclusive jet measurements with the ATLAS experiment at the LHC”. In: *PoS* ICHEP2020 (2021), p. 482. DOI: 10.22323/1.390.0482.

[216] P. Zyla et al. “Review of Particle Physics”. In: *PTEP* 2020.8 (2020), p. 083C01. DOI: 10.1093/ptep/ptaa104.

[217] G. Aad et al. “Search for pair production of a new heavy quark that decays into a W boson and a light quark in pp collisions at $\sqrt{s} = 8$ TeV with the ATLAS detector”. In: *Phys. Rev. D* 92.11 (2015), p. 112007. DOI: 10.1103/PhysRevD.92.112007. arXiv: 1509.04261 [hep-ex].

[218] M. Aaboud et al. “Search for pair production of heavy vector-like quarks decaying to high-p_T W bosons and b quarks in the lepton-plus-jets final state in pp collisions at $\sqrt{s} = 13$ TeV with the ATLAS detector”. In: *JHEP* 10 (2017), p. 141. DOI: 10.1007/JHEP10(2017)141. arXiv: 1707.03347 [hep-ex].

[219] M. Aaboud et al. “Combination of the searches for pair-produced vector-like partners of the third-generation quarks at $\sqrt{s} = 13$ TeV with the ATLAS detector”. In: *Phys. Rev. Lett.* 121.21 (2018), p. 211801. DOI: 10.1103/PhysRevLett.121.211801. arXiv: 1808.02343 [hep-ex].

[220] M. Aaboud et al. “Search for single production of vector-like quarks decaying into Wb in pp collisions at $\sqrt{s} = 13$ TeV with the ATLAS detector”. In: *JHEP* 05 (2019), p. 164. DOI: 10.1007/JHEP05(2019)164. arXiv: 1812.07343 [hep-ex].

[221] A. M. Sirunyan et al. “Search for pair production of vector-like quarks in the $\mathrm{bW\overline{b}W}$ channel from proton-proton collisions at $\sqrt{s} = 13$ TeV”. In: *Phys. Lett. B* 779 (2018), pp. 82–106. DOI: 10.1016/j.physletb.2018.01.077. arXiv: 1710.01539 [hep-ex].

[222] A. M. Sirunyan et al. “Search for vectorlike light-flavor quark partners in proton-proton collisions at $\sqrt{s}$ =8 TeV”. In: *Phys. Rev. D* 97 (2018), p. 072008. DOI: 10.1103/PhysRevD.97.072008. arXiv: 1708.02510 [hep-ex].

[223] A. M. Sirunyan et al. “Search for vector-like T and B quark pairs in final states with leptons at $\sqrt{s} = 13$ TeV”. In: *JHEP* 08 (2018), p. 177. DOI: 10.1007/JHEP08(2018)177. arXiv: 1805.04758 [hep-ex].

[224] A. M. Sirunyan et al. “Search for vector-like quarks in events with two oppositely charged leptons and jets in proton-proton collisions at $\sqrt{s} = 13$ TeV”. In: *Eur. Phys. J. C* 79.4 (2019), p. 364. DOI: 10.1140/epjc/s10052-019-6855-8. arXiv: 1812.09768 [hep-ex].

[225] A. M. Sirunyan et al. “A search for bottom-type, vector-like quark pair production in a fully hadronic final state in proton-proton collisions at $\sqrt{s} = 13$ TeV”. In: *Phys. Rev. D* 102 (2020), p. 112004. DOI: 10.1103/PhysRevD.102.112004. arXiv: 2008.09835 [hep-ex].

[226] B. Holdom. “Two U(1)’s and Epsilon Charge Shifts”. In: *Phys. Lett. B* 166 (1986), pp. 196–198. DOI: 10.1016/0370-2693(86)91377-8.

[227] L. Di Luzio, M. Kirk, A. Lenz, and T. Rauh. “ΔM_s theory precision confronts flavour anomalies”. In: *JHEP* 12 (2019), p. 009. DOI: 10.1007/JHEP12(2019)009. arXiv: 1909.11087 [hep-ph].

[228] S. Dwivedi, D. Kumar Ghosh, A. Falkowski, and N. Ghosh. “Associated Z' production in the flavorful $U(1)$ scenario for $R_{K^{(*)}}$”. In: *Eur. Phys. J. C* 80.3 (2020), p. 263. DOI: 10.1140/epjc/s10052-020-7810-4. arXiv: 1908.03031 [hep-ph].

[229] M. Chala, A. Lenz, A. V. Rusov, and J. Scholtz. “ΔA_{CP} within the Standard Model and beyond”. In: *JHEP* 07 (2019), p. 161. DOI: 10.1007/JHEP07(2019)161. arXiv: 1903.10490 [hep-ph].

[230] R. Bause, M. Golz, G. Hiller, and A. Tayduganov. “The new physics reach of null tests with $D \to \pi\ell\ell$ and $D_s \to K\ell\ell$ decays”. In: *Eur. Phys. J. C* 80.1 (2020). [Erratum: Eur.Phys.J.C 81, 219 (2021)], p. 65. DOI: 10.1140/epjc/s10052-020-7621-7. arXiv: 1909.11108 [hep-ph].

[231] Y. S. Amhis et al. “Averages of b-hadron, c-hadron, and τ-lepton properties as of 2021”. In: *Phys. Rev. D* 107.5 (2023), p. 052008. DOI: 10.1103/PhysRevD.107.052008. arXiv: 2206.07501 [hep-ex].

[232] J. Kang and P. Langacker. “Z ’ discovery limits for supersymmetric E(6) models”. In: *Phys. Rev. D* 71 (2005), p. 035014. DOI: 10.1103/PhysRevD.71.035014. arXiv: hep-ph/0412190.

[233] T. Steudtner. “Safe Z' for LFUV”. In: *56th Rencontres de Moriond on Electroweak Interactions and Unified Theories*. May 2022. arXiv: 2205.06646 [hep-ph].

[234] “Test of lepton universality in $b \to s\ell^+\ell^-$ decays”. In: (Dec. 2022). arXiv: 2212.09152 [hep-ex].

[235] “Measurement of lepton universality parameters in $B^+ \to K^+\ell^+\ell^-$ and $B^0 \to K^{*0}\ell^+\ell^-$ decays”. In: (Dec. 2022). arXiv: 2212.09153 [hep-ex].

[236] B. Capdevila, A. Crivellin, and J. Matias. “Review of Semileptonic B Anomalies”. In: (Sept. 2023). arXiv: 2309.01311 [hep-ph].

[237] B. Allanach and J. Davighi. “The Rumble in the Meson: a leptoquark versus a Z’ to fit b $\to$ s$\mu^+\mu^-$ anomalies including 2022 LHCb $R_{K^{(*)}}$ measurements”. In: *JHEP* 04 (2023), p. 033. DOI: 10.1007/JHEP04(2023)033. arXiv: 2211.11766 [hep-ph].

[238] M. Algueró, A. Biswas, B. Capdevila, S. Descotes-Genon, J. Matias, and M. Novoa-Brunet. “To (b)e or not to (b)e: no electrons at LHCb”. In: *Eur. Phys. J. C* 83.7 (2023), p. 648. DOI: `10.1140/epjc/s10052-023-11824-0`. arXiv: `2304.07330 [hep-ph]`.

[239] G. Hiller and F. Kruger. “More model-independent analysis of $b \to s$ processes”. In: *Phys. Rev. D* 69 (2004), p. 074020. DOI: `10.1103/PhysRevD.69.074020`. arXiv: `hep-ph/0310219`.

[240] R. Bause, H. Gisbert, M. Golz, and G. Hiller. “Interplay of dineutrino modes with semileptonic rare B-decays”. In: *JHEP* 12 (2021), p. 061. DOI: `10.1007/JHEP12(2021)061`. arXiv: `2109.01675 [hep-ph]`.

[241] D. M. Straub. “flavio: a Python package for flavour and precision phenomenology in the Standard Model and beyond”. In: (Oct. 2018). arXiv: `1810.08132 [hep-ph]`.

[242] G. Hiller, D. Loose, and I. Nišandžić. “Flavorful leptoquarks at the LHC and beyond: spin 1”. In: *JHEP* 06 (2021), p. 080. DOI: `10.1007/JHEP06(2021)080`. arXiv: `2103.12724 [hep-ph]`.

[243] A. M. Sirunyan et al. “Search for resonant and nonresonant new phenomena in high-mass dilepton final states at $\sqrt{s} = 13$ TeV”. In: *JHEP* 07 (2021), p. 208. DOI: `10.1007/JHEP07(2021)208`. arXiv: `2103.02708 [hep-ex]`.

[244] B. C. Allanach. “$U(1)_{B_3-L_2}$ explanation of the neutral current B—anomalies”. In: *Eur. Phys. J. C* 81.1 (2021). [Erratum: Eur.Phys.J.C 81, 321 (2021)], p. 56. DOI: `10.1140/epjc/s10052-021-08855-w`. arXiv: `2009.02197 [hep-ph]`.

[245] B. Allanach and A. Mullin. “Plan B: New Z' models for $b \to sl^+l^-$ anomalies”. In: (June 2023). arXiv: `2306.08669 [hep-ph]`.

[246] B. C. Allanach and J. Davighi. “Naturalising the third family hypercharge model for neutral current B-anomalies”. In: *Eur. Phys. J. C* 79.11 (2019), p. 908. DOI: `10.1140/epjc/s10052-019-7414-z`. arXiv: `1905.10327 [hep-ph]`.

[247] B. Allanach and E. Loisa. “Flavonstrahlung in the $\mathrm{B_3}-\mathrm{L_2}$Z’ model at current and future colliders”. In: *JHEP* 03 (2023), p. 253. DOI: `10.1007/JHEP03(2023)253`. arXiv: `2212.07440 [hep-ph]`.

[248] A. Falkowski and K. Mimouni. “Model independent constraints on four-lepton operators”. In: *JHEP* 02 (2016), p. 086. DOI: `10.1007/JHEP02(2016)086`. arXiv: `1511.07434 [hep-ph]`.

[249] A. A. Babich, G. Della Ricca, J. Holt, P. Osland, A. A. Pankov, and N. Paver. “Model independent constraints on contact interactions from LEP-2 data analysis”. In: *Eur. Phys. J. C* 29 (2003), pp. 103–109. DOI: `10.1140/epjc/s2003-01206-5`. arXiv: `hep-ph/0212163`.

[250] J. Brod, M. Gorbahn, and E. Stamou. “Updated Standard Model Prediction for $K \to \pi\nu\bar{\nu}$ and ϵ_K”. In: *PoS* BEAUTY2020 (2021), p. 056. DOI: `10.22323/1.391.0056`. arXiv: `2105.02868 [hep-ph]`.

[251] A. J. Buras, J. Girrbach-Noe, C. Niehoff, and D. M. Straub. “$B \to K^{(*)}\nu\bar{\nu}$ decays in the Standard Model and beyond”. In: *JHEP* 02 (2015), p. 184. DOI: `10.1007/JHEP02(2015)184`. arXiv: `1409.4557 [hep-ph]`.

[252] W. Altmannshofer et al. “The Belle II Physics Book”. In: *PTEP* 2019.12 (2019). Ed. by E. Kou and P. Urquijo. [Erratum: PTEP 2020, 029201 (2020)], p. 123C01. DOI: `10.1093/ptep/ptz106`. arXiv: `1808.10567 [hep-ex]`.

[253] G. Paz and J. Roy. “Remarks on the Z’ Drell-Yan cross section”. In: *Phys. Rev. D* 97.7 (2018), p. 075025. DOI: `10.1103/PhysRevD.97.075025`. arXiv: `1711.02655 [hep-ph]`.

[254] B. C. Allanach, J. M. Butterworth, and T. Corbett. “Collider constraints on Z' models for neutral current B-anomalies”. In: *JHEP* 08 (2019), p. 106. DOI: `10.1007/JHEP08(2019)106`. arXiv: `1904.10954 [hep-ph]`.

[255] B. C. Allanach, J. M. Butterworth, and T. Corbett. “Large hadron collider constraints on some simple Z' models for $b \to s\mu^+\mu^-$ anomalies”. In: *Eur. Phys. J. C* 81.12 (2021), p. 1126. DOI: `10.1140/epjc/s10052-021-09919-7`. arXiv: `2110.13518 [hep-ph]`.

[256] K. Long, D. Lucchesi, M. Palmer, N. Pastrone, D. Schulte, and V. Shiltsev. “Muon colliders to expand frontiers of particle physics”. In: *Nature Phys.* 17.3 (2021), pp. 289–292. DOI: `10.1038/s41567-020-01130-x`. arXiv: `2007.15684 [physics.acc-ph]`.

[257] G.-y. Huang, S. Jana, F. S. Queiroz, and W. Rodejohann. “Probing the RK(*) anomaly at a muon collider”. In: *Phys. Rev. D* 105.1 (2022), p. 015013. DOI: `10.1103/PhysRevD.105.015013`. arXiv: `2103.01617 [hep-ph]`.

[258] G. Hiller and M. Schmaltz. “Diagnosing lepton-nonuniversality in $b \to s\ell\ell$”. In: *JHEP* 02 (2015), p. 055. DOI: `10.1007/JHEP02(2015)055`. arXiv: `1411.4773 [hep-ph]`.

[259] A. Greljo, J. Salko, A. Smolkovič, and P. Stangl. “Rare b decays meet high-mass Drell-Yan”. In: *JHEP* 05 (2023), p. 087. DOI: `10.1007/JHEP05(2023)087`. arXiv: `2212.10497 [hep-ph]`.

[260] M. Ciuchini, M. Fedele, E. Franco, A. Paul, L. Silvestrini, and M. Valli. “Constraints on lepton universality violation from rare B decays”. In: *Phys. Rev. D* 107.5 (2023), p. 055036. DOI: `10.1103/PhysRevD.107.055036`. arXiv: `2212.10516 [hep-ph]`.

[261] T. Hurth, F. Mahmoudi, and S. Neshatpour. “B anomalies in the post-RK(*) era”. In: *Phys. Rev. D* 108.11 (2023), p. 115037. DOI: `10.1103/PhysRevD.108.115037`. arXiv: `2310.05585 [hep-ph]`.

[262] B. Capdevila. “Status of the global $b \to s\ell^+\ell^-$ fits”. In: *PoS* FPCP2023 (Oct. 2023), p. 010. DOI: `10.22323/1.445.0010`.

[263] N. Gubernari, M. Reboud, D. van Dyk, and J. Virto. “Dispersive Analysis of $B \to K^{(*)}$ and $B_s \to \phi$ Form Factors”. In: *JHEP* 12 (2023), p. 153. DOI: `10.1007/JHEP12(2023)153`. arXiv: `2305.06301 [hep-ph]`.

[264] B. Allanach, F. S. Queiroz, A. Strumia, and S. Sun. “Z' models for the LHCb and $g-2$ muon anomalies”. In: *Phys. Rev. D* 93.5 (2016). [Erratum: Phys.Rev.D 95, 119902 (2017)], p. 055045. DOI: `10.1103/PhysRevD.93.055045`. arXiv: `1511.07447 [hep-ph]`.

[265] R. Fleischer, E. Malami, A. Rehult, and K. K. Vos. “New Perspectives for Testing Electron-Muon Universality”. In: (Mar. 2023). arXiv: `2303.08764 [hep-ph]`.

[266] L. Di Luzio, M. Kirk, and A. Lenz. “B_s-$\bar{B}_s$ mixing interplay with B anomalies”. In: *10th International Workshop on the CKM Unitarity Triangle*. Nov. 2018. arXiv: `1811.12884 [hep-ph]`.

[267] B. Grinstein, M. J. Savage, and M. B. Wise. “B —> X(s) e+ e- in the Six Quark Model”. In: *Nucl. Phys. B* 319 (1989), pp. 271–290. DOI: `10.1016/0550-3213(89)90078-3`.

[268] A. J. Buras and M. Munz. “Effective Hamiltonian for B —> X(s) e+ e- beyond leading logarithms in the NDR and HV schemes”. In: *Phys. Rev. D* 52 (1995), pp. 186–195. DOI: `10.1103/PhysRevD.52.186`. arXiv: `hep-ph/9501281`.

[269] C. Cornella, G. Isidori, M. König, S. Liechti, P. Owen, and N. Serra. “Hunting for $B^+ \to K^+\tau^+\tau^-$ imprints on the $B^+ \to K^+\mu^+\mu^-$ dimuon spectrum”. In: *Eur. Phys. J. C* 80.12 (2020), p. 1095. DOI: `10.1140/epjc/s10052-020-08674-5`. arXiv: `2001.04470 [hep-ph]`.

[270] J. P. Lees et al. “Search for $B^+ \to K^+\tau^+\tau^-$ at the BaBar experiment”. In: *Phys. Rev. Lett.* 118.3 (2017), p. 031802. DOI: `10.1103/PhysRevLett.118.031802`. arXiv: `1605.09637 [hep-ex]`.

[271] A. Crivellin and M. Kirk. “Diquark explanation of b→sℓ+ℓ-”. In: *Phys. Rev. D* 108.11 (2023), p. L111701. DOI: `10.1103/PhysRevD.108.L111701`. arXiv: `2309.07205 [hep-ph]`.

[272] R. Gauld, F. Goertz, and U. Haisch. “An explicit Z’-boson explanation of the $B \to K^*\mu^+\mu^-$ anomaly”. In: *JHEP* 01 (2014), p. 069. DOI: 10.1007/JHEP01(2014)069. arXiv: 1310.1082 [hep-ph].

[273] A. J. Buras, F. De Fazio, J. Girrbach, and M. V. Carlucci. “The Anatomy of Quark Flavour Observables in 331 Models in the Flavour Precision Era”. In: *JHEP* 02 (2013), p. 023. DOI: 10.1007/JHEP02(2013)023. arXiv: 1211.1237 [hep-ph].

[274] A. J. Buras. “Z'-Tandem Mechanism for the Suppression of New Physics in Quark Mixing with Implications for K, D and B Decays”. In: (Feb. 2023). arXiv: 2302.01354 [hep-ph].

[275] M. Fernández Navarro and S. F. King. “Tri-hypercharge: a separate gauged weak hypercharge for each fermion family as the origin of flavour”. In: *JHEP* 08 (2023), p. 020. DOI: 10.1007/JHEP08(2023)020. arXiv: 2305.07690 [hep-ph].

[276] A. Khodjamirian and A. A. Petrov. “Direct CP asymmetry in $D \to \pi^-\pi^+$ and $D \to K^-K^+$ in QCD-based approach”. In: *Phys. Lett. B* 774 (2017), pp. 235–242. DOI: 10.1016/j.physletb.2017.09.070. arXiv: 1706.07780 [hep-ph].

[277] A. Pich, E. Solomonidi, and L. Vale Silva. “Final-state interactions in the CP asymmetries of charm-meson two-body decays”. In: *Phys. Rev. D* 108.3 (2023), p. 036026. DOI: 10.1103/PhysRevD.108.036026. arXiv: 2305.11951 [hep-ph].

[278] A. Lenz, M. L. Piscopo, and A. V. Rusov. “Two body non-leptonic D^0 decays from LCSR and implications for Δa_{CP}^{dir}”. In: (Dec. 2023). arXiv: 2312.13245 [hep-ph].

[279] S. Schacht. “A U-spin anomaly in charm CP violation”. In: *JHEP* 03 (2023), p. 205. DOI: 10.1007/JHEP03(2023)205. arXiv: 2207.08539 [hep-ph].

[280] R. Bause, H. Gisbert, M. Golz, and G. Hiller. “Exploiting CP-asymmetries in rare charm decays”. In: *Phys. Rev. D* 101.11 (2020), p. 115006. DOI: 10.1103/PhysRevD.101.115006. arXiv: 2004.01206 [hep-ph].

[281] Y. Grossman, A. L. Kagan, and Y. Nir. “New physics and CP violation in singly Cabibbo suppressed D decays”. In: *Phys. Rev. D* 75 (2007), p. 036008. DOI: 10.1103/PhysRevD.75.036008. arXiv: hep-ph/0609178.

[282] J. Fuentes-Martin, A. Greljo, J. Martin Camalich, and J. D. Ruiz-Alvarez. “Charm physics confronts high-p_T lepton tails”. In: *JHEP* 11 (2020), p. 080. DOI: 10.1007/JHEP11(2020)080. arXiv: 2003.12421 [hep-ph].

[283] R. Aaij et al. “Search for Rare Decays of D0 Mesons into Two Muons”. In: *Phys. Rev. Lett.* 131.4 (2023), p. 041804. DOI: 10.1103/PhysRevLett.131.041804. arXiv: 2212.11203 [hep-ex].

[284] H. Gisbert, M. Golz, and D. S. Mitzel. “Theoretical and experimental status of rare charm decays”. In: *Mod. Phys. Lett. A* 36.04 (2021), p. 2130002. DOI: 10.1142/S0217732321300020. arXiv: 2011.09478 [hep-ph].

[285] M. Ablikim et al. “Search for the decay $D^0 \to \pi^0\nu\bar{\nu}$”. In: *Phys. Rev. D* 105.7 (2022), p. L071102. DOI: 10.1103/PhysRevD.105.L071102. arXiv: 2112.14236 [hep-ex].

[286] R. Bause, H. Gisbert, M. Golz, and G. Hiller. “Rare charm $c \to u\nu\bar{\nu}$ dineutrino null tests for e^+e^- machines”. In: *Phys. Rev. D* 103.1 (2021), p. 015033. DOI: 10.1103/PhysRevD.103.015033. arXiv: 2010.02225 [hep-ph].

[287] A. M. Sirunyan et al. “Search for Low-Mass Quark-Antiquark Resonances Produced in Association with a Photon at $\sqrt{s}$ =13 TeV”. In: *Phys. Rev. Lett.* 123.23 (2019), p. 231803. DOI: 10.1103/PhysRevLett.123.231803. arXiv: 1905.10331 [hep-ex].

[288] B. A. Dobrescu and F. Yu. “Dijet and electroweak limits on a Z' boson coupled to quarks”. In: (Dec. 2021). arXiv: `2112.05392 [hep-ph]`.

[289] B. A. Dobrescu and C. Frugiuele. “Hidden GeV-scale interactions of quarks”. In: *Phys. Rev. Lett.* 113 (2014), p. 061801. DOI: `10.1103/PhysRevLett.113.061801`. arXiv: `1404.3947 [hep-ph]`.

[290] A. Aranda and C. D. Carone. “Limits on a light leptophobic gauge boson”. In: *Phys. Lett. B* 443 (1998), pp. 352–358. DOI: `10.1016/S0370-2693(98)01309-4`. arXiv: `hep-ph/9809522`.

[291] B. Batell et al. “Hadrophilic dark sectors at the Forward Physics Facility”. In: *Phys. Rev. D* 105.7 (2022), p. 075001. DOI: `10.1103/PhysRevD.105.075001`. arXiv: `2111.10343 [hep-ph]`.

[292] D. C. Bailey and S. Davidson. “Is there a vector boson coupling to baryon number?” In: *Phys. Lett. B* 348 (1995), pp. 185–189. DOI: `10.1016/0370-2693(95)00052-M`. arXiv: `hep-ph/9411355`.

[293] S. Cheng, A. Khodjamirian, and A. V. Rusov. “Pion light-cone distribution amplitude from the pion electromagnetic form factor”. In: *Phys. Rev. D* 102.7 (2020), p. 074022. DOI: `10.1103/PhysRevD.102.074022`. arXiv: `2007.05550 [hep-ph]`.

[294] C. Bruch, A. Khodjamirian, and J. H. Kuhn. “Modeling the pion and kaon form factors in the timelike region”. In: *Eur. Phys. J. C* 39 (2005), pp. 41–54. DOI: `10.1140/epjc/s2004-02064-3`. arXiv: `hep-ph/0409080`.

[295] R. Baldini Ferroli, A. Mangoni, and S. Pacetti. “G-parity violating amplitudes in the $J/\psi \to \pi^+\pi^-$ decay”. In: *Phys. Rev. C* 98.4 (2018), p. 045210. DOI: `10.1103/PhysRevC.98.045210`. arXiv: `1611.04437 [hep-ph]`.

[296] S. Centelles Chuliá, R. Srivastava, and A. Vicente. “The inverse seesaw family: Dirac and Majorana”. In: *JHEP* 03 (2021), p. 248. DOI: `10.1007/JHEP03(2021)248`. arXiv: `2011.06609 [hep-ph]`.

[297] M. Fabbrichesi, E. Gabrielli, and G. Lanfranchi. “The Dark Photon”. In: (May 2020). DOI: `10.1007/978-3-030-62519-1`. arXiv: `2005.01515 [hep-ph]`.

[298] P. Ilten, Y. Soreq, M. Williams, and W. Xue. “Serendipity in dark photon searches”. In: *JHEP* 06 (2018), p. 004. DOI: `10.1007/JHEP06(2018)004`. arXiv: `1801.04847 [hep-ph]`.

[299] R. Aaij et al. “Search for $A' \to \mu^+\mu^-$ Decays”. In: *Phys. Rev. Lett.* 124.4 (2020), p. 041801. DOI: `10.1103/PhysRevLett.124.041801`. arXiv: `1910.06926 [hep-ex]`.

[300] M. Campajola. “Dark Sector first results at Belle II”. In: *Phys. Scripta* 96.8 (2021), p. 084005. DOI: `10.1088/1402-4896/abfef2`. arXiv: `2208.01101 [hep-ex]`.

[301] M. Ablikim et al. “Search for invisible decays of a dark photon using e+e− annihilation data at BESIII”. In: *Phys. Lett. B* 839 (2023), p. 137785. DOI: `10.1016/j.physletb.2023.137785`. arXiv: `2209.13893 [hep-ex]`.

[302] J. P. Lees et al. “Search for Invisible Decays of a Dark Photon Produced in e^+e^- Collisions at BaBar”. In: *Phys. Rev. Lett.* 119.13 (2017), p. 131804. DOI: `10.1103/PhysRevLett.119.131804`. arXiv: `1702.03327 [hep-ex]`.

[303] B. Bhattacharya, S. Kumbhakar, D. London, and N. Payot. “U-spin puzzle in B decays”. In: *Phys. Rev. D* 107.1 (2023), p. L011505. DOI: `10.1103/PhysRevD.107.L011505`. arXiv: `2211.06994 [hep-ph]`.

Glossary

ACC anomaly cancellation condition. 76, 77

ADM anomalous dimension matrix. 10

AF asymptotic freedom. 1, 16, 24, 26, 27, 29

AS asymptotic safety. 1, 16–18, 42, 48, 61, 116

BAU baryon asymmetry of the universe. 1, 7

BM benchmark model. 86, 88–90, 92, 95–98, 100, 104–109, 111, 112, 114, 115

BSM physics beyond the Standard Model. 1–3, 7, 8, 10, 16–18, 20–34, 37, 38, 40, 42–55, 57–67, 70–77, 79, 81–85, 89–98, 100–102, 114–117, 120–123, 125

c.l. confidence level. 37, 40, 55, 67, 68, 79, 80, 96, 101, 102, 104, 107, 108

CKM Cabibbo-Kobayashi-Maskawa. 2, 6, 7, 41, 68, 70, 79, 81, 83, 85, 87, 103, 119

d.o.f. degrees of freedom. 5, 8, 48, 110, 125

EFT effective field theory. 2, 3, 8–11, 18, 81, 98–100, 110, 114, 115

EW electroweak. 42, 67, 69, 72, 78, 87, 88, 97, 114, 115, 117

EWSB electroweak symmetry breaking. 3–6, 10, 55, 68, 77, 78, 86

FCNC flavor changing neutral current. 2, 7, 8, 11, 39, 41, 42, 48, 68, 76, 78, 79, 81, 84, 87, 97, 105, 116, 117

FP fixed point. 16–18, 51

GIM Glashow-Iliopolus-Maiani. 2, 79

GUT grand unified theory. 17, 42

GY gauge-Yukawa. 1, 12, 13, 16, 17, 23, 48, 61

HFLAV Heavy Flavor Averaging Group. 80, 104

IR infrared. 14, 17

ISR initial state radiation. 108, 112

LFU lepton flavor universality. 2, 11, 81, 82, 98–100, 102

LFUV lepton flavor universality violating. 82

LFUV lepton flavor universality violation. 100

LFV lepton flavor violating. 11, 41, 78, 87

LFV lepton flavor violation. 7, 41

LH left-handed. 3, 4, 6, 23, 69, 83, 85, 95–97, 118

LHC Large Hadron Collider. 1, 22, 31, 69, 71, 84, 98

LHCb Large Hadron Collider beauty. 1, 8, 82, 98, 100, 102

LHS left-hand side. 109

LO leading order. 9, 11, 54, 79, 80, 96, 97, 104

NP new physics. 1, 2, 7, 8, 10, 11, 18, 20, 21, 24, 43, 62, 67, 72, 77–79, 81–83, 86, 88, 92, 94, 95, 97–102, 107, 109, 113, 114, 117

PDF parton distribution function. 89, 96

PMNS Pontecorvo-Maki-Nakagawa-Sakata. 7, 85

PS Planck safety. iii, 1, 2, 16, 18, 20, 21, 26–29, 31–38, 40–43, 46, 48–54, 60, 61, 63–68, 71, 73, 75, 76, 81, 84, 89, 90, 92, 94, 95, 98, 114–117, 125

QCD quantum chromodynamics. 1, 3, 10, 13, 25, 82, 96, 110

QED quantum electrodynamics. 3, 10, 13

QFT quantum field theory. 1, 3, 12, 17, 76

RG renormalization group. iii, 1, 11–31, 33–38, 42–45, 47, 48, 50, 51, 53, 55, 58, 60–67, 75–78, 80, 82, 83, 85, 89–92, 94, 95, 103, 104, 111, 113–117

RGE renormalization group equation. 1, 2, 12, 13, 16–18, 21–23, 45, 63, 114–116

RH right-handed. 3, 4, 7, 23, 69, 76, 77, 84, 85, 87, 89, 92, 95–98, 105, 108, 110, 118

RHS right-hand side. 80, 109

SM Standard Model of particle physics. 1–45, 47, 48, 50, 51, 54–56, 59–61, 63, 65, 67–73, 75–85, 92, 95–101, 103, 104, 109, 110, 112, 114, 116, 118, 119, 121–123

SMEFT Standard Model Effective Field Theory. 2, 10, 11, 37, 40, 42, 61, 66–68, 73, 75, 82, 100, 117

SSB spontaneous symmetry breaking. 5, 43, 44, 54, 116, 123

UV ultraviolet. 1, 2, 8–10, 12–18, 21, 26, 35, 37, 76, 114, 115, 117

VEV vacuum expectation value. 5, 6, 54, 55, 72, 86, 123, 125

VLF vector-like fermion. 1, 2, 17, 23, 24, 26, 28, 29, 31–36, 38–42, 60–62, 66, 76, 81, 98, 107, 108, 112–114, 116, 117, 120–122

VLL vector-like lepton. 28–31, 38, 41, 61, 62, 72, 121, 122

VLQ vector-like quark. 26, 27, 38, 41, 42, 61, 65, 68–70, 72–75, 116

WC Wilson coefficient. 8–11, 40, 66–68, 82, 83, 86–89, 92, 97–102, 104, 117

WET Weak Effective Theory. 2, 11, 81, 82, 86, 99, 101, 102, 104, 110, 114, 117